ADAPTING A CRYOGEN-FREE MEASUREMENT SYSTEM FOR GEOLOGICAL MATERIALS: METHOD DEVELOPMENT FOR THERMAL CONDUCTIVITY MEASUREMENTS BELOW 300 K WITH APPLICATIONS TO PLANETARY SCIENCE

COSETTE M. GILMOUR

A DISSERTATION SUBMITTED TO THE FACULTY OF GRADUATE STUDIES IN PARTIAL FULFILLMENT OF THE REQUIREMENTS FOR THE DEGREE OF DOCTOR OF PHILOSOPHY

GRADUATE PROGRAM IN EARTH AND SPACE SCIENCE
YORK UNIVERSITY
TORONTO, ONTARIO

July, 2025

© Cosette M. Gilmour, 2025

Abstract

The thermal properties of airless planetary bodies like asteroids are essential to understanding their thermal evolution. While remote sensing missions collect thermal data, this is limited to surface properties. As such, little is known about internal heat flow. Thermal models are used to predict thermal evolution, but the limited availability of thermal property data constrains their accuracy. To improve these models, meteorites provide a way to investigate thermal properties under controlled laboratory conditions, as they are preserved fragments of planetary bodies. This study reports thermal conductivity measurements of meteorites between 5 and 300 K under vacuum ($< 10^{-4}$ mbar), acquired using a Cryogen-Free Measurement System (CFMS) that was adapted for geological applications. Measurements were first collected for single-crystal minerals and obsidian to refine sample preparation and measurement procedures. This included developing techniques for handling friable samples, establishing thermal equilibration protocols, and implementing a data quality assessment method based on empirical observations of instrument performance. Above 100 K, radiative heat loss contributes to the measured thermal conductivity, resulting in values that exceed the true conductive behaviour. A correction procedure was applied using low-temperature model fits specific to each material. The single-crystal minerals exhibit anisotropic thermal conductivity and show trends consistent with phonon-dominated transport, where thermal conductivity is expected to increase as T^3 at low temperatures, peak, and then decrease as $1/T$ at higher temperatures; however, this full behaviour was not always observed within the measured range. In contrast, obsidian shows a plateau followed by a gradual increase in thermal conductivity with temperature, consistent with the behaviour of amorphous solids. Meteorites exhibit more complex behaviour. Despite being composed mainly of crystalline materials, phonon transport is suppressed by porosity and grain boundaries, resulting in thermal conductivity trends similar to disordered materials. These factors also drive anisotropy due to structural heterogeneity. The results of this study agree well with literature values, validating the use of the CFMS for geological analysis. The data collected in this study will support improved modelling of heat flow in small planetary bodies.

Dedication

For David, my loving husband.

Here's to *our* thesis, girl dinners, and a broken washing machine.

Acknowledgments

I want to extend a special, heartfelt thank you to two people I consider my unofficial co-supervisors: Jim Freemantle—without you, there would be no PhD. Thank you for your patience, dedication, and EMF powers. Dr. Emmanuel Lalla, who stepped in during the final months of writing this dissertation. There are honestly no words to express how grateful I am for the time you took to read my dissertation and provide awesome feedback.

Thank you to my supervisor, Mike, who became an expert at handling my existential crises. I am grateful for you not giving up on me, and having the patience and understanding to allow me to finish at my own pace.

I must thank my lil sis, Dr. Aleks Gawronska! You have been such a rock throughout this journey. We have been through so much together, raising puppies, getting married, and completing our PhDs! Thank you for listening to all my rants and the co-working sessions.

Thank you to all my friends and family who have been along this journey with me. Your support has been so wonderful throughout this journey.

My parents... Thank you. Thank you. Thank you. This has been the most challenging time of our lives, especially with the distance between us. Thank you for pushing me to keep going even when I wanted to stop. I miss you both terribly and I cannot wait to celebrate this huge accomplishment with you! I promise this is my last degree!!

I am forever grateful for my husband, David. Thank you for being a shoulder to cry on, the best cheerleader, for keeping the house together these last few months, and for always believing in me. I can't wait to see what is next for us! Te amo mi amor.

And in the famous words of Snoop Dogg:

> *I want to thank me. I want to thank me for believing in me. I want to thank me for doing all this hard work. I want to thank me for having no days off. I want to thank me for never quitting.*

Contents

Abstract ii

Dedication iii

Acknowledgments iv

Table of Contents v

List of Tables ix

List of Figures x

1 Introduction 1

1.1 Motivation 1

1.2 Objectives and Overview 3

1.3 Thermal Conductivity Investigations 5

1.3.1 Terrestrial Materials 5

1.3.2 Meteorites 7

2 Principles of Heat Transfer 11

2.1 Heat Transfer Processes 11

2.1.1 Conduction 11

2.1.2 Convection 13

2.1.3 Radiation 14

2.2 Thermal Conductivity 16

2.2.1 Kinetic Theory 16

2.2.2 Energy Carriers 20

2.2.3 Crystalline Insulators 21

2.2.4 Amorphous Solids 27
2.2.5 Summary 30

3 Cryogen-Free Measurement System 32

3.1 Instrument Design 32
3.1.1 System Overview 33
3.1.2 Thermal Probe 37
3.1.3 Heat Transfer Considerations 41
3.2 Measurement Configuration for Geological Samples 42
3.2.1 Analysis Method 43
3.2.2 Sample Geometry 45
3.2.3 Thermal Transport Settings 46
3.2.4 Thermalization Time 48
3.3 Data Analysis Methods 52
3.3.1 Sources of Uncertainty 52
3.3.2 Data Quality Check 54
3.3.3 Radiative Heat Loss 59
3.4 Copper Reference Sample 66
3.4.1 Results 68
3.4.2 Radiative Heat Loss Correction 68

4 Sample Selection, Preparation, and Characterization 74

4.1 Sample Selection 74
4.2 Sample Preparation 76
4.2.1 Attachment of Thermal Assemblies 78
4.3 Single-Crystal Minerals 90
4.3.1 Quartz 94
4.3.2 Calcite 96

4.3.3 Albite . . . 101
4.3.4 Pyrite . . . 104
4.3.5 Obsidian . . . 108
4.4 Meteorites . . . 109
4.4.1 Background Information . . . 109
4.4.2 Meteorite Samples . . . 112
4.4.3 Additional Analysis . . . 123

5 Results: Single-Crystal Minerals 127
5.1 Radiative Heat Loss Corrections . . . 127
5.2 Thermal Conductivity . . . 129
5.2.1 Results . . . 129
5.2.2 Discussion . . . 142
5.2.3 Conclusion . . . 152
5.3 Preliminary Obsidian Data . . . 153
5.4 Summary Table . . . 157

6 Results: Meteorites 159
6.1 Results . . . 160
6.1.1 Thermal Conductivity . . . 160
6.1.2 Density and Porosity . . . 171
6.2 Discussion and Conclusions . . . 178

7 Emissivity of Geological Samples 181
7.1 Introduction to Emissivity . . . 181
7.2 Single-Crystal Emissivity . . . 185
7.3 Meteorite Emissivity . . . 191
7.4 Thermal Assembly Considerations . . . 192

8 Conclusions and Future Work **195**

8.1 Conclusion 195

8.2 Future Work 198

References **200**

Appendices **234**

A CFMS Data Quality Check MATLAB Code **234**

A.1 Main MATLAB Script 234

A.2 MATLAB Function Files 244

A.3 Python Script for Configuration File Parsing 246

B Taylor Series Expansion of the Stefan–Boltzmann Law **247**

C Quantitative XRD Results for Minerals **248**

D Individual Thermal Conductivity Data (Uncorrected) **249**

E Average Emissivity Calculation **255**

List of Tables

1 Physical and thermal properties of selected meteorite types at 200 K. 10

3.2 Magnitude of uncertainties. 54

3.3 Coefficients used in Equation 3.15 to fit the trend of the copper wire data. . 70

4.1 Single crystal properties and dimensions 92

4.2 Summary of meteorites 122

4.3 Dimensions of meteorite samples. 122

5.1 Re-post of Table 4.1: Single crystal properties and dimensions 127

5.2 Best fit, temperature range, and R^2 values for the anisotropic minerals. . . . 129

5.3 Calcite measured and corrected thermal conductivity (k) at 300 K. 138

5.4 Reported thermal conductivity (k) values for quartz at 300 K. 144

5.5 Reported thermal conductivity (k) values for calcite at 300 K. 148

5.6 Reported thermal conductivity (k) values for albite at 300 K. 149

5.7 Reported thermal conductivity (k) values for pyrite at 300 K. 152

5.8 Summary of sample properties and thermal conductivity results for single-crystal minerals and obsidian. 158

6.1 Repost of Table 4.2: Summary of meteorites 159

6.2 Best-fit coefficients for ordinary chondrites using the model $k = \frac{aT^2+bT+c}{1+dT}$. . . 165

6.3 Meteorite physical properties 172

7.1 Calculated average emissivity values for single crystal samples. 186

C.1 Quantitative XRD results using a database standard (ICDD PDF-2). 248

List of Figures

2.1 Thermal conductivity of different materials as a function of temperature . . 20

2.2 The three primary phonon scattering mechanisms in insulators 22

2.3 Phonon-phonon scattering processes 23

2.4 Schematic plot of phonon mean free path vs. temperature 24

2.5 Schematic plot of heat capacity vs. temperature 25

2.6 Limitations in phonon-free mean based on crystal diameter and impurities . 26

2.7 Schematic plot of thermal conductivity vs. temperature controlled by heat capacity and mean free path 26

2.8 Atomic structure of crystalline vs. amorphous solids 27

2.9 Thermal conductivity of crystalline quartz and silica glass 28

2.10 Simplified schematic of temperature-dependent thermal conductivity 31

3.1 Image of the Cryogen Free Measurement System 32

3.2 Schematic diagram of the CFMS cooling process 34

3.3 Image of a Pulse Tube cryocooler used to cool the CFMS 35

3.4 Helium compressor connected to the CFMS 36

3.5 Thermal transport probe 37

3.6 Sample platform with a geological sample attached. 38

3.7 Sensitivity of E-type and K-type thermocouples 39

3.8 Configuration of the CFMS thermal transport probe 40

3.9 An example plot of heater power vs. ΔT for a quartz sample at 200 K . . . 44

3.10 Thermal conductivity measurements of a serpentinite rock sample demonstrating importance of thermalization 50

3.11 Thermal conductivity measurements of a calcite sample with varying thermalization times 51

3.12 Temperature of a calcite sample over time. 51

3.13 Example of a quality check for quartz at 150 K that satisfies all three quality criteria . . . 56
3.14 Example of a quality check for calcite at 10 K that satisfies all three quality criteria . . . 57
3.15 Example of a quality check output for an obsidian measurement at 100 K . . 57
3.16 Example of a quality check output for a pyrite measurement at 70 K 58
3.17 Thermal conductivity vs. temperature (<30 K) for a sample of calcite 58
3.18 Schematic of the sample configuration with thermal assemblies and temperature gradient . . . 60
3.19 Correction process for radiative heat loss . . . 64
3.20 NIST thermal conductivity vs. temperature of different copper purities . . . 67
3.21 Schematic of the mounting configuration of the copper wire sample. 67
3.22 Comparison of uncorrected thermal conductivity data of the copper wire over six years . . . 69
3.23 Comparison of measured and corrected thermal conductivity data of the copper wire . . . 70
3.24 Zoomed in version of Figure 3.23 . . . 71
3.25 Copper: Δk vs. T^3 . . . 71
3.26 Comparison of corrected copper thermal conductivity data with copper standards from NIST (2010). . . . 73
4.1 Low-speed saw used to cut samples . . . 77
4.2 Helping-hands station . . . 78
4.3 Step 1: Prepare heat sink connecting wire . . . 79
4.4 Step 2: Silver epoxy preparation . . . 80
4.5 Step 3: Attaching the heat sink connecting wire . . . 81
4.6 Step 4: Securing the sample for thermal assembly attachment . . . 82
4.7 Step 5: Preparing the sample for thermal assembly attachments . . . 84

4.8 Step 6: Heat assembly attachment 85
4.9 Step 7: Thermocouple assembly attachment 87
4.10 Step 8: Add epoxy around the sample at each assembly point 89
4.11 The seven crystal systems. Figure adapted from Davies (2013). 93
4.12 Quartz crystallographic system 94
4.13 Quartz-1 sample preparation ($\parallel$ c-axis) 95
4.14 Quartz-2 sample preparation ($\perp$ c-axis) 95
4.16 XRD pattern of quartz 96
4.15 Cut samples of Quartz-1 and Quartz-2 96
4.17 Calcite crystal system 97
4.18 XRD pattern of calcite 98
4.19 Calcite rhombohedral crystal cut into pieces. 98
4.20 Preparation of calcite sample 1a-4a-b 99
4.21 Preparation of calcite sample 1a-5d 99
4.22 Preparation of calcite sample 1a-6-1 100
4.23 Preparation of calcite samples 1b-6-1, 1b-6-2, and 1b-6-5 100
4.24 Example of calcite sample 101
4.25 Triclinic crystal system 102
4.26 Albite cleavage planes and twinning 103
4.27 The two albite samples 103
4.28 XRD pattern of albite 104
4.29 Pyrite crystal system 105
4.30 Pyrite cube from which the three pyrite samples used in this study were cut. 105
4.31 XRD pattern of pyrite 106
4.32 Pyrite-1 and Pyrite-2 samples 107
4.33 Pyrite-3 sample 107
4.34 Obsidian sample (amorphous) 108

4.35 XRD pattern of obsidian 109
4.36 North Chile meteorite 113
4.37 North Chile sample, four sides 114
4.38 Holbrook meteorite 115
4.39 Holbrook sample, four sides 116
4.40 Buzzard Coulee meteorite 117
4.41 Buzzard Coulee-1 sample, four sides 118
4.42 Buzzard Coulee-2 sample, four sides 119
4.43 Allende meteorite 120
4.44 Allende sample, four sides 121
4.45 Gas pycnometer used for volume and density measurements 124
4.46 Scale used to weigh meteorites 124
4.47 XCT imaging system 126
4.48 Interior views of the XCT imaging system with a sample 126
5.1 Thermal conductivity results of quartz (25 to 300 K) 131
5.2 Quartz: Comparison of CFMS-measured data and data corrected for radiative heat loss 132
5.3 Radiation component (k_{rad}) vs. T^3 for the two quartz samples 132
5.4 Thermal conductivity results of the calcite "a samples" between 5 and 300 K 133
5.5 Thermal conductivity results of the calcite "b samples" between 5 and 300 K 133
5.6 Calcite thermal conductivity between 5 and 300 K 134
5.7 Calcite thermal conductivity between 50 and 300 K 135
5.8 Calcite "a samples": Comparison of CFMS-measured data and data corrected for radiative heat loss 136
5.9 Calcite "b samples": Comparison of CFMS-measured and corrected data for radiative heat loss 137
5.10 Radiation component (k_{rad}) as a function of T^3 for the six calcite samples. . 138

5.11 Thermal conductivity results for the two albite samples between 5 and 300 K 139
5.12 Albite-1 thermal conductivity between 10 and 80 K 140
5.13 Albite: Comparison of CFMS-measured and corrected data for radiative heat loss 140
5.14 Radiation component (k_{rad}) vs. T^3 for the two albite samples 141
5.15 Pyrite thermal conductivity between 5 and 300 K 142
5.16 Obsidian thermal conductivity between 5 and 300 K (uncorrected) 153
5.17 Corrected thermal conductivity results of obsidian 155
5.18 CFMS vs. Corrected thermal conductivity of obsidian (40 to 300 K) 156
5.19 Plot of k_{rad} vs. T^3 for obsidian 157
6.1 Measured thermal conductivity between 5 and 300 K for the three ordinary chondrite samples 161
6.2 Thermal conductivity of stony meteorites (Opeil et al., 2012) 162
6.3 Thermal conductivity measurements of CM carbonaceous chondrites (Opeil et al., 2020) 162
6.4 Thermal conductivity measurements of lunar meteorites (Macke et al., 2024). 163
6.5 Thermal conductivity of Holbrook: CFMS vs. Opeil et al. (2012) 163
6.6 Empirically corrected thermal conductivity for Holbrook and Buzzard Coulee samples. 166
6.7 Comparison between the corrected thermal conductivity data for Holbrook from this study and the two Holbrook samples reported by Opeil et al. (2012). 166
6.8 Comparison of CFMS-measured and corrected data for radiative heat loss in the ordinary chondrites 167
6.9 Radiation component (k_{rad}) as a function of T^3 for Buzzard Coulee-1 (left) and Buzzard Coulee-2 (right). 168
6.10 Radiation component (k_{rad}) as a function of T^3 for Holbrook. 168
6.11 Measured thermal conductivity between 140 and 300 K for Allende 169

6.12 Thermal conductivity of the North Chile meteorite compared with four iron meteorites from Noyes et al. (2022) . . . 171
6.13 XCT images of Holbrook . . . 173
6.14 XCT images of Buzzard Coulee-1 . . . 174
6.15 XCT images of Buzzard Coulee-2 . . . 174
6.16 XCT images of Allende . . . 175
6.17 Thermal conductivity at 200 K as a function of 1/porosity. . . . 177
6.18 Thermal conductivity at 140 K as a function of bulk density . . . 177
6.19 Comparison of thermal conductivity data from this study and Opeil et al. (2012). . . . 180
7.1 Emissivity spectra for different particle sizes of quartz (Lyon, 1964) . . . 183
7.2 Comparison of emissivity derived from reflectance spectra with a directly measured emissivity spectrum . . . 184
7.3 Emissivity spectra of two solid quartz samples measured along the c- and a-axes 187
7.4 Emissivity spectra of five solid calcite samples from the ASU Spectral Library 187
7.5 Emissivity spectrum of pyrite . . . 188
7.6 Emissivity spectrum of albite . . . 188
7.7 Emissivity spectrum of obsidian . . . 189
7.8 Average emissivity comparison of varying silicate grain sizes under ambient and simulated lunar conditions . . . 190
7.9 Copper heater tab showing a semi-reflective surface with fine surface marks . 194
D.1 Individual thermal conductivity measurements for quartz . . . 249
D.2 Individual thermal conductivity measurements for calcite . . . 250
D.3 Individual thermal conductivity measurements for calcite < 100 K . . . 251
D.4 Individual thermal conductivity measurements for albite . . . 252
D.5 Individual thermal conductivity measurements for pyrite . . . 253
D.6 Individual thermal conductivity measurements for the obsidian sample . . . 254

1 Introduction

1.1 Motivation

Understanding the thermal properties of airless planetary bodies, including the Moon and asteroids, is essential for expanding our knowledge of the Solar System. In particular, the thermal properties of asteroids are physical characteristics that have significantly influenced their evolution. These thermophysical properties are defined primarily by thermal inertia (I) (Equation 1.1) and thermal diffusivity (α) (Equation 1.2), both of which depend on a body's thermal conductivity (k), specific heat capacity (C), and density (ρ).

$$I = \sqrt{\rho C k} \tag{1.1}$$

$$\alpha = \frac{k}{\rho C} \tag{1.2}$$

Thermal inertia is a property that describes how effectively a surface resists changes in temperature as it heats or cools, whereas thermal diffusivity governs the rate at which heat flows through the body itself. Thermal inertia helps predict surface conditions such as roughness and grain size (Emery et al., 2014; MacLennan and Emery, 2022). It also plays a critical role in orbital dynamics through its influence on the Yarkovsky and YORP (Yarkovsky–O'Keefe–Radzievskii–Paddack) effects, which describe how solar heating alters an asteroid's orbital energy and axial spin, respectively (Bottke et al., 2006; Delbó et al., 2007; Vokrouhlický et al., 2015). Thermal diffusivity, on the other hand, controls the rate of internal thermal evolution (McSween et al., 2002; Opeil et al., 2010; Sahijpal, 2022). As heat diffuses through an asteroid's interior, secondary alteration processes (aqueous alteration and thermal metamorphism) can occur, progressively modifying the body's composition (Keil, 2000). The extent of these changes depends on the thermal diffusivity and the nature of the asteroid's primitive material.

Sample return missions, such as OSIRIS-REx (Origins, Spectral Interpretation, Resource Identification, and Security – Regolith Explorer) and Hayabusa2, are essential for providing surface thermal data, particularly thermal inertia (Arai et al., 2017; Okada et al., 2017; DellaGiustina et al., 2019; Rozitis et al., 2020; Rozitis et al., 2022). However, insight into the internal heat flow and the thermal evolution of asteroids relies heavily on thermal models, which in turn depend on assumed values for thermal diffusivity (McSween et al., 2002; Ganguly et al., 2016; Schwinger et al., 2016; Gail and Trieloff, 2018; Sahijpal, 2021). To improve these models and gain a deeper understanding of heat transfer within airless bodies, direct measurements of thermal conductivity, specific heat capacity, and density are needed.

Meteorites offer a unique opportunity to study the thermal properties of planetary materials. As fragments of parent bodies ejected by impact events and delivered to Earth, they provide direct physical samples that can be studied in detail. Among their measurable thermal properties, thermal conductivity remains the least studied. Obtaining direct thermal conductivity measurements is essential for understanding how meteorite parent bodies store and conduct heat over time. This study aims to provide thermal conductivity data that modellers can use to improve the accuracy of thermal evolution models, which often rely on the thermal conductivity of individual meteoritic minerals, analogue materials, or calculated values based on compositional or structural assumptions (e.g., Cohen and Coker, 2000; Schubert et al., 2007; Prialnik and Merk, 2008; Guilbert-Lepoutre et al., 2011; Henke et al., 2012; Henke et al., 2016; Gail and Trieloff, 2019). These approaches typically overestimate thermal conductivity relative to actual meteorites (Opeil et al., 2012) and often assume zero porosity or a constant thermal conductivity that does not vary with temperature. As a result, such models tend to overestimate thermal diffusivity and, consequently, the rate of thermal evolution. Direct measurements from meteorites, therefore, provide essential data for accurately representing planetary materials in thermal models.

1.2 Objectives and Overview

The Planetary Instrumentation Laboratory (PIL) at York University is equipped with a Cryogen-Free Measurement System (CFMS), designed by Cryogenic Ltd, capable of measuring the physical properties of samples between 5 K and 300 K under vacuum ($<10^{-4}$ mbar). Since asteroid surface temperatures can drop as low as 50 K (Delbó and Harris, 2002), the CFMS is well-suited for thermal conductivity experiments on planetary materials. Although these systems are primarily used to analyze industrial materials such as metals, ceramics, and electronics, extending their use to geological samples, particularly meteorites, represents a novel extension of the system's capabilities.

The central objective of this PhD research is to develop a reliable and reproducible method for measuring the thermal conductivity of meteorites using the CFMS. This work builds on previous studies of Opeil et al. (2010; 2012; 2020), who were the first to directly measure meteorite thermal conductivity below 300 K under vacuum conditions. Their measurements were conducted using a Quantum Design Physical Property Measurement System, which operates similarly to the CFMS but employs a different technique: a heat-pulse method, where brief pulses of heat are applied to a sample until a target temperature difference is achieved. In contrast, the CFMS uses a steady-state method, where heat is continuously applied to the sample to maintain a stable temperature gradient across it. Because both systems operate under comparable conditions (<300 K, vacuum), results from this study can be directly compared to those of Opeil et al. to validate both the method and results. The data in this PhD study represent the first thermal property measurements reported by the PIL, obtained using the CFMS.

Because meteorite samples are limited and highly valuable, initial experiments with the CFMS were conducted on terrestrial geological samples, specifically single-crystal minerals. These samples are ideal for evaluating instrument performance and refining the measurement methodology, due to their well-known properties. Notably, thermal conductivity is an

anisotropic property that can be measured directly. It changes depending on the direction of heat flow relative to the crystallographic axes, making these minerals well-suited for method development and refinement.

This research also examines how porosity and density influence the thermal conductivity of meteorites. Previous work by Opeil et al. (2012) demonstrated a strong inverse relationship between thermal conductivity and porosity, while Szurgot (2011a) and Szurgot (2011b) reported a direct correlation with bulk density. Measuring these properties is therefore a vital component of this study. In particular, porosity data offer insight into how microstructural features limit heat transport in stony meteorites. When combined with thermal conductivity measurements, they enable more accurate estimates of parent body thermal diffusivity. Ultimately, this study contributes critical thermophysical data that can be used to improve thermal evolution models of small planetary bodies.

The following summary outlines how this dissertation is structured to achieve the objectives of this PhD research.

- Chapter 1 presents background information on thermal conductivity investigations of both terrestrial materials (rocks and minerals) and meteorites.

- Chapter 2 discusses the principles of heat transfer and provides the theoretical background necessary to understand thermal transport in solids. This includes an overview of the three primary heat transfer processes—conduction, convection, and radiation—as well as the fundamentals of kinetic theory and its relation to thermal conductivity. The chapter also examines thermal energy carriers in crystalline solids and describes heat transfer behaviour in insulators and amorphous materials.

- Chapter 3 introduces the Cryogen-Free Measurement System (CFMS), which is used to measure the thermal conductivity of geological samples. It outlines the key measurement configurations required for these samples and describes the data analysis methods, including the approach used to correct for thermal radiation effects. The

chapter also presents results from a copper reference sample to validate both the instrument's performance and the analysis procedures.

- Chapter 4 describes the samples used in this study, including single-crystal minerals, obsidian (volcanic glass), and meteorites. It also details the sample selection process and preparation procedures.

- Chapters 5 and 6 present the thermal conductivity results obtained in this study. Chapter 5 focuses on single-crystal minerals and the obsidian sample, while Chapter 6 presents results for meteorites, including density and porosity data.

- Chapter 7 investigates the emissivity of geological samples and details a method for estimating average emissivity. This work supports the correction of radiative heat loss in thermal conductivity measurements.

- Chapter 8 summarizes the findings of this research and outlines directions for future work.

1.3 Thermal Conductivity Investigations

1.3.1 Terrestrial Materials

The thermal conductivity (k) of terrestrial geological materials, including rocks and minerals, has been studied since the early 1900s. The first detailed investigation was published by Eucken in 1911. Later, Birch and Clark (1940a, 1940b) conducted an extensive two-part study measuring the thermal conductivity of rocks and minerals between 0°C and 400°C. Several well-cited studies on the thermal properties of rocks and minerals were published between the late 1960s and 1990s (Clark, 1966; Horai and Simmons, 1969; Horai, 1971; Dreyer, 1974; Čermák and Rybach, 1982; Diment and Pratt, 1988; Robertson, 1988; Clauser and Huenges, 1995). To date, most thermal conductivity investigations have focused on measurements under atmospheric and mantle conditions ($T \geq 300\,\mathrm{K}$; $P \geq 1\,\mathrm{atm}$) (Walsh

and Decker, 1966; Beck et al., 1978; Manga and Jeanloz, 1997; Vosteen and Schellschmidt, 2003; Hofmeister et al., 2007; Goncharov et al., 2009; Xiong et al., 2021), heat flow through sedimentary basins (Blackwell and Steele, 1989; Vasseur et al., 1995; Gallagher et al., 1997; Labus and Labus, 2018; Tang et al., 2021), or engineering applications such as building materials and geothermal systems (Sibbitt et al., 1978; Yaşar and Erdoğan, 2008; Di Sipio et al., 2013; Stylianou et al., 2016; Huang et al., 2021).

Low-temperature thermal conductivity measurements (below 300 K) on terrestrial samples are rare, with only a few studies available (de Haas and Biermasz, 1935; Popov et al., 2013; Zuñiga-Puelles et al., 2019; Halbert and Parnell, 2022). The lack of data is not surprising. First, cryogenic temperatures (< 120 K) do not occur naturally on Earth, which limits the relevance of such measurements for terrestrial heat flow studies. Second, thermal conductivity is challenging to measure in geological materials because heat transfer is sensitive to their physical and chemical properties.

The physical properties of minerals, which are the primary constituents of rocks, are governed by their crystallographic structure and symmetry (Wenk and Bulakh, 2016). The crystallographic axes determine whether a mineral is isotropic (i.e., with uniform properties in all directions) or anisotropic (i.e., with properties that vary by direction). Many minerals are anisotropic, meaning their thermal conductivity depends on the direction of heat flow relative to their crystallographic axes. Mineral composition also plays an important role, as thermal conductivity depends on which atoms are present, how they are bonded, and how they interact with lattice vibrations, known as phonons (Horai and Simmons, 1969; Spitzer, 1970; Sharma and Bahadur, 1975; Duda et al., 2011; Giri et al., 2018).

Many physical and chemical factors influence the thermal conductivity of rocks, including porosity, density, mineral distribution, grain size, water content, degree of alteration, and temperature and pressure (Čermák and Rybach, 1982; Robertson, 1988; Clauser and Huenges, 1995; Midttomme and Roaldset, 1998; Opeil et al., 2012). Among these, porosity plays a significant role, as it typically reduces thermal conductivity because pore spaces act

as barriers to heat flow (Robertson and Peck, 1974; Robertson, 1988; Clauser and Huenges, 1995; Smith et al., 2013). Since thermal conductivity is sensitive to different factors, it can vary considerably even among samples of the same rock type, making it a complicated property to characterize in geological materials.

1.3.2 Meteorites

As mentioned above, thermal conductivity, specific heat capacity, and density are the three essential properties that define a planetary body's thermal inertia (Equation 1.1) and thermal diffusivity (Equation 1.2). Although this dissertation focuses on thermal conductivity, this section outlines the major studies that have contributed to our understanding of these three physical properties in meteorites.

The first reported values of thermal conductivity for stony meteorites were presented by Matsui and Osako (1979) and Yomogida and Matsui (1983), who derived results for 25 samples using measurements of thermal diffusivity, specific heat capacity, and density. During the Apollo era, similar methods were applied to lunar rocks, with several studies reporting thermal diffusivity values that allowed thermal conductivity to be inferred (Horai and Fujii, 1972; Fujii and Osako, 1973; Mizutani and Osako, 1974; Horai and Winkler, 1975). Butler and Jenkins (1963) extended this approach to an iron meteorite, measuring both thermal diffusivity and specific heat capacity over a wide temperature range (-150°C to 300°C) to determine conductivity. More recently, the same strategy has continued to be used in meteorite studies, particularly by Szurgot and collaborators (Szurgot et al., 2008; Szurgot, 2011b; Szurgot et al., 2012; Szurgot et al., 2014; Szurgot, 2021; Altunayar-Unsalan et al., 2025).

To date, only a few studies have directly measured the thermal conductivity of meteorites at low temperatures (5 to 300 K), namely Opeil et al. (2010), Opeil et al. (2012), Opeil et al. (2020), Noyes et al. (2022), and Macke et al. (2024). Collectively, these studies report thermal conductivity data for 32 meteorites. Their findings suggest that thermal conductivity

is strongly influenced by sample porosity, as well as by impurities and defects within the mineral grains themselves. Soini et al. (2020) compiled a thermal conductivity database for 38 meteorites; however, all of these measurements were conducted at room temperature. Beech et al. (2009) reported high-temperature measurements (300 to 800 K) for the Gao-Guenie meteorite, motivated by interest in ablation behaviour, asteroid interior modelling, and orbital evolution (YORP).

Specific heat capacity measurements have been conducted by a number of researchers, most commonly using differential scanning calorimetry to analyze meteorites (Beech et al., 2009; Szurgot et al., 2008; Szurgot et al., 2012; Wach et al., 2013; Wach et al., 2014; Altunayar-Unsalan et al., 2021; Piqueux et al., 2021; Altunayar-Unsalan et al., 2025). The most comprehensive low-temperature data (5 to 300 K) have been obtained by Opeil et al. (2012), Opeil et al. (2020), Noyes et al. (2022), and Macke et al. (2024) using a Quantum Design Physical Property Measurement System. Additionally, Consolmagno et al. (2013) introduced a cost-effective method for measuring specific heat capacity between 77 K and 300 K using liquid nitrogen, which was later applied by Macke et al. (2019) to analyze 60 meteorites.

Density and porosity have been extensively measured across a wide range of meteorite types. Consolmagno and Britt (1998) developed a non-destructive method to determine these properties using the Archimedean glass bead technique. This approach was applied in subsequent studies by Britt and Consolmagno (2003) and Consolmagno et al. (2008). The most comprehensive compilation of meteorite density and porosity data was presented by Macke (2010), who used a gas pycnometer to measure grain density and the Archimedean glass bead method to determine bulk density and porosity. Macke's work has since been expanded through additional density and porosity measurements of meteorites (Macke et al., 2010; Macke et al., 2011a; Macke et al., 2011b; Macke et al., 2016).

In this PhD study, five meteorite samples were analyzed: two samples of Buzzard Coulee (H4 chondrite), Holbrook (L/LL6 chondrite), Allende (CV3 chondrite), and North Chile

(iron meteorite). The classification of these meteorites is explained in Chapter 4. Table 1 summarizes the thermal conductivity and specific heat capacity values at 200 K, along with the corresponding density and porosity data for each meteorite group. The average values for H chondrites are used to represent Buzzard Coulee. Due to the limited available data for CV chondrites, Allende is representative of this group. Holbrook is classified as an L/LL6 chondrite, indicating it contains fragments of both L and LL chondrites; therefore, the values listed in the table are averages of the L and LL chondrite groups. Similarly, the iron meteorite values represent an average of iron meteorites. Thermal inertia and thermal diffusivity values in the table are calculated from the thermal and physical properties provided.

Table 1: Physical and thermal properties of selected meteorite types at 200 K.

Meteorite Type	**Thermal Conductivity** ($W/m \cdot K$)	**Specific Heat** ($J/kg \cdot K$)	**Bulk Density** (kg/m^3)	**Porosity** (%)	**Thermal Inertia** ($J\ m^{-2}\ K^{-1}\ s^{-1/2}$)	**Thermal Diffusivity** (mm^2/s)
H Chondrite	2.1 ± 1.1	504 ± 27	3350 ± 190	7 ± 4.9	1883 ± 499	1.24 ± 0.66
L & LL Chondrites	1.7 ± 1.3	506 ± 0	3250 ± 100	6.7 ± 3.6	1672 ± 640	1.03 ± 0.79
Allende (CV3)	1.4 ± 0.1	501 ± 21	2860 ± 40	21.93 ± 1.06	1416 ± 60	0.98 ± 0.08
Iron	28 ± 4	388 ± 5	7080 ± 170	0.84 ± 7.42	8770 ± 638	10.19 ± 1.48

- H chondrite averages from Ostrowski and Bryson (2019).
- L and LL chondrite averages based on data compiled by Ostrowski and Bryson (2019).
- Allende thermal conductivity and specific heat capacity from Szurgot (2011b); density and porosity averages from Macke (2010).
- Iron meteorite thermal conductivity and specific heat capacity from Noyes et al. (2022). Density from Ostrowski and Bryson (2019); porosity calculated using the average bulk and grain densities reported therein.

2 Principles of Heat Transfer

2.1 Heat Transfer Processes

The principles of heat transfer are defined by three processes: conduction, convection, and radiation. Conduction is the primary heat transfer method in this study, although convection and radiation are addressed in the thermal conductivity measurement process, described in Chapter 3 (Sections 3.1.3 and 3.3.3). A detailed description of each heat transfer process is provided below.

2.1.1 Conduction

Conduction occurs when heat is transferred through a solid object to a cooler area, usually when the heat comes into direct physical contact with the object. Thermal conduction is typically discussed in terms of heat flux, which is the flow of thermal energy per unit area, q'' (W m^{-2}), expressed as:

$$q'' = \frac{\dot{Q}}{A} \tag{2.1}$$

where $\dot{Q}$ is the heat transfer rate (W) and A is the area of the heated surface (m^2).

The heat flux, which describes how heat travels from a hot region to a cold region through a solid, is governed by Fourier's Law:

$$q'' = -k\nabla T \tag{2.2}$$

where k is the material's thermal conductivity (W m^{-1} K^{-1}) and ∇T (K m^{-1}) is the temperature gradient in three dimensions. Equation 2.2 represents the differential form. For one-dimensional heat flow, it simplifies to:

$$q'' = -k\frac{dT}{dx} \tag{2.3}$$

In Fourier's law, the temperature gradient points in the opposite direction to the heat flux. As a result, the gradient is negative when heat flows from a hot area to a cold one. To comply with the second law of thermodynamics, which states that heat always transfers from a hot region to a cold region, Fourier's law incorporates a negative sign to ensure the heat flux remains positive.

The one-dimensional case pertains to the thermal conductivity measurements in this research, which are conducted under steady-state conditions. In steady-state heat transfer, each end of a sample is maintained at a constant temperature across a finite length. In this setup, the temperature gradient dT/dx is approximated by $\Delta T/L$, where ΔT is the temperature difference between two points and L is the distance between them. The smaller this distance, the closer the approximation comes to representing the actual temperature gradient at a specific location, as $\Delta T/L$ approaches the true value of dT/dx in the limit as $L \to 0$.

With steady-state conduction, the temperature difference is typically defined as $\Delta T = T_{hot} - T_{cold}$ so that ΔT is positive. As a result, Equation 2.4 becomes:

$$q'' = k\frac{\Delta T}{L} \tag{2.4}$$

The thermal conductivity of a material can then be calculated from the heat flux and temperature gradient by rearranging Equation 2.4:

$$k = q''\frac{L}{\Delta T} \tag{2.5}$$

Substituting $q'' = \dot{Q}/A$ gives:

$$k = \frac{\dot{Q}}{A}\frac{L}{\Delta T} \tag{2.6}$$

This equation defines thermal conductivity as the rate of heat flow per unit area across a constant temperature gradient maintained over a known length. Thermal conductivity is an

intrinsic property that indicates how effectively heat transfers through a material. It does not depend on the dimensions of the material (i.e., the thermal conductivity of a gold block is the same as that of a gold nugget).

Thermal conductance, denoted as G, is the property that defines how much heat flows through a material, taking into account both thermal conductivity and the material's geometry, including area and length. It represents the rate of heat flow, which can also be expressed as power ($\dot{Q} = P$), in relation to a temperature difference. Equation 2.4 can then be expanded to

$$G = \frac{P}{\Delta T} = \frac{kA}{L} \tag{2.7}$$

The inverse of thermal conductance is thermal resistivity, R, which quantifies how much a material resists heat flow:

$$R = \frac{L}{kA} \tag{2.8}$$

Increasing the length over which heat must transfer leads to greater thermal resistance.

Thermal conductivity and thermal conductance provide a comprehensive description of heat transfer through a material and its geometry. Both properties are essential to the analysis conducted in this project.

2.1.2 Convection

Convection is the process through which heat is transferred in a liquid or gas by the movement of the fluid, circulating heat from warmer to cooler regions. When heat flows from a solid object into a fluid, the rate of heat transfer by convection is defined by:

$$\dot{Q} = \frac{Q}{\Delta t} = hA\Delta T \tag{2.9}$$

where:

- $\dot{Q}$ is the heat transfer rate (Watts, W),

- Q is the total amount of heat transferred (Joules, J),
- Δt is the time over which the heat is transferred (seconds, s),
- h is the heat transfer coefficient (W m^{-2} K^{-1}),
- A is the area of the heated surface (m^2),
- $\Delta T = T_{\text{solid}} - T_{\text{fluid}}$ is the temperature difference between the solid surface and the surrounding fluid (kelvin, K).

The heat transfer coefficient can also be related to the heat flux, q'' (W m^{-2}), by:

$$h = \frac{q''}{\Delta T} \tag{2.10}$$

where the heat flux, previously defined in Equation 2.1, is the heat transfer rate per unit area:

$$q'' = \frac{\dot{Q}}{A}$$

2.1.3 Radiation

Radiation occurs when materials emit infrared electromagnetic waves as a result of their internal thermal energy. Thermal energy refers to the random motion of atoms and molecules within a material, and this motion can lead to the emission of radiation through the formation of oscillating dipoles. All surfaces emit and absorb radiation based on their temperature, and when a temperature difference exists between two surfaces, heat is transferred from the hotter surface to the cooler one. Unlike conduction and convection, radiation does not require a surrounding medium and can occur in a vacuum.

The rate of radiative heat transfer between two surfaces, expressed as power P (recall that $P = \dot{Q}$), is defined by the Stefan–Boltzmann law:

$$P = \sigma \varepsilon A \left(T_{\text{hot}}^4 - T_{\text{cold}}^4 \right) \tag{2.11}$$

where:

- P is the net radiative heat transfer rate (W),
- σ is the Stefan–Boltzmann constant, $5.670 \times 10^{-8}\ \mathrm{W\,m^{-2}\,K^{-4}}$,
- ε is the emissivity of the hot surface (unitless),
- A is the surface area of the hot surface (m^2),
- T_{hot} and T_{cold} are the temperatures (K) of the hot and cold surfaces, respectively.

Emissivity is an essential component of Equation 2.11, as it defines how effectively an object radiates thermal radiation compared to a perfect blackbody ($\varepsilon = 1$). An object with an emissivity of 0 is considered an ideal reflector (i.e., it does not absorb or emit any radiation).

The amount of radiation emitted per unit area is the emissive power, E (W m^{-2}), defined as:

$$E = \frac{P}{A} \tag{2.12}$$

where P is the total power emitted (W) and A is the surface area (m^2). For a perfect blackbody, the emissive power is given by:

$$E = \sigma T^4 \tag{2.13}$$

where T is the absolute temperature of the surface in kelvin (K).

Radiation is an important concept to consider when conducting thermal conductivity measurements, as radiative heat loss can affect measurements at higher temperatures. This effect is discussed in detail in Chapter 3.

2.2 Thermal Conductivity

2.2.1 Kinetic Theory

Equations 2.6 and 2.7 describe how thermal conductivity can be determined if thermal conductance is known. As discussed above, thermal conductivity is an intrinsic property of a material, whereas thermal conductance depends on the geometry of the sample. However, these equations do not address how thermal conductivity varies with temperature. This relationship is explored here using concepts from kinetic theory.

Fourier's law relates heat flux to thermal conductivity across a temperature gradient (Equation 2.4). This law implies that thermal energy transfer occurs through the random motion of particles. According to Kittel (2005), if thermal energy were not randomized (i.e., energy travelled straight from hot to cold), then the heat flux would depend solely on the temperature difference ΔT, rather than the gradient dT/dx.

The thermal conductivity of a crystalline solid can be determined using a kinetic theory model that relates energy transport to the motion and collisions of energy carriers:

$$k = \frac{1}{3} C v \ell \tag{2.14}$$

where:

- C is the heat capacity per unit volume of the energy carriers (J m^{-3} K^{-1}),
- v is the average velocity of the energy carriers (m s^{-1}), and
- ℓ is the mean free path (m) — the average distance an energy carrier travels before scattering.

This equation is based on the kinetic model for heat transfer in gases (Kittel, 2005; White, 2018). The concept behind Equation 2.14 is outlined in Kittel (2005) and summarized here, supplemented with lecture material (Colorado School of Mines, 2014; Özatay, 2021).

Understanding Equation 2.14 involves expressing heat flux (W/m^2) as the product of the particle flux, ϕ ($particle \cdot m^{-2} \cdot s^{-1}$), and the energy transported by a single energy carrier, E (J):

$$q'' = \phi E \tag{2.15}$$

The particle flux in the x-direction, ϕ_x, refers to the number of energy carriers crossing a unit area per unit time along the direction of heat flow (Equation 2.16). In a one-dimensional system, this is typically the same direction as the applied temperature gradient.

$$\phi_x = \frac{N}{A\Delta t} = \frac{nV}{A\Delta t} = \frac{n(\Delta x A)}{A\Delta t} = n\langle v_x \rangle \tag{2.16}$$

where:

- N is the number of energy carriers (unitless)
- n is the number of energy carriers per unit volume (m^{-3})
- V is the volume (m^3)
- Δx is the distance travelled by the energy carriers in the x-direction (m)
- Δt is the travel time (s)
- A is the cross-sectional area (m^2)
- $\langle v_x \rangle$ is the average energy carrier velocity (m/s)

The energy transported by each energy carrier can be approximated as:

$$E = c\Delta T \tag{2.17}$$

where c is the heat capacity per carrier ($J \cdot K^{-1} \cdot carrier^{-1}$), and ΔT represents the temperature difference in kelvin (K) across the mean free path as the carrier moves from a hotter

region (e.g., $T + \Delta T$) to a cooler one (e.g., T). Substituting the equations for ϕ_x and E into the heat flux equation gives:

$$q'' = -n\langle v_x \rangle c \Delta T \tag{2.18}$$

The negative sign reflects that heat flows from hot to cold—that is, in the direction of decreasing temperature. This is consistent with Fourier's law, which defines the heat flux as being proportional to the negative temperature gradient.

The temperature difference, with respect to the mean free path ℓ, can be expressed as:

$$\Delta T = \frac{dT}{dx}\ell \tag{2.19}$$

Where the heat flux then becomes:

$$q'' = -n\langle v_x \rangle c \frac{dT}{dx}\ell \tag{2.20}$$

The average particle velocity in the x-direction $\langle v_x \rangle$ can be expressed in terms of the mean free path and the average time between collisions (τ):

$$\langle v_x \rangle = \frac{\ell}{\tau} \Rightarrow \ell = \langle v_x \rangle \tau \tag{2.21}$$

Substituting this into the previous equation:

$$q'' = -n\langle v_x^2 \rangle c\tau \frac{dT}{dx} \tag{2.22}$$

In kinetic theory, particle motion is randomized between collisions due to thermal energy. As a result, the total velocity is distributed in all directions:

$$\langle v^2 \rangle = \langle v_x^2 \rangle + \langle v_y^2 \rangle + \langle v_z^2 \rangle \tag{2.23}$$

However, it is assumed that the velocities are the same in all directions, such that:

$$\langle v_x^2 \rangle = \langle v_y^2 \rangle = \langle v_z^2 \rangle \tag{2.24}$$

Therefore,

$$\langle v^2 \rangle = 3\langle v_x^2 \rangle \Rightarrow \langle v_x^2 \rangle = \frac{1}{3}\langle v^2 \rangle \tag{2.25}$$

Recognizing that $nc = C$, the heat capacity per volume, and $\ell = \langle v \rangle \tau$, and assuming that v remains constant for thermal particles, the heat flux in one dimension becomes:

$$q'' = -\frac{1}{3} C v \ell \frac{dT}{dx} \tag{2.26}$$

which leads back to Equation 2.14:

$$k = \frac{1}{3} C v \ell$$

This expression shows that thermal conductivity depends on a material's heat capacity, the velocity of energy carriers, and their mean free path. While v is often assumed to be constant—as in the Debye model (Kittel, 2005)—both the heat capacity and mean free path vary with temperature, making thermal conductivity strongly temperature-dependent. However, temperature is not the only factor: Figure 2.1 illustrates how thermal conductivity also varies significantly between materials, due to differences in composition, purity, and material structure. These trends are explored in the following sections.

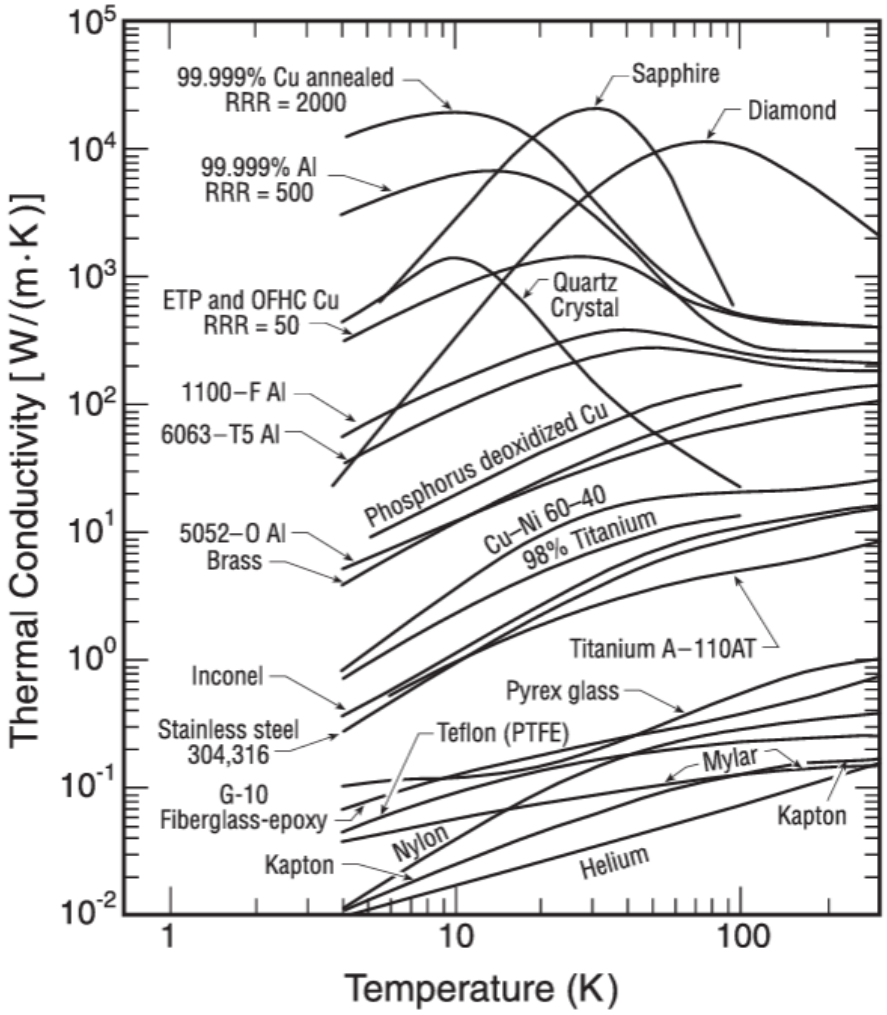

Figure 2.1: Thermal conductivity of different materials as a function of temperature. Figure from Ekin (2006).

2.2.2 Energy Carriers

Two primary particles carry energy through solids: electrons and phonons. Phonons are quasiparticles that are quanta of lattice vibrations. They are considered analogous to photons, which are the quanta of electromagnetic radiation.

In insulators such as rocks and minerals, phonons are the dominant carriers of energy. In contrast, the thermal conductivity of metals and semiconductors is controlled by both electrons and phonons, such that the total thermal conductivity is the sum of the electron

(electronic) thermal conductivity (k_e) and phonon (lattice) thermal conductivity (k_p):

$$k = k_e + k_p \tag{2.27}$$

For pure metals, the flow of electrons greatly exceeds the flow of phonons, resulting in thermal conductivity that's almost entirely determined by the electronic contribution (Uher, 2006). The electronic thermal conductivity is described by the Wiedemann-Franz law:

$$k_e = \sigma L T \tag{2.28}$$

where

- σ is the electrical conductivity (S m^{-1}), which is the inverse of electrical resistivity: $\sigma = \frac{1}{\rho}$ $(\Omega \cdot m)$
- L is the Lorenz number, 2.4453×10^{-8} $W\Omega K^{-2}$
- T is temperature (K)

The derivation of Equation 2.28 is provided in Yang (2006) and Uher (2006). In pure metals, the Wiedemann-Franz law states that electronic thermal conductivity at a given temperature is directly proportional to electrical conductivity. However, thermal conductivity becomes more complex in impure metals and semiconductors, where both electrons and phonons transfer energy. In this case, the Lorenz number L often deviates from its theoretical value (Nolas and Goldsmid, 2006; Uher, 2006), and the total thermal conductivity must be separated into its electronic and lattice components to evaluate each contribution (e.g., Nolas and Goldsmid (2006) and Tritt and Weston (2006)).

2.2.3 Crystalline Insulators

Thermal conductivity in crystalline insulators is governed by phonon scattering, which primarily occurs through phonon-phonon scattering, phonon-boundary scattering, and phonon-

defect (or impurity) scattering (Figure 2.2). Scattering of phonons introduces thermal resistance to heat flow.

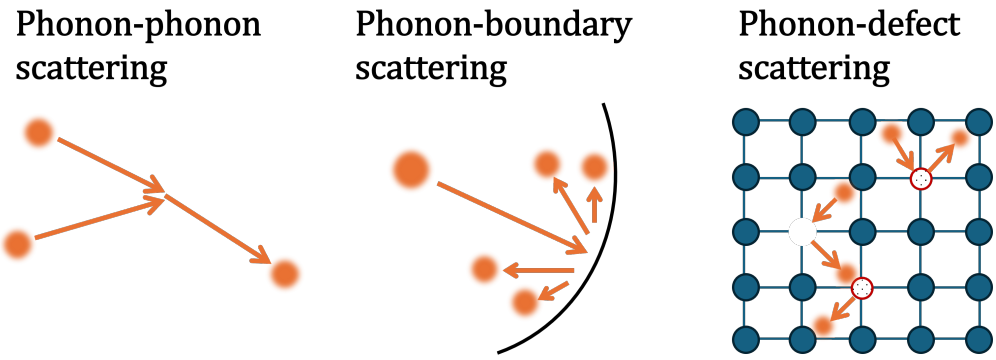

Figure 2.2: The three primary phonon scattering mechanisms in insulating crystalline solids. Image adapted from Hooshmand Zaferani et al. (2019) and Qian et al. (2021).

The number of thermally excited phonons in the crystal lattice determines the phonon mean free path. At high temperatures (e.g., 300 K), many phonons become excited, leading to frequent phonon-phonon collisions and a short mean free path. As the temperature decreases, the number of excited phonons reduces, resulting in fewer collisions and longer mean free paths. In crystalline solids, there are two types of phonon-phonon scattering: normal and Umklapp. Both processes involve interactions among three phonons and are described in terms of phonon momentum, known as wave vectors ($\vec{k}$):

$$\vec{k_1} + \vec{k_2} = \vec{k_3} + \vec{G} \tag{2.29}$$

Here, $\vec{G}$ is the reciprocal lattice vector that ensures momentum is conserved during phonon-phonon collisions. In a crystal, phonons are described in terms of reciprocal space, which defines how wave vectors behave in the repeating crystal lattice. The primitive unit cell of reciprocal space is known as the first Brillouin zone. This zone defines how phonon momentum behaves and is conserved throughout the crystal.

If $\vec{G} = 0$, phonon collisions are considered normal processes, and the phonon momentum is entirely conserved within the Brillouin zone. Umklapp processes occur when $\vec{G} \neq 0$, and

the resulting wave vector from the phonon collision extends outside the Brillouin zone. The reciprocal lattice vector $\vec{G}$ shifts the wave vector back into the zone, reversing its direction relative to the phonon flow, ensuring momentum is conserved. This reversal reduces the net phonon momentum in the direction of heat flow, creating thermal resistance within the crystal (Murashov and White, 2006; White, 2018). Both of these scenarios are illustrated in Figure 2.3.

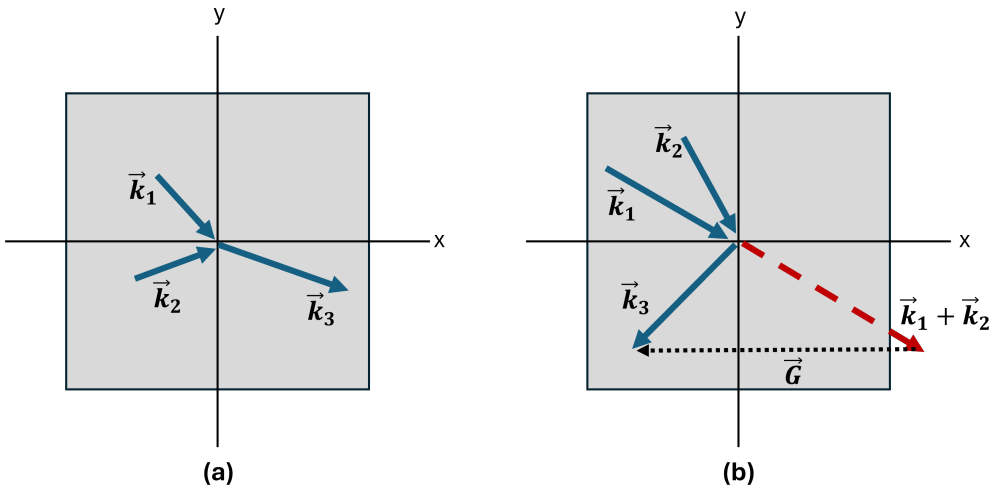

Figure 2.3: Phonon-phonon scattering processes. (a) Normal process, $\vec{k_1} + \vec{k_2} = \vec{k_3}$ (b) Umklapp process, $\vec{k_1} + \vec{k_2} = \vec{k_3} + \vec{G}$, where $\vec{G}$ is the reciprocal lattice vector. The gray square is the first Brillouin zone. Image is re-created after Kittel (2005). Note that in Kittel (2005), $\vec{G}$ is pointed towards the reciprocal vector (red line), but here it is in the opposite direction to emphasize that $\vec{k}_3 = \vec{k}_1 + \vec{k}_2 - \vec{G}$.

Umklapp processes govern the behaviour of thermal conductivity at high temperatures. Normal processes do not directly contribute to thermal resistance, but they are essential for maintaining thermal equilibrium among phonons (Yang, 2006).

As temperature decreases, the number of thermally excited phonons drops, allowing phonons to travel longer distances before scattering. This increase in phonon mean free path leads to a $k \sim 1/T$ dependence at high temperatures, where Umklapp processes dominate. At low temperatures, however, phonon scattering is primarily limited by finite-size effects, such as grain boundaries and crystal surfaces, and by defects or impurities within the crystal lattice. These include point defects (e.g., vacancies, atomic substitutions, isotopic variations)

and line defects such as dislocations (Enss and Hunklinger, 2005; Murashov and White, 2006; Kim, 2015; Hooshmand Zaferani et al., 2019; Shin et al., 2020). These boundaries and imperfections place an upper limit on the phonon mean free path, causing ℓ to remain constant at low temperatures (Figure 2.4). Without these phonon scattering mechanisms, thermal conductivity would infinitely increase as T approaches 0.

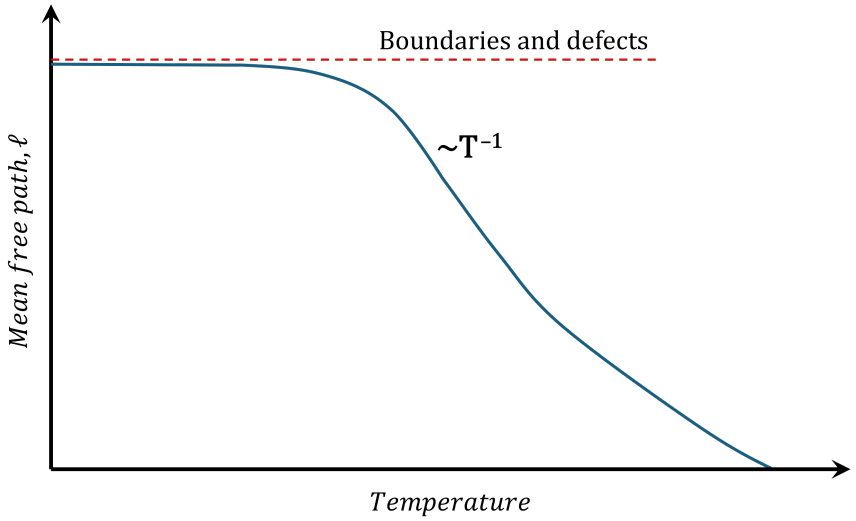

Figure 2.4: Schematic plot illustrating phonon mean free path as a function of temperature. At high temperatures, the mean free path follows a $1/T$ trend due to phonon-phonon scattering. At lower temperatures, it becomes independent of temperature, as it is limited by boundaries and defects in the crystal. Figure adapted from Tec-Science (2020).

At low temperatures, thermal conductivity follows a T^3 trend governed by the volumetric heat capacity C of the material. According to the Debye model, which describes the vibrational behaviour of atoms in a crystal lattice, heat capacity itself scales with temperature as $C \propto T^3$ at low temperatures. As temperature increases, the heat capacity gradually approaches the Debye temperature Θ_d, which corresponds to the highest phonon frequency that can be thermally excited. For nonmetallic materials at $T >> \Theta_d$, the heat capacity approaches a constant value of $C = 3R$ (Figure 2.5), as described by the Dulong-Petit law (Fitzgerel and Verhoek, 1960). Here, R is the ideal gas constant (8.314 J K^{-1} mol^{-1}).

Both phonon-defect and phonon-boundary scattering influence the temperature at which thermal conductivity reaches its peak. The low-temperature T^3 region of thermal conduc-

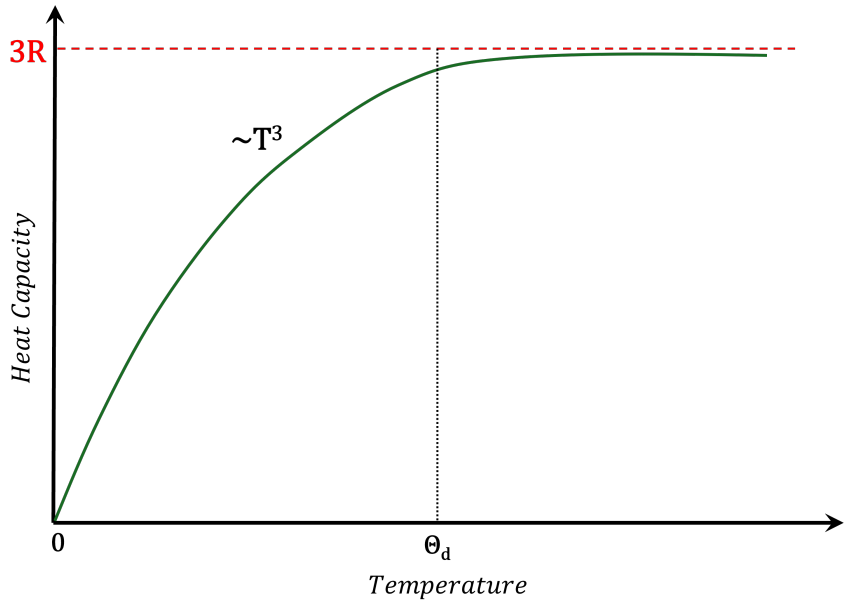

Figure 2.5: Schematic plot showing heat capacity as a function of temperature. At low temperatures, the heat capacity follows a T^3 trend. As the temperature increases and approaches the Debye temperature (Θ_d), the heat capacity begins to level off and eventually approaches the limiting value of $C = 3R$. Figure adapted from Tec-Science (2020).

tivity is primarily dominated by phonon-boundary scattering. This relationship was first described by Casimir (1938), who demonstrated that phonon scattering is limited by the physical size of a crystal, leading to a constant mean free path that is approximately equal to the sample diameter ($\ell \approx D$). Crystals with smaller diameters exhibit a lower mean free path limit, whereas larger samples allow phonons to travel further before colliding with the surface boundary. As the temperature increases, defect scattering becomes more pronounced, causing thermal conductivity to deviate from the T^3 trend (Al-Edani and Dubey, 1978). The fewer impurities present in a crystal, the fewer defects it contains, resulting in a longer mean free path between colliding phonons. Consequently, the size and purity of a crystal determine the magnitude and temperature of its thermal conductivity maximum (Figure 2.6).

When the temperature dependence of both phonon mean free path and heat capacity are combined, they produce the characteristic shape of thermal conductivity as a function of temperature for crystalline solids, as shown in Figure 2.7.

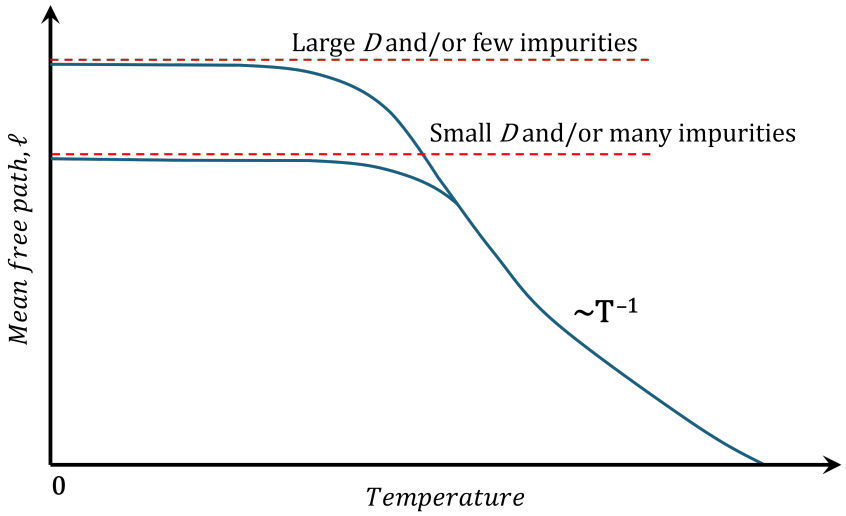

Figure 2.6: Schematic plot showing how crystal diameter (D) and impurities or defects limit the phonon mean free path as a function of temperature. Figure adapted from Tec-Science (2020).

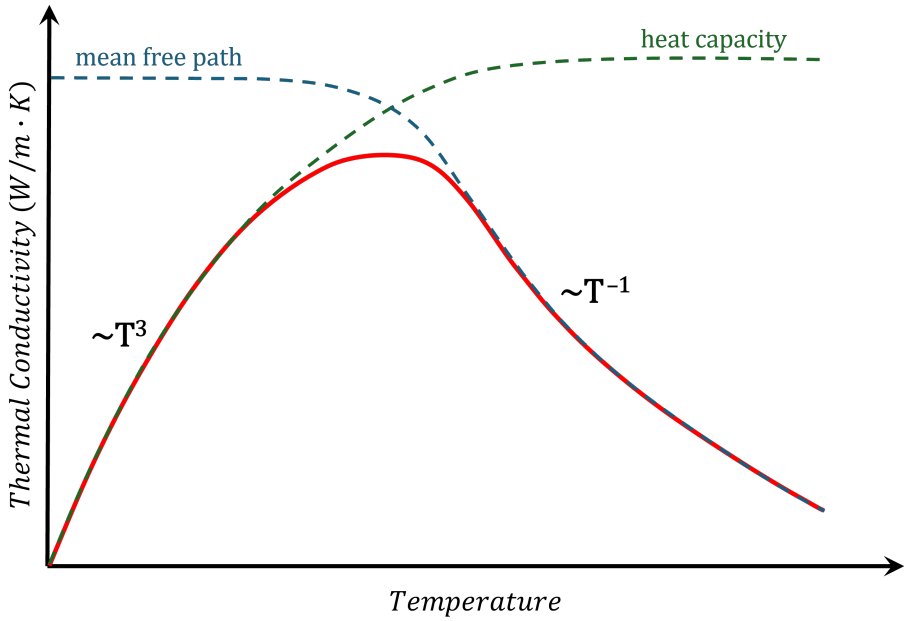

Figure 2.7: Schematic plot showing thermal conductivity (red curve) as a function of temperature. The shape of the thermal conductivity curve is governed by the heat capacity at low temperatures and the mean free path at high temperatures. Figure adapted from Tec-Science (2020).

2.2.4 Amorphous Solids

Thermal energy transfer through amorphous solids (e.g., glass, plastic, rubber, vitreous silica) is much less understood than in crystalline materials. It is a highly complex topic that warrants a more thorough investigation than what is presented here. A summary is provided here, as thermal conductivity measurements were completed on a sample of obsidian (volcanic glass).

Unlike crystalline solids, which have a structured, repeating atomic lattice, amorphous solids are characterized by a random, disordered atomic arrangement that lacks long-range periodicity (Figure 2.8). This means that there is no repeating pattern throughout the material's atomic structure. As a result, amorphous materials exhibit different thermal conductivity trends than crystalline materials, typically with lower values that increase slowly with temperature (Figure 2.9).

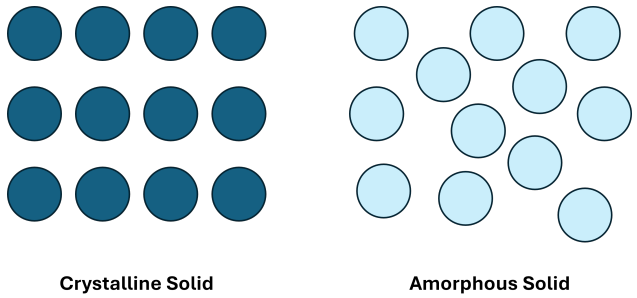

Figure 2.8: Atomic structure of crystalline vs. amorphous solids.

Due to the absence of periodicity, energy is transferred differently in amorphous solids compared to crystalline materials. This difference in behaviour is due to two vibrational modes referred to as propagons and diffusons (Allen et al., 1999). The following definitions are summarized from Moon and Minnich (2016) and Zhou et al. (2020).

Propagons are delocalized, wave-like modes with wavelengths longer than the interatomic spacing. They are analogous to phonons and dominate thermal transport at low temperatures.

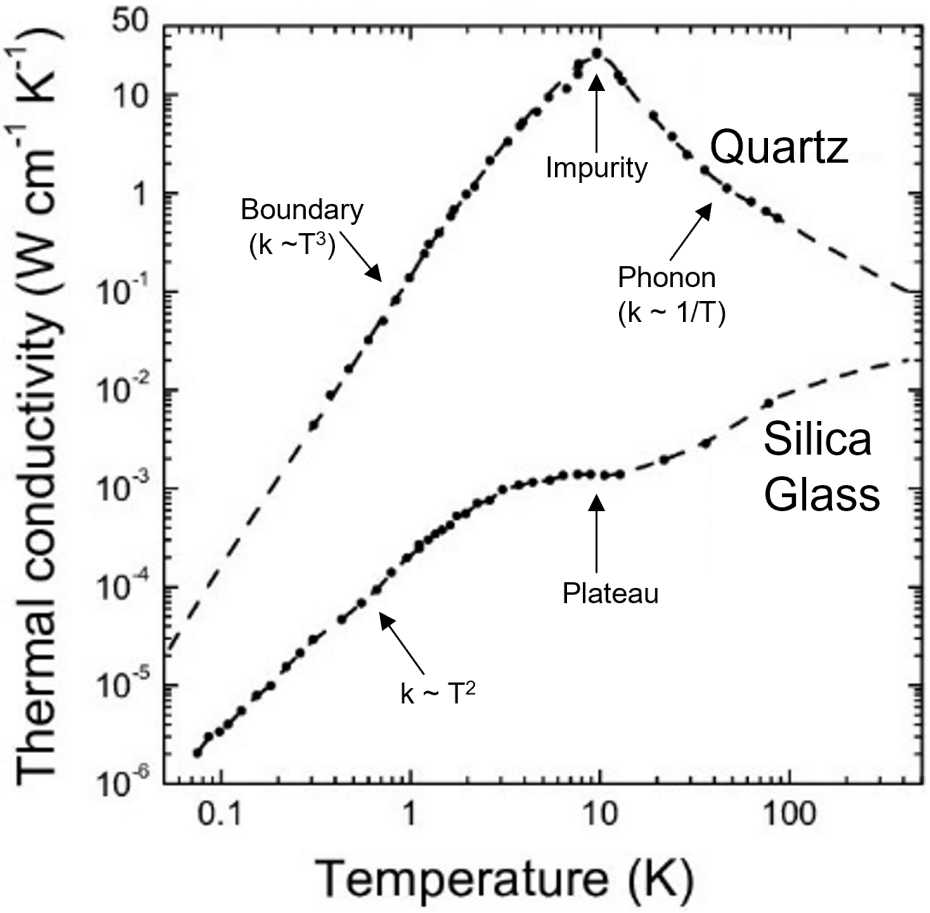

Figure 2.9: Thermal conductivity of crystalline quartz and silica glass. Image adapted from Courtens et al. (2007).

Diffusons are also delocalized but do not behave like waves. Instead, they diffuse thermal energy through a random-walk process within the atomic structure. The random-walk concept was first introduced by Einstein and later refined by Cahill and Pohl (1988, 1989). It describes how vibrational energy is transferred through the nearest-neighbour coupling of atoms, allowing energy to diffuse through the atomic structure.

Allen et al. (1999) also defined a third type of vibrational mode known as locons, which occur at high frequencies and are spatially localized modes. Because of their localization, these modes do not directly contribute to energy transfer; however, at temperatures above 400 K, they are known to interact with diffusons and influence thermal conductivity (Lv and Henry, 2016).

In amorphous solids, the temperature dependence of thermal conductivity is divided into three regions:

(1) $T < 1$ K

(2) 10K $< T <$ 30 K

(3) $T >$ 30 K

At temperatures below 1 K, thermal conductivity follows a T^2 trend. This behaviour is attributed to a type of defect scattering where low-frequency vibrations interact with atomic two-level systems (TLS) (Anderson et al., 1972; Phillips, 1972). Two-level systems, as described by Cahill and Pohl (1988) and Yu and Carruzzo (2022), consist of atoms or small groups of atoms located in adjacent positions in the atomic structure where the local energy is minimized. These atoms tunnel back and forth between the sites and interact with low-energy vibrational modes, such as phonons (Anderson et al., 1972; Phillips, 1972) or propagons (Allen et al., 1999).

The equation for thermal conductivity, $k = \frac{1}{3}Cv\ell$ (Equation 2.14), applies in this low-temperature region. Here, the mean free path follows $\ell \sim T^{-1}$ due to phonon-TLS scattering, while the heat capacity of amorphous solids at these temperatures follows $C \sim T^3$ trend. Together, these relationships produce the observed $k \sim T^2$ behaviour (Cahill and Pohl, 1988; Yu and Carruzzo, 2022).

Between 10 and 30 K, the thermal conductivity plateaus and becomes nearly independent of temperature. The nature of this plateau is not fully understood. It was first noted by Birch and Clark (1940a) and Kittel (1949) that the mean free path of phonons above the plateau becomes comparable to the interatomic spacing. Later, Allen et al. (1999) associated the plateau with the transition zone between propagons and diffusons. This transition is thought to be related to the boson peak, which represents an excess in the vibrational density of states in amorphous solids (Schober, 2004; Schirmacher et al., 2007; Shintani and Tanaka, 2008; Baggioli and Zaccone, 2020; Moriel et al., 2024). The boson peak has been identified in glasses with neutron and Raman scattering experiments (Malinovsky and Sokolov, 1986;

Wischnewski et al., 1998). It occurs near the frequency where the Ioffe-Regel limit is reached, which marks a shift in how vibrational energy is scattered (i.e., from propagating to diffusing) (Allen et al., 1999; Lubchenko and Wolynes, 2003; Shintani and Tanaka, 2008; Monaco and Mossa, 2009; Beltukov et al., 2013; Beltukov et al., 2016). This criterion is met when the wavelength of a vibrational mode is approximately equal to the interatomic spacing.

Above the plateau (T $>$ 30 K), the thermal conductivity increases and either reaches a second plateau or continues to rise at a slow rate. This behaviour is explained by the minimum thermal conductivity model, originally proposed by Slack (1979) for nonmetallic crystals, and later refined for amorphous solids by Cahill and Pohl (1987). The minimum thermal conductivity represents the lowest limit at which thermal energy can effectively diffuse through the interatomic spaces. This limit was initially explained in terms of the phonon mean free path, where ℓ is equal to the interatomic spacing. Allen et al. (1999) later refined this idea with diffusons that transport energy through diffusion rather than phonon-based interactions.

The fundamentals of amorphous thermal conductivity go much deeper than what is presented here. However, this summary covered the key concepts of energy transfer in amorphous materials that are sufficient for this project, particularly the temperature dependence of thermal conductivity.

2.2.5 Summary

To summarize this chapter, Figure 2.10 illustrates how various phonon scattering mechanisms—such as boundary, impurity, electron, and phonon-phonon interactions—govern the temperature dependence of thermal conductivity in both crystalline and amorphous solids.

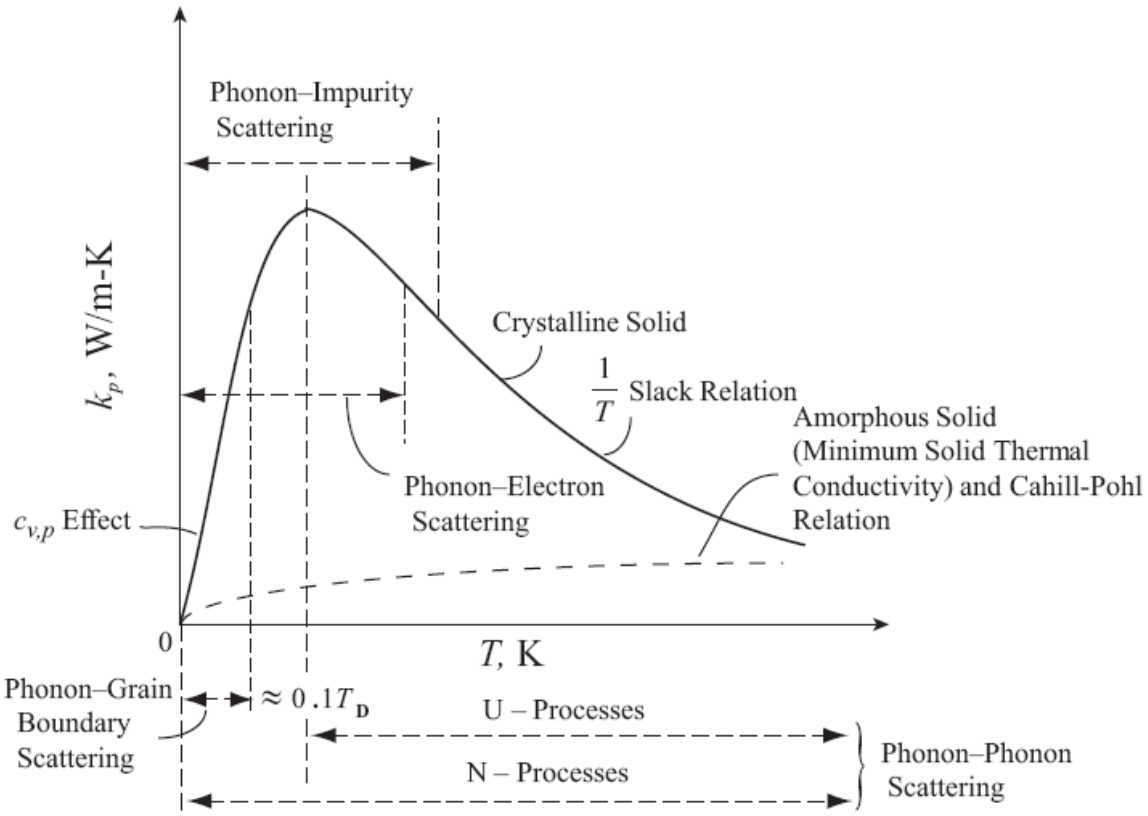

Figure 2.10: Schematic showing how thermal conductivity varies with temperature in crystalline and amorphous solids. In crystalline materials, conductivity increases at low temperatures due to rising heat capacity, peaks at approximately $0.1T_D$ (Debye temperature), and then decreases as phonon scattering (by other phonons, impurities, and electrons) becomes dominant. In amorphous solids, conductivity is lower and nearly constant, following the Cahill-Pohl minimum thermal conductivity model. Figure from Kaviany (2008)

.

3 Cryogen-Free Measurement System

3.1 Instrument Design

The mini Cryogen-Free Measurement System (CFMS) is a multifunctional system designed to measure the resistivity, magnetic susceptibility, and thermal properties (conductivity and heat capacity) of a wide range of industrial materials, such as metals, ceramics, and electronics (Figure 3.1). The CFMS can measure these properties from 5 K (-268°C) to 300 K (27°C), and is equipped with a 5 Tesla superconducting magnet for optional magnetic field measurements. The CFMS has an absolute accuracy of ±5%, meaning its measured thermal conductivity values are expected to be within 5% of the true value for a given sample, under proper operating conditions.

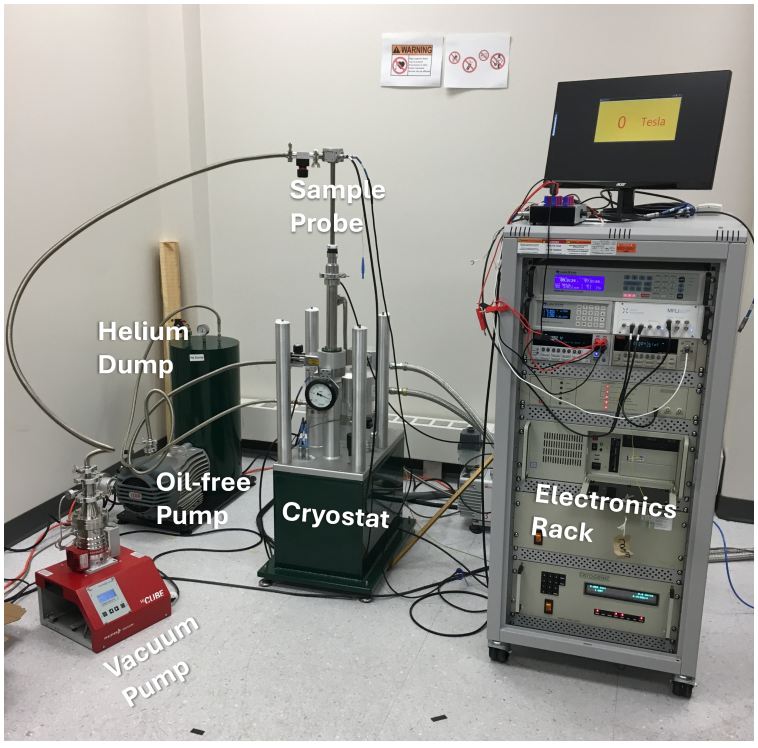

Figure 3.1: The mini Cryogen-Free Measurement System in the Planetary Instrumentation Laboratory at York University. The red vacuum pump, attached to the sample probe, ensures that the sample environment remains under vacuum during measurements.

Traditionally, cryogenic temperatures (< 123 K/-150°C) are achieved by using cryogenic liquids, such as helium or nitrogen. The CFMS, however, reaches these temperatures through a cryogen-free design that utilizes helium gas and a cold head. A cold head (also known as a cryocooler) is a device commonly used in cryogenic studies to achieve low temperatures using compressed gas (De Waele, 2011). In other words, the cryocooler is a highly efficient, ultra-low-temperature refrigerator.

Compared to liquid helium-cooled systems, cryogen-free systems offer several benefits, primarily lower operating costs and easier use (personal communication, S. Connaught, former Cryogenic Ltd employee, September 18, 2018). Since liquid helium is highly volatile, transferring it into a cryogen system requires careful handling. Once it's cooled, it needs to be constantly monitored to prevent evaporation. As a result, users feel pressure to collect valuable data with every system cool-down. In contrast, a cryogen-free system, such as the CFMS, uses a helium compressor that requires only a power source and a cold water supply. The compressor circulates helium gas to achieve cooling, making it more practical and cost-effective to operate.

Cryogen-free systems, however, have two disadvantages (personal communication, S. Connaught, former Cryogenic Ltd employee, Sept 18, 2018). First, the cryocooler can introduce vibrations that may affect measurements, particularly in magnetic experiments. Fortunately, this equipment is designed to mitigate vibration issues. Secondly, a cryogen-free system delivers less cooling power than liquid cryogen systems. For instance, liquid helium systems can apply several watts of power (heat) to a sample while maintaining a temperature of 2 K. Cryogen-free systems, however, lack this capability; achieving 2 K measurements is not the objective of this study.

3.1.1 System Overview

To understand how temperature is controlled in the CFMS, a schematic of the system is provided in Figure 3.2, which illustrates the flow of helium gas through the system. The CFMS

relies on two independent sources of helium: (1) compressed helium circulated through a cryocooler cold head (Figure 3.3), and (2) helium stored in the helium dump. The cryocooler is connected to a helium compressor (Figure 3.4), which is cooled by a cold water supply. The compressed helium travels to the cryocooler and initiates the cooling process of the cryostat, which houses the cryocooler, magnet, and sample space.

Helium gas from the dump (Figure 3.2) flows independently through the gas inlet to the cryocooler, where the helium is cooled to two critical temperatures: 40 K (1st stage) and 4 K (2nd stage). The significance of these two temperature stages is discussed below.

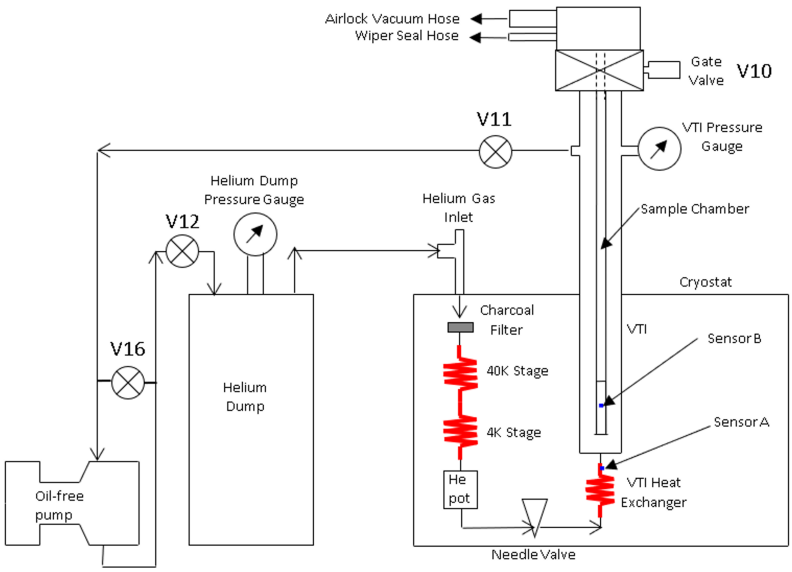

Figure 3.2: Schematic diagram of the CFMS cooling process. The cryostat is a vacuum-insulated chamber which thermally shields the magnet and VTI. Sensors A and B are thermometers that measure the temperatures of the VTI heat exchanger and sample, respectively. V# indicates valves. Image from Cryogenic Limited (2018).

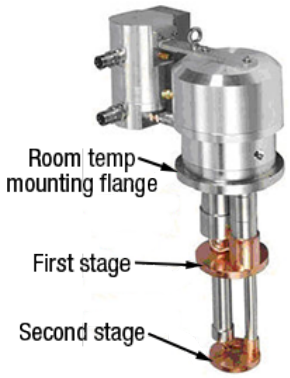

Figure 3.3: Image of a Pulse Tube cryocooler used to cool the CFMS. Image from Lake Shore Cryotronics (n.d.).

Referring to Figure 3.2, the helium in the dump first moves towards the helium gas inlet, where it passes through a charcoal filter that removes impurities in the gas. Next, the helium gas is passed through the first stage (40 K), which pre-cools the gas and cools the components inside the cryostat. The second stage (4.2 K) provides cooling to the magnet and Variable Temperature Insert (VTI). As the gas flows through the second stage, it is cooled down to 4.2 K. At this temperature, gaseous helium condenses into a liquid, which collects in the helium pot. The goal is to maintain the helium pot at a temperature between approximately 3.6 K and 4.2 K. Next, the liquid helium passes through the needle valve, which regulates the flow rate of liquid helium through the system. The flow rate is defined by a user-set pressure, where the optimal pressure is between 3 and 10 mbar. Ensuring that the system maintains a consistent flow rate is crucial in the cooling process; if the flow rate is too low there is not enough cooling power, whereas if the flow rate is too high there will be excess heat in the helium circuit which will heat the entire system, making it difficult to cool the VTI (Cryogenic Limited, 2018). At the point of passing through the needle valve, the liquid helium interacts with the VTI heat exchanger. The VTI controls the temperature of the system used to analyze a sample. The VTI enables analysis over a wide temperature range, as it heats the liquid helium to the user-programmed temperature (i.e., between 5 and 300 K). The helium then travels up through the system, where it returns to the helium dump. The oil-free pump powers this cycle. As the sample probe is connected to a vacuum



Figure 3.4: Helium compressor connected to the CFMS. The compressor delivers compressed helium gas to the cold head, which in turn cools the CMFS.

pump while in the CFMS (Figure 3.1), this ensures that the sample chamber is isolated from the circulating helium gas.

In the CFMS, two key temperatures are measured using Cernox^{TM} thermometers: Sensor A and Sensor B (Figure 3.2). Sensor A tracks the VTI temperature, while Sensor B measures the sample temperature. The thermometer near Sensor A is positioned next to a heater that controls the temperature of the helium gas, which in turn sets the environmental temperature for the sample. Closer to the sample, the thermometer at Sensor B is placed next to a heater that fine-tunes the sample's temperature.

3.1.2 Thermal Probe

Thermal measurements with the CFMS are performed using a thermal transport probe (Figure 3.5). At the end of the probe is the sample platform, where the sample is mounted (Figure 3.6). The sample platform serves as a heat sink and contains a Cernox^{TM} thermometer and platform heater. The temperature of the sample platform corresponds to the temperature of the sample chamber and defines the cold end temperature of the sample.



Figure 3.5: Thermal transport probe utilized for measuring thermal properties in the CFMS. The length of the probe is approximately 1.4 m.

A thermocouple and heater—referred to as the thermal assemblies—are attached to the sample and connected to the sample platform via a four-way and three-way push pin connector, respectively. The heater consists of a 10 kΩ resistor mounted on a copper-alloy tab, which is bonded with STYCAST 2850FT, a thermally conductive black epoxy. The heater is connected to the sample platform with thin manganin wires. The temperature difference, ΔT, between the hot and cold ends of the sample is measured with a thermo-

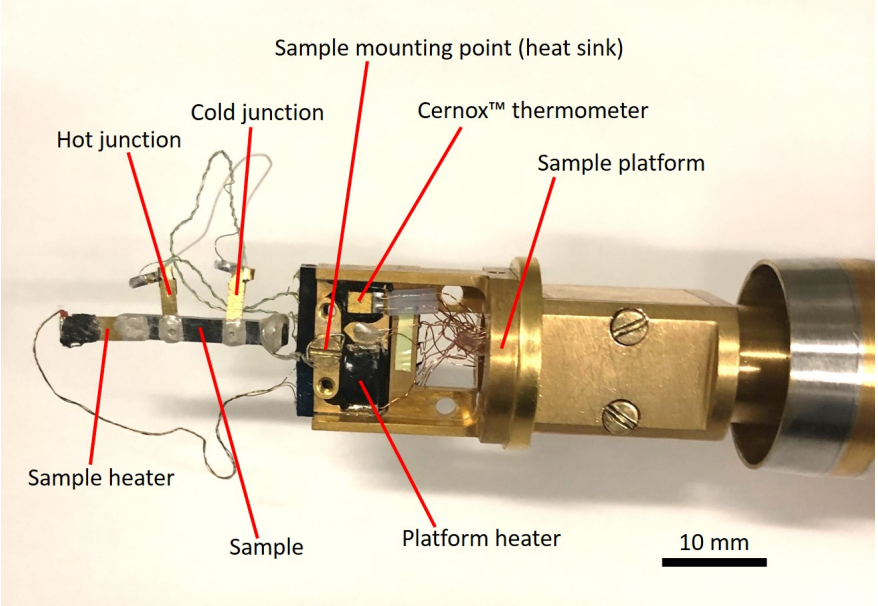

Figure 3.6: Sample platform with a geological sample attached. The cold and hot junctions are the ends of the thermocouple.

couple. For this study, two thermocouples were used: K-type (Chromel-Alumel) and E-type (Nickel-Chromium/Constantan). As with the heater, the junctions of the thermocouple are attached to copper-alloy tabs using STYCAST epoxy. This ensures good thermal contact without any electrical connection. An additional constantan wire is connected between the two thermocouple junctions to measure the voltage generated in the sample as it is heated. This configuration enables measurements of both thermal conductivity and the Seebeck effect, if desired.

The K-type thermocouples were attached to the mineral samples and iron meteorite, while the E-type was used for the stony meteorite samples. Both K-type and E-type thermocouples are suitable for thermal measurements at cryogenic temperatures with the proper calibration, as they offer higher sensitivity at low temperatures compared to other thermocouple types (The Engineering ToolBox, 2003). However, the sensitivity of both thermocouples is reduced at temperatures below 50 K (Figure 3.7), which can make thermal conductivity measurements at these temperatures challenging (refer to Section 3.2.1). For thermal conductivity measurements of stony meteorites, the E-type thermocouple is more suitable due

to its higher sensitivity, especially considering that stony meteorites generally have thermal conductivity values below 4 W m^{-1} K^{-1} (Opeil et al., 2010; Opeil et al., 2012; Opeil et al., 2020).

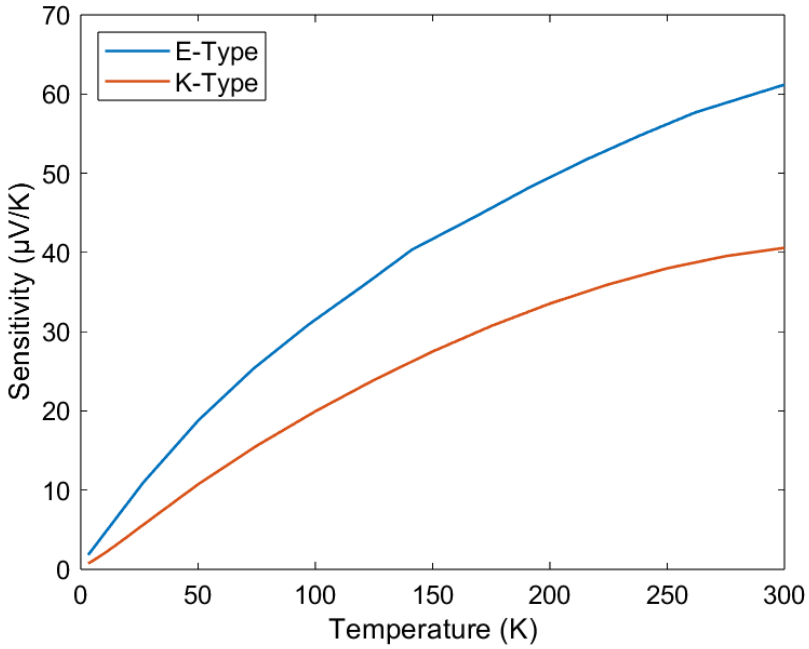

Figure 3.7: Sensitivity of E-type and K-type thermocouples.

The heater and thermocouple junctions are attached to the sample with electrically conductive silver epoxy (RS Pro). To ensure good electrical contact, the epoxy was selectively applied around the sides of the sample where the thermocouples and heater are attached. To attach the sample to the sample platform, a tinned copper wire is wrapped around the cold end of the sample and secured with silver epoxy. The wire is then wrapped around the mounting point on the sample platform, which is a small screw attached to a copper block. This configuration is shown in detail in Chapter 4.

After the sample has been mounted to the sample platform, a radiation shield is placed over the sample (Figure 3.8a). This shield helps mitigate heat loss due to radiation during measurements. Care is taken to ensure that the sample holder wires do not touch the sample or the shield to prevent excess heat transfer through the wires (see Section 3.1.3 below). An inner vacuum chamber (IVC) is then placed over the radiation shield, encapsulating the

sample chamber (Figure 3.8). The IVC is cone-sealed to the probe and held in place with a retaining nut. Before inserting the probe into the CFMS, the probe is connected to a turbo vacuum pump (Figure 3.1) for 30 minutes to evacuate the probe to a pressure $< 10^{-4}$ mbar. This ensures that the sample and probe are thermally isolated from the VTI and surrounding helium gas during sample loading and analysis. The probe is kept under vacuum during measurements. The importance of the radiation shield and the IVC is discussed below.

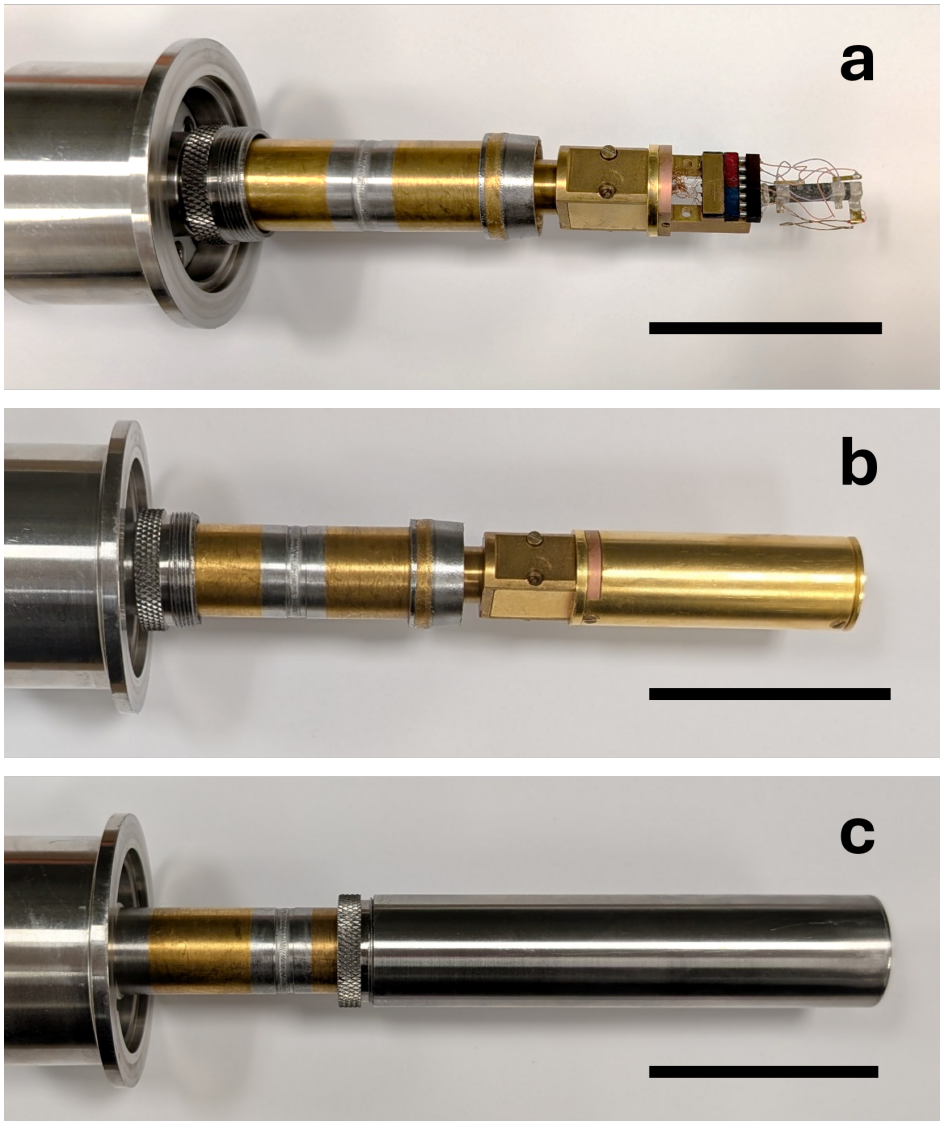

Figure 3.8: Configuration of the CFMS thermal transport probe. (a) Sample attached to the sample holder, which is attached to the end of the probe. (b) Radiation shield placed over the sample and sample holder. (c) Inner Vacuum Chamber (IVC) placed over top the radiation shield. The black scale bars are 5 cm.

3.1.3 Heat Transfer Considerations

During thermal conductivity measurements, most of the heat is transferred through the sample, from the heater to the heat sink. However, heat can also transfer through other paths, which can affect the accuracy of the results by causing heat loss. These paths include thermal convection of the surrounding helium gas, the wires connected to the heater and the hot junction thermocouple end, as well as thermal radiation. With these additional paths, the associated heat loss can effectively lead to an overestimation of the measured thermal conductivity:

$$k(T) = k_s + k_g + k_w + k_{\text{rad}} \tag{3.1}$$

where k_s is the sample's thermal conductivity, k_g is the conductivity of the gas, k_w is the conductivity of wires, and k_{rad} is thermal radiation. The challenge with thermal conductivity measurements is minimizing the heat loss from these other sources. The CFMS thermal probe and sample platform have been designed specifically to reduce heat transfer through these paths.

When the thermal conductivity of geological samples is measured under atmospheric pressure or greater, the thermal conductivity of the surrounding gas/air (k_g) effectively increases the thermal conductivity of the sample as gas fills the pore spaces (Woodside and Messmer, 1961; Horai and Fujii, 1972; Fujii and Osako, 1973; Mizutani and Osako, 1974; Horai and Winkler, 1975). It is well known that the thermal conductivity of gas increases with pressure; however, at vacuum pressures less than 10^{-2} mbar, the thermal conductivity of gas becomes negligible (Lang et al., 2016); therefore, the effect of pore fluid pressure becomes eliminated. As the thermal probe and sample in the IVC (Figure 3.8c) are continuously pumped to a pressure below 10^{-4} mbar while inside the CFMS, the thermal conductivity of gas is eliminated as a source of heat transfer.

Minimizing heat loss through conduction in the connecting wires of the heated assemblies can be achieved by using thin, long wires with low thermal conductivity. Before conducting

thermal conductivity measurements of a sample, background ΔT measurements are taken to account for the influence of the wires and sample platform. These background contributions are generally negligible compared to a sample's conductivity. Additionally, at room temperature, the thermal conductance of the wires does not exceed 10 μW K^{-1}. If the thermal conductance of the sample at room temperature is at least 100 times greater (on the order of 1 to 10 mW K^{-1}), the effect of the heater and thermocouple wires can be ignored (Cryogenic Limited, 2019). To ensure the sample's thermal conductance falls between 1 and 10 mW K^{-1} at room temperature, the cross-sectional area of the sample and the length between thermocouple tabs must be carefully considered. The importance of sample geometry is discussed in Section 3.2. If the thermal conductance of a sample at room temperature is below 1 mW K^{-1}, then the conductance of the wires must be factored into the total measured conductance to ensure accurate results (Cryogenic Limited, 2019).

Lastly, to reduce heat loss from thermal radiation, a radiation shield is placed over the sample and sample platform (Figure 3.8). While the shield does not entirely eliminate thermal radiation, it effectively contains the heat loss within the sample chamber. As a result, radiation-induced heat loss remains present in the measured thermal conductivity, such that $k(T) = k_s + k_{rad}$. To obtain the true thermal conductivity of a sample, the radiation component must be removed during the post-processing of data. The removal process is addressed in Section 3.3.3.

3.2 Measurement Configuration for Geological Samples

The CFMS is a complex system that requires patience and an iterative approach to method development. To achieve optimal thermal conductivity measurements, the CFMS settings must be configured for each sample. Four important measurement configuration parameters must be considered when completing thermal conductivity measurements: analysis method, sample geometry, thermal transport settings, and thermalization time.

3.2.1 Analysis Method

Thermal conductivity measurements acquired with the CFMS in this study were collected using a steady-state method. With this method, a temperature gradient (ΔT) is created across the sample by heating one end of the sample (hot end). The cold end of the sample is thermalized to the temperature of the sample chamber (refer to Section 3.2.4 for more information on thermalization). The CFMS measures the ΔT between the thermocouple junctions (Figure 3.6) and the amount of heating power (P) required to maintain the ΔT over a specified time (e.g., 180 seconds).

There are two main instruments used to measure the heater power and the temperature gradient. A source meter (Keithley 2400) supplies a current (I) to the heater (10 kΩ resistor) and measures the corresponding voltage (V) to calculate the applied heating power using $P = IV$. The amount of current supplied via the source meter during a measurement depends on how much heater power is needed to maintain a certain ΔT. A nanovoltmeter (Keithley 2182) measures the voltage difference between the thermocouple tabs, and the CFMS software converts the voltage to temperature to get ΔT.

To minimize error from temperature drift and electronic noise, each thermal conductivity measurement is performed using a small array of ΔT values. At each measurement temperature, the system measures ΔT and the corresponding heating power three times. Acquiring four or more ΔT measurements in the array has a minimal influence on the accuracy of the results and adds more time to the analysis (personal communication, Dr. D. Gillingham, Cryogenic Ltd Project Engineer, March 26, 2019). Engineers at Cryogenic Ltd have established that a suitable ΔT range is 0.1, 0.2, and 0.3 K. The thermal conductivity results in this study confirm that this is an optimal range. However, for crystalline material, a smaller ΔT range—such as 0.05, 0.1, and 0.15 K—may be necessary for low temperature measurements (< 40 K) to improve accuracy and reduce temperature drift caused by conductive heat loss. The need for a smaller ΔT range is due to the combined effect of reduced thermocouple sensitivity (Figure 3.7) and increased heat flow through crystalline samples

at lower temperatures. At these temperatures, applying enough heat to achieve ΔT = [0.1 K, 0.2 K, 0.3 K] can make it difficult for the system to reach the target configuration settings (see Section 3.2.3), ultimately lowering the measurement accuracy. A lower ΔT array range enables the system to reliably reach and maintain the desired configuration settings, resulting in more accurate and stable thermal conductivity measurements.

Once the array of the ΔT measurements is collected, a linear plot of heater power vs. ΔT is generated (Figure 3.9), where the slope is the thermal conductance (G) of the sample. Knowing the conductance, the thermal conductivity at a given temperature, $k(T)$, can be calculated with the following equation, where L is the length between the centers of the thermocouple tabs and A is the cross-sectional area of the sample:

$$k(T) = \frac{P \cdot L}{\Delta T \cdot A} = \frac{G \cdot L}{A} \tag{3.2}$$

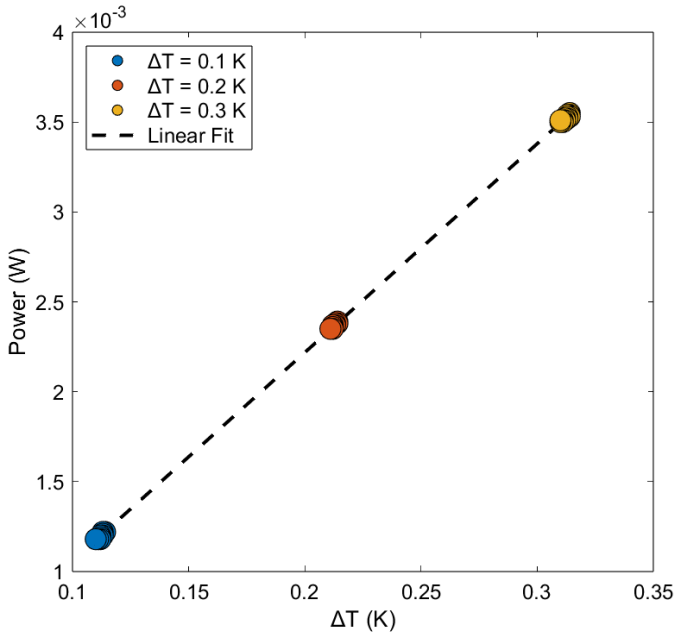

Figure 3.9: An example plot of heater power vs. ΔT for a quartz sample at 200 K. Data points for the array ΔT = [0.1 K, 0.2 K, 0.3 K] were collected over 180 seconds.

3.2.2 Sample Geometry

When performing thermal conductivity analysis, the geometry of geological samples must be carefully considered. As mentioned in Section 3.1.3, a sample's conductance at room temperature should exceed 1 $mW \cdot K^{-1}$ to minimize the effect of heat loss through connecting wires. This requirement depends on both the sample's cross-sectional area and the distance between the centers of the thermocouples, as defined by the following equation:

$$G = \frac{k \cdot A}{L} \tag{3.3}$$

This formula is a rearrangement of Equation 3.2. Because conductance is proportional to both cross-sectional area (A) and thermal conductivity (k), materials with high conductivity (e.g., metals) can be analyzed using smaller sample dimensions. In contrast, dielectric materials such as rocks and minerals require a larger cross-sectional area to ensure that the thermal conductance exceeds 1 $mW \cdot K^{-1}$ at room temperature. Additionally, the length between the thermocouple tabs (L) can be reduced to further increase conductance.

Determining appropriate sample dimensions to satisfy the thermal conductance requirements is challenging because thermal conductivity must be known to calculate conductance using Equation 3.3. This situation is counterintuitive, given that thermal conductivity is the very property under investigation and is not known. Cryogenic Ltd recommends cutting dielectric samples into bars with dimensions of 2 x 2 x 15 mm. However, achieving these dimensions for geological material is quite difficult, as most samples become brittle at this size and often break during preparation. Samples with a width and height between 2 and 3 mm and a length of approximately 20 mm have been found to meet both mechanical stability and thermal performance requirements.

3.2.3 Thermal Transport Settings

The thermal transport settings control how the CFMS operates and collects measurements. These include the PID (proportional-integral-derivative) software loop, the ΔT tolerance, the power drift limit, the stability time, and the time-out duration. These settings are sample-dependent and must be configured in the software for each new sample. Additionally, these settings need to be adjusted across the temperature range of the experiment (e.g., 5 to 300 K) to account for variations in the sample's thermal conductivity and thermocouple sensitivity. The CFMS software allows users to define different settings for specific temperature intervals (e.g., 300–180 K; 180–50 K; 50–20 K; 20–5 K). Each interval is identified by its upper temperature boundary (e.g., 300 K, 180 K, 50 K, 20 K), and the software automatically updates the settings as the temperature changes during a measurement run (e.g., 300 to 100 K). A description of each thermal transport setting is provided below.

Stability Time

The stability time defines how long a ΔT measurement must remain stable while heat is applied to the sample. The data collected over this period is averaged by the software and plotted on the power versus ΔT plot (Figure 3.9). At higher temperatures, this is typically set to 180 seconds. As the temperature decreases, the stability time must be shortened to account for increased noise in the measurements due to reduced thermocouple sensitivity (Figure 3.7). At temperatures below 50 K, stability times of 30 or 60 seconds are often used. Once the ΔT tolerance is met, the system collects multiple data points over the defined stability period; these points are then used to generate the P vs. ΔT plot (e.g., Figure 3.9).

ΔT Tolerance

The ΔT tolerance specifies how much the measured ΔT can deviate from the expected value. Before the ΔT array measurements, the CFMS records the background ΔT to account for thermal conductance through the connecting wires and sample platform (Section 3.1.3).

The expected ΔT is the value programmed by the user (e.g., 0.1 K, 0.2 K, 0.3 K) plus the background ΔT. Once the ΔT measurements are stable enough that they do not exceed the tolerance, the software records the ΔT measurements over the stability time. At high temperatures, a ΔT tolerance of 0.005 K is recommended; however, as the temperature of the measurements decreases, the tolerance needs to increase to accommodate an increase in instrument noise and temperature drift. Temperatures below 50 K typically require a larger tolerance of 0.01 to 0.015 K.

Power Drift Limit

Similar to the ΔT tolerance, the power drift limit specifies how much the power can drift while maintaining a stable ΔT. A reasonable power drift limit for geological samples ranges between 10^{-6} and 10^{-4} W; a good starting point at higher temperatures is 3×10^{-5} W. The power drift limit typically needs to decrease as temperature decreases to accommodate temperature drift and electronic noise. If the recorded power does not meet the specified tolerance, the measurement will time out.

Time-out Duration

The time-out duration specifies how long a ΔT measurement can run. The typical duration is 1000 seconds, but it can be shorter if preferred. If the ΔT and/or power measurements do not reach stability before the time-out, it indicates that the PID values (described below), ΔT tolerance, or power drift limit need to be adjusted. All measurements should finish before the time-out duration.

PID Settings

During measurements, the heater is controlled by a proportional-integral-derivative (PID) control loop to maintain a constant ΔT. The proportional (P) component adjusts the heater power based on how much the measured ΔT deviates from the expected ΔT. If the P value

is set too high, it can cause oscillations in the data that can cause the system to not reach the desired target ΔT by the end of the time-out duration. If it is too low, the system will have a large steady-state error and will not reach the target ΔT.

After the initial response of the P component, the integral (I) corrects the offset errors in the measurements over time to help the system reach the target ΔT. If the I value is set too high, it can lead to oscillations in the ΔT measurements, making it difficult to reach the target. If it is too low, the heater may not be able to supply enough power to reach the target value before the measurement times out.

A derivative (D) component, which responds to the rate of change in a system, is typically not included in cryogenic control loops (D = 0). This is because it is highly sensitive to noise, especially at low temperatures in the CFMS, where noise can be misinterpreted as a change in the system (Sheats et al., 2006).

Finding the appropriate PI values requires some trial and error. For crystalline mineral samples, a general guideline is $P \approx \frac{1}{6}G$ and $I \approx \frac{1}{60}G$, where the thermal conductance (G) can be estimated using literature thermal conductivity values and Equation 3.3. However, this guideline is no longer applicable at temperatures below 30 K, where increased noise affects the system response, and the PI values must be determined experimentally. During meteorite analysis, it was discovered that the measurements did not adhere to the general rule at any temperature; therefore, their PI values had to be determined through iterative tuning.

3.2.4 Thermalization Time

For thermal conductivity measurements using the CFMS, samples must be thermally equilibrated to the chamber temperature before each measurement. As rocks and minerals are good insulators, heat transfers much more slowly compared to conductors. As a result, geological samples are subject to thermal gradients that take longer to dissipate as they are heated and cooled in the system. If a temperature gradient exists in the sample during ther-

mal conductivity measurements, the results can be higher than expected when the sample is cooled, or lower than expected when heated. This phenomenon is demonstrated with data from a serpentinite rock (Figure 3.10) and a sample of calcite (Figure 3.11).

The serpentinite rock is made up of two serpentine-group minerals, chrysotile and lizardite ($Mg_3Si_2O_5(OH)_4$), and chromite ($FeCr_2O_4$). This sample was measured in the early stages of this study; however, the research focus shifted to single-crystal minerals to develop the CFMS method, as their phonon behaviour is better understood and more predictable than that of heterogeneous rock samples (see Section 4.1). Although this project includes meteorite rock samples, the serpentinite data was not pursued further in the interest of time. Nonetheless, the measurements from this sample provide an excellent illustration of the importance of proper thermalization.

Figures 3.10 and 3.11 show two distinct trends in the data that were collected when the samples were not fully thermalized. When the sample is cooled down (e.g., from 300 to 100 K), more heat flows through the sample than expected, resulting in high thermal conductivity measurements compared to fully thermalized data. Conversely, when the sample is heated (e.g., 100 to 300 K), less heat is transferred, resulting in lower thermal conductivity measurements.

At temperatures below 100 K, the data begins to converge regardless of the thermalization time. For crystalline materials like calcite, this suggests that such samples start to thermalize more quickly due to the increase in thermal conductivity at temperatures below 100 K, and thus heat is transferred more rapidly. It is expected that once the peak thermal conductivity has been reached, and the thermal conductivity begins to decrease at low temperatures, the required thermalization time will increase. Although the thermal conductivity of the serpentinite sample decreases with temperature, similar to that of amorphous materials, the data still converge at 100 K, despite the decrease in conductivity. This suggests that temperature gradient effects may be associated with thermal radiation, which becomes prominent in geological samples at temperatures above 150 K (Section 3.3.3). Iterative test-

ing revealed that a thermalization period of 2.5 hours between measurements is optimal for minimizing temperature gradient effects in geological samples (Figures 3.10 and 3.11). A plot showing cool-down and warm-up temperatures over time is provided in Figure 3.12 to illustrate further the length of thermalization time required during thermal conductivity measurements.

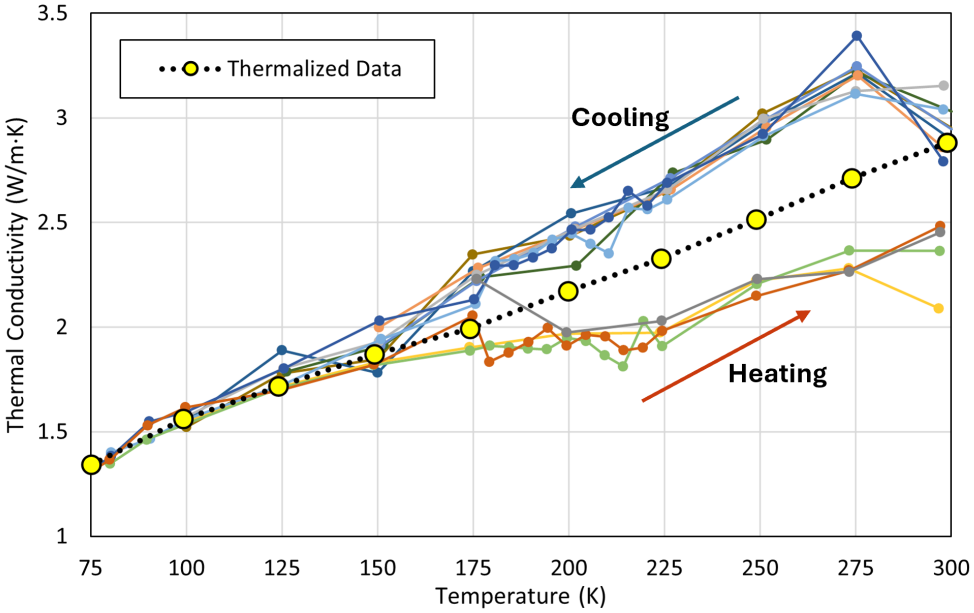

Figure 3.10: Thermal conductivity of a serpentinite rock sample, with data collected using a thermalization time of 2.5 hours indicated by yellow dots and a black dotted line. Data collected with thermalization times of less than 2 minutes are represented by the remaining plots. Arrows indicate the cooling and heating trends.

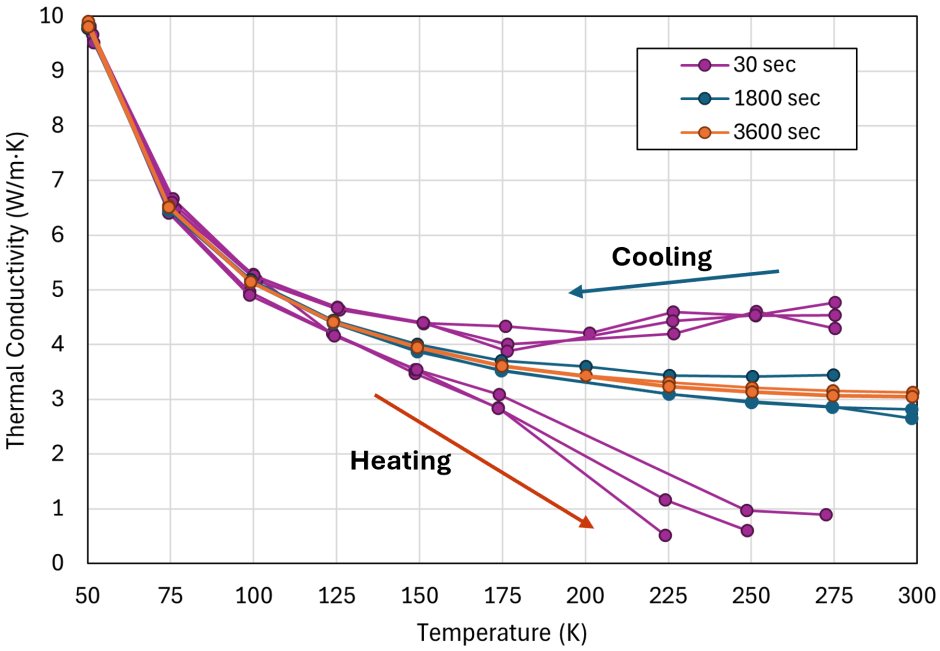

Figure 3.11: Thermal conductivity measurements of a calcite sample with varying thermalization times: 30 seconds, 1800 seconds, and 3600 seconds. Arrows indicate the cooling and heating trends.

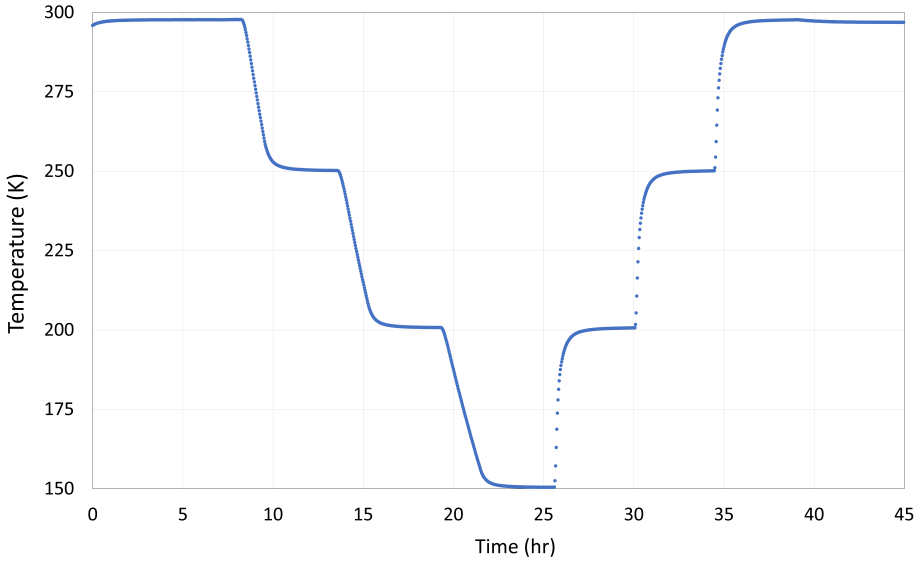

Figure 3.12: Temperature of a calcite sample over time. This plot illustrates the time typically required for a sample to cool down or heat up and reach thermal equilibrium.

3.3 Data Analysis Methods

3.3.1 Sources of Uncertainty

The total error in the thermal conductivity measurements was propagated from uncertainties in thermal conductance (G), length between the thermocouple tabs (L), and the cross-sectional area of the sample (A). As thermal conductivity is defined by Equation 3.2

$$k = \frac{GL}{A}$$

the error in k was determined using the standard propagation of uncertainty for functions involving multiplication and division of independent variables. According to this rule, the relative error in a product and/or quotient is the square root of the sum of the squared relative errors of each component. This gives:

$$\delta k = k\sqrt{\left(\frac{\delta G}{G}\right)^2 + \left(\frac{\delta L}{L}\right)^2 + \left(\frac{\delta A}{A}\right)^2} \tag{3.4}$$

This formulation is standard in experimental error analysis (e.g., Taylor, 1997) and assumes that the errors in G, L, and A are uncorrelated.

The length between thermocouple tab centers (L), as well as the sample's height (h) and width (w), were measured using a caliper with an accuracy of $\pm 5 \times 10^{-3}$ mm. Each dimension was measured multiple times—up to 30 measurements per sample—to determine the average values for L and A, where $A = h \times w$. The standard error (SE) of the mean was used to represent uncertainties in δL, δh, and δw, and the uncertainty in area (δA) was calculated by propagating the height and width uncertainties using the product rule.

Since the CFMS measures the thermal conductance of the sample rather than the thermal conductivity directly, several factors can contribute to the uncertainty in conductance (δG), including:

- PID settings

- Range of ΔT values
- Heat loss from radiation and conduction through gas and wires
- Thermocouple sensitivity
- Helium flow rate
- Instrument error from the source meter and nanovoltmeter
- Thermalization time

The P and ΔT values are measured using a source meter and a nanovoltmeter, respectively (Section 3.2.1). Individual measurements of both power and ΔT are highly stable, with the source meter and nanovoltmeter each maintaining six-digit resolution during operation. Identifying the individual contributions of the other sources listed above is tedious and can lead to an overestimation of the overall uncertainty. Therefore, it is best to determine the uncertainty of thermal conductance based on a primary source.

As described in Section 3.2.1, thermal conductance at a given temperature is determined from the slope of the linear fit to the plot of heater power versus ΔT (Figure 3.9). Ideally, this relationship would be perfectly linear, but drift in both P and ΔT prevents a perfect fit. As a result, the uncertainty in the slope of the regression line represents the uncertainty in thermal conductance, δG.

Drift in P and ΔT primarily originates from variations in cooling power throughout the system. As discussed in Section 3.1.1, the helium flow rate through the CFMS is critical for maintaining stable cooling. At higher temperatures (>50 K), the system is less sensitive to flow rate fluctuations, resulting in more stable measurements. However, at lower temperatures, adequate flow is essential; insufficient cooling power leads to increased temperature drift, which raises the uncertainty in low-temperature measurements.

In summary, the CFMS measurements are quite precise, and the uncertainties in L, A, and G are relatively small (Table 3.2). As a result, there is high confidence in the thermal

conductivity measurements presented in this study. That said, some low-temperature results do exhibit larger uncertainties, primarily due to decreased thermocouple sensitivity and temperature drift.

Table 3.2: Magnitude of uncertainties.

Uncertainty	**Magnitude**
δL	10^{-5} to 10^{-6} m
δA	10^{-6} m^2
δG	T($\geq$50 K): 10^{-5} to 10^{-6} W K^{-1} T($<$50 K): 10^{-3} to 10^{-4} W K^{-1}
δk	T($\geq$50 K): 10^{-1} to 10^{-3} W m^{-1} K^{-1} T($<$50 K): 10^{0} to 10^{-3} W m^{-1} K^{-1}

3.3.2 Data Quality Check

Measurements with the CFMS can take several days to complete due to the time required to heat or cool a sample and allow for thermalization (Section 3.2.4). Because of this extended duration, the measurements are not actively monitored. To assess data quality after collection, a MATLAB code was developed to review and process the thermal conductivity data (Appendix A). The code provides a quick assessment of each measurement run, based primarily on configuration settings (Section 3.2.3) and temperature drift. If poor or failed measurements are detected, this indicates to the user that the configuration settings and cooling conditions need to be reviewed and adjusted for future runs. The quality assessment criteria used by the code are described in this section.

The CFMS software reports thermal conductance and conductivity for each temperature point. However, the reported conductance is calculated from the slope of averaged power and ΔT values collected during the stability time (Section 3.2.3). This averaging can mask the variability caused by temperature drift, leading to an underestimation of uncertainty.

To address this, the MATLAB code recalculates conductance from the raw, individual data points to better account for drift. In most cases, the percent difference between the recalculated and reported conductance values is less than 1%; however, at lower temperatures (< 30 K), the difference can reach up to 5% due to greater sensitivity to drift. All thermal conductivity values reported in this study are based on the recalculated conductance.

The coefficient of determination (R^2) is used to evaluate the linearity between the raw heater power and ΔTvalues. Since CFMS measurements are generally very stable (as discussed above), R^2 values are typically ≥ 0.99. In rare cases where $R^2 < 0.9$, the cause is usually an instrument glitch or insufficient cooling power.

Configuration settings are evaluated by plotting ΔT and P over the settle time for each ΔT measurement. These plots help determine whether the programmed PID settings are appropriate or whether a timeout occurred. A timeout may result even when PID values are reasonable if the ΔT tolerance or power drift limit is too strict. If the plots appear stable and well-behaved in this case, the data is typically considered usable.

Temperature drift is also evaluated as part of the quality check. This refers to changes in the heat sink temperature, which is in thermal equilibrium with the sample chamber. If the drift is too large, the sample is effectively exposed to a range of temperatures rather than a stable set point, which can affect its thermal response and reduce the accuracy of the results. Drift is calculated as the difference between the effective temperature and the final temperature. The final temperature is defined as the heat sink temperature at the last measurement point of the third element of the ΔT array (e.g., $\Delta T = 0.3$ K). The effective temperature corresponds to the start of the settle time for the first element (e.g, $\Delta T= 0.1$ K). For this study, a drift threshold of 1 K is used for measurements ≥ 50 K and 2 K for measurements < 50 K.

Examples of the MATLAB quality check process are shown in Figures 3.13 to 3.16. Figures 3.13 and 3.14 present datasets that pass all the quality checks, while Figures 3.15 and 3.16 are cases where the data did not meet the criteria.

Although not a component of the MATLAB code, the cooling power is also important to consider when evaluating the quality of low-temperature data. At temperatures ≤ 20 K, the helium pot temperature should be less than 4 K (ideally ~ 3.7 K) to ensure there is enough cooling power. If the temperature of the helium pot is greater than 4 K, then the measured thermal conductivity will be lower than expected due to insufficient cooling power, which prevents the sample from fully reaching thermal equilibrium (Figure 3.17).

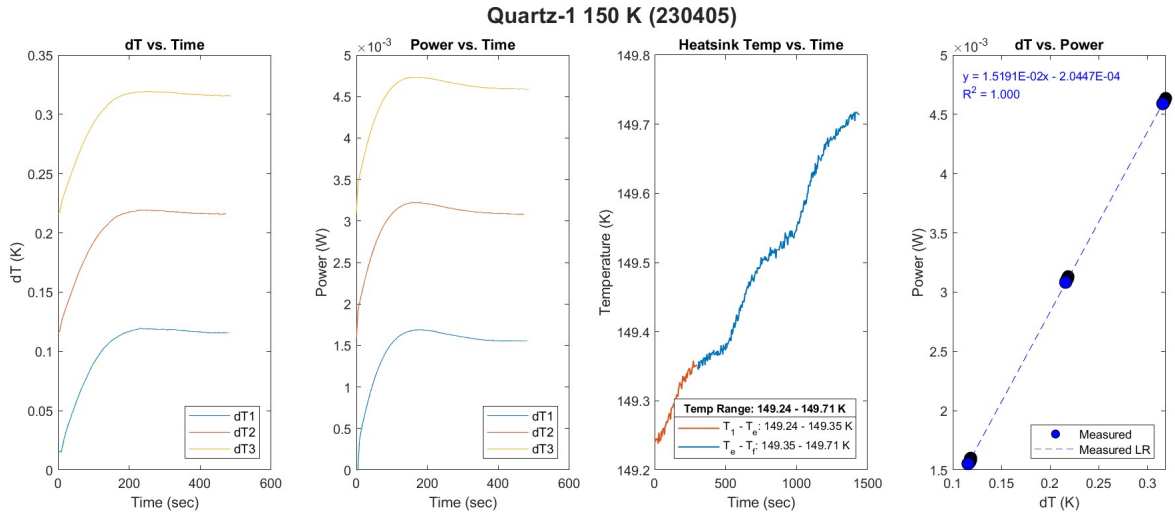

Figure 3.13: Example of a quality check output for a quartz measurement at 150 K that satisfies all three quality criteria.

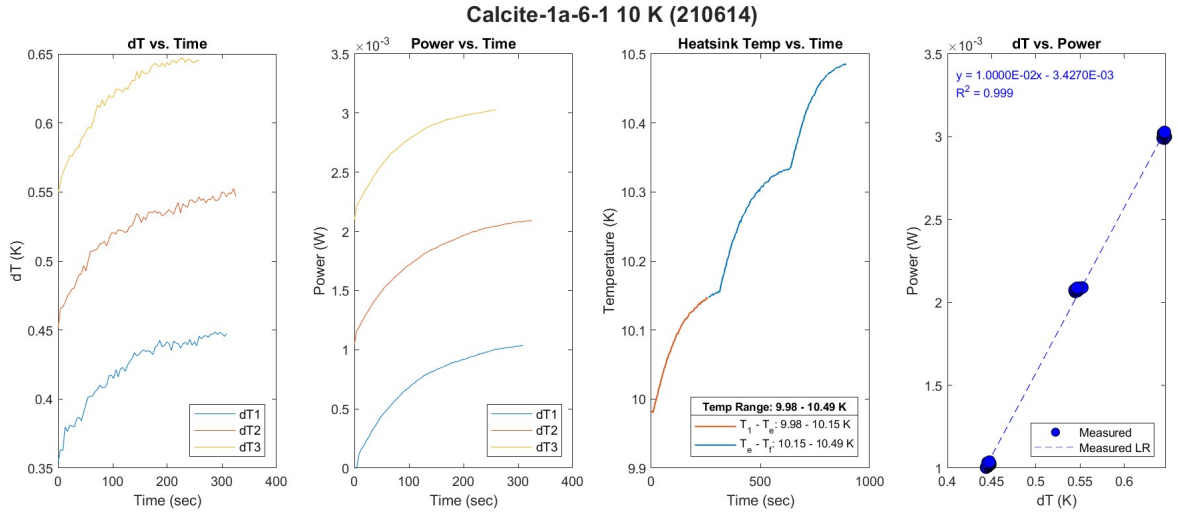

Figure 3.14: Example of a quality check output for a calcite measurement at 10 K that satisfies all three quality criteria. Note the noise in the ΔT measurements due to the decreased sensitivity of the thermocouple at low temperatures.

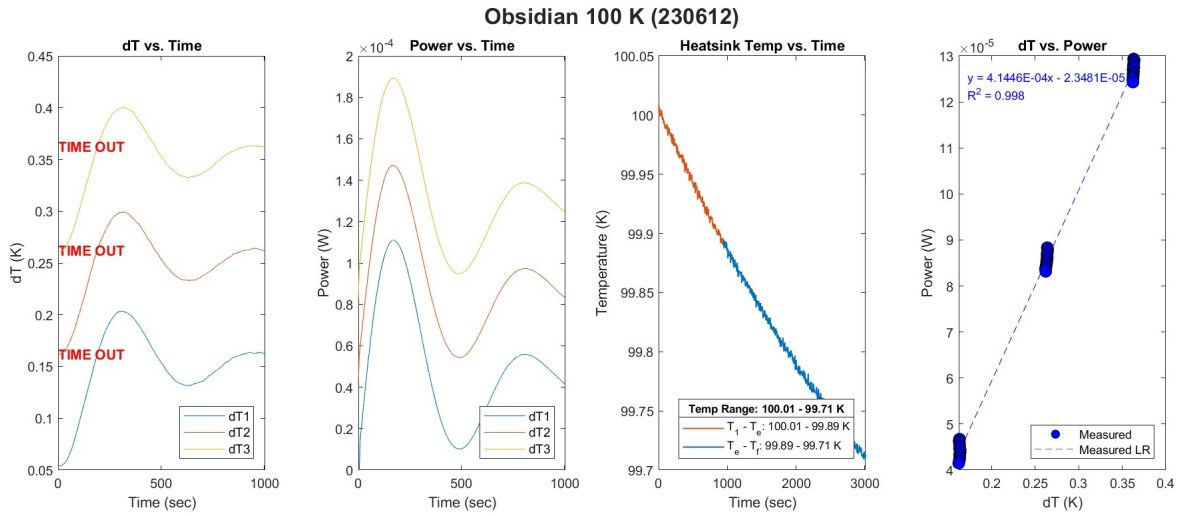

Figure 3.15: Example of a quality check output for an obsidian measurement at 100 K. Note that the data timed out due to the oscillations in the ΔT and heater data. Additionally, note the decrease in heat sink temperature, which suggests that the PID settings may need adjustment.

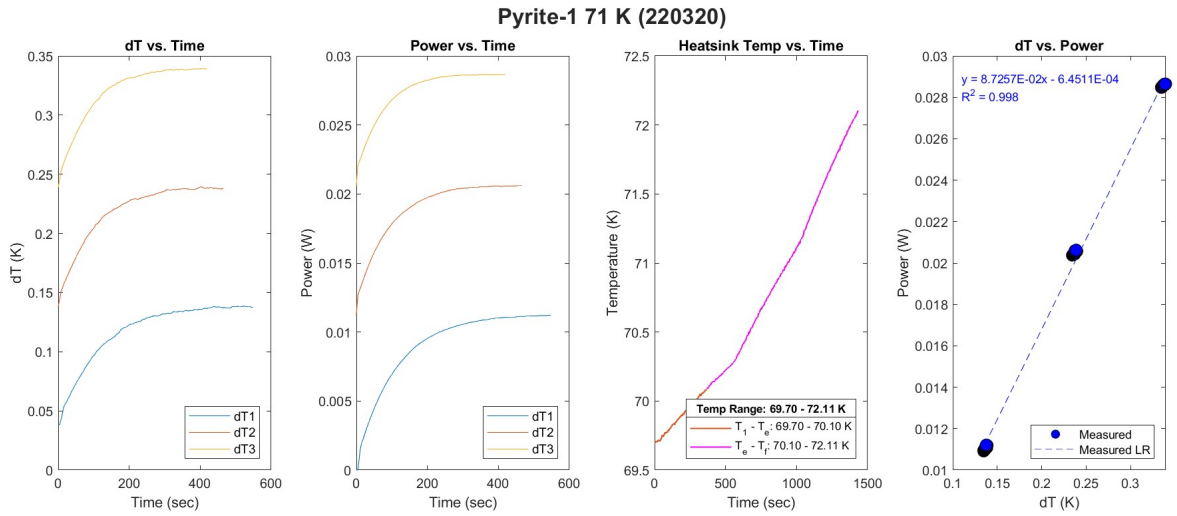

Figure 3.16: Example of a quality check output for a pyrite measurement at 70 K. Although the ΔT and power plots look good, the temperature drift of the heat sink is > 1 K (alerted by the effective temperature line changing to pink).

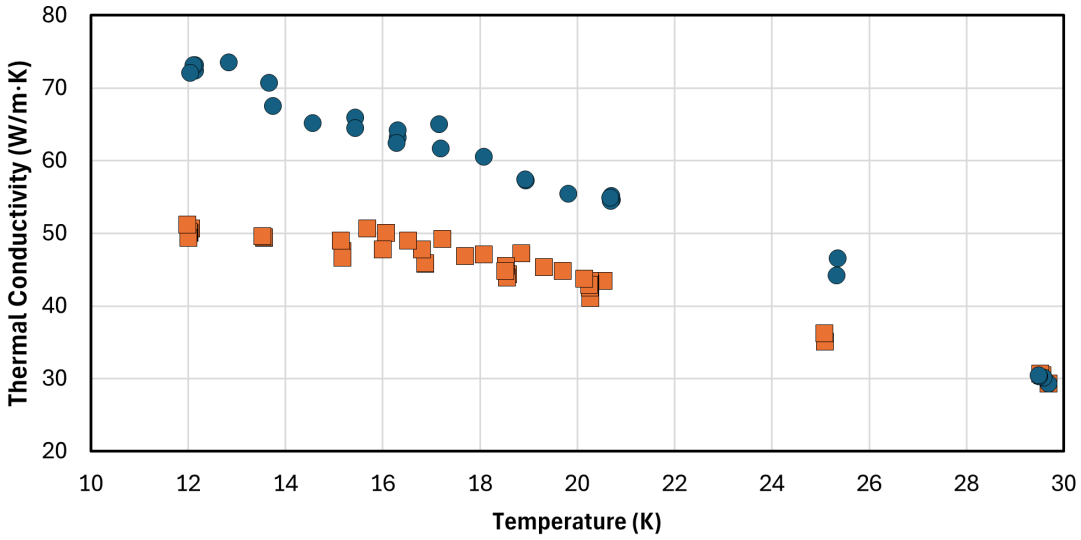

Figure 3.17: Thermal conductivity vs. temperature plot for a sample of calcite at low temperatures (<30 K). This plot illustrates the importance of cooling power in this range. The blue circles represent data collected with adequate cooling power (He pot temperature = 3.6 K), while the orange squares represent data collected with insufficient cooling power (He pot temperature = 4.3 K).

3.3.3 Radiative Heat Loss

Radiative heat loss becomes increasingly important at higher temperatures, typically above 100 K, where it can significantly affect thermal conductivity measurements. Although a radiation shield is placed over the sample at the end of the thermal transport probe (Figure 3.8b), it only reduces how much heat is lost—it does not eliminate it. Some heat is still radiated within the sample chamber during measurements, which must be accounted for during data post-processing. The amount of radiative heat loss is defined by the Stefan-Boltzmann law:

$$P_r = \sigma A \varepsilon T^4 \tag{3.5}$$

where:

- P_r = radiated power (W)
- σ = Stefan-Boltzmann constant (5.6704×10^{-8} W m^{-2} K^{-4})
- A = surface area of the radiating object (m^2)
- ε = emissivity of the radiating object (unitless)
- T = temperature (K)

In the CFMS, the sample chamber is thermalized to an isothermal temperature T, while the sample is heated to a temperature of $T + \Delta T$. In this setup, the sample emits radiation outward (P_{out}) while also absorbing radiation emitted from the inner wall of the radiation shield (P_{in}):

$$P_{out} = \sigma A \varepsilon (T + \Delta T)^4 \tag{3.6}$$

$$P_{in} = \sigma A \varepsilon T^4 \tag{3.7}$$

The total radiative power, P_r, is given by:

$$P_r = P_{out} - P_{in} = \sigma A \varepsilon \left[(T + \Delta T)^4 - T^4 \right] \tag{3.8}$$

However, this equation oversimplifies the radiative heat loss occurring during conductance measurements. Radiation in the system also originates from the heater and hot junction of the thermocouple. Additionally, the silver epoxy used to bond the thermal assemblies to the sample contributes to radiation. Radiative heat loss from the wires is not considered, as their surface area is negligible compared to that of the sample.

Considering all sources of radiative heat loss within the sample chamber environment, Equation 3.8 is expanded to:

$$P_r = \sigma \left(\frac{A_s}{2} \varepsilon_s + A_{hot} \varepsilon_{hot} + A_{htr} \varepsilon_{htr} + A_{ep,h} \varepsilon_{ep,h} \right) \left[(T + \Delta T)^4 - T^4 \right] \tag{3.9}$$

where the subscripts correspond to: s = sample, hot = thermocouple hot junction, htr = heater, ep,h = epoxy on the hot side of the sample. The components of this equation are best understood with reference to Figure 3.18.

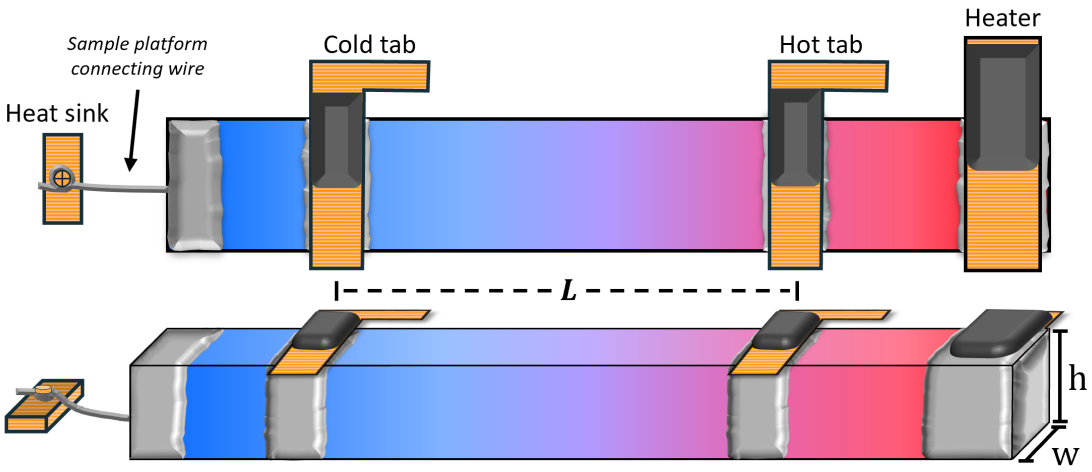

Figure 3.18: A schematic of the sample configuration with thermal assemblies (not to scale) and temperature gradient. The silver areas represent the epoxy. Components that are on the heated side of the sample (heater, hot junction of the thermocouple, and corresponding epoxy) will radiate heat along with the sample. The black areas on top of the copper tabs represent the STYCAST black epoxy.

While the entire sample emits thermal radiation, the contribution is temperature dependent due to the T^4 dependence in the Stefan–Boltzmann law. Although the temperature

difference across the sample is small, the hotter end emits slightly more radiation. As a result, the effective surface area used in Equation 3.9 is approximated as one-half of the total sample surface, corresponding to the heated end. This area is further reduced to account for regions covered by epoxy, the heater, and the hot tab, such that:

$$A_s = \frac{A_s}{2} - A_{ep,h} - (l_{hot} w_s) - (l_{htr} w_s) \tag{3.10}$$

where l = length and w = width (Figure 3.18).

Correcting conductance measurements using Equation 3.9 poses challenges. First, the emissivity values of the sample, heater, hot tab, and epoxy are unknown. While they can be estimated, direct measurement is preferred since emissivity strongly depends on the sample type and experimental environment (see Chapter 7). Second, accurately determining the surface areas of the heated assemblies and epoxy is difficult due to their irregular shapes, often leading to an underestimation of radiative power. Cryogenic Limited (2019) recognizes these challenges and suggests two approaches to estimate radiation contribution:

1. Measure the thermal conductivity of multiple samples with different surface-to-volume ratios

2. Use the T^3 dependence of radiative heat loss in post-processing

The first method is not well-suited to geological materials, particularly rocks, as varying the sample size may introduce differences in porosity, mineralogy, and grain size and boundaries, all of which affect thermal conductivity. In the second method, radiative power (P_r) is directly proportional to T^3. This T^3 term comes from the Taylor expansion of Equation 3.8 (Appendix B):

$$P_r = 4\sigma A \varepsilon T^3 \Delta T \tag{3.11}$$

Radiative heat loss can become a non-negligible factor in steady-state thermal conductivity measurements, particularly above 100 K, due to the T^3 dependence of radiative heat

transfer (Equation 3.11). For geological samples, these effects may become more noticeable closer to 200 K (Clauser and Huenges, 1995; Tritt and Weston, 2006).

As described in Chapter 2, the total thermal conductivity (k_T) of a crystalline solid consists of both electronic (k_E) and lattice (k_L) components: $k_T = k_E + k_L$. Radiative heat loss primarily affects the lattice component because phonon–phonon scattering creates oscillations within the crystal lattice that generate electromagnetic fields that emit thermal infrared radiation. In contrast, electrons scatter through the lattice without producing electromagnetic fields that contribute significantly to radiative transfer.

Therefore, the total thermal conductivity can be expressed as $k_T = k_E + (k_L + k_{rad})$, where k_{rad} is the radiative conductivity component. In insulating materials, k_E is negligible, so the measured thermal conductivity becomes $k_T = k_L + k_{rad}$.

The radiative conductivity component k_{rad} can be estimated from the optical properties of the material using:

$$k_{\text{rad}} = \frac{16n^2\sigma T^3}{3e} \tag{3.12}$$

where n is the refractive index, σ is the Stefan–Boltzmann constant, and e is the mean extinction coefficient. While this equation is widely cited in geoscience literature (Kanamori et al., 1968; Fukao, 1969; Aronson et al., 1970; Beck et al., 1978; MacPherson and Schloessin, 1982; Robertson, 1988; Murashov and White, 2006; Thomas et al., 2012b), it is typically applied to mantle conditions involving high temperatures and pressures.

MacPherson and Schloessin (1982) introduced an alternative method to estimate radiative heat loss based on their high-temperature thermal conductivity measurements (>300 K). Rather than relying on optical properties, they based their approach on deviations observed in a log–log plot of $\log(k)$ vs. $\log(T)$ for calcite ($CaCO_3$) and halite (NaCl). They observed that the data followed a linear trend at lower temperatures but began to deviate between 500 and 600 K due to the influence of radiative effects. By extrapolating the linear trend, they isolated the radiative component as the difference between the total (k_T) and extrapolated (corrected, k_c) conductivities: $k_{\text{rad}} = k_T - k_c$. When k_{rad} was plotted against T^3, the result

was a linear relationship, consistent with the expected temperature dependence of radiative heat transfer.

A similar method to MacPherson and Schloessin (1982) was applied to low-temperature measurements (< 300 K) by Pope et al. (2001), with their findings also summarized in Tritt and Weston (2006). In their work, they corrected the radiative contributions to the thermal conductivity of a quasicrystal—a solid with an ordered structure but lacking periodic atomic repetition—whose total conductivity included contributions from both electronic and lattice components. Since radiation primarily affects the lattice component, Pope et al. (2001) first estimated the electronic contribution using the Wiedemann–Franz law (Chapter 2, Equation 2.28) and subtracted it from the total conductivity to isolate the lattice term: $k_L = k_T - k_E$.

At temperatures above the thermal conductivity peak, crystalline materials typically follow a $k \propto 1/T$ trend (Chapter 2). Pope et al. (2001) fit the lattice conductivity data between the peak and 150 K using the model $k_L = a(1/T)$ and extrapolated this fit to 300 K. The difference between the extrapolated (corrected) and measured lattice conductivity is the radiative component k_{rad}. They also found that k_{rad} varies linearly with T^3. This correction process is illustrated in Figure 3.19.

The low-temperature fitting method by Pope et al. (2001) was applied to the crystalline minerals in this study. Unlike in their work, subtraction of the electronic component was not required, as the materials analyzed are insulators and electronic contributions to thermal conductivity are negligible. Thermal conductivity was plotted against $1/T$ to identify linear trends at low temperatures, where radiative losses are minimal. To avoid bias from high-temperature deviations, fitting was limited to data below 200 K. The optimal range was selected using statistical criteria including the coefficient of determination (R^2), errors in the slope and intercept, root mean square error (RMSE), and residual analysis. Extrapolation of the fitted model to 300 K yielded corrected thermal conductivity values that exclude radiative contributions from both the sample and thermal mounting assemblies.

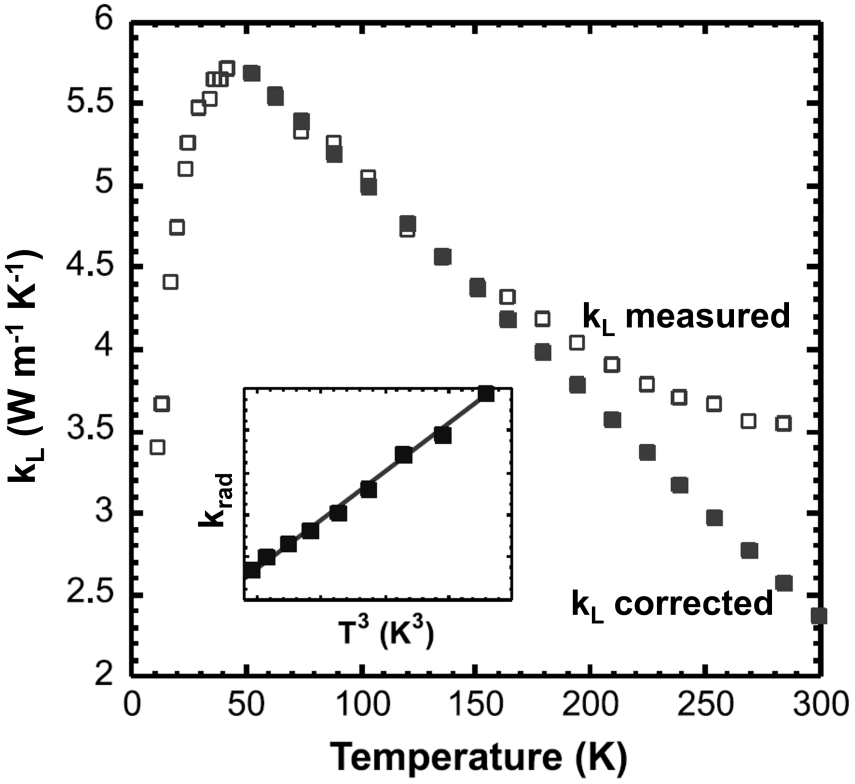

Figure 3.19: The measured lattice thermal conductivity (k_L, open squares) is compared to the corrected values (solid squares), which were extrapolated from a $1/T$ fit. The difference between the measured and corrected values corresponds to the radiative component. The inset shows that k_{rad} varies linearly with T^3. Figure adapted from Pope et al. (2001), with terminology modified to match that used in this study.

This correction method, however, was not suitable for the thermal conductivity data of obsidian or the meteorite samples. Instead, a logarithmic fit was applied to the obsidian data (Chapter 5), while an empirical fit was derived to correct the meteorite data, as described in Chapter 6.

To estimate the error in the corrected thermal conductivity, three primary sources of error were propagated: (1) the residual between the extrapolated data and the measured value (R), (2) the measurement error from the experimental setup, which includes the propagated error from ΔT and heater power (conductance) and sample geometry (Equation 3.4), and (3) a 5% systematic accuracy term that accounts for instrumentation limits and potential

model bias:

$$\sigma_k = \sqrt{R^2 + \sigma_{\text{meas}}^2 + (0.05 \times k_{\text{corrected}})^2} \tag{3.13}$$

The residual term becomes increasingly dominant at higher temperatures, where radiative heat loss scales with T^3, as described by the Taylor expansion of the Stefan-Boltzmann law (Equation 3.11). This results in a growing difference between the measured and extrapolated thermal conductivity, causing the total error to increase with temperature.

Equation 3.13 was adapted from the relative error correction described by Macke et al. (2024) for heat pulse analysis with the Quantum Design measurement system. In that method, each error source is expressed as a fractional term, and the total error is multiplied by the measured thermal conductivity to obtain an absolute error.

$$\sigma(k) = k \times \left\{ \left[\frac{R_{\Delta T}}{\Delta T}\right]^2 + \left[\frac{2IR\delta I}{P}\right]^2 + \left[\frac{0.2R_{\text{loss}}}{P}\right]^2 + \left[\frac{0.1\Delta T K_{\text{shoes}}}{P}\right]^2 \right\}^{1/2} \tag{3.14}$$

The first term represents the residual error from the curve fit. The second term accounts for fluctuations in heater power due to variations in current (I) and resistance (R). The third term estimates radiative losses as 20% due to errors in surface area and emissivity. And lastly, the fourth term accounts for heat loss through the sample mounts (K_{shoes}), using a 10% correction factor.

Unlike the fractional-error approach used in the heat pulse method (Equation 3.14), the error terms in this study are expressed in absolute units (W m^{-1} K^{-1}). This is because the primary sources of error were quantified in absolute terms through residual analysis and measurement errors. While Equation 3.13 accounts for the primary error sources in steady-state measurements, it may require refinement in cases where radiative losses are modelled explicitly using emissivity, geometry, and surface area (Equation 3.9) rather than approximated through extrapolation and fit-based error propagation.

3.4 Copper Reference Sample

Copper is an excellent heat conductor and has a well-known thermal conductivity at temperatures below 300 K documented by the National Institute of Standards and Technology (NIST) (formally National Bureau of Standards) (Childs et al., 1973; Hust and Lankford, 1984; Simon et al., 1992; Powell et al., 1996; NIST, 2010). The NIST thermal conductivity data for copper were collected using cryostat apparatuses similar to the CFMS (Powell et al., 1957; Hust et al., 1970)—measurements were also performed under vacuum to eliminate convective and conductive heat transfer through air, and samples were shielded to prevent radiative heat loss.

A plot of thermal conductivity for oxygen-free copper from NIST is provided in Figure 3.20. This figure illustrates the variation in thermal conductivity with different purities of copper. The purities are defined by the residual-resistivity ratio (RRR), which is the ratio of the resistivity of the sample at 4.2 K and 300 K. The higher the RRR, the greater the purity of the copper. Between 150 and 300 K, the thermal conductivity is similar among the different RRR copper types, where it is $\sim$400 W m^{-1} K^{-1} at 300 K. At temperatures below 150 K, the conductivity becomes distinct with respect to the RRR value. Comparing the thermal conductivity of a copper wire measured with the CFMS to accepted standard values for copper provides confidence in the measurement technique and serves as a validation of the system's performance. It is important to note that the RRR value of the copper wire measured with the CFMS is unknown; however, this does not discount the results.

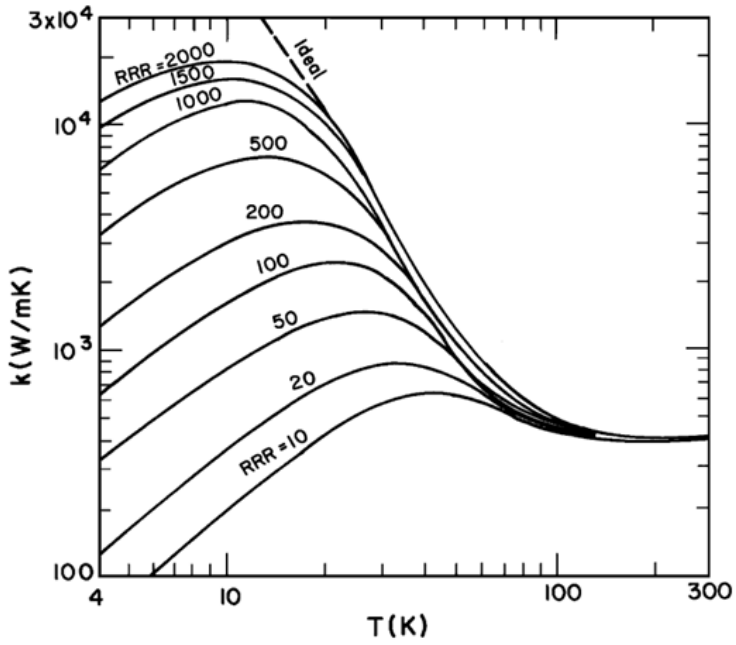

Figure 3.20: NIST thermal conductivity (W m^{-1} K^{-1}) vs. temperature (K) of different copper purities (RRR). Figure is a reprint by Van Sciver (2012), originally by Powell and Fickett (1979) (source not available).

The thermal conductivity of a 0.2 mm diameter copper wire was measured between 5 and 300 K ($A = 3.21 \times 10^{-8}$ m^2, $L = 1.34 \times 10^{-2}$ m). The copper wire mounting configuration is illustrated in Figure 3.21. Although similar to the geologic sample configuration, the copper wire is directly connected to the heat sink by wrapping the wire around the heat sink junction. Instead of using silver epoxy to attach the thermocouple and heater, they are bonded using solder.

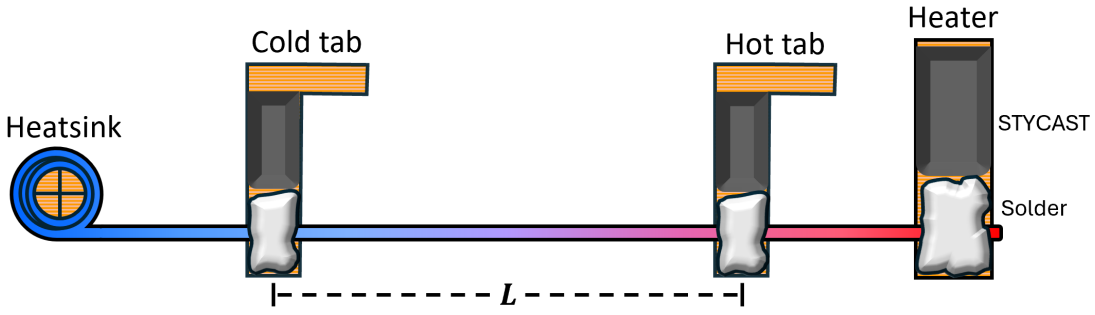

Figure 3.21: Schematic of the mounting configuration of the copper wire sample. Not to scale.

The copper wire was provided as a standard by Cryogenic Ltd during the installation of the CFMS to test and learn the operating procedures. The copper wire is enamelled with a single, thin coat of polyurethane[1]. The polyurethane coating does not affect the thermal conductivity of the copper wire, as the enamel simply acts as an insulator to protect the wire. This is further supported by the very low thermal conductivity of polyurethane, which is $\sim$0.2 W m^{-1} K^{-1} (Ltd, 2024; Zhou et al., 2024; NIST, n.d.).

3.4.1 Results

The thermal conductivity of copper between 5 and 300 K was collected over three different time periods: 2018, 2021, and 2024. The average results for each of period, shown in Figure 3.22, compare well and support both the reliability of the CFMS and the reproducibility of thermal conductivity measurements over a six-year span. However, as illustrated in Figure 3.22, above 150 K the thermal conductivity increases, reaching an average value of (552 ± 5) W m^{-1} K^{-1} at 300 K. This upward trend is indicative of radiative heat loss (Rudajevová et al., 2006; Tomás et al., 2015; Gałązka et al., 2016). A red, dashed line at 400 W m^{-1} K^{-1}—the expected thermal conductivity of copper at 300 K—is included in Figure 3.22 to emphasize the upward trend in data.

3.4.2 Radiative Heat Loss Correction

A similar correction method to Pope et al. (2001), described in Section 3.3.3, was applied to the copper thermal conductivity measurements. However, instead of separating the electronic and lattice thermal conductivities, the data were simply fit to the equation derived for the thermal conductivity of copper by NIST (2010):

$$k(T) = 10^{\frac{a+cT^{0.5}+eT+gT^{1.5}+iT^2}{1+bT^{0.5}+dT+fT^{1.5}+hT^2}} \tag{3.15}$$

[1]Kg 0.2mm Solderable Grade 1 Enamelled Copper Wire On D200 Reel, *Scientific Wire Company*, `https://www.scientificwire.com/acatalog/SX0200S-D200.html`

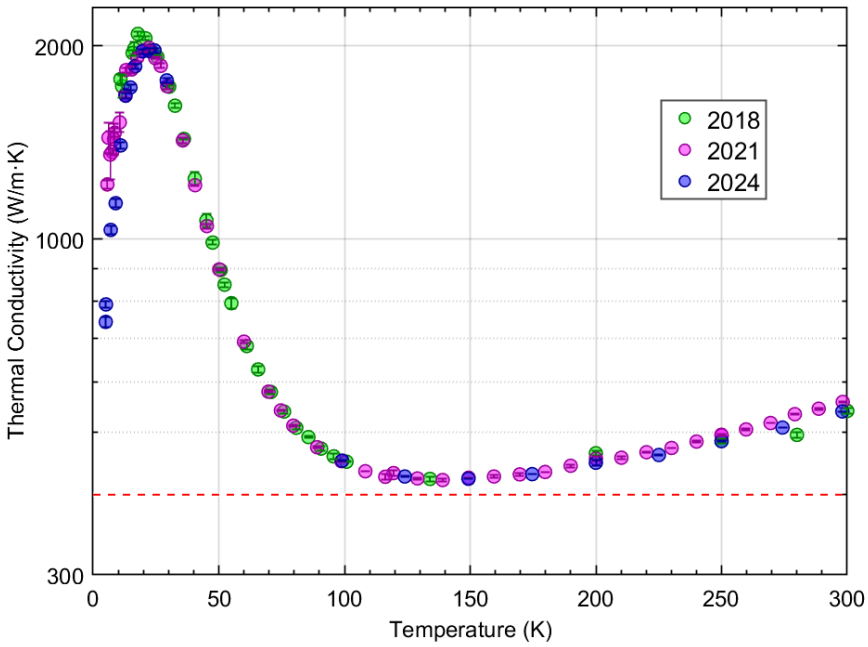

Figure 3.22: Comparison of uncorrected thermal conductivity data of the copper wire over six years. The red dashed line at 400 W m^{-1} K^{-1} emphasizes the expected thermal conductivity of copper at 300 K. The upward trend in the data is due to radiative heat loss.

In this equation, T represents temperature. The best-fit range for the data was found to be between 20 and 140 K ($R^2 = 0.9992$). The fit coefficients for the CFMS copper data are provided in Table 3.3. Using Equation 3.15, the data were extrapolated to 300 K to correct for heat loss due to radiation (Figure 3.23). The error bars on the corrected values were determined by propagating the residuals from the fit, measurement error, and a 5% systematic accuracy term, as defined in Equation 3.13 (Section 3.3.3). The corrected data falls closely along the 400 W m^{-1} K^{-1} line. The thermal conductivity of copper at 300 K, after correction, is 398 ± 17 W m^{-1} K^{-1}, which aligns with the expected value and falls within the 5% accuracy range of the CFMS.

To further illustrate the radiation correction, data from 135 to 300 K are shown in Figure 3.24. A plot of Δk vs. T^3, where Δk is the difference between the total measured thermal conductivity (k_T) and the corrected value (k_C), confirms that the increase in thermal conductivity at high temperatures is due to radiative heat loss (Figure 3.25).

Table 3.3: Coefficients used in Equation 3.15 to fit the trend of the copper wire data.

Coefficient	Fit
a	-3.6640
b	-0.9492
c	0.9882
d	0.4500
e	0.5940
f	-0.07059
g	-0.1445
h	0.00419
i	0.00997

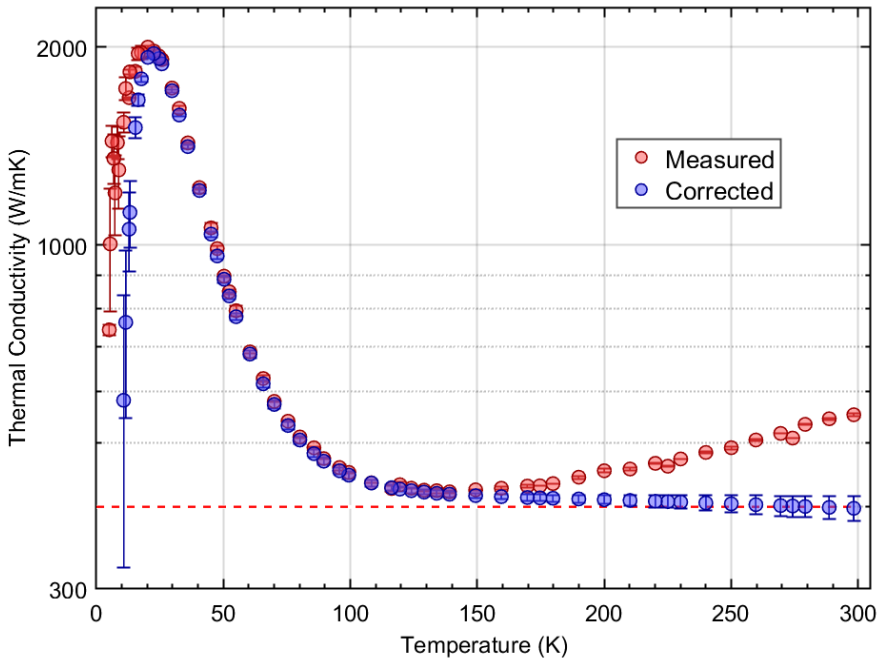

Figure 3.23: Comparison of measured and corrected thermal conductivity data of the copper wire. The data is the average of all measurements collected for the copper wire.

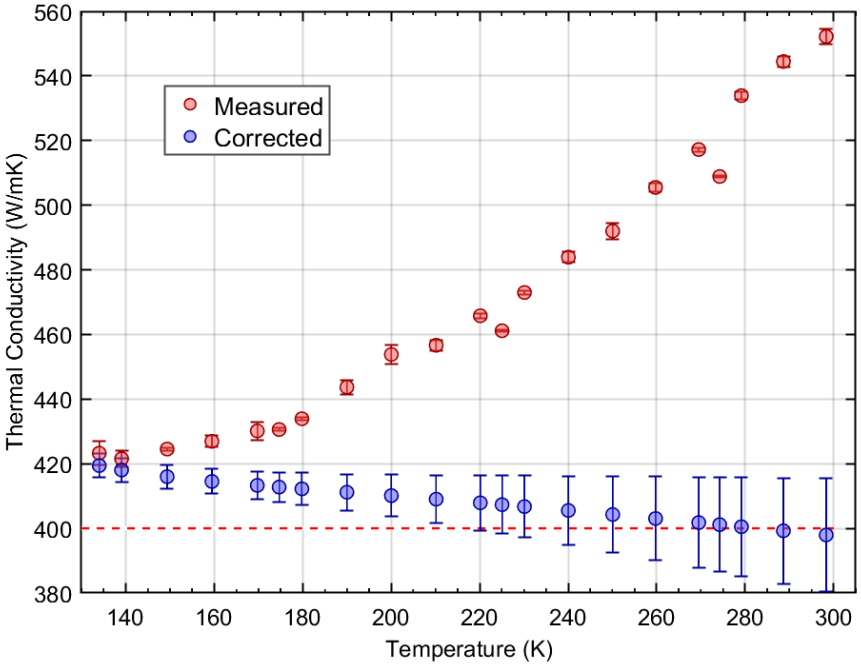

Figure 3.24: A zoomed in version of Figure 3.23 to emphasize the copper wire data correction for radiative heat loss.

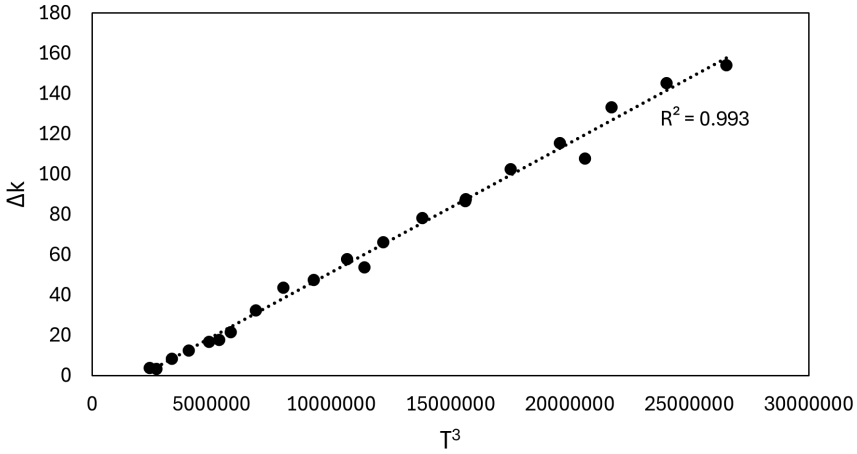

Figure 3.25: The difference between the total measured thermal conductivity of the copper wire and corrected conductivity ($\Delta k = k_T - k_C$) plotted against T^3.

Theoretically, the electronic and lattice components of thermal conductivity should be separated when applying a radiative correction, as outlined by Pope et al. (2001). However, this step was not necessary when using the NIST equation (Equation 3.15), as it accounts

for both components in the fit. Since the CFMS is also capable of measuring the electrical resistance, the method proposed by Pope et al. (2001) should be explored further and compared with the NIST-based correction used for copper in this study.

The corrected thermal conductivity of copper is compared to NIST standard curves for RRR50, RRR100, RRR150, RRR300, and RRR500 copper (NIST, 2010) in Figure 3.26. Additional thermal conductivity data for RRR80 copper were extracted from Xia et al. (2022) for further comparison. As shown in Figure 3.26, the copper wire data above 20 K align closely with the RRR copper trends, most closely matching RRR80. Since the data consistently fall just below the RRR80 line, it is likely that the wire corresponds to approximately RRR75. This can be confirmed by measuring its resistivity at 4.2 K and 300 K using the CFMS to calculate the residual resistivity ratio.

In contrast, the thermal conductivity below 20 K deviates from the expected behaviour, suggesting that the CFMS configuration settings and/or cooling power were not sufficient in this range, despite the measurements passing the data quality checks (Section 3.3.2). To estimate the expected trend, the low-temperature data were extrapolated using Equation 3.15, shown as the blue dashed line in Figure 3.20. However, this fit fails below 20 K, indicating that the fit coefficients (Table 3.3) do not accurately capture the low-temperature behaviour. The ideal trend in this range is shown by the red dashed line in Figure 3.26, which was estimated based on the slope of the RRR80 data below 20 K.

Despite the increased uncertainty at low temperatures, the copper wire results demonstrate that the CFMS provides reliable, accurate, and precise thermal conductivity measurements.

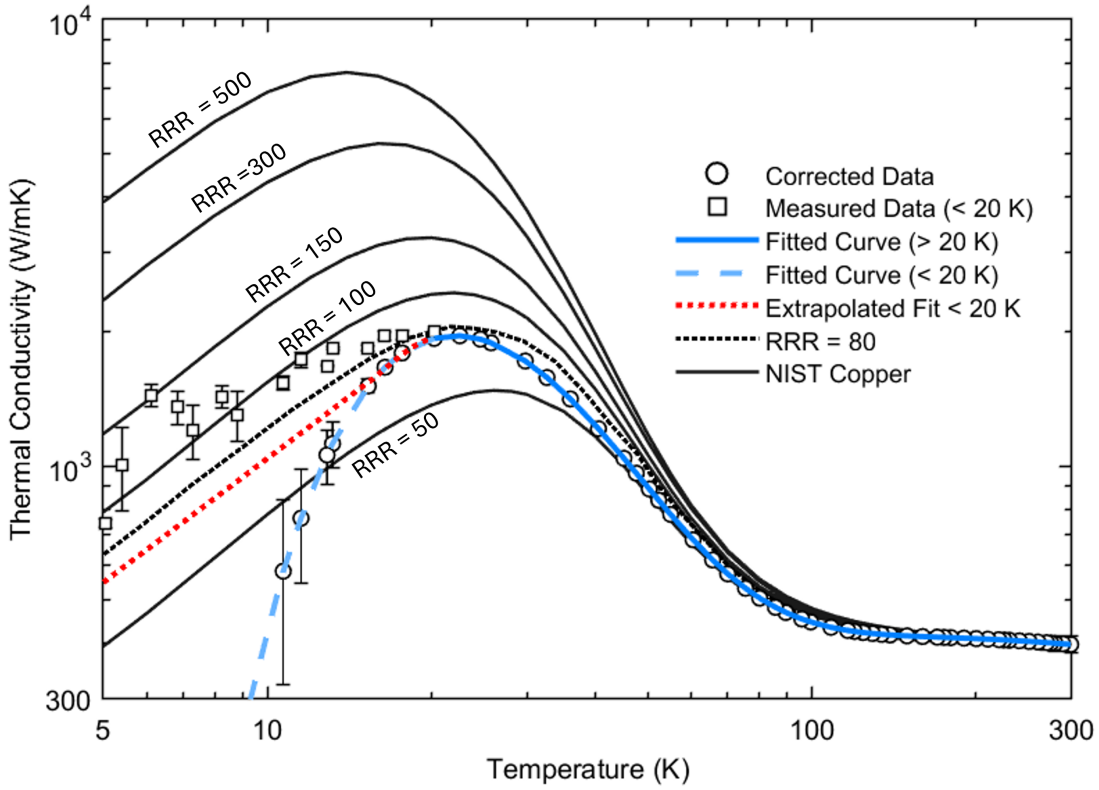

Figure 3.26: Comparison of the corrected copper thermal conductivity data with copper standards from NIST (2010). The RRR = 80 curve was extracted from Xia et al. (2022). The blue fitted curve was generated using Equation 3.15, with the dashed portion indicating the extrapolated trend below 20 K. The red dashed line represents an idealized fit to the copper data below 20 K. Measured copper data below 20 K is also shown to illustrate the source of the underfit in the extrapolated curve.

4 Sample Selection, Preparation, and Characterization

4.1 Sample Selection

Careful consideration was given to selecting geological samples suitable for this study. Although the study ultimately aims to measure the thermal conductivity of meteorites, terrestrial minerals were initially used to refine the CFMS method, as these materials were readily available and more practical for initial testing.

This PhD project began with the intent to measure the thermal conductivity of terrestrial minerals commonly found in carbon-rich stony asteroids (e.g., olivine, pyroxene, calcite, plagioclase, magnetite, chromite, and graphite) under space-like conditions ($T < 300$ K, under vacuum). The objective was to use these measurements to estimate the bulk thermal conductivity of asteroids. However, several limitations became apparent early on.

Many of the minerals collected were not compositionally pure and contained trace amounts of minerals uncommon in planetary materials (e.g., biotite, quartz). Since thermal conductivity is sensitive to composition, even minor inclusions could skew the results and lead to estimates that do not accurately represent the mineral constituents of asteroid materials. Variations in elemental composition, particularly in minerals that form solid solutions, also affect thermal conductivity. In a solid solution, different elements can substitute for one another within a mineral's crystal structure without changing the overall structure itself. However, these substitutions can significantly influence physical properties, including thermal conductivity. For example, endmembers of olivine (forsterite (Mg-rich) and fayalite (Fe-rich)) and plagioclase (albite (Na-rich) and anorthite (Ca-rich)) mineral series are known to have distinct thermal conductivities (Horai and Simmons, 1969; Horai, 1971; Čermák and Rybach, 1982; Diment and Pratt, 1988). Forsterite and enstatite, the Mg-rich endmembers of olivine and pyroxene, respectively, are the major phases in stony asteroids. However, obtaining samples of these minerals that were large, homogeneous, and suitable for thermal

conductivity measurements proved difficult. After contacting several mineralogists and mineral dealers, it became clear that naturally occurring samples meeting the necessary size and quality were unlikely to be found. Instead, all recommended sourcing lab-grown crystals.

Crystallographic orientation added another layer of complexity. Many asteroid-forming minerals are anisotropic, meaning their thermal conductivity varies with direction. Because minerals in meteorites are randomly oriented, it's valuable to measure conductivity along known crystallographic axes. Unfortunately, some minerals, such as magnetite, chromite, and graphite, commonly form as aggregates, whereby the crystallographic axes cannot be isolated. Single-crystal samples of such minerals are typically rare, expensive, or too small for analysis.

Porosity also needs to be considered in estimating the bulk thermal conductivity of asteroids. Pore spaces increase phonon-boundary scattering, which alters the thermal conductivity curve from the typical crystalline behaviour discussed in Chapter 2. This effect is well documented in previous studies by Opeil et al. (2010, 2012, 2020) and is seen in the serpentinite data presented in Chapter 3 (Figure 3.10), where conductivity decreases with decreasing temperature. To estimate bulk thermal conductivity from individual mineral data, the effects of porosity would need to be modelled.

Due to these limitations, the focus of the project shifted. Rather than estimating bulk asteroid thermal conductivity from measurements of constituent minerals, the CFMS was used in a more materials-science-focused approach to analyze well-characterized single crystals. Minerals selected for this work—quartz, pyrite, calcite, and albite—were readily available in the Planetary Instrumentation Laboratory (PIL) and offered a range of properties helpful in testing the system. Quartz was chosen in part because its crystallographic axes are easily identified in prism form (see Section 4.3), and its anisotropic thermal conductivity is well documented at high temperatures (Birch and Clark, 1940a; Clark, 1966; Horai and Simmons, 1969; Beck et al., 1978; Kanamori et al., 1968), making it ideal for validating low-temperature measurements. Calcite, also anisotropic and compositionally pure, served as another strong

candidate with reported thermal conductivity values for specific crystallographic orientations (Birch and Clark, 1940a; Clark, 1966; Dreyer, 1974). Albite is another anisotropic mineral, and often displays crystal twinning (repeating lattice structure), which offers a unique case for thermal conductivity analysis. Additionally, this study presents what appears to be the first low-temperature analysis of albite and calcite. Pyrite, an isotropic mineral, provided a valuable contrast to the anisotropic samples, and data have been published for this mineral between 50 and 300 K (Popov et al., 2013).

These single-crystal measurements facilitated direct comparison with published data and provided a controlled means to explore how anisotropy influences thermal conductivity. A sample of obsidian (volcanic glass) was also included to examine the behaviour of an amorphous material. Measuring single-crystal samples provided an effective way to evaluate the performance of the CFMS, confirm the expected trends in the thermal conductivity data (see Chapter 2), and assess how well the results align with established reference data.

The meteorites selected for this study were chosen to ensure that the CFMS results are comparable to the Opeil studies. These include an iron meteorite, two ordinary chondrites, and one carbonaceous chondrite. Sample selection was limited to the size and availability of material from the University of Alberta Meteorite Collection.

4.2 Sample Preparation

This section describes the preparation process of geological samples analyzed with the CFMS, including the attachment of thermal assemblies (heater and thermocouple).

Samples were first cut into millimetre-sized rectangular prisms using a Buehler Iso-met low-speed saw (Figure 4.1). The target dimensions for each sample were approximately 20 mm in length and between 2 and 3 mm in both width and height. These dimensions leave enough space inside the radiation shield to prevent the thermal assembly wires from touching the sample or the radiation shield, which could create unwanted heat conduction paths.

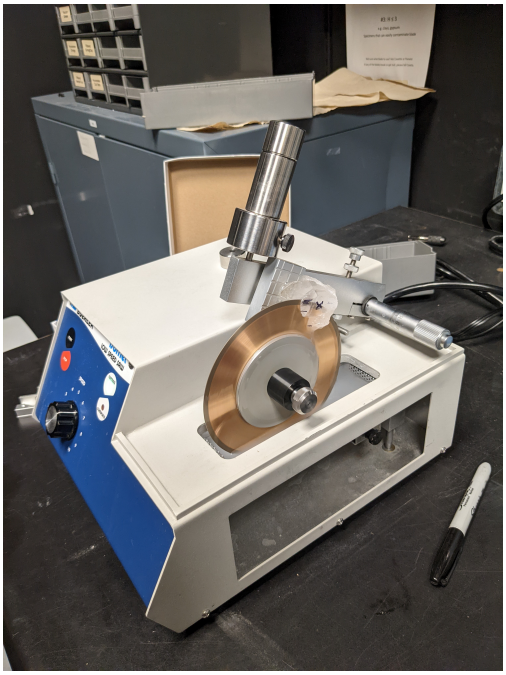

Figure 4.1: Buehler Iso-met low-speed saw used to cut samples. A sample of quartz is shown.

Samples were initially cut with width and height dimensions between approximately 3 and 4 mm. If either dimension was smaller than 3 mm, the sample often broke during cutting, as vibrations from the saw could compromise its structural integrity.

To achieve the ideal cross-sectional dimensions, samples were polished by hand using silicon carbide paper after cutting. This process removed the rough surface left by the saw and was also used to refine the width and height to the 2 to 3 mm range. Once polished, the sample was rinsed with isopropyl alcohol to clean the surface and prepare it for the attachment of the thermal assemblies.

Because the cutting and polishing stages are not perfectly precise due to human error, the largest source of uncertainty in thermal conductivity measurements comes from the sample dimensions (Section 3.3). To account for this, the width and height of each sample were measured at over 30 points along its length to capture dimensional variability.

4.2.1 Attachment of Thermal Assemblies

This section outlines the procedure for attaching the thermal assemblies to a geological sample. A helping-hands station was used to hold the sample in place during attachment of the assemblies, including the heat sink connecting wire (Figure 4.2).

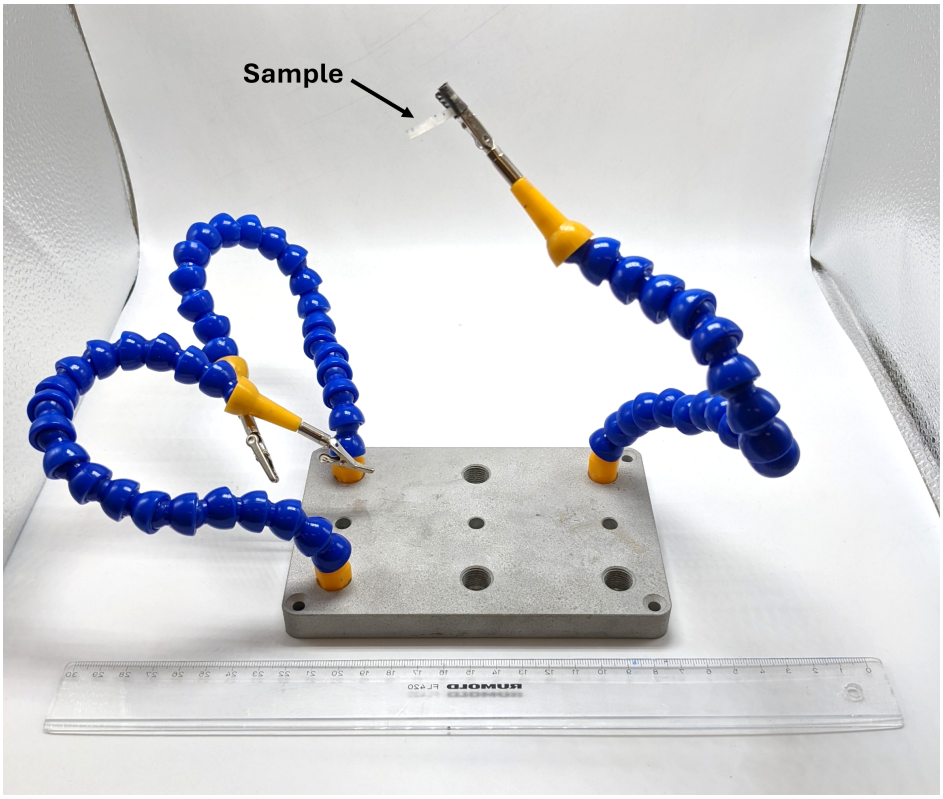

Figure 4.2: The helping-hands station used to hold the sample during attachment of the thermal assemblies (heater and thermocouple) and heat sink connection.

Step 1: Heat Sink Wire

A tinned copper wire was first fitted around the end of the sample, where it would later be secured with epoxy, to establish a thermal connection to the heat sink (Figure 4.3a).

To do this, the sample was carefully secured between the rubber-tipped ends of one helping-hand from the station. The wire was then gently wrapped around the sample, and the two ends were twisted together to form a loop (Figure 4.3b). If preferred, the wire can be wrapped around twice before twisting. The fit of the wire does not need to be perfect, as

any small gaps between the wire and the sample are filled with epoxy in Step 3. Once the wire was wrapped around the sample, it was carefully removed (Figure 4.3c) to prepare for epoxy application.

Meteorites (not pictured): Although the helping-hands tool is gentle enough to hold samples without damage, it was not used for meteorites to avoid the risk of breakage. Instead, a square-head screwdriver with cross-sectional dimensions similar to those of the meteorite samples was used to wrap and shape the wire. Minor adjustments to the wire loop (e.g., gently squeezing one end) were made as needed to ensure a proper fit. This approach eliminated applying unnecessary force to the meteorites during Step 1.

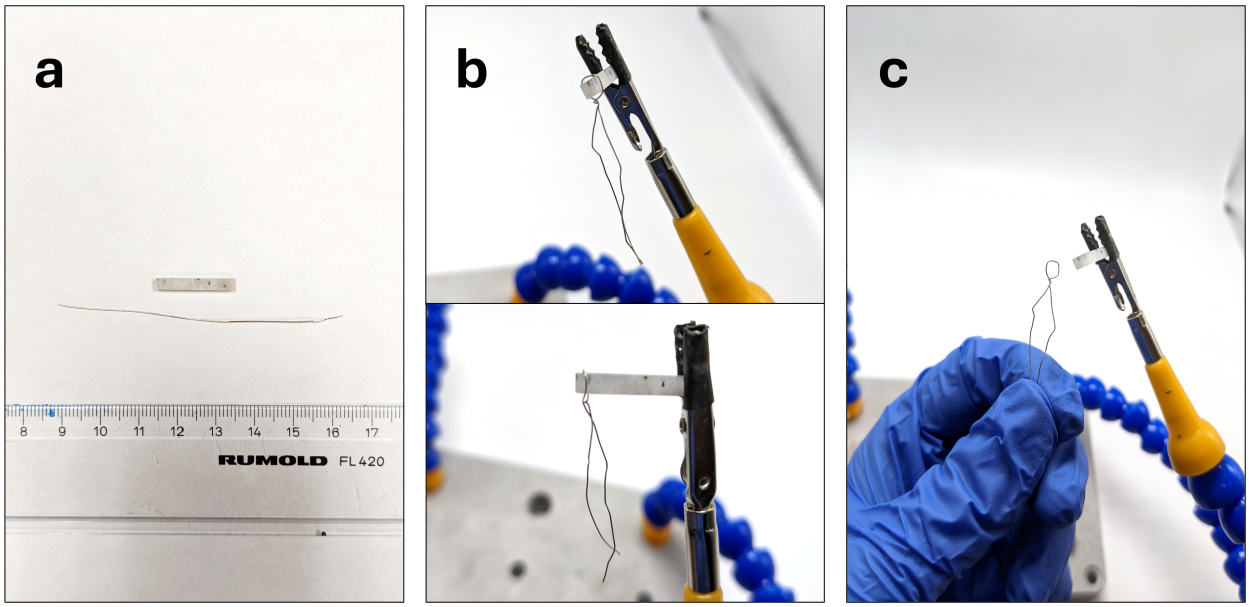

Figure 4.3: Step 1: Preparing the heat sink connecting wire. (a) The sample and tinned copper wire prior to wrapping. (b) The wire is wrapped around the sample and twisted to form a loop. (c) The wire is carefully removed to prepare for the application of epoxy. See text for details.

Step 2: Mix the Silver Epoxy

Silver epoxy (RS PRO Silver Conductive Adhesive Epoxy) was prepared by measuring equal parts (by weight) of hardener and resin and mixing thoroughly for approximately one minute (Figure 4.4). This step was typically completed immediately after Step 1, as the epoxy

begins to set within 10 to 15 minutes after mixing. Under ambient conditions, the epoxy takes approximately 24 hours to cure.

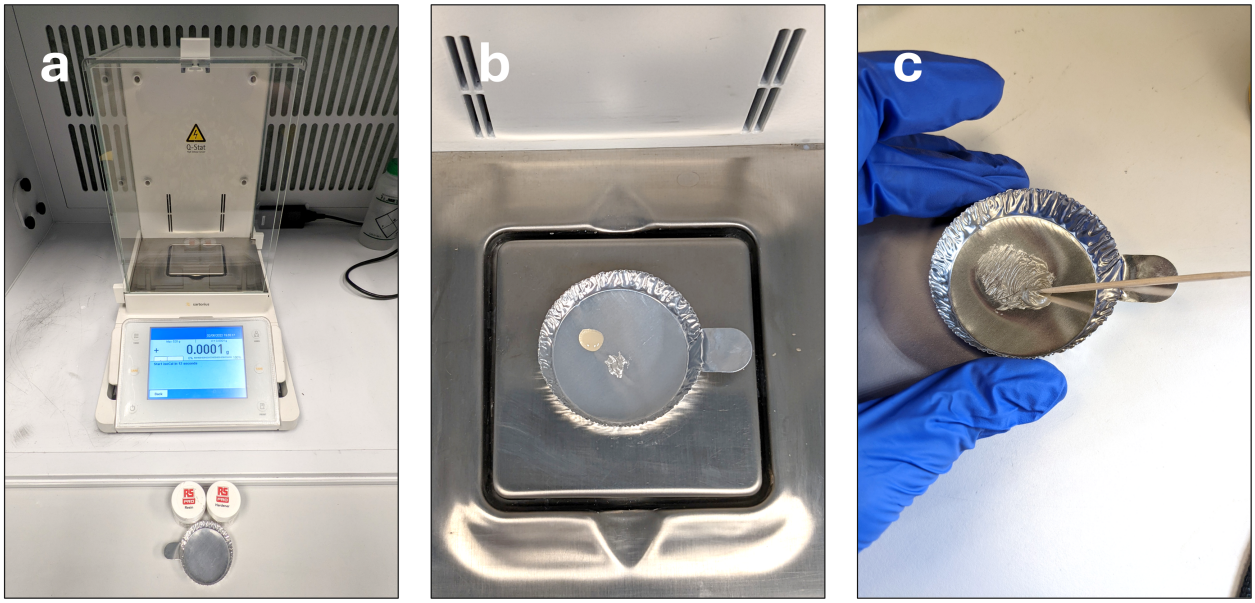

Figure 4.4: Step 2: Preparation of the silver epoxy. (a) A high-precision scale was used to weigh equal parts hardener and resin. (b) Example of equal parts in a mixing cup. (c) The hardener and resin were mixed with a toothpick until uniform.

Step 3: Attach the Heat Sink Wire

A small amount of epoxy was applied to the end of the sample using a toothpick (Figure 4.5a). The connecting wire was then gently slid into place over the epoxy (Figure 4.5b). Once in place, additional epoxy was applied on top of the wire, ensuring that it filled any gaps between the wire and the sample (Figure 4.5c). After the epoxy was applied, a fine-tipped cotton swab dipped in isopropyl alcohol was used to clean up any excess epoxy (Figure 4.5d). It is important to tidy the connection at this stage to ensure there is sufficient space to attach the cold junction end of the thermocouple later on.

Once the epoxy was applied, the helping-hand was adjusted so that the sample hung vertically (Figure 4.5e). This orientation allows gravity to help the epoxy settle into any remaining gaps and build up a strong connection around the wire. The sample was left in this position for 24 hours to allow the epoxy to cure fully.

Meteorites (not pictured): This process was also followed for the meteorite samples; however, the sample was held in hand rather than with the helping-hand tool. After the epoxy was applied, the meteorite was carefully placed horizontally on the helping-hands platform so that the epoxy-coated section hung over the edge. This prevents the epoxy from bonding the sample to the platform. Since the sample is not hung vertically, extra care was taken to apply sufficient epoxy to fill any gaps that may occur.

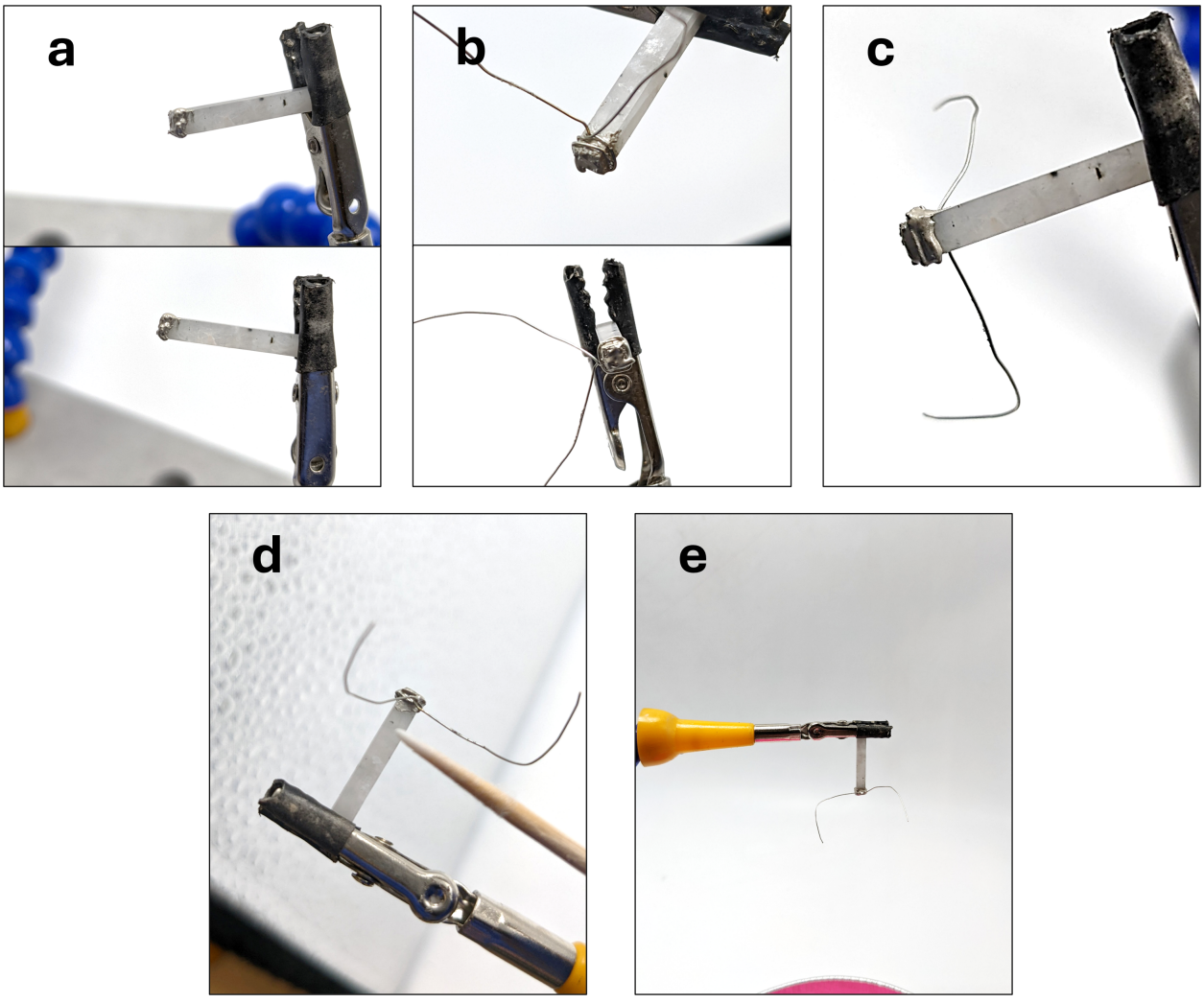

Figure 4.5: Step 3: Attaching the heat sink connecting wire. (a) Epoxy is applied to the end of the sample. (b) The wire is carefully slid back into place over the epoxy. (c) Additional epoxy is applied to fill any gaps. (d) Excess epoxy is cleaned with a fine-tipped cotton swab dipped in isopropyl alcohol. (e) The sample is left to hang vertically while the epoxy cures. See text for details.

Step 4: Securing Sample to Helping-Hands Platform

From this step onward, the methods are the same for the mineral and meteorite samples.

After the epoxy is cured, the thermal assemblies can be attached. The helping-hands platform was used as a base to secure the sample in place (Figure 4.6). The connecting wire was threaded through one of the larger holes in the platform (Figure 4.6a & b). It was then gently folded along the bottom of the platform (Figure 4.6c) and held in place once the platform was set back down. At this point, the sample is ready for the thermal assemblies to be attached (Figure 4.6d).

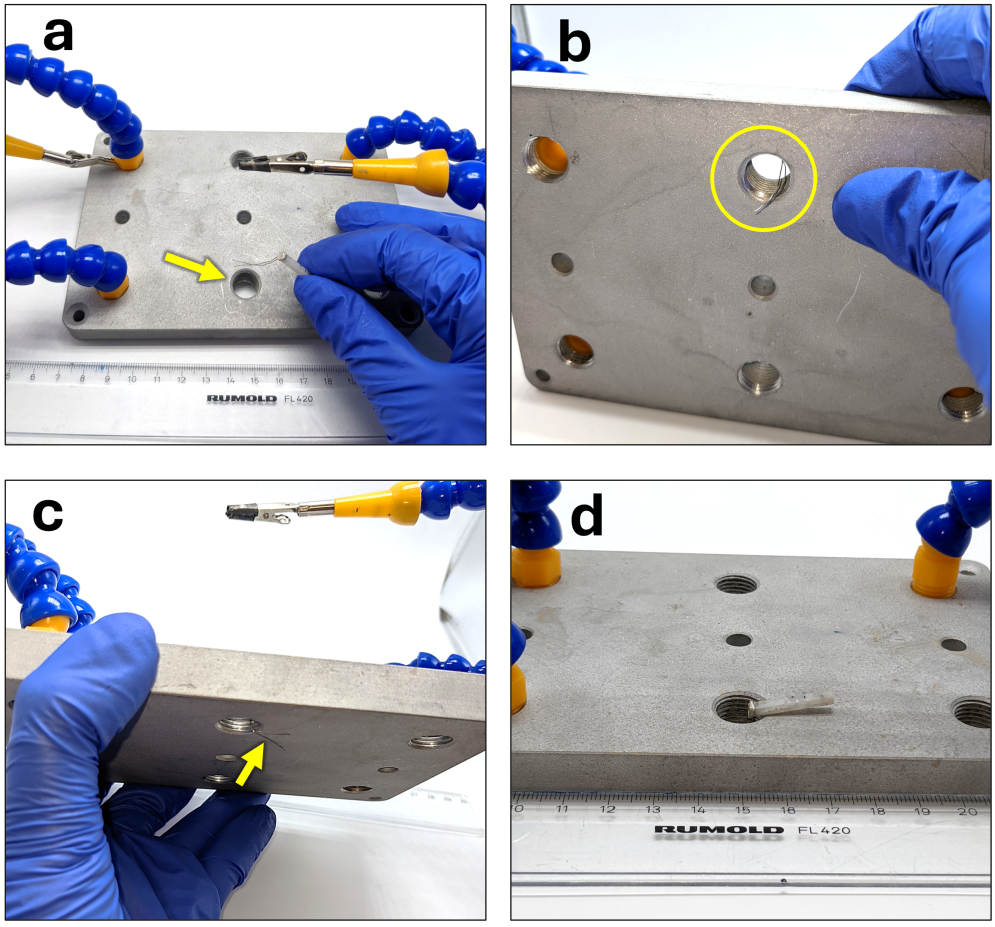

Figure 4.6: Step 4: Using the helping-hands platform to hold the sample in place. (a) The sample's connecting wire threaded through one of the larger holes. (b) The wire sticking out the bottom of the platform. (c) The wire folded along the bottom to hold the sample. (d) The sample held in place and ready for the thermal assemblies to be attached.

Step 5: Prepare Sample for Assembly Attachments

Before the thermal assemblies were attached, the sample surface was cleaned with isopropyl alcohol and a fine-tipped cotton swab (Figure 4.7, a & b). Two toothpicks were then positioned where the heater and cold junction thermocouple tab would be attached (Figure 4.7c). The helping-hands were adjusted to apply enough tension to hold the toothpicks firmly in place. These toothpicks are used to keep the assemblies in place while the epoxy cures.

Next, the assemblies were inspected to determine the best orientation for attachment, ensuring that the assembly tabs would not come in contact with each other (e.g., avoiding contact between the hot junction and heater tabs) (Figure 4.7d). Once a suitable orientation was determined, a batch of silver epoxy was prepared as described in Step 2.

Step 6: Heater Attachment

It is easiest to attach the heater assembly first. The toothpick on the heater end was removed, taking care not to shift the helping-hand from its position. Note that the toothpick on the cold junction end usually stays in place to help secure the sample; however, it was removed in Figure 4.8 to provide a better view of the heater assembly.

A small dab of epoxy was first applied to the heater end of the sample (Figure 4.8a). The heater was carefully placed on top of the epoxy and secured by reattaching the toothpick to the helping-hand (Figure 4.8b). Any excess epoxy that squeezed out was cleaned using a fine-tipped cotton swab dipped in isopropyl alcohol (Figure 4.8c). It is best practice to have a clean edge along the heater (Figure 4.8d).

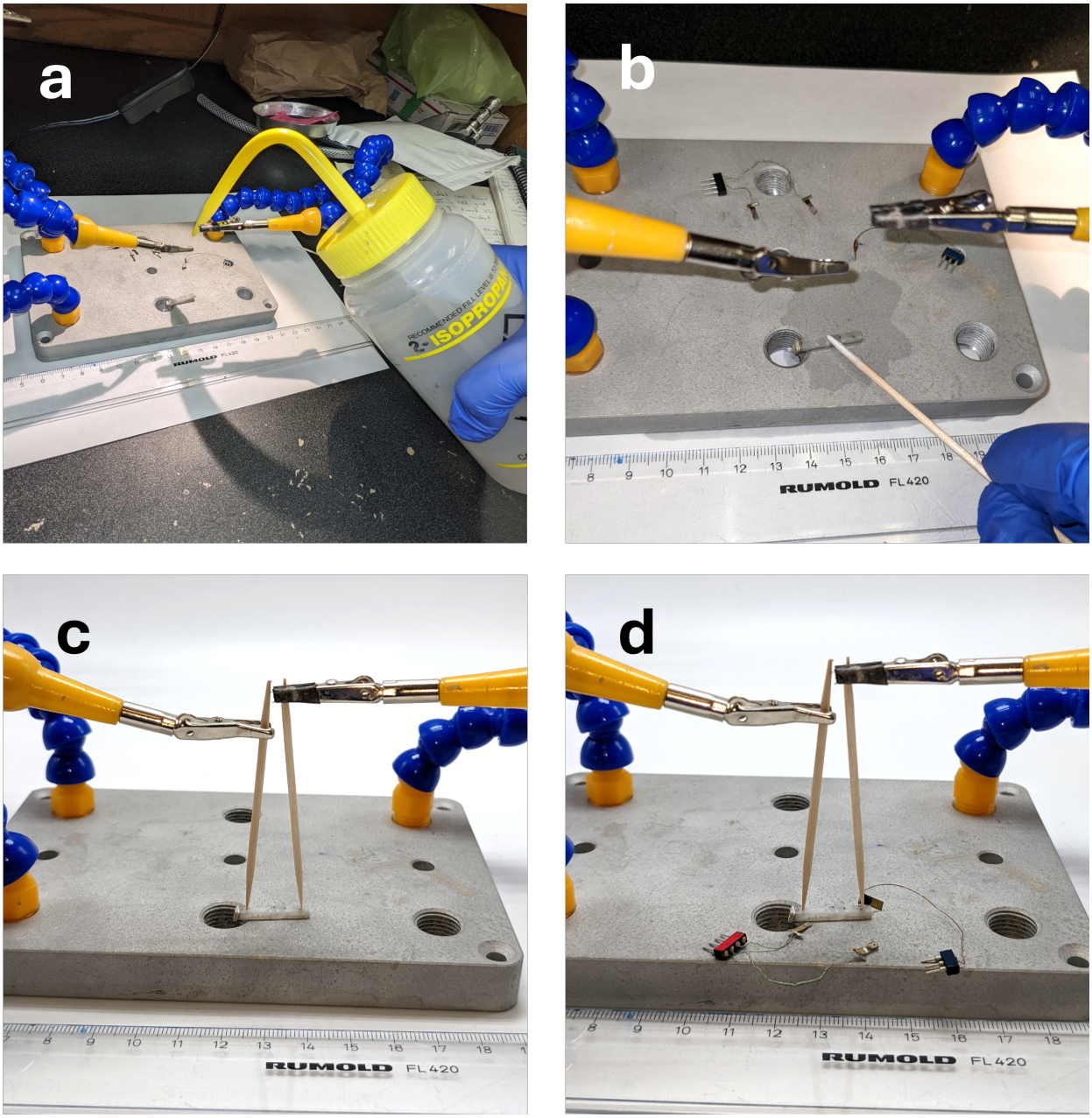

Figure 4.7: Step 5: Preparing the sample for thermal assembly attachments. (a & b) Cleaning the surface with isopropyl alcohol. (c) Positioning the toothpicks to support the heater and thermocouple assemblies. (d) Confirming the layout of the assemblies before attachment. See text for details.

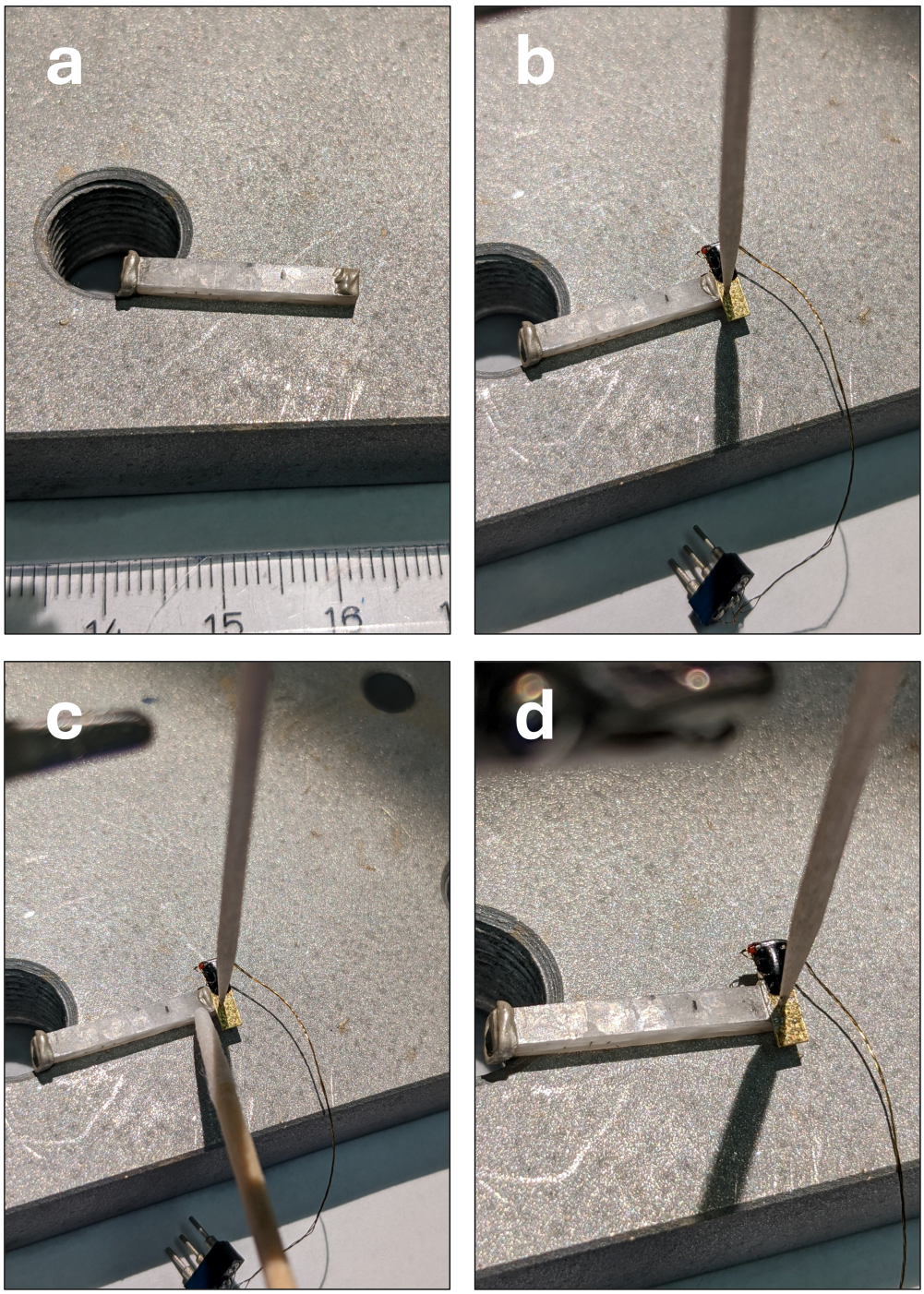

Figure 4.8: Step 6: Attaching the heater assembly. (a) Epoxy is applied to the heater end of the sample. (b) The heater is positioned and held in place with a toothpick. (c) Excess epoxy is cleaned using a cotton swab dipped in isopropyl alcohol. (d) Final setup with the heater in place and clean edges. See text for details.

Step 7: Thermocouple Attachment

To attach the thermocouple to the sample, it is best to start with the cold junction tab and let the epoxy set before attaching the hot junction tab. This is because it is difficult to get three helping-hands to hold toothpicks in such a small space. Also, if the hot tab is attached on the same day as the heater and cold junction tabs, the cold junction can shift out of place while the epoxy is still fresh.

As with the heater, a small dab of epoxy was placed near the heat sink end of the sample (Figure 4.9a). Care was taken to leave enough space between the epoxy and heat sink connection so that the epoxy did not spread into that area. The cold junction tab was placed on top of the epoxy and secured with a toothpick (Figure 4.9b). Any excess epoxy was cleaned up with a fine-tipped cotton swab dipped in isopropyl alcohol (not shown). The edges of the cold junction should be clean, just like the heater (Figure 4.9c).

The heater and cold junction attachments were left to cure for at least 12 hours before the hot junction tab was attached (Figure 4.9d). The process for attaching the hot tab is the same as the cold tab. A reasonable gap was left between the heater and the hot junction tab. Recall that the spacing between the thermocouple tabs plays an important role in reducing heat loss through the connecting wires (Section 3.1.3), so placement of the thermocouple tabs is important to consider.

The sample was removed from the helping-hands platform at least 12 hours after the hot tab was attached; however, it is best to leave it for a full 24 hours to ensure the epoxy is completely cured before proceeding to the final step.

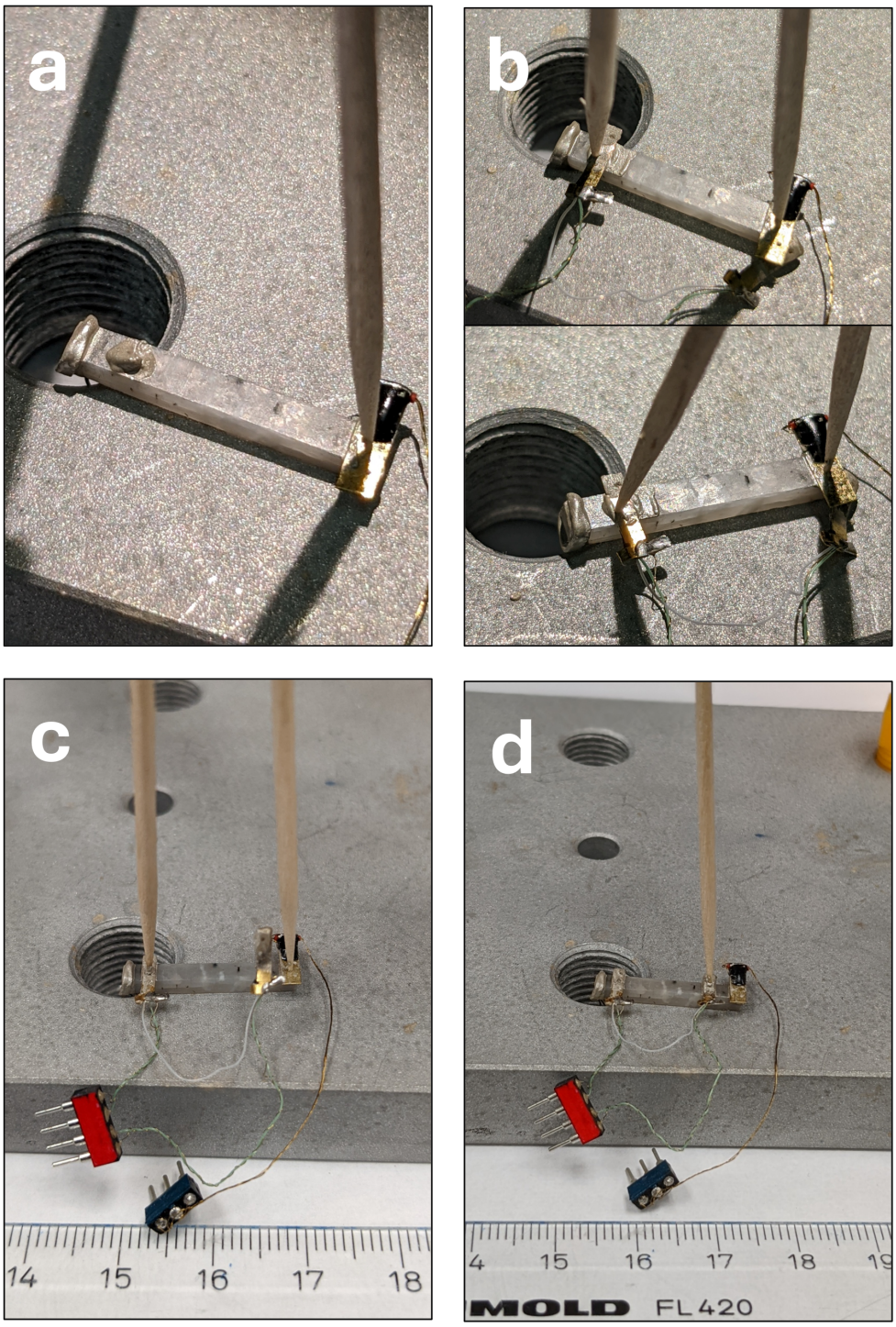

Figure 4.9: Step 7: Attaching the thermocouple assembly. (a) Epoxy is applied near the heat sink end of the sample. (b) The cold junction tab is secured with a toothpick. (c) The cold junction tab after cleaning. (d) The sample the following day with the hot junction tab set in place. See text for details.

Step 8: Surrounding Epoxy

The final step in the thermal assembly attachment process is to apply silver epoxy around the sample at each assembly point, including both ends of the sample (Figure 4.10). This step ensures the thermal assemblies have a good electrical contact with the sample.

To apply the surrounding epoxy, the sample was held by the heat sink connecting wires. Using a toothpick, epoxy was applied around the cold junction and heater areas, as well as both ends of the sample. It is often easier to start with these areas, let them sit for at least 12 hours, and then return to apply epoxy around the hot junction area.

Once the epoxy is applied, the surrounding areas were cleaned using isopropyl alcohol and a fine-tipped cotton. The epoxy should be cleaned so that it is approximately the same width as the assembly tabs.

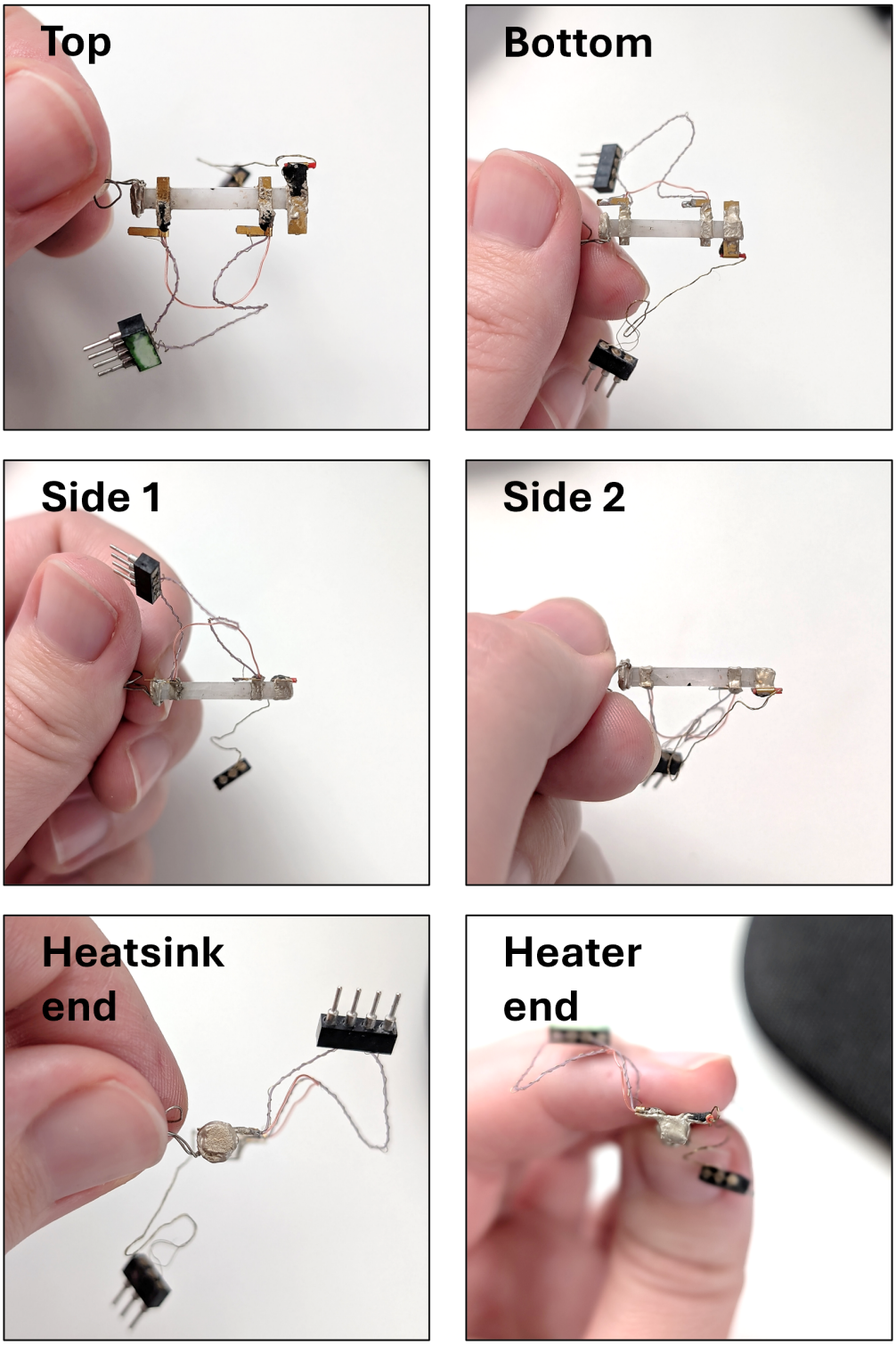

Figure 4.10: Step 8: Apply epoxy around the sample at each assembly point, including both ends. See text for details.

4.3 Single-Crystal Minerals

A total of 14 single-crystal minerals, including one amorphous sample, were analyzed using the CFMS. These include two quartz samples, six calcite samples, two albite samples, three pyrite samples, and one obsidian (volcanic glass) sample. Quartz, calcite, and albite are anisotropic minerals, while pyrite and obsidian are isotropic.

To understand anisotropy and its effects on thermal conductivity, a brief overview of crystal structure and crystal systems is provided here.

A mineral is defined as a naturally occurring solid with well-defined chemistry and crystal structure (Wenk and Bulakh, 2016). The physical properties of a mineral, including thermal conductivity, depend on its internal atomic arrangement, which defines its crystal structure. In crystalline materials, atoms are arranged in an orderly, repeating pattern called a unit cell. The repetition of this unit cell forms the crystal lattice. Vibrations in the crystal lattice, known as phonons, are the primary carriers of thermal energy in insulating crystalline materials (see Chapter 2).

Single-crystal minerals have a uniform atomic structure throughout their entire volume, unlike mineral aggregates, which are composed of multiple crystals that have grown together. In contrast, amorphous materials like glass lack a defined structure; their atoms are arranged randomly, without a repeating pattern.

Crystal systems classify minerals based on their symmetry and structural geometry. There are seven crystal systems, arranged from highest to lowest symmetry: cubic, hexagonal, trigonal, tetragonal, orthorhombic, monoclinic, and triclinic (Figure 4.11). Symmetry refers to the repetition of patterns or features within the crystal structure. As symmetry decreases across the crystal systems, the length of the crystallographic axes and the angles become less uniform.

These structural differences lead to anisotropy, where a material's physical properties vary depending on the direction in which they are measured. In anisotropic, crystalline

materials, this occurs because atomic bonding and spacing differ along crystallographic axes. As phonons move through the lattice, their interactions depend on the arrangement of atoms, which affects how efficiently heat is conducted. As a result, heat may travel more easily along one axis than another.

Isotropic materials, on the other hand, have the same physical properties in all directions. This includes minerals in the cubic crystal system as well as amorphous solids like obsidian. Although glass is disordered and lacks a regular lattice, its lack of structural directionality means properties like thermal conductivity remain constant regardless of orientation.

Additionally, the distinction between a crystal face and a cleavage plane needs to be clarified. A crystal face is a flat surface that forms as the mineral grows during crystallization. In contrast, cleavage refers to planes of weakness in the crystal structure along which a mineral can break. These cleavage planes can be mistaken for crystal faces, especially in minerals where the cleavage is well-developed.

A summary of crystal system, anisotropy, and geometric dimensions for each sample in this study is provided in Table 4.1, with detailed descriptions given in the following subsections. To support this study, X-ray diffraction (XRD) measurements were performed on offcuts from the same parent samples used in the thermal conductivity analysis to assess their purity. The measurements were collected by Aurelio Sanz Arranz at the University of Valladolid as part of the Planetary Instrumentation Laboratory (PIL) LIBS[2]-Raman Sensor (LIRS) project (Code: 9F063-140572/024/MTB), which developed an integrated Raman, LIF[3], and LIBS instrument and accompanying database, supported by complementary techniques including XRD. The XRD data was processed by Dr. Emmanuel Lalla (former PIL postdoctoral researcher).

XRD analysis was carried out using the portable Terra-Insitu instrument, which is based on the same CheMin technology currently operating on NASA's Curiosity rover. This instrument can perform both XRD and X-ray fluorescence (XRF) analyses. For XRD, it uses

[2]Laser-Induced Breakdown Spectroscopy (LIBS)
[3]Laser-Induced Fluorescence (LIF)

a cobalt-based X-ray source and a cooled detector to capture diffraction patterns.

Each sample (∼10 g) was ground using an agate mortar and sieved to a fine powder (less than 100 μm). One diffraction scan was collected for each sample, totalling four scans, which took approximately 30 minutes per scan. The resulting patterns were used to identify the mineral phases present, using XPowder software and reference data from the ICDD PDF-2[4]. More details on this technique can be found in Ella et al. (2020a, 2020b). Quantitative XRD results are provided in Appendix C.

Table 4.1: Single-crystal mineral properties and dimensions.

Sample	**Crystal System**	**Anisotropy**	**Dimensions (mm)** $w \times h \times l$	**A (mm^2)**	**L (mm)**
Quartz-1	Trigonal	Anisotropic	$2.65 \times 2.64 \times 20.3$	6.971 ± 0.006	11.429 ± 0.007
Quartz-2			$2.59 \times 2.60 \times 20.0$	6.737 ± 0.007	12.127 ± 0.013
Calcite-1a-4a-b	Trigonal	Anisotropic	$3.02 \times 2.71 \times 19.2$	8.201 ± 0.005	11.427 ± 0.007
Calcite-1a-5d			$2.86 \times 3.01 \times 19.6$	8.618 ± 0.010	11.846 ± 0.008
Calcite-1a-6-1			$2.76 \times 2.72 \times 18.7$	7.518 ± 0.024	10.218 ± 0.007
Calcite-1b-6-1			$2.89 \times 2.11 \times 21.4$	6.085 ± 0.006	11.721 ± 0.018
Calcite-1b-6-2			$2.80 \times 2.93 \times 19.0$	8.218 ± 0.002	11.288 ± 0.013
Calcite-1b-6-5			$2.61 \times 2.91 \times 21.3$	7.593 ± 0.007	11.549 ± 0.007
Albite-1	Triclinic	Anisotropic	$2.48 \times 2.52 \times 20.6$	6.249 ± 0.009	12.061 ± 0.006
Albite-2			$2.40 \times 2.59 \times 19.9$	6.202 ± 0.009	12.182 ± 0.008
Pyrite-1	Cubic	Isotropic	$2.03 \times 2.07 \times 19.9$	4.196 ± 0.003	11.043 ± 0.014
Pyrite-2			$2.89 \times 3.12 \times 17.4$	9.014 ± 0.009	10.024 ± 0.009
Pyrite-3			$1.67 \times 1.22 \times 20.0$	2.027 ± 0.004	11.917 ± 0.006
Obsidian	Amorphous	Isotropic	$2.51 \times 2.63 \times 20.1$	6.598 ± 0.007	12.829 ± 0.009

[4]International Centre for Diffraction Data Powder Diffraction File (ICDD PDF-2)

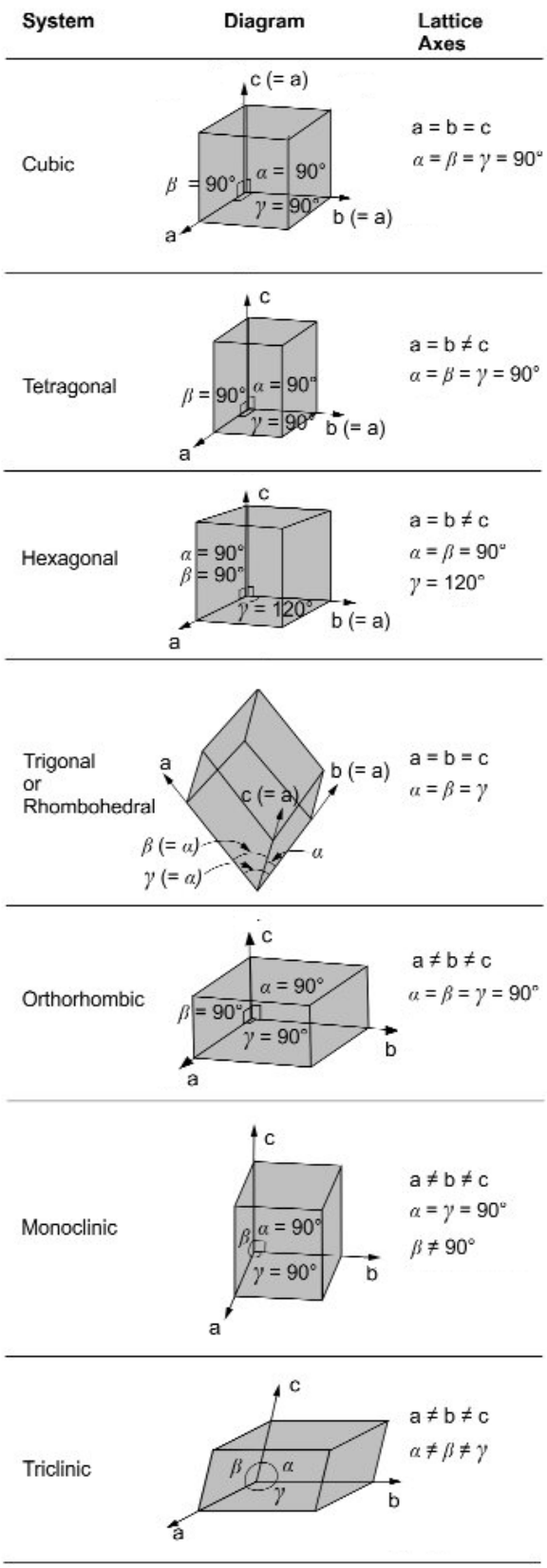

Figure 4.11: The seven crystal systems. Figure adapted from Davies (2013).

4.3.1 Quartz

Quartz belongs to the trigonal crystal system, but is commonly described using its hexagonal lattice framework ($a_1 = a_2 \neq c$; $\alpha = \beta = 90°, \gamma = 120°$) (Figure 4.12). The characteristic prismatic crystal habit of quartz makes it easy to identify the crystallographic axes in a hand sample. Two quartz samples were cut from a quartz prism in two directions: one parallel to the c-axis (Quartz-1, Figure 4.13) and one perpendicular (Quartz-2, Figure 4.14). The two samples oriented with respect to the crystallographic axes are shown in Figure 4.15. The quartz sample appears pure upon visual inspection, although wisps and small bubbles are present throughout, likely due to gas trapped during crystallization. XRD analysis indicates that the quartz samples are 99% pure (Figure 4.16). The remaining 1% likely corresponds to peaks that could not be resolved or did not match the reference pattern in the PDF-2 database (standard 461045).

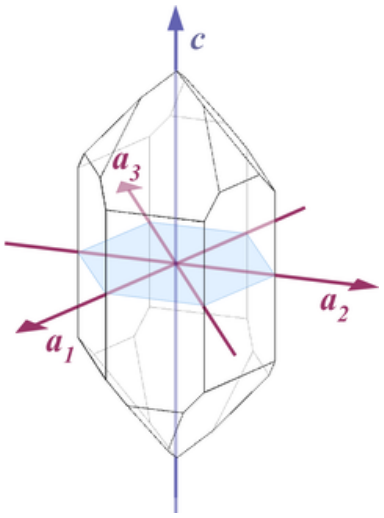

Figure 4.12: Trigonal crystal system of quartz. Image from The Quartz Page (2016).

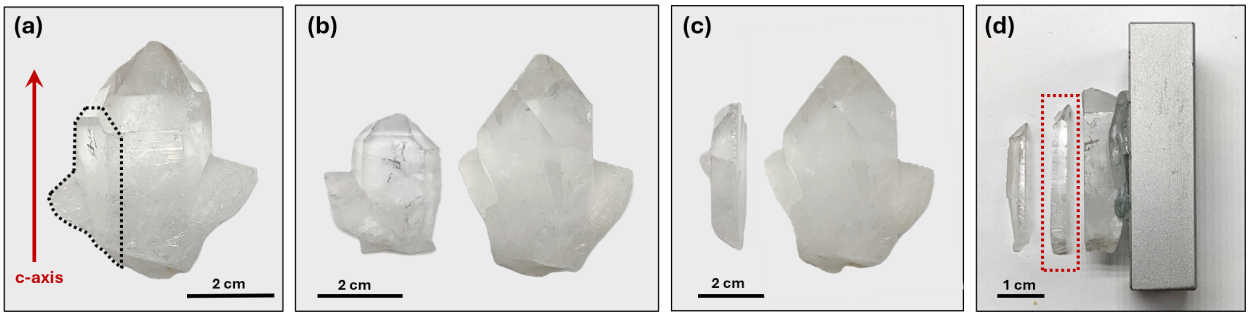

Figure 4.13: Preparation of the **Quartz-1** sample, cut parallel to the c-axis. **(a)** Quartz crystal oriented along the c-axis (red arrow). The black outlined section indicates the portion that was cut to prepare the sample. **(b)** The cut section laid flat. **(c)** The same cut section viewed on its side. **(d)** The cut section mounted on the low-speed saw sample holder with Crystalbond, then cut into three pieces. The piece outlined in red was selected to create the Quartz-1 sample.

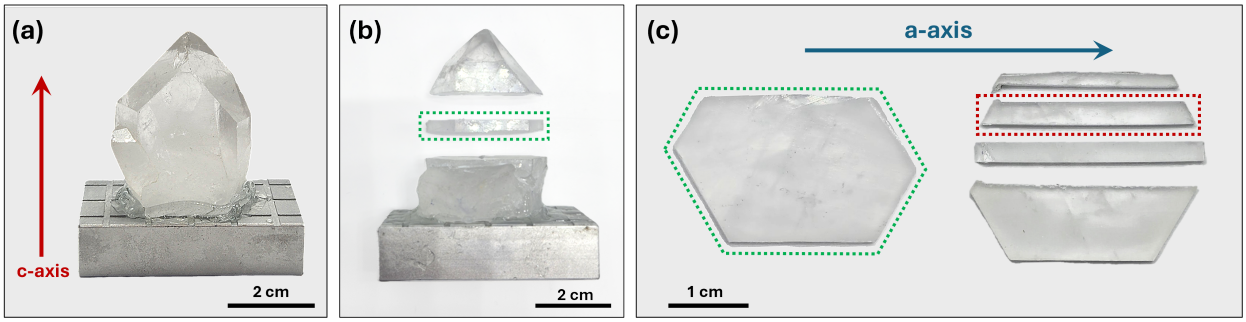

Figure 4.14: Preparation of the **Quartz-2** sample, cut perpendicular to the c-axis (parallel to a-axis). **(a)** Quartz sample mounted to the low-speed saw sample holder with Crystalbond. This is the top half of the same specimen shown in Figure 4.13a. **(b)** The crystal cut into three pieces perpendicular to the c-axis. The piece outlined in green was selected for preparing the Quartz-2 sample. **(c)** *Left:* The selected piece laid flat to show its orientation relative to the a-axis. *Right:* The piece cut into four sections; the piece outlined in red was selected create the Quartz-2 sample.

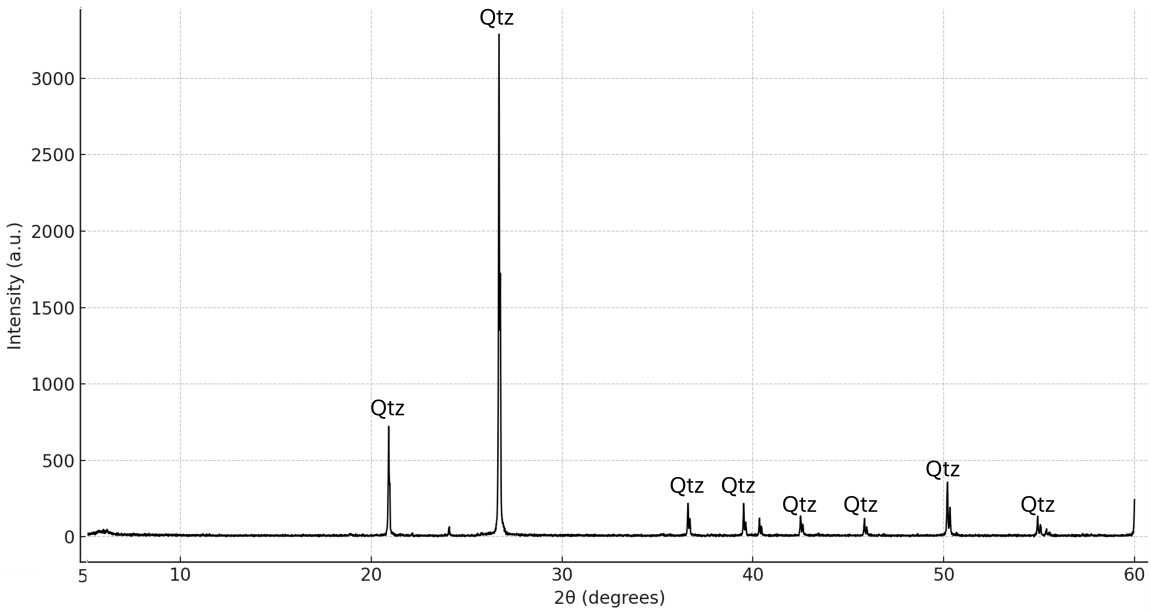

Figure 4.16: XRD pattern of quartz (99% purity), matched against PDF-2 database standard 461045.

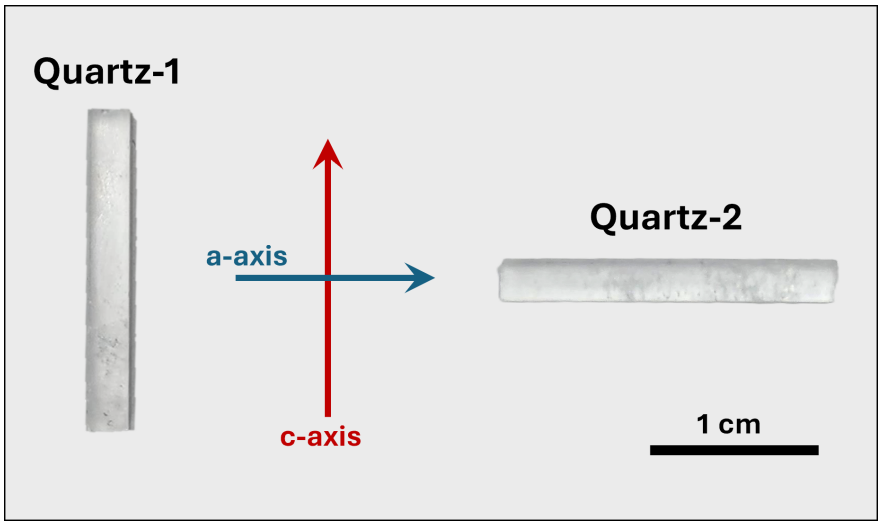

Figure 4.15: Cut samples of Quartz-1 and Quartz-2, orientated with respect to the crystallographic axes (c and a).

4.3.2 Calcite

Six calcite ($CaCO_3$) samples were cut from a rhombohedral, white calcite crystal (Figure 4.19). Like quartz, calcite also belongs to the trigonal crystal system, with its axes

similarly described using the hexagonal framework ($a_1 = a_2 \neq c;\ \alpha = \beta = 90°,\ \gamma = 120°$). XRD analysis indicates that the calcite sample is 98% pure, with the remaining 2% consisting of peaks that were either unresolved or did not match the PDF-2 database standard (standard 721214; Figure 4.18). Among the anisotropic minerals selected for this project, identifying the crystallographic axes in rhombohedral, opaque calcite is particularly challenging, as cleavage planes are often mistaken for crystal faces. However, given the high purity of the samples, the goal of this study was to measure thermal conductivity at random orientations to assess how much it fluctuates within a single piece of calcite.

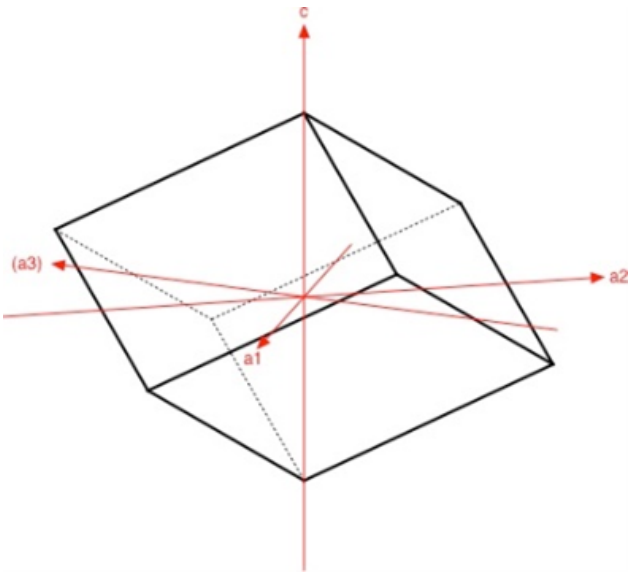

Figure 4.17: Trigonal crystal system of calcite. Image from Richards (2015).

Of the six calcite samples measured, samples 1a-4a-b, 1a-5d, and 1a-6-1 are cut parallel to each other (Figure 4.20 to 4.22). The samples 1b-6-1, 1b-6-2, and 1b-6-5 are also cut parallel to one another (Figure 4.23), where the "a-samples" are perpendicular to the "b-samples". An example of what the calcite samples look like after they are polished to the proper dimensions is provided in Figure 4.24.

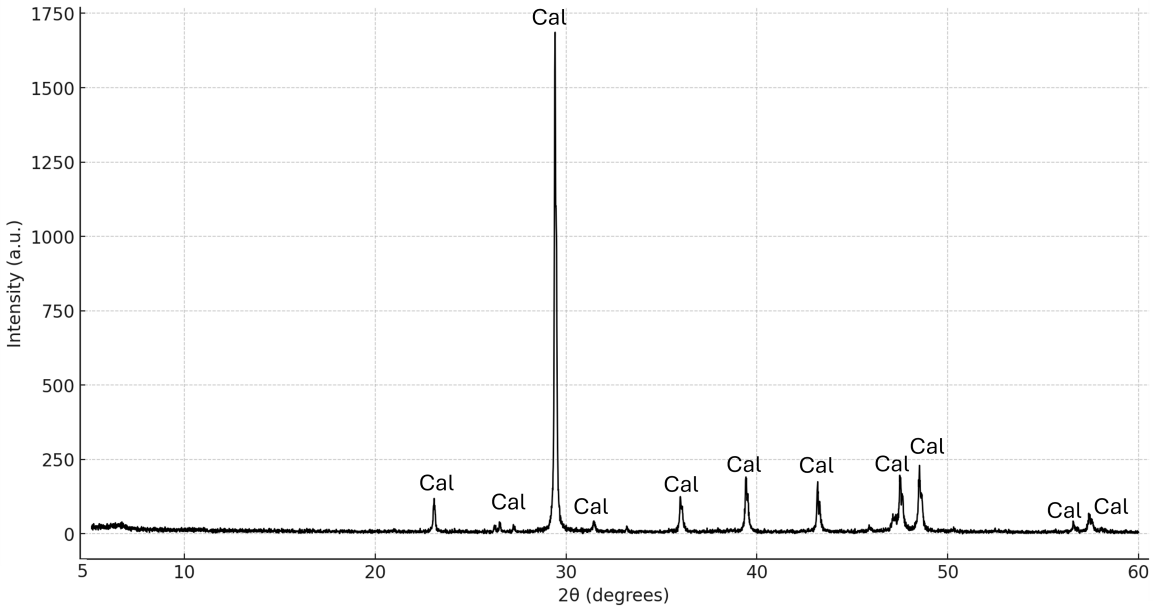

Figure 4.18: XRD pattern of calcite (98% purity), matched against PDF-2 database standard 721214.

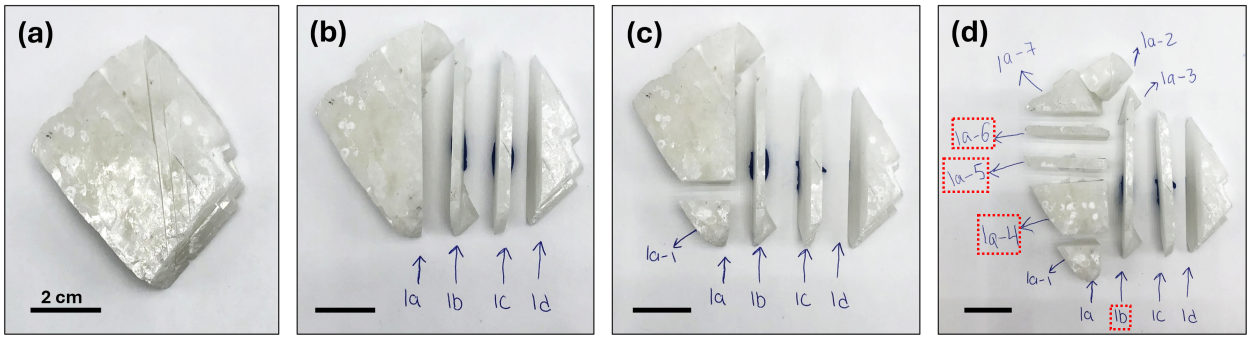

Figure 4.19: **(a)** Rhombohedral calcite used in this study. **(b-d)** The crystal is cut into multiple sections. The red-outlined sample names in (d) indicate the pieces that were selected to prepare the six calcite samples.(Figures 4.20 - 4.23). Scale bars in (b) to (d) are 2 cm.

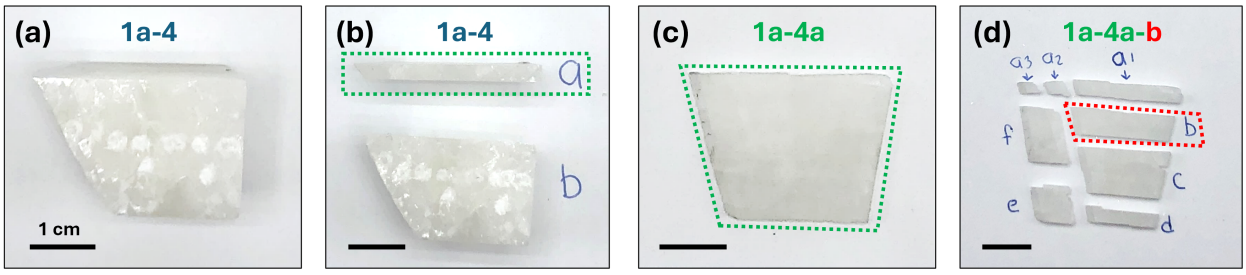

Figure 4.20: Preparation of calcite sample **1a-4a-b**. **(a)** Sample 1a-4 from Figure 4.19d. **(b)** Sample 1a-4 cut into two pieces: 1a-4a and 1a-4b. The 1a-4a sample, outlined in green, was chosen to prepare a sample. **(c)** Sample 1a-4a laid flat. **(d)** Sample 1a-4a cut into multiple pieces. The red-outlined piece "b" was selected and polished to create the 1a-4a-b calcite sample. Scale bars in (b) to (d) are 1 cm.

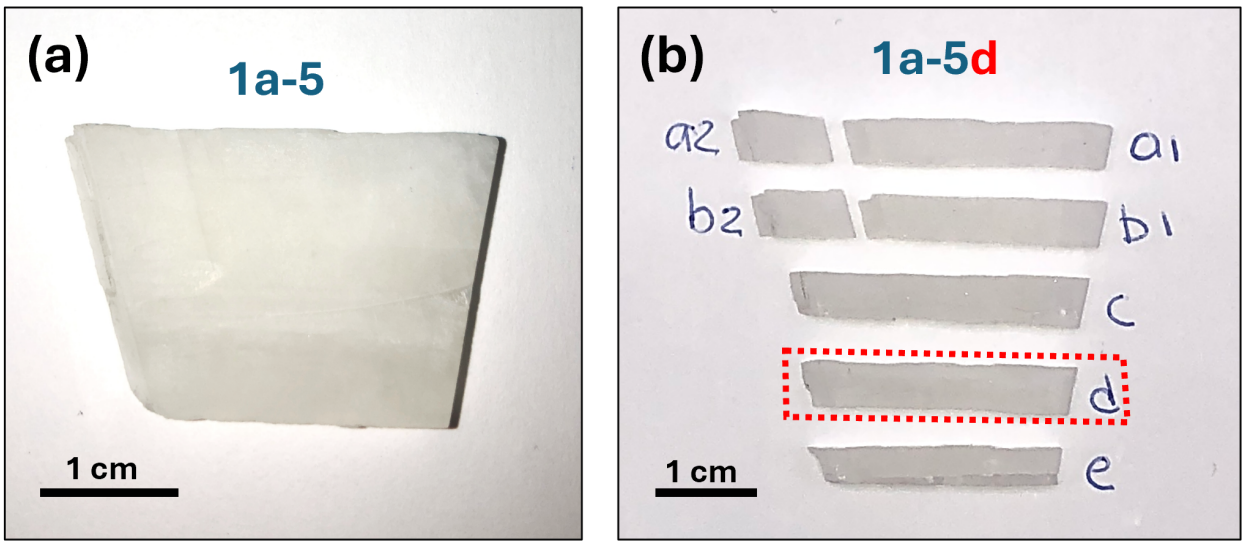

Figure 4.21: Preparation of calcite sample **1a-5d**. **(a)** Sample 1a-5 from Figure 4.19d laid flat. **(b)** Sample 1a-5 cut into multiple pieces. The red-outlined piece "d" was selected and polished to create the 1a-5d calcite sample.

.

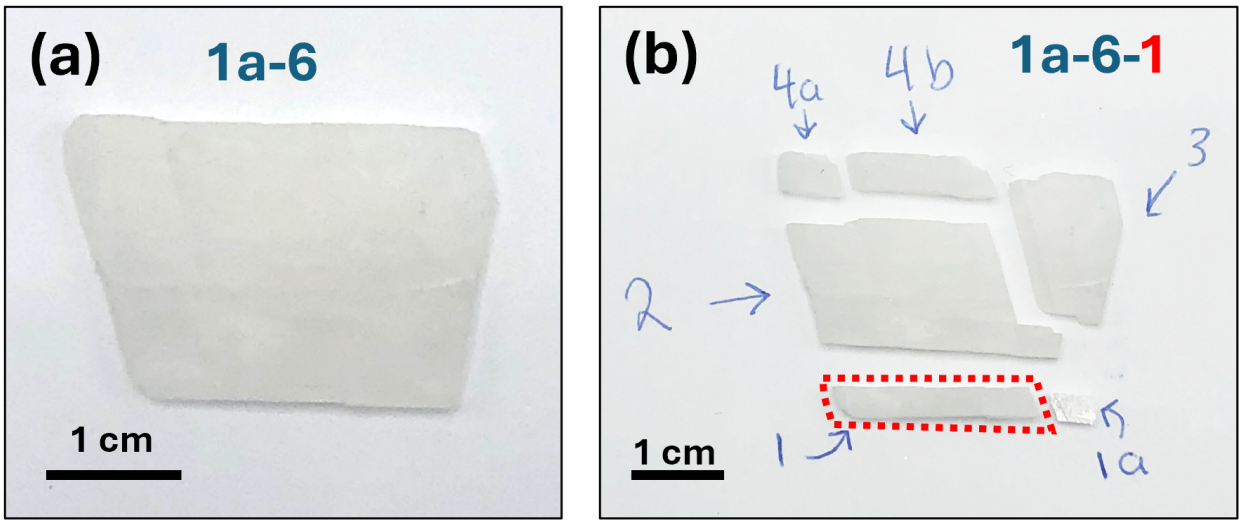

Figure 4.22: Preparation of calcite sample **1a-6-1**. **(a)** Sample 1a-6 from Figure 4.19d laid flat. **(b)** Sample 1a-6 cut into multiple pieces. The red-outlined piece "1" was selected and polished to create the 1a-6-1 calcite sample.

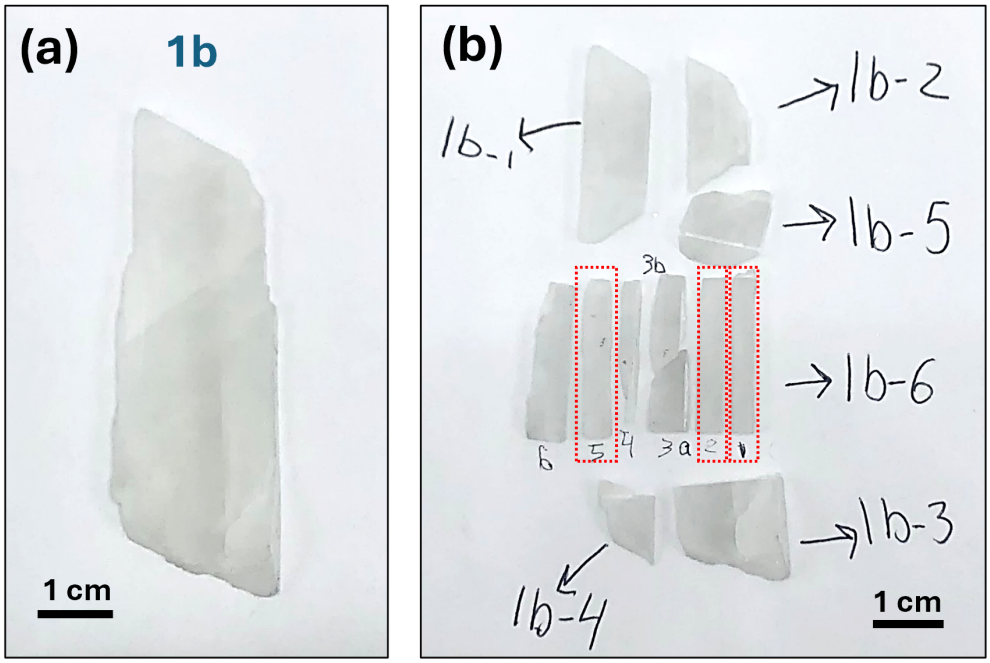

Figure 4.23: Preparation of calcite samples **1b-6-1**, **1b-6-2**, and **1b-6-5**. **(a)** Sample 1b from Figure 4.19d laid flat. **(b)** Sample 1b cut into multiple pieces. The red-outlined pieces in the "1b-6" row were selected and polished to create three parallel samples.

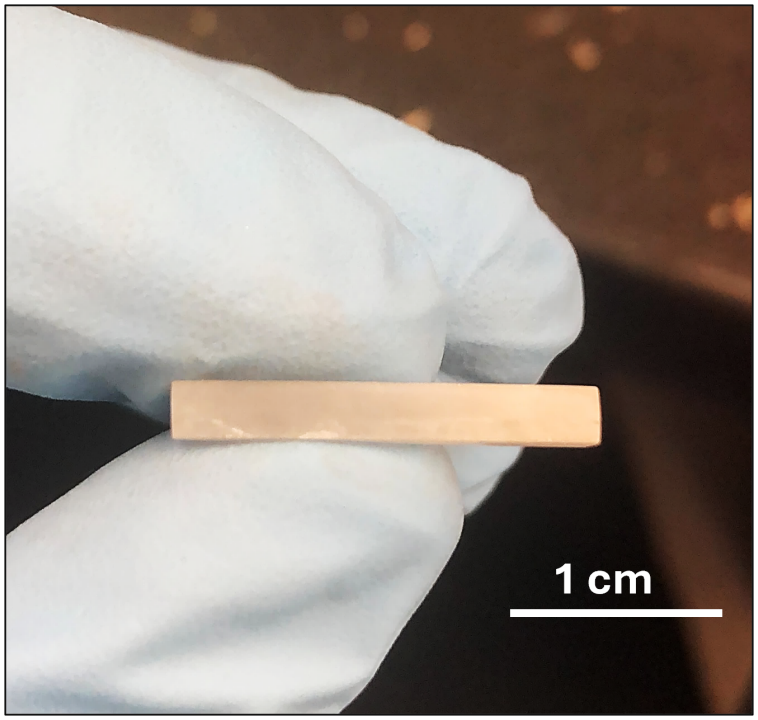

Figure 4.24: This figure shows an example of a prepared calcite sample, representative of the six samples used in this study.

4.3.3 Albite

Albite is the sodium-rich endmember ($NaAlSi_3O_8$) of the plagioclase feldspar solid solution series, and belongs to the triclinic crystal system ($a \neq b \neq c$; $\alpha \neq \beta \neq \gamma$) (Figure 4.25). As the triclinic system has the lowest symmetry (Figure 4.11), there are no visual clues in the hand sample to identify the **a** and **c** crystallographic axes. The direction of the b-axis, however, can be inferred, as it is normal to one of albite's cleavage planes. Albite crystals typically cleave with a 90° angle between the (010) and (001) planes (Figure 4.26a,b), offering an opportunity to investigate heat flow relative to the cleavage planes. Albite also displays polysynthetic twinning—repeated patterns of the crystal lattice—that appear as parallel striations on the (001) cleavage plane (Figure 4.26c). The twin planes are parallel to (010), which corresponds to the direction of the b-axis.

Two samples of albite were prepared for this study (Figure 4.27). Albite-1 was cut parallel to the (010) twin planes, such that heat flows perpendicular to the b-axis. Albite-2 is cut

along the b-axis, perpendicular to (010).

XRD analysis reveals that the albite samples are 96% pure, with 4% remaining unidentified (Figure 4.28). Visual inspection of the albite crystal showed trace amounts of biotite distributed throughout the sample (Figure 4.26), which likely accounts for the unidentified fraction.

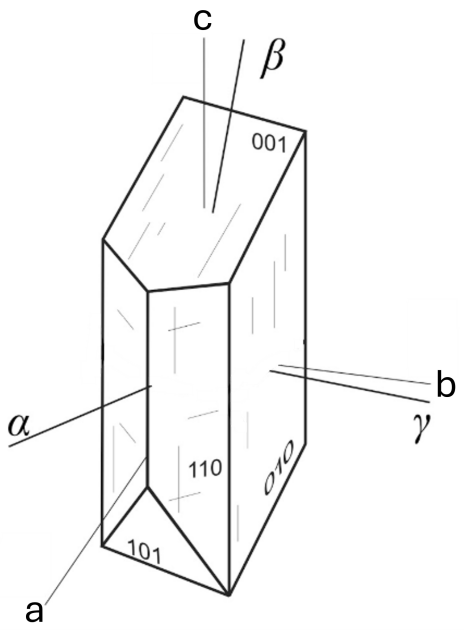

Figure 4.25: Triclinic crystal system of albite. The crystallographic axes are labelled a, b, and c, and the angles between them are α, β, and γ, where $a \neq b \neq c$ and $\alpha \neq \beta \neq \gamma$. Image adapted from Zakharov (n.d.).

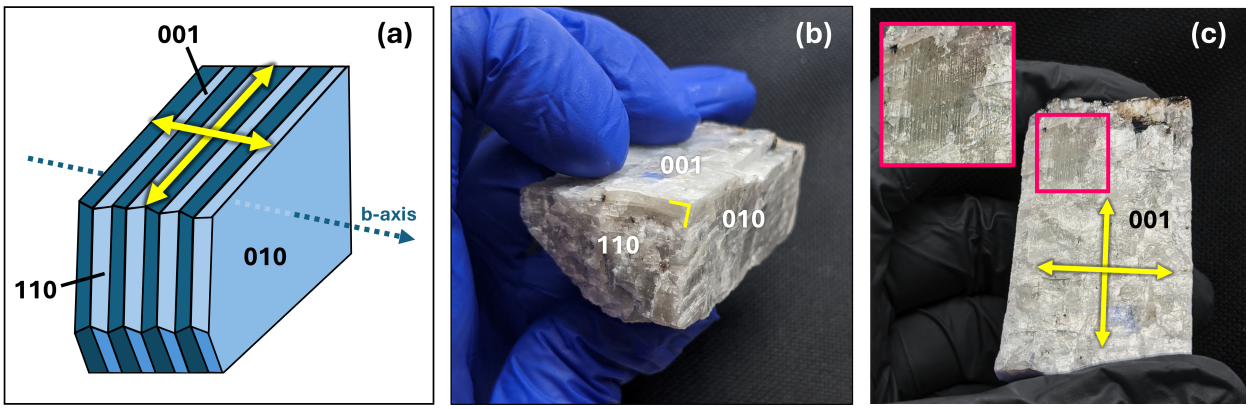

Figure 4.26: **(a)** Schematic diagram of albite showing its three cleavage planes: (001) is the perfect cleavage plane, (010) is the good cleavage plane, and (110) is a fractured surface. Polysynthetic twinning is seen on the (001) plane, with twin planes parallel to (010). The b-axis is perpendicular to the (010) plane and runs parallel to the twin planes. Yellow arrows indicate the directions in which the albite crystal was cut to prepare two thermal conductivity samples. Image adapted from Encyclopædia Britannica (1998) and Farmer (2014). **(b)** Photograph of the albite specimen from which the samples were cut. The (001), (010), and (110) cleavage planes are labelled, and the 90° angle between (001) and (010) is highlighted. **(c)** View of the (001) cleavage plane. The inset (pink box) shows the visible polysynthetic twin striations. Yellow arrows show the directions in which the two albite samples were cut relative to the twin striations. Black areas are biotite.

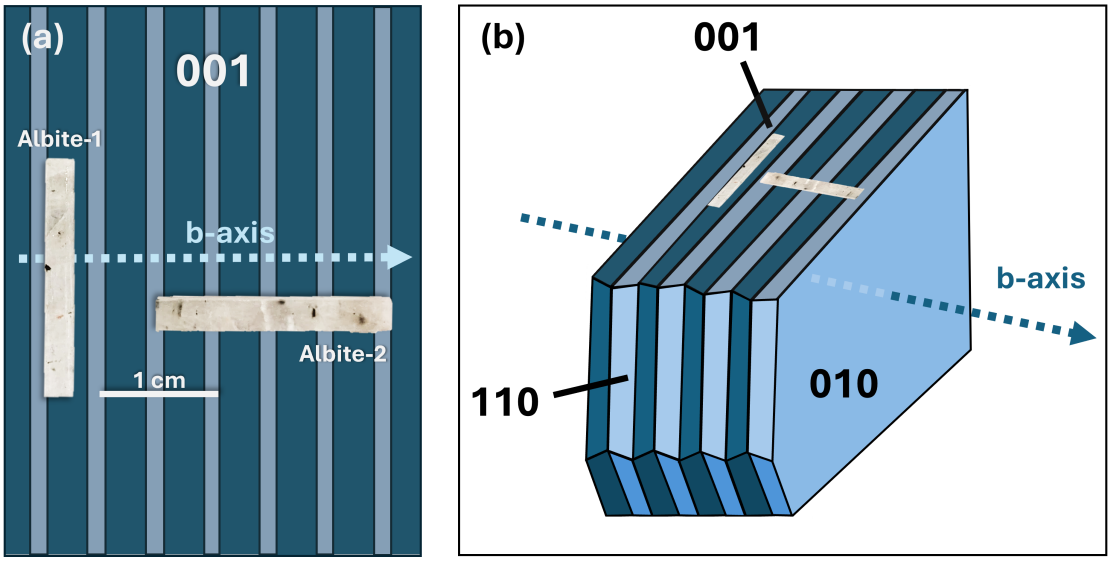

Figure 4.27: **(a)** The two albite samples overlaid on a schematic of the (001)cleavage plane to illustrate the orientation in which they were cut. The b-axis runs parallel to the twin planes. The 1 cm scale bar applies only to the sample images; the schematic of the twin planes is not to scale. **(b)** Repeat of Figure 4.26a, now showing the two samples projected onto the (001) plane.

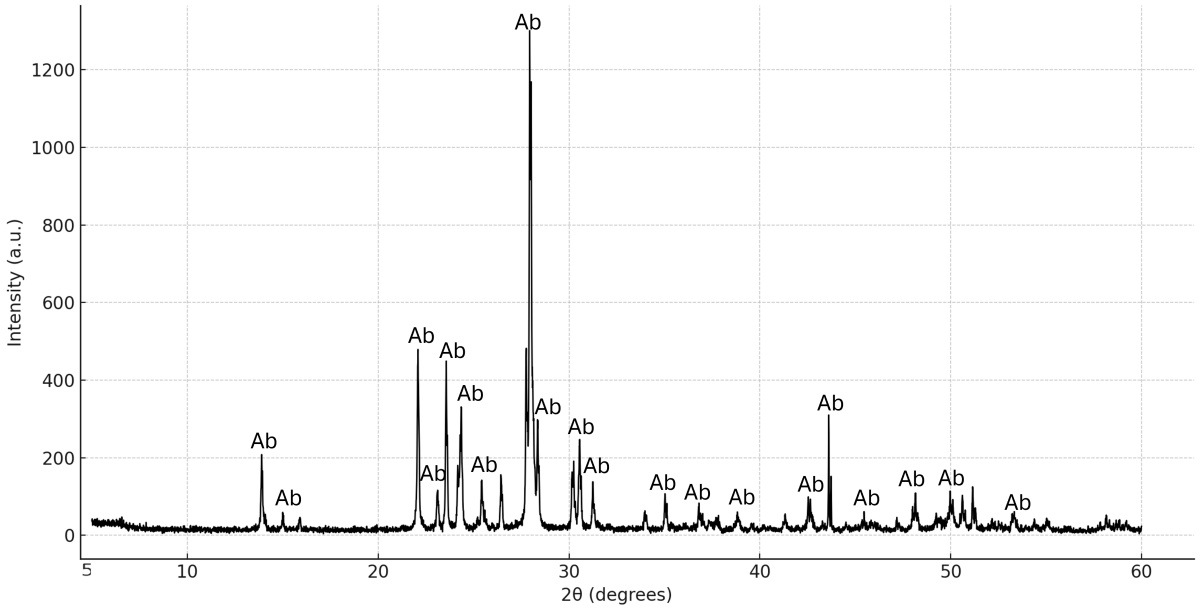

Figure 4.28: XRD pattern of albite (96% purity), matched against PDF-2 database standard 090466.

4.3.4 Pyrite

Pyrite (FeS_2) is an isotropic mineral that belongs to the cubic (isometric) crystal system ($a = b = c;\ \alpha = \beta = \gamma = 90°$) (Figure 4.29). This means that the cutting orientation relative to the crystallographic axes is not a concern when preparing samples for thermal conductivity measurements. The three pyrite samples were cut with different cross-sectional areas from a single pyrite cube (Figure 4.30): Pyrite-1 = 4.2 mm^2, Pyrite-2 = 9.02 mm^2, Pyrite-3 = 2.0 mm^2 (Table 4.1). These varying sample sizes were chosen to investigate the relationship between sample size and thermal conductivity. As discussed in Section 2.2.3, sample dimensions become increasingly important at low temperatures, where phonon-boundary scattering dominates the heat transfer process.

XRD analysis of pyrite reveals that it is 96% pure (Figure 4.31), with the remaining 4% corresponding to other mineral phases. Although the pyrite cube appeared homogeneous on the macroscopic scale, microscopic images of the samples reveal the presence of trace minerals (Figures 4.32 and 4.33). Based on surface appearance, Pyrite-1 appears to have

the most uniform composition of the three samples. The compositions of the trace minerals could not be resolved by XRD analysis due to their small size; however, a simple HCl reaction test confirmed the presence of calcite.

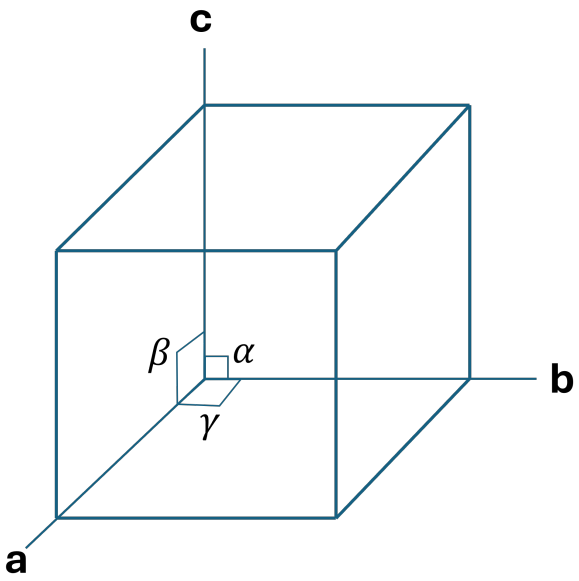

Figure 4.29: Cubic (isometric) crystal system of pyrite. Image adapted from Le Comptoir Géologique (2025)

.

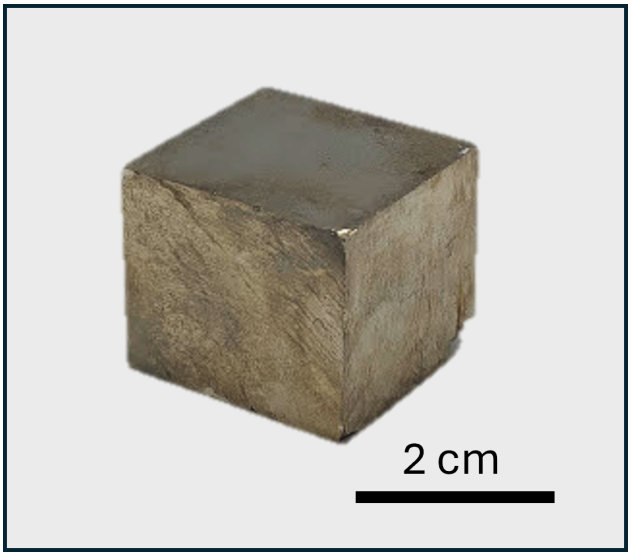

Figure 4.30: Pyrite cube from which the three pyrite samples used in this study were cut.

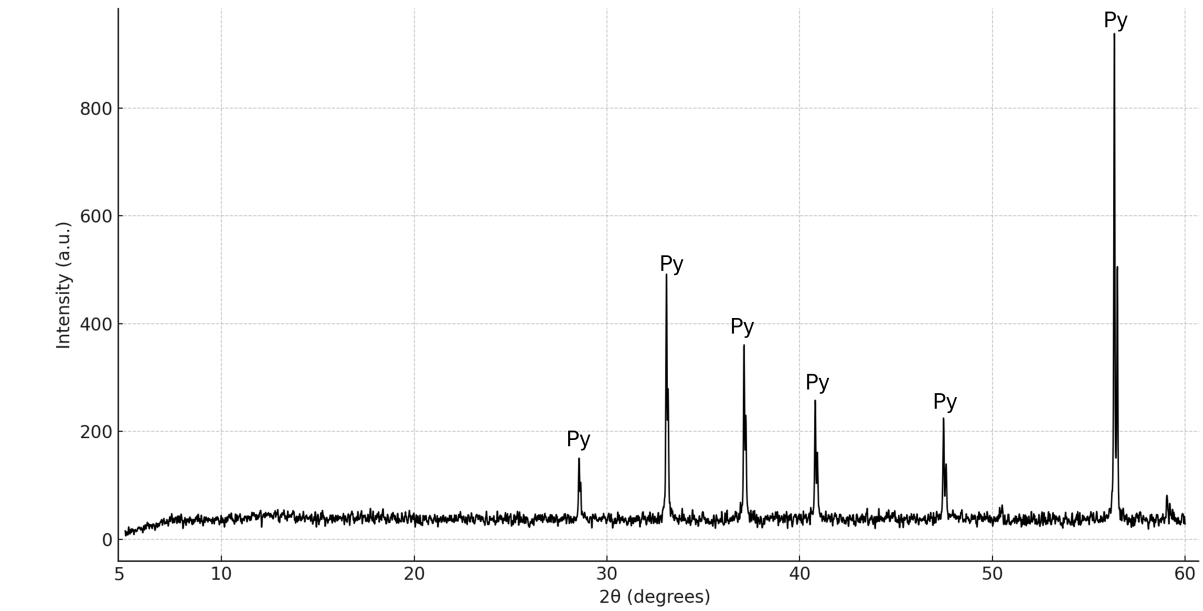

Figure 4.31: XRD pattern of pyrite (96% purity), matched against PDF-2 database standard 060710.

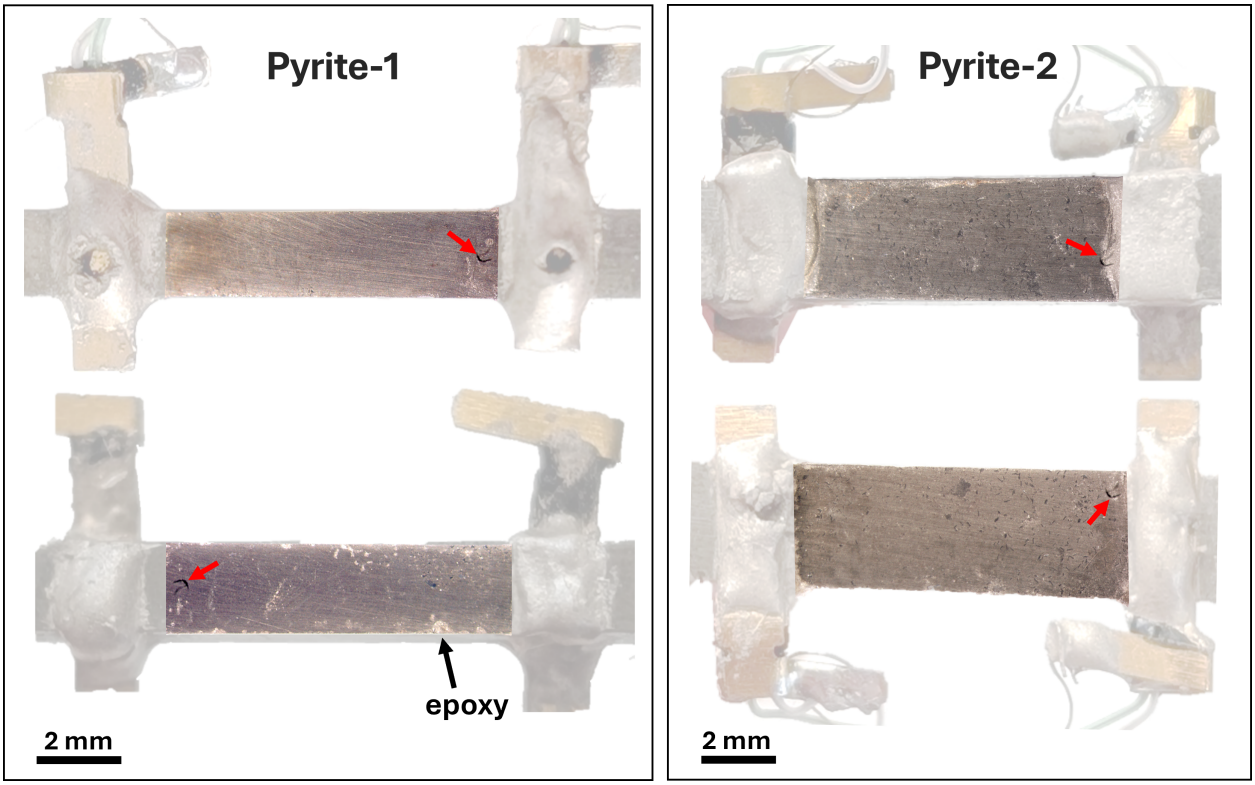

Figure 4.32: Microscope images of Pyrite-1 and Pyrite-2, showing front and back surfaces. The center region of each sample corresponds to the ΔT measurement zone (between the thermocouple junctions), which is highlighted to reveal trace minerals, visible as small black specks. Red arrows indicate microscope artifacts. Pyrite-2 appears to contain more inclusions than Pyrite-1.



Figure 4.33: Composite microscope images of Pyrite-3, showing two polished surfaces. Trace mineral inclusions are visible throughout the sample as small black specks.

4.3.5 Obsidian

Obsidian is volcanic glass formed by the rapid cooling of lava, which prevents crystallization and results in a disordered atomic structure. Although it is considered an igneous rock, obsidian is amorphous and was included in the single-crystal investigation to compare thermal conductivity trends between crystalline and non-crystalline materials. Due to its disordered atomic structure, obsidian is isotropic, so the cutting direction does not need to be considered when preparing a sample. One obsidian sample was prepared for this study (Figure 4.34). XRD analysis confirms the amorphous nature of the sample, as amorphous materials typically produce low-intensity, broad, and featureless diffraction patterns due to the absence of crystallinity (Figure 4.35) (Nunes et al., 2005; Popova et al., 2014; Rowe and Brewer, 2018).

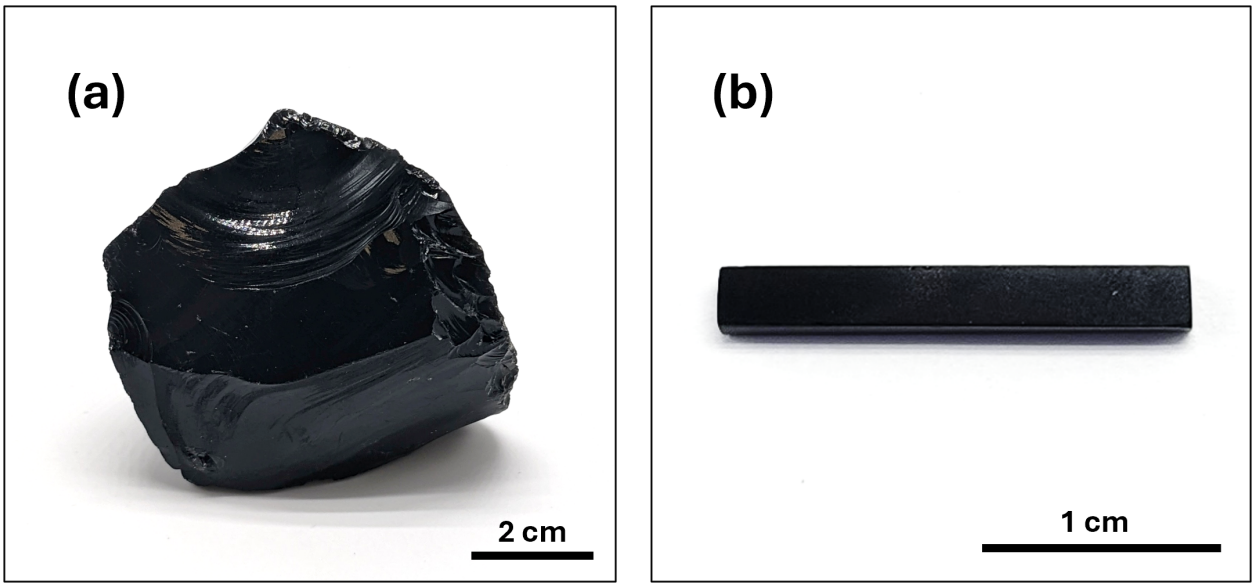

Figure 4.34: **(a)** Obsidian specimen used to prepare a sample for this study. **(b)** Obsidian sample prepared for thermal conductivity measurements.

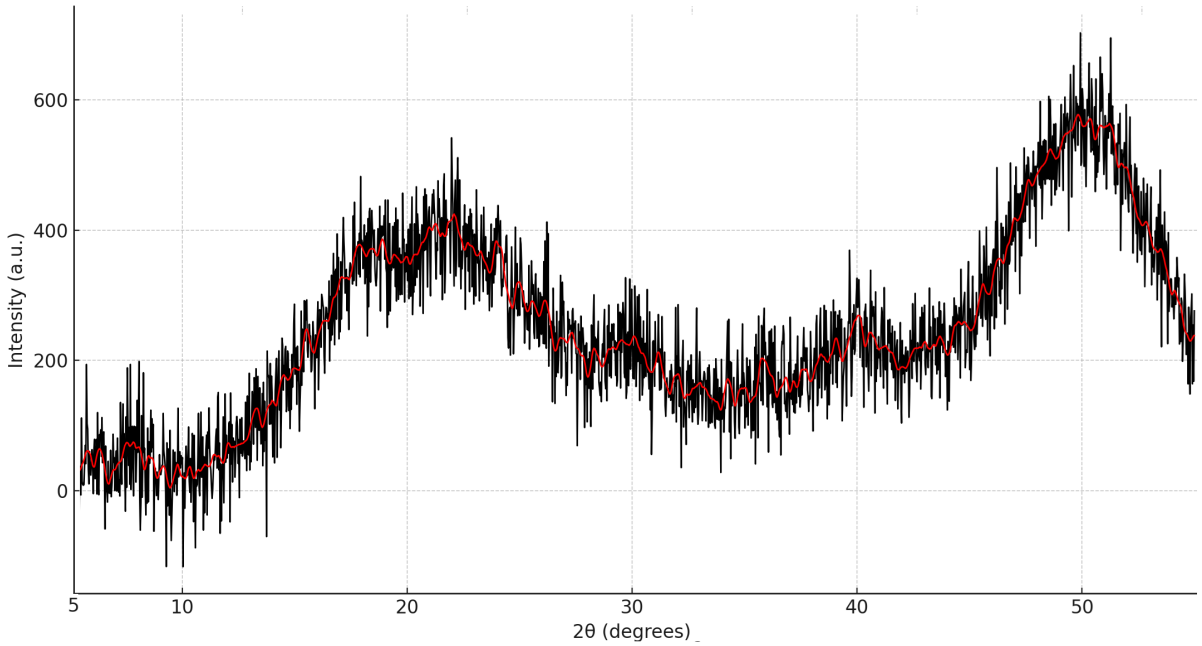

Figure 4.35: XRD pattern of obsidian, characteristic of amorphous materials. The black line shows the raw intensity data, while the red line represents a smoothed curve used to estimate the background signal.

4.4 Meteorites

4.4.1 Background Information

This section provides an introduction to the geology of meteorites, focusing on the types analyzed in this study. Portions of the content are adapted from my MSc thesis (Gilmour, 2017) and subsequent publications (Gilmour et al., 2019; Gilmour and Herd, 2020), but have been reworded and reorganized to align with the scope and objectives of the present work. The meteorite groups discussed include the chondrites, which are stony meteorites defined by the presence of small, round grains known as chondrules. Chondrites are typically classified into three main types: ordinary, enstatite, and carbonaceous. This study includes two ordinary chondrites (Buzzard Coulee and Holbrook), one carbonaceous chondrite (Allende), and one iron meteorite (North Chile).

Ordinary Chondrites

Ordinary chondrites are the most common among the three chondrite types. They originate from undifferentiated stony asteroids, meaning the parent body did not separate into a crust, mantle, and core. As a result, ordinary chondrites contain a mixture of silicate minerals (olivine, pyroxene, and plagioclase) present in both the chondrules and the fine-grained matrix, along with iron-nickel (Fe-Ni) metal and troilite (FeS) (Brearley and Jones, 1998).

The ordinary chondrites are divided into three groups—H, L, and LL—based on their Fe-Ni metal content. On average, H chondrites contain 18.2 wt.% metal, L chondrites contain 8.4 wt.%, and LL chondrites contain the least amount with 3.5 wt.% (Dunn et al., 2010). These differences reflect varying oxidation states of the parent bodies. LL chondrites are the most oxidized, and therefore contain the least metal, as most of the iron is incorporated into silicate minerals rather than occurring as metallic iron (Snelling, 2014).

Ordinary chondrites are further classified by petrological type, which reflects the degree of thermal metamorphism experienced by the parent body. The petrological classification ranges from type 3 to type 6 (Sears and Dodd, 1988; Brearley and Jones, 1998). Type 3 chondrites are considered the most primitive, as they show little to no metamorphic alteration and preserve original textures and mineral compositions. Types 4 through 6 represent progressively higher levels of thermal metamorphism, with type 6 being the most metamorphosed. As metamorphism progresses, the original textures and compositions of the primitive material gradually become more homogeneous.

Carbonaceous Chondrites

Carbonaceous chondrites are the most primitive type of meteorite, containing the oldest known objects in the solar system, referred to as Calcium-Aluminum-rich Inclusions (CAIs). These meteorites also contain chondrules, and their bulk mineralogy includes carbonates (calcite and dolomite), troilite, magnetite, olivine, pyroxene and organic compounds (Brearley and Jones, 1998).

There are eight main groups of carbonaceous chondrites, which are classified based on their elemental and isotopic composition: CI, CM, CR, CK, CV, CH, CB, and CO. The first letter "C" indicates that the meteorite is carbonaceous, and the second letter typically refers to the type specimen from that group, such as Murchison for CM chondrites. In the case of CH, the "H" refers to high metal content. Although metal is generally uncommon in carbonaceous chondrites, it is present in the less oxidized groups, including CB, CH, CR, CO, and CV (Brearley and Jones, 1998; Krot et al., 2014). When a carbonaceous chondrite does not match the composition of any known group, it is classified as an ungrouped meteorite. Two well-known examples of ungrouped carbonaceous chondrites include Tagish Lake and Tarda.

Some carbonaceous chondrites have undergone aqueous alteration. This is indicated by the presence of hydrous minerals such as saponite and serpentine, which form when water interacts with olivine and pyroxene (Browning et al., 1996; Hanowski and Brearley, 2001; Rubin et al., 2007), as well as by water content (Howard et al., 2014; Gilmour et al., 2019; Bates et al., 2024). The extent of aqueous alteration is described using petrological types 1 and 2, with type 1 representing the most altered. These petrological types apply to the CI, CM, and CR chondrites (Howard et al., 2014; Krot et al., 2014), as well as the ungrouped meteorites Tagish Lake (Herd et al., 2011; Blinova et al., 2014; Gilmour et al., 2019) and Tarda (Bates et al., 2024; Schrader et al., 2024). The remaining carbonaceous groups are either unequilibrated (type 3) or have undergone minor thermal metamorphism (type 4), except for CK chondrites, which show evidence of metamorphism up to type 6 (Krot et al., 2014).

Iron Meteorites

Iron meteorites are believed to originate from the cores of differentiated parent bodies, although some may have a non-magmatic origin, such as from impact melts (Wasson et al., 1980; Choi et al., 1995). They are comprised primarily of Fe-Ni metal and may contain mi-

nor amounts of troilite, phosphides, and silicates (Mittlefehldt et al., 1998). Two dominant Fe-Ni metal phases are commonly found in iron meteorites: kamacite (low-Ni phase) and taenite (high-Ni phase).

Iron meteorites are classified based on both their structure and chemical composition. Structural classification is determined by the presence or absence of the Widmanstätten pattern (Buchwald, 1975a). This pattern is a distinctive arrangement of kamacite and taenite lamellae that becomes visible when a polished surface is etched with acid. The three main structural types are hexahedrites, octahedrites, and ataxites. Octahedrites are further divided into subtypes based on the width of the kamacite and taenite lamellae, ranging from coarse to fine. Hexahedrites and ataxites do not display a Widmanstätten pattern, as they consist almost entirely of a single metal phase: kamacite in hexahedrites and taenite in ataxites.

The main chemical groups of iron meteorites include IAB, IIAB, IIIAB, IVA, and IVB, with several additional subgroups. These groups are defined primarily by their nickel content and by the trace element concentrations of gallium (Ga), germanium (Ge), and iridium (Lovering et al., 1957; Wasson, 1967). The Roman numerals (I-IV) represent the main chemical groups, based on Ge and Ga content, while the letters differentiate subgroups within each group.

4.4.2 Meteorite Samples

Five meteorite samples were prepared for thermal conductivity measurements: North Chile (iron), Allende (carbonaceous chondrite), two samples of Buzzard Coulee (ordinary chondrite), and Holbrook (ordinary chondrite). The thermal conductivity of two Holbrook samples was previously reported by Opeil et al. (2012), providing an opportunity to compare results obtained using different cryogenic instruments. A thermal conductivity value for Allende was reported by Szurgot (2011b); however, it was derived indirectly from thermal diffusivity, bulk density, and specific heat capacity. Therefore, this study presents the first di-

rect thermal conductivity measurements for Allende, as well as for North Chile and Buzzard Coulee.

Dr. Chris Herd provided the meteorite samples from the University of Alberta Meteorite Collection, and they were cut by Dr. Patrick Hill, a former postdoctoral researcher in Dr. Herd's lab. Sample dimensions were refined by polishing with silicon carbide paper. Descriptions of the meteorites are provided below and summarized in Tables 4.2 and 4.3.

North Chile

North Chile is a IIAB hexahedrite composed almost entirely of kamacite metal (low Ni phase), with rhabdite ($[Fe,Ni]_3P$) inclusions throughout (Buchwald, 1975c; Wasson et al., 1989; Wasson et al., 1998; Campbell and Humayun, 1999; Nolze et al., 2006; Gilmour and Herd, 2020). The North Chile sample used in this project has cracks and scratches on its surface, but otherwise appears homogeneous on the macroscale (Figures 4.36 & 4.37). Rhabdite crystals are only visible on the micron scale (Gilmour and Herd, 2020).

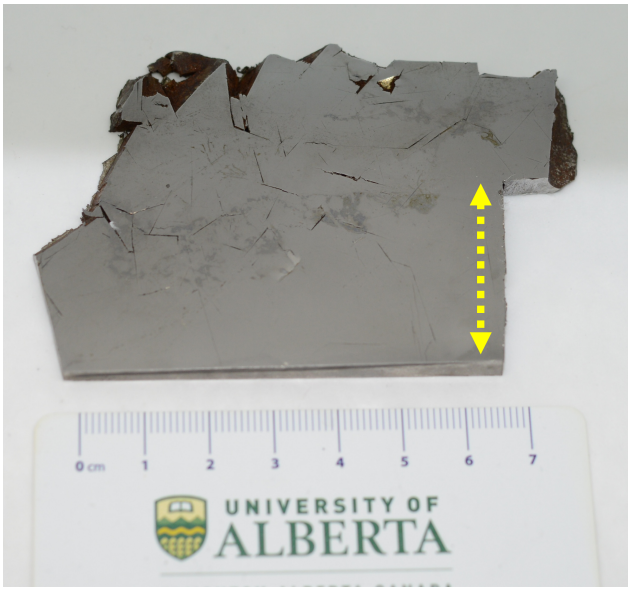

Figure 4.36: North Chile meteorite from the University of Alberta Meteorite Collection. The yellow arrow indicates the location from which the sample used in this study was cut. *Photo by Dr. Patrick Hill.*

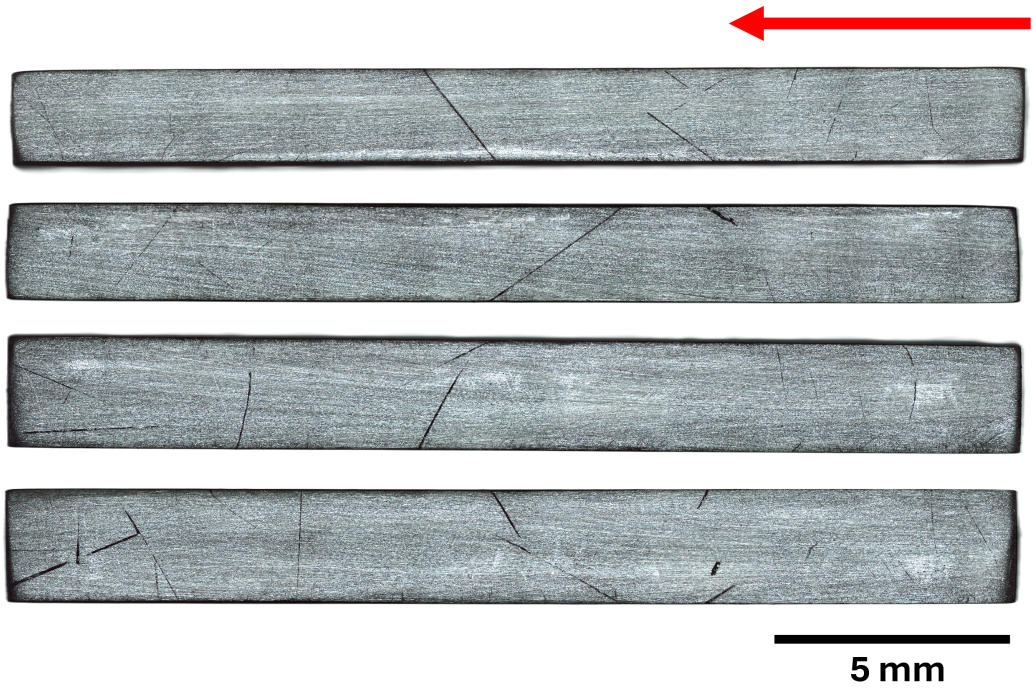

Figure 4.37: Composite microscope images of the four sides of the North Chile iron meteorite. Cracks and scratches are apparent on the surface. The red arrow indicates the direction of heat flow through the sample. *University of Alberta Meteorite Collection ID: MET6579/4-1*

Holbrook

Holbrook is an L/LL6 ordinary chondrite, meaning it exhibits properties of both L and LL chondrites. Specifically, its olivine composition is typical of L chondrites, while the cobalt concentration in kamacite aligns more closely with LL chondrites (Rubin, 1990). Additionally, oxygen isotope measurements for different Holbrook samples span the upper limit of L chondrites and extend into the LL region (Rubin, 1990; Rubin et al., 2008).

Holbrook is composed of olivine, hypersthene (pyroxene), plagioclase, Fe-Ni metal (kamacite and taenite), troilite, and chromite (Mason and Wiik, 1961). Samples collected sometime after its initial fall in 1912 show clear evidence of weathering (Gibson and Bogard, 1978; Bland et al., 1998; Pillinger et al., 2013). During the weathering of ordinary chondrites, metal and Fe-rich silicates undergo oxidation (Bland et al., 2006), which appears as rusty brown areas around metal grains (Figures 4.38 and 4.39).



Figure 4.38: Holbrook meteorite from the University of Alberta Meteorite Collection. The yellow arrow indicates the location from which the sample used in this study was cut. The rust-coloured areas result from metal oxidation caused by weathering. *Photo by Dr. Patrick Hill.*

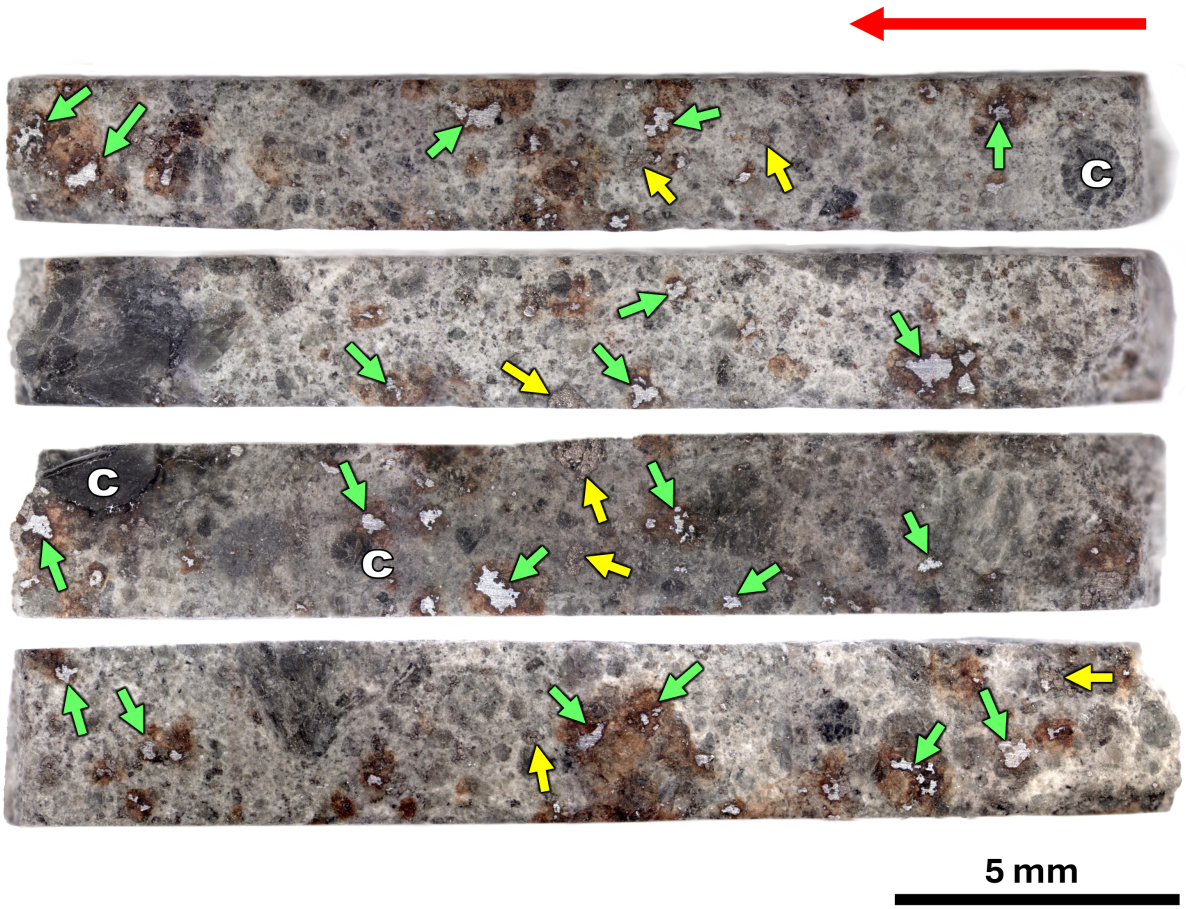

Figure 4.39: Composite microscope images of the four sides of the Holbrook sample. Chondrules are indicated by "C" on or next to some examples. Examples of metal (green arrows) and troilite (yellow arrows) are shown. Note the rusted areas around the metal, caused by oxidation due to weathering. The red arrow indicates the direction of heat flow through the sample. *University of Alberta Meteorite Collection ID: MET7179/3-1*

Buzzard Coulee

Buzzard Coulee is an H4 ordinary chondrite. It was collected shortly after its fall and is considered a pristine sample, showing no evidence of terrestrial weathering (Hildebrand et al., 2009; Hutson et al., 2009). Its composition includes two types of pyroxene, olivine, troilite, Fe-Ni metal (kamacite and taenite), and devitrified alkali-rich glass, with minor amounts of chromite, merrilite, pentaldante, augite, and traces of spinel and silica glass (Walton and Herd, 2009a; Walton and Herd, 2009b; Higgins et al., 2011). Buzzard Coulee is slightly shocked and classified as a monomict breccia (Hutson et al., 2009; Higgins et al., 2011;

Gilmour and Herd, 2020). A breccia is a rock composed of angular, fragmented clasts, and a monomict breccia contains clasts of the same lithology as the surrounding matrix (Wahl, 1952; Bischoff et al., 2006).

Buzzard Coulee is considered anomalous among H chondrites due to low variability in its physical properties, such as bulk density, porosity, and magnetic susceptibility (Fry et al., 2013). Additionally, its metal grains have minimal variation in platinum group element (PGE) concentrations compared to other type 4 chondrites (Gilmour and Herd, 2020). Thermal conductivity measurements of Buzzard Coulee will help assess whether its unusual physical properties are also reflected in its thermal behaviour.

Two Buzzard Coulee samples, cut from different sections of a single piece, were prepared for this study (Figure 4.40). Microscope images show silicate grains and chondrites, Fe-Ni metal, and troilite (Figures 4.41 and 4.42).



Figure 4.40: Buzzard Coulee meteorite from the University of Alberta Meteorite Collection. The yellow and blue arrows show the locations from which two samples (labelled BC-1 and BC-2) were cut. *Photo by Dr. Patrick Hill.*

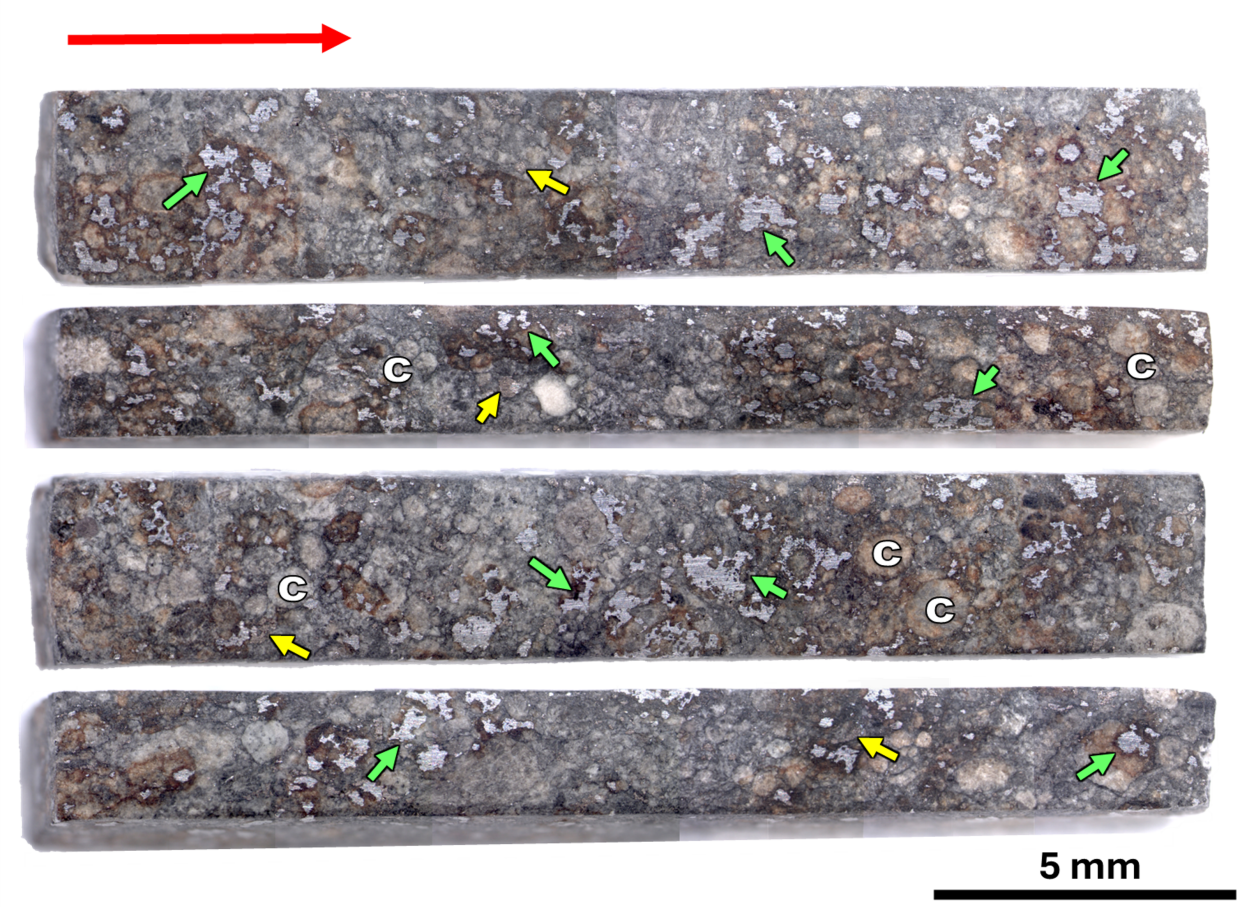

Figure 4.41: Composite microscope images of the four sides of the Buzzard Coulee-1 sample. Chondrules are indicated by "C" on or next to some examples. Examples of metal (green arrows) and troilite (yellow arrows) are shown. The red arrow indicates the direction of heat flow through the sample. *University of Alberta Meteorite Collection ID: MET1161-1-3-1*

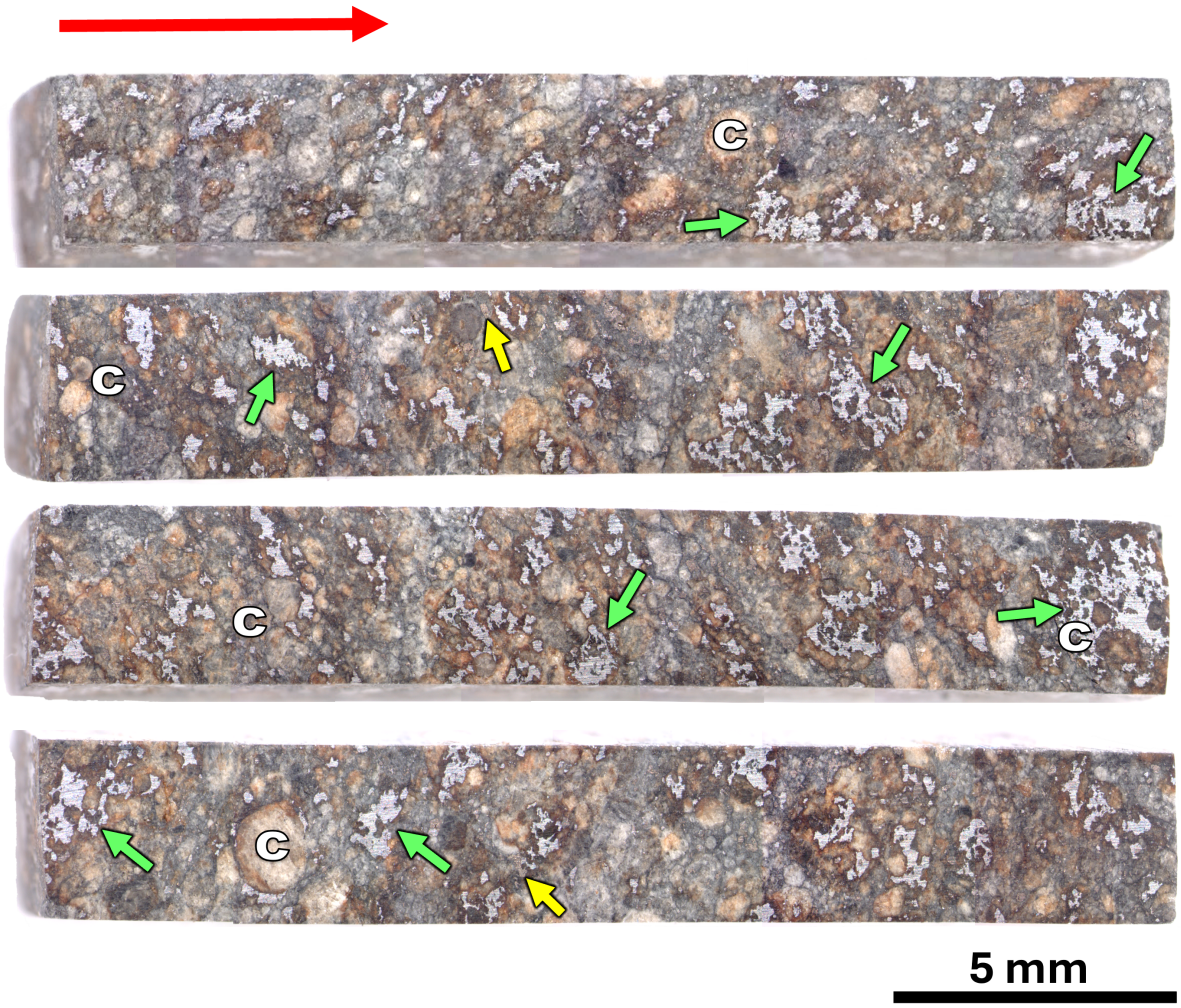

Figure 4.42: Composite microscope images of the four sides of the Buzzard Coulee-2 sample. Chondrules are indicated by "C" on or next to some examples. Examples of metal (green arrows) and troilite (yellow arrows) are shown. The red arrow indicates the direction of heat flow through the sample. *University of Alberta Meteorite Collection ID: MET1161-1-4-1*

Allende

Allende is one of the most well-known and extensively studied meteorites, with over 2 tons of material collected to date. It is classified as a CV3 primitive accretionary breccia (Bischoff et al., 2006). Although designated as a type 3 chondrite, evidence suggests that Allende has been subject to both aqueous and thermal alteration (Kojima and Tomeoka, 1996; Bonal et al., 2006). Allende has a relatively low carbon content ($\sim 0.3\%$) compared to other carbonaceous chondrites (Mason, 1975; Kerridge, 1985).

Allende is composed of 57% matrix and 43% inclusions (Fendrich and Ebel, 2021). The matrix consists of fine grained olivine, clinopyroxene, spinel, troilite, pentlandite, chromite, nepheline, and sodalite (Mason, 1975; Kornacki and Wood, 1984; Toriumi, 1989). The inclusions include olivine, pyroxene, and aluminum-rich chondrules, fragmented and isolated silicate grains and polycrystalline aggregates, and refractory inclusions such as calcium-aluminum-rich inclusions (CAIs) and amoeboid olivine aggregates (AOAs) (Mason, 1975; Fendrich and Ebel, 2021).

One sample of Allende was prepared for thermal conductivity measurements (Figures 4.43 and 4.44).



Figure 4.43: Allende meteorite from the University of Alberta Meteorite Collection. The yellow arrow indicates the location from which the sample was cut. *Photo by Dr. Patrick Hill.*

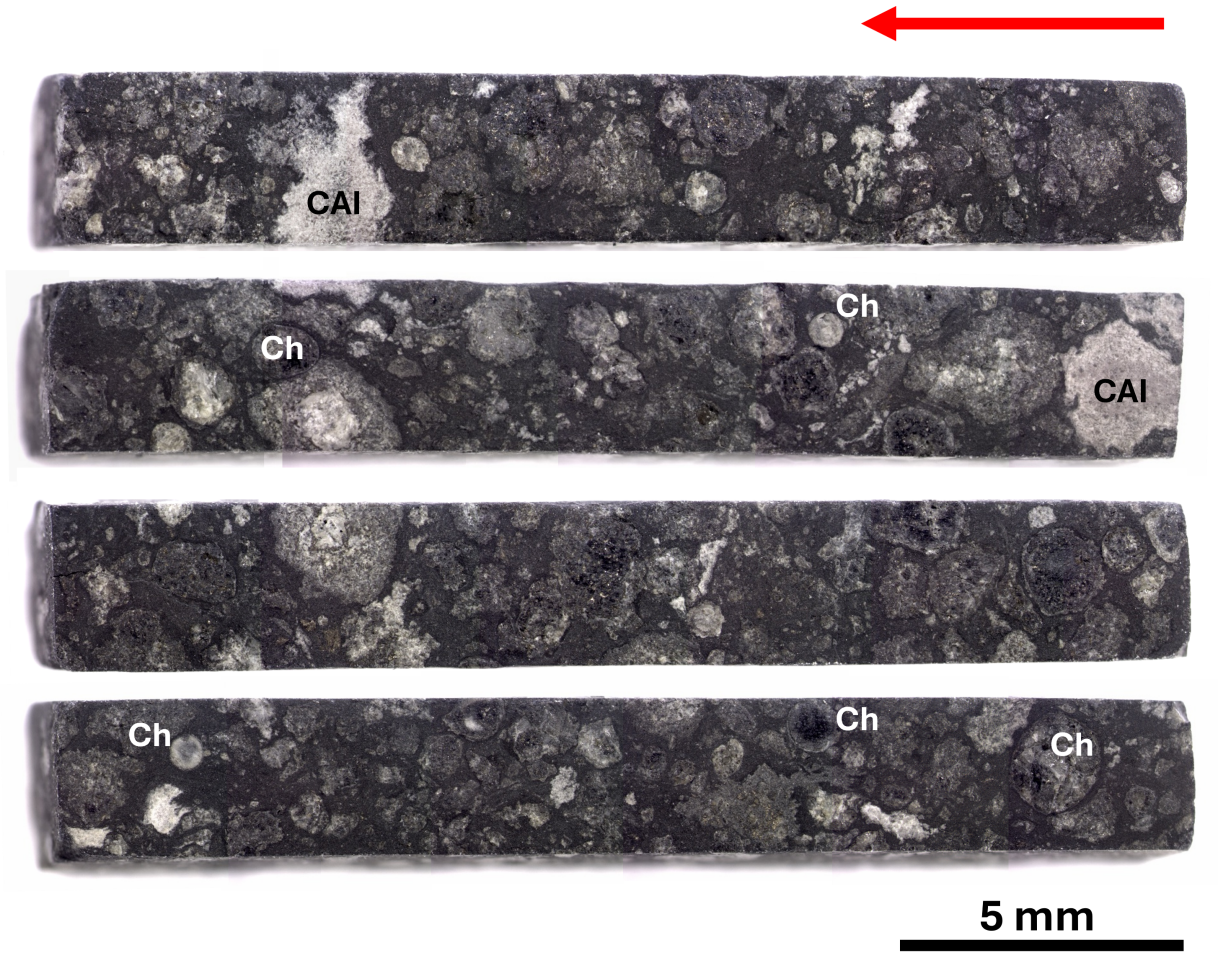

Figure 4.44: Composite microscope images of the four sides of the Allende. Some examples of chondrules "Ch" and CAIs are highlighted on the figure. The red arrow indicates the direction of heat flow through the sample. *University of Alberta Meteorite Collection ID: MET7100-A-201-1-3-1*

Table 4.2: Summary of meteorites

Meteorite	**Type**	**Shocked?**	**Weathered?**	**Mineralogy**
North Chile	IIAB	No	No	Fe-Ni metal (kamacite), rhabdite inclusions
Holbrook	L/LL6	Yes	Yes	Olivine, pyroxene, plagioclase, Fe-Ni metal, troilite, chromite
Buzzard Coulee	H4	Yes	No	Olivine, pyroxene, Fe-Ni metal, troilite, devitrified glass
Allende	CV3	No	No	Olivine, pyroxene, carbonates, spinel, chromite, troilite, CAIs, AOAs

Table 4.3: Dimensions of meteorite samples.

Meteorite	**Type**	**Dimensions (mm)** $w \times h \times l$	**A (mm^2)**	**L (mm)**
North Chile	IIAB	2.42 × 2.09 × 21.5	5.045 ± 0.006	11.24 ± 0.01
Allende	CV3	2.78 × 2.87 x 20.1	7.955 ± 0.007	11.46 ± 0.05
Buzzard Coulee-1	H4	3.25 × 2.25 × 20.1	7.309 ± 0.006	12.012 ± 0.007
Buzzard Coulee-2	H4	2.74 × 2.69 × 20.1	7.356 ± 0.006	11.959 ± 0.008
Holbrook	L/LL6	2.65 × 3.07 × 20.0	8.13 ± 0.02	11.45 ± 0.01

4.4.3 Additional Analysis

To complement the thermal conductivity data, volume and density measurements, along with X-ray computed tomography (XCT) imagery, were acquired. These data provide insight into the density and porosity of the meteorites, which are key factors influencing thermal conductivity (e.g., Opeil et al. (2012)).

Volume and Density

The skeletal volume (V_s) and grain density (ρ_g) of the meteorites were measured with a Micromeritics® Instrument Corporation Accupyc® II 1340 Gas Displacement Pycnometer (Figure 4.45). Prior to pycnometer measurements, the meteorites were weighed using a Sartorius MSA524P-100 DI Cubis Precision Balance, accurate to ±0.0001 g (Figure 4.46). The bulk volume (V_b) was calculated from the measured sample dimensions ($w \times h \times l$) (Table 4.3), and then the bulk density (ρ_b) is determined from Equation 4.1, where m is the mass of the sample. Porosity (Φ) of the sample can then be calculated from the bulk and skeletal volumes using Equation 4.2.

$$\rho_b = \frac{m}{V_b} \tag{4.1}$$

$$\Phi = \frac{V_b - V_s}{V_b} \tag{4.2}$$



Figure 4.45: MicromeriticsMAP® Instrument Corporation AccupycMAP® II 1340 Gas Displacement Pycnometer.

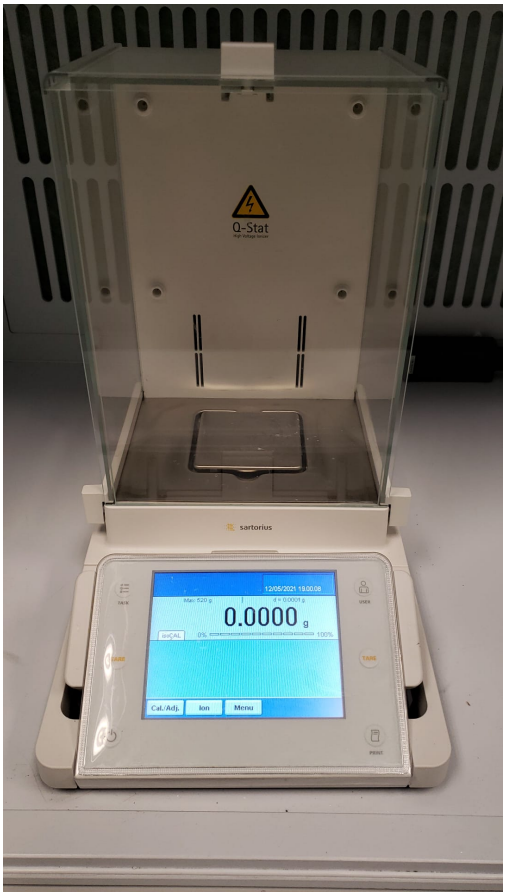

Figure 4.46: Sartorius MSA524P-100 DI Cubis Precision Balance (±0.0001g)

XCT Imagery

X-ray computed tomography (XCT) images were acquired at the Canadian Centre for Electron Microscopy (CCEM) at McMaster University in Hamilton, ON. XCT provides three-dimensional views of the meteorite samples, revealing the distribution of porosity within each sample and highlighting compositional and textural variations along the heat flow direction. While XCT is commonly used to measure the total sample volume, including both bulk and skeletal volumes, this study focused on imaging the central half of each sample to optimize resolution. This region corresponds with the area where the thermal gradient is measured (i.e., between thermocouple tabs), offering a detailed visualization of porosity and grain boundaries within this area.

The Zeiss Xradia 630 Versa X-ray computed tomography (XCT) system was used to examine the shape and internal structure of the meteorite samples, including their pore distribution (Figures 4.47 and 4.48). To capture fine details, the scan was set to a resolution of 4.88 μm using a geometric magnification of 7.06X and an optical magnification of 0.4X. The samples were scanned at 70 kV and 8.5 W with a Zeiss LE4 source filter. A total of 3001 images (projections) were collected over a full 360° rotation, with each projection exposed for 14 seconds. Image acquisition and 3D reconstruction were performed using Zeiss NavX 1.0 and Xradia Reconstructor software, which applied filtered back projection with adjustments for beam hardening and alignment. The resulting 3D volumes were then processed in Dragonfly (v2024.1; Object Research Systems, Inc.) for visualization and pore analysis. The image collection and processing were completed by Dr. Pardis Mohammadpour (CCEM postdoctoral researcher).



Figure 4.47: The Zeiss Xradia 630 Versa XCT system in the Canadian Centre for Electron Microscopy (CCEM) at McMaster University. The exterior and interior of the instrument are displayed on the left and right, respectively.

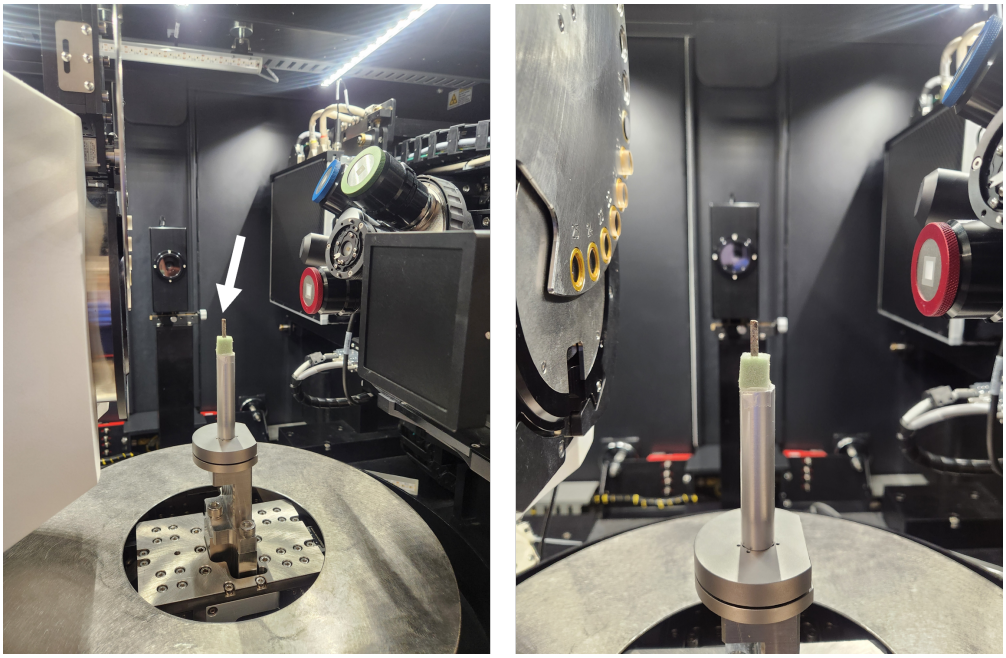

Figure 4.48: Two interior views of the Zeiss Xradia 630 Versa XCT system with a sample mounted for analysis (highlighted by the white arrow in the left image). The sample measures approximately 2 mm wide.

5 Results: Single-Crystal Minerals

This chapter presents the thermal conductivity data for the single-crystal mineral samples, including obsidian. It begins with an overview of the radiative heat loss corrections, followed by a review and discussion of the thermal conductivity results. Table 4.1 from Chapter 4 is re-posted as Table 5.1 for easy reference.

Table 5.1: Re-post of Table 4.1: Single crystal properties and dimensions.

Sample	**Crystal System**	**Anisotropy**	**Dimensions (mm)** $w \times h \times l$	**A (mm^2)**	**L (mm)**
Quartz-1	Trigonal	Anisotropic	$2.65 \times 2.64 \times 20.3$	6.971 ± 0.006	11.429 ± 0.007
Quartz-2			$2.59 \times 2.60 \times 20.0$	6.737 ± 0.007	12.127 ± 0.013
Calcite-1a-4a-b	Trigonal	Anisotropic	$3.02 \times 2.71 \times 19.2$	8.201 ± 0.005	11.427 ± 0.007
Calcite-1a-5d			$2.86 \times 3.01 \times 19.6$	8.618 ± 0.010	11.846 ± 0.008
Calcite-1a-6-1			$2.76 \times 2.72 \times 18.7$	7.518 ± 0.024	10.218 ± 0.007
Calcite-1b-6-1			$2.89 \times 2.11 \times 21.4$	6.085 ± 0.006	11.721 ± 0.018
Calcite-1b-6-2			$2.80 \times 2.93 \times 19.0$	8.218 ± 0.002	11.288 ± 0.013
Calcite-1b-6-5			$2.61 \times 2.91 \times 21.3$	7.593 ± 0.007	11.549 ± 0.007
Albite-1	Triclinic	Anisotropic	$2.48 \times 2.52 \times 20.6$	6.249 ± 0.009	12.061 ± 0.006
Albite-2			$2.40 \times 2.59 \times 19.9$	6.202 ± 0.009	12.182 ± 0.008
Pyrite-1	Cubic	Isotropic	$2.03 \times 2.07 \times 19.9$	4.196 ± 0.003	11.043 ± 0.014
Pyrite-2			$2.89 \times 3.12 \times 17.4$	9.014 ± 0.009	10.024 ± 0.009
Pyrite-3			$1.67 \times 1.22 \times 20.0$	2.027 ± 0.004	11.917 ± 0.006
Obsidian	Amorphous	Isotropic	$2.51 \times 2.63 \times 20.1$	6.598 ± 0.007	12.829 ± 0.009

5.1 Radiative Heat Loss Corrections

As a detailed discussion of radiation heat loss and the correction method was provided in Chapter 3, only a summary is included here.

In steady-state, low-temperature thermal conductivity measurements, heat loss due to radiation becomes apparent at temperatures above 100 K due to the T^3 dependence of radiative heat transfer. This T^3 term comes from the Taylor expansion of the Stefan-Boltzmann equation (Appendix B), where $P_r = 4\sigma A \varepsilon T^3 \Delta T$. For thicker samples, such as those used in

this study, radiation effects may not become apparent until 200 K (Clauser and Huenges, 1995; Tritt and Weston, 2006). In insulating solids, thermal energy is transferred dominantly by phonons, and the electron component is negligible. Radiative heat loss primarily influences the lattice component of thermal conductivity (k_L), as oscillations produced by phonon–phonon interactions within the crystal lattice give rise to electromagnetic fields that emit thermal infrared radiation. Therefore, the total measured thermal conductivity is equal to the lattice thermal conductivity and radiative component (k_{rad}), such that $k_T = k_L + k_{rad}$.

The correction method used in this study is based on the work of MacPherson and Schloessin (1982) and Pope et al. (2001), who isolated the lattice thermal conductivity from the radiative component by applying a linear fit to the data and extrapolating it (Chapter 3.3.3). In the temperature range where radiative heat loss becomes significant (typically above 100 K), thermal conductivity is expected to follow a $1/T$ dependence. This reflects the reduction in phonon mean free path due to phonon-phonon (Umklapp) scattering, which dominates heat transport in this regime (Chapter 2.2.3). Accordingly, thermal conductivity data for the single-crystal minerals in this study were plotted as a function of $1/T$ to identify the appropriate fitting region.

A linear fit based on the model $k = a(1/T)$ (Pope et al., 2001) was applied to a selected range of data between the thermal conductivity peak and 200 K. A summary of the fit parameters is provided in Table 5.2. Notably, Albite-2 did not follow a $1/T$ dependence, and the pyrite samples could not be fit in a physically meaningful way. Thus, the pyrite samples are omitted from the table. Both cases are discussed in the following sections. For Albite-1 and the calcite samples, including an intercept term b in the model ($k = a(1/T) + b$) improved the overall fit, yielding extrapolated values that compare well with literature data. However, it is important to note that the inclusion of the intercept represents an empirical modification to the model; it may account for random variability in the data or reflect minor contributions from defect-related scattering. The amorphous behaviour of obsidian presents a more complex case and is addressed separately in Section 5.3.

Table 5.2: Best fit, temperature range, and R^2 values for the anisotropic minerals.

Sample	**Best Fit**	**Range (K)**	$\boldsymbol{R}^2$
Quartz-1	$k = (3720 \pm 15)(1/T)$	30–270	0.996
Quartz-2	$k = (1982 \pm 6)(1/T)$	70–180	0.996
Calcite-1a-4a-b	$k = (836 \pm 8)(1/\mathrm{T}) + (0.95 \pm 0.08)$	60–175	0.996
Calcite-1a-5d	$k = (683 \pm 10)(1/\mathrm{T}) + (0.98 \pm 0.11)$	50–180	0.990
Calcite-1a-6-1	$k = (310 \pm 4)(1/\mathrm{T}) + (1.00 \pm 0.07)$	30–150	0.992
Calcite-1b-6-1	$k = (412 \pm 4)(1/\mathrm{T}) + (1.20 \pm 0.04)$	60–175	0.993
Calcite-1b-6-2	$k = (415 \pm 2)(1/\mathrm{T}) + (1.45 \pm 0.02)$	75–175	0.998
Calcite-1b-6-5	$k = (392 \pm 3)(1/\mathrm{T}) + (1.29 \pm 0.03)$	70–175	0.995
Albite-1	$k = (11.1 \pm 0.3)(1/\mathrm{T}) + (1.331 \pm 0.006)$	35–100	0.975
Albite-2*	$k = aT^{-4} + bT^{-3} + cT^{-2} + dT^{-1} + e$	5–100	0.985

* Albite-2 4th order coefficients:
$a = (-8.3 \pm 1.2) \times 10^3$
$b = (4.2 \pm 0.4) \times 10^3$
$c = -673 \pm 53$
$d = 25 \pm 2$
$e = 2.53 \pm 0.03$

5.2 Thermal Conductivity

5.2.1 Results

The thermal conductivity plots for the single-crystal minerals are presented in this section, while obsidian is discussed separately in Section 5.3. The data shown here represent averaged measurements at each temperature, with corrections applied to account for radiative heat loss at higher temperatures. In each plot, the transition from measured to corrected data is indicated by a change in colour (dark to light), marking the temperature range where the influence of radiative effects becomes apparent in the results.

To further illustrate the impact of radiative heat loss, additional plots are included that compare the measured (CFMS) data with the corrected data. These comparisons show the extent of the correction and the temperature ranges affected. The difference between the

measured and corrected data, which is the radiative contribution k_{rad}, is also plotted as a function of T^3 for each sample. This serves as a diagnostic check to confirm that radiative heat transfer is the primary cause of the increased thermal conductivity observed at higher temperatures (MacPherson and Schloessin, 1982; Pope et al., 2001; Tritt and Weston, 2006).

All individual thermal conductivity measurements that passed the quality check process are included in Appendix D.

Quartz

The thermal conductivity of the quartz samples cut parallel and perpendicular to the c-axis (Quartz-1 and Quartz-2, respectively) between 25 and 300 K is shown in Figure 5.1. Although the fitting range was limited to a maximum of 200 K, the effects of radiative heat loss in Quartz-1 are not apparent until 270 K (Figure 5.2); however, the onset of radiation effects may occur at some point between 200 and 300 K due to variability in the data across this range. For Quartz-2, radiative effects become apparent above 180 K (Figure 5.2). Figure 5.3 shows the radiative contribution (k_{rad}) as a function of T^3 for each sample, with R^2 values of 0.838 for Quartz-1 and 0.979 for Quartz-2 based on linear fits.

At 300 K, the average thermal conductivity of the CFMS-measured data is 13.10 ± 0.01 W m^{-1} K^{-1} for Quartz-1 and 8.23 ± 0.01 W m^{-1} K^{-1} for Quartz-2. After applying the radiation corrections with the fitting parameters listed in Table 5.2, the corresponding values are 12.48 ± 0.31 W m^{-1} K^{-1} ($\parallel c$) and 6.65 ± 0.80 W m^{-1} K^{-1} ($\perp c$).

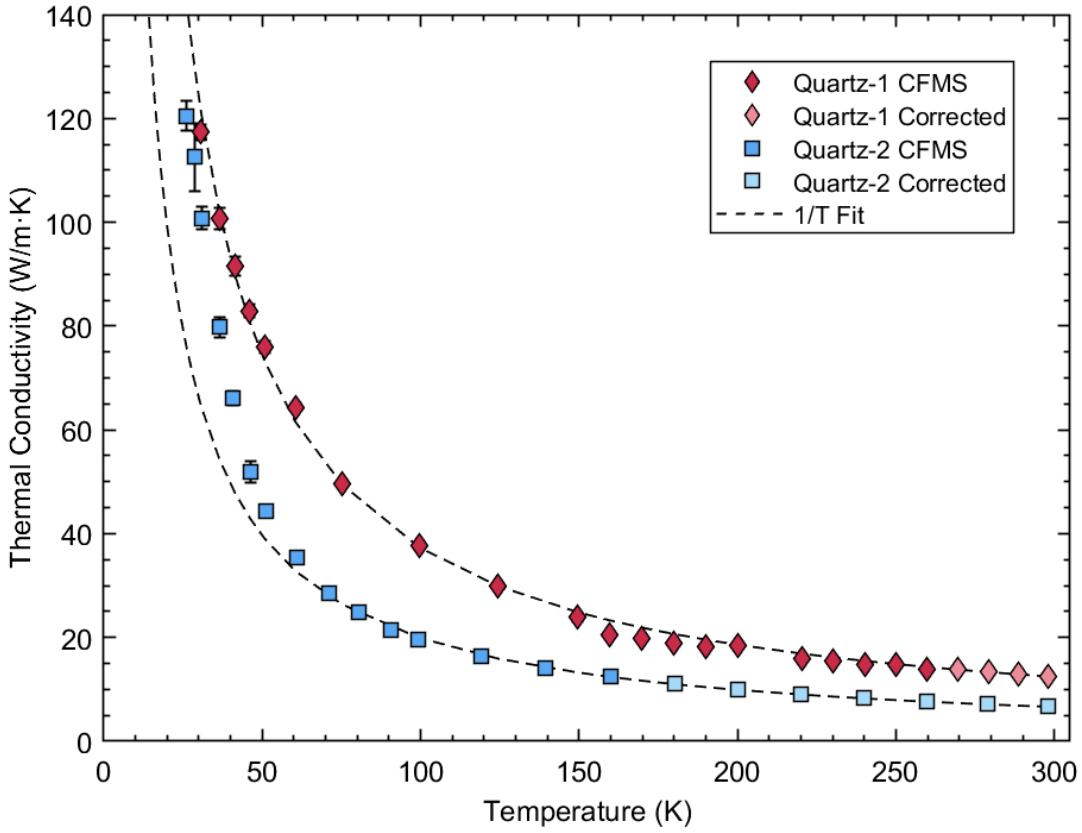

Figure 5.1: Thermal conductivity results for the two quartz samples: Quartz-1, cut parallel to the c-axis, and Quartz-2, cut perpendicular. The $1/T$ trend lines are included for reference. The transition from CFMS-measured data to corrected data is indicated by a change in colour (dark to light), which also highlights the temperature range where radiative heat loss effects are observed. At temperatures above 50 K, the error bars are smaller than the symbols and are not visible in the plot.

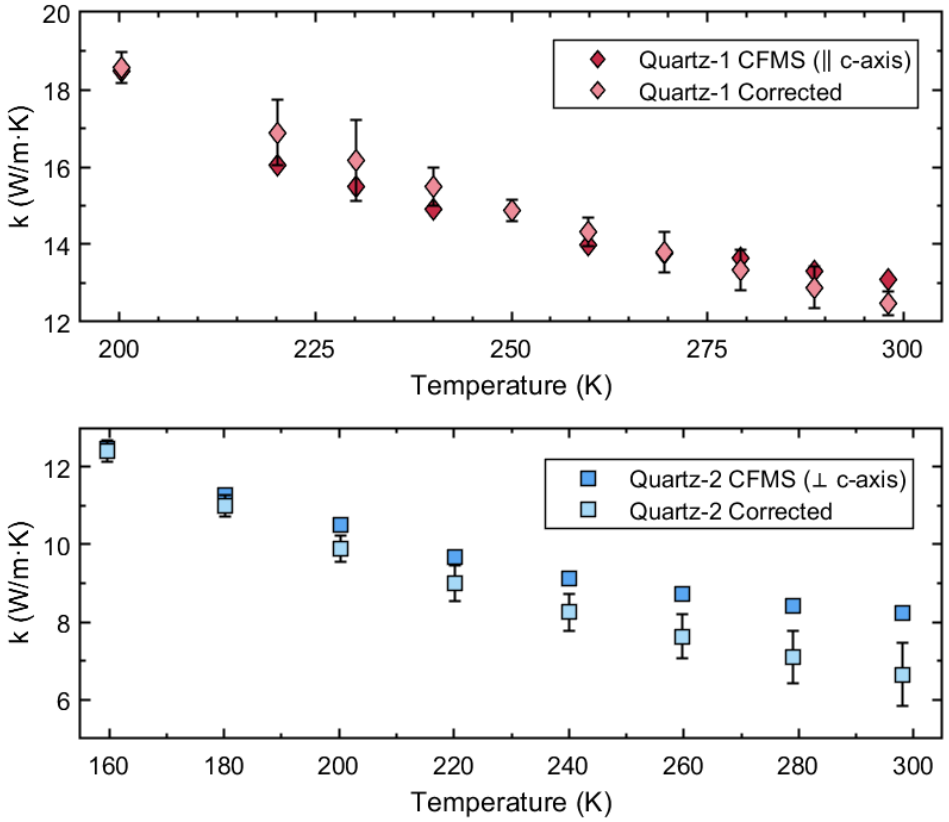

Figure 5.2: Comparison of CFMS-measured data and data corrected for radiative heat loss for Quartz-1 (top) and Quartz-2 (bottom).

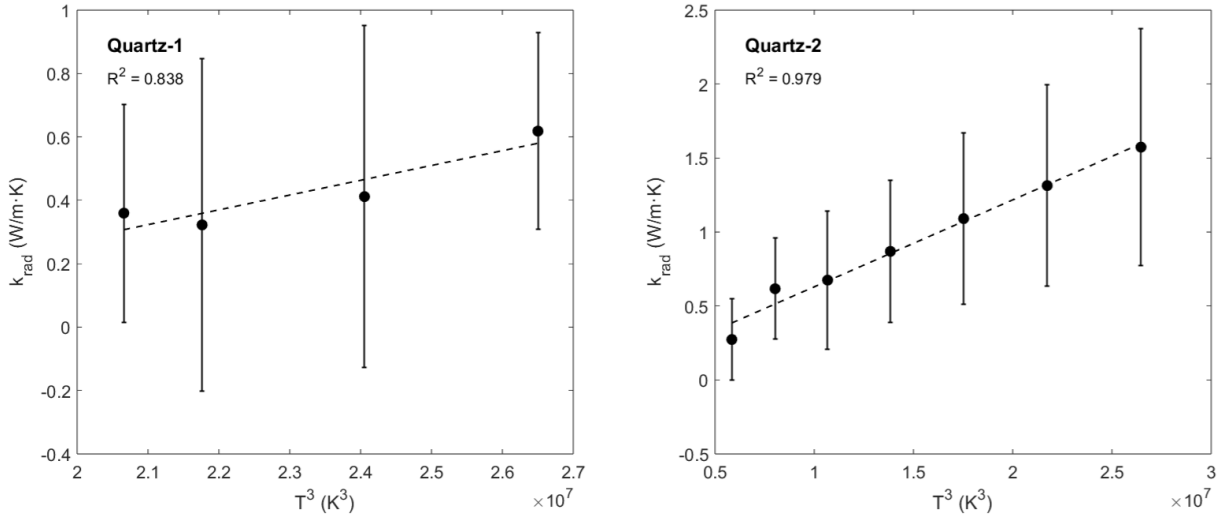

Figure 5.3: Radiation component (k_{rad}) as a function of T^3 for Quartz-1 (left) and Quartz-2 (right).

Calcite

The thermal conductivity results of the six calcite samples between 5 and 300 K are presented individually in Figure 5.4 ("a samples") and Figure 5.5 ("b samples"), collectively in Figure 5.6, and from 50 to 300 K in Figure 5.7, where the data clearly follows the $1/T$ trend.

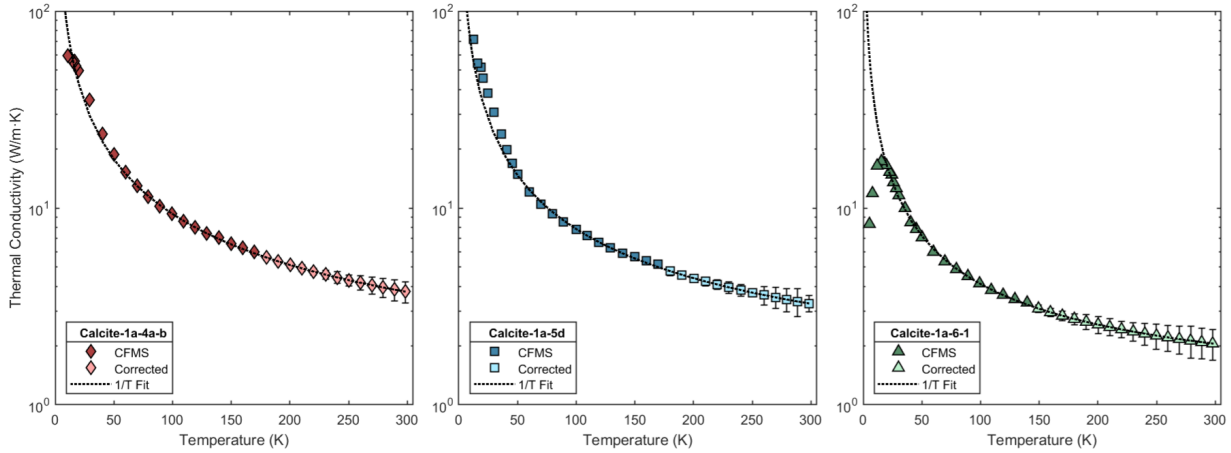

Figure 5.4: Thermal conductivity results of the three calcite "a samples" (1a-4a-b, 1a-5d, 1a-6-1) between 5 and 300 K. The $1/T$ trend lines are included for reference. The transition from CFMS-measured data to corrected data is indicated by a change in colour (dark to light), which highlights the temperature range where radiative heat loss effects are observed.

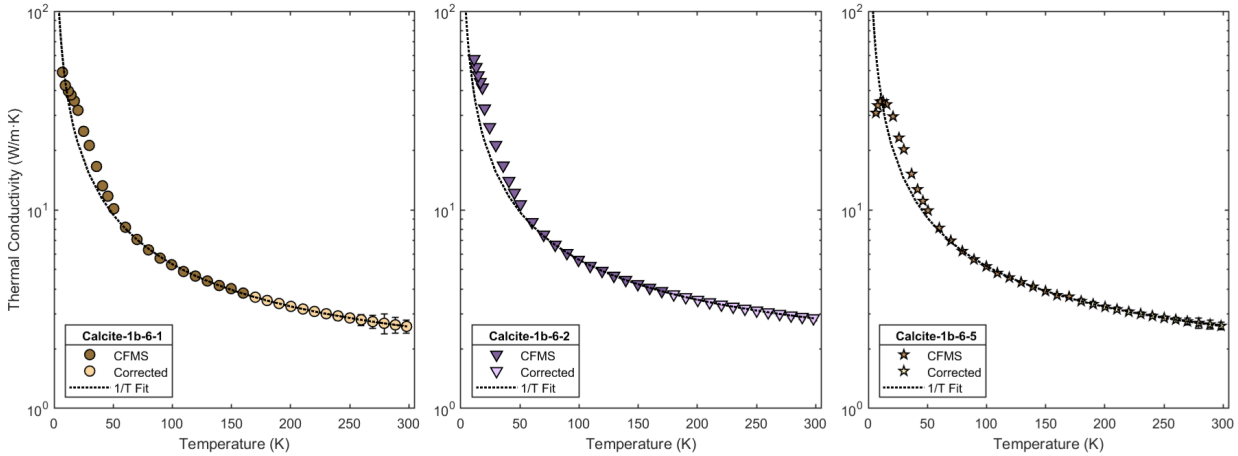

Figure 5.5: Thermal conductivity results of the three calcite "b samples" (1b-6-1, 1b-6-2, and 1b-6-5). The $1/T$ trend lines are included for reference. The transition from CFMS-measured data to corrected data is indicated by a change in colour (dark to light), which highlights the temperature range where radiative heat loss effects are observed.

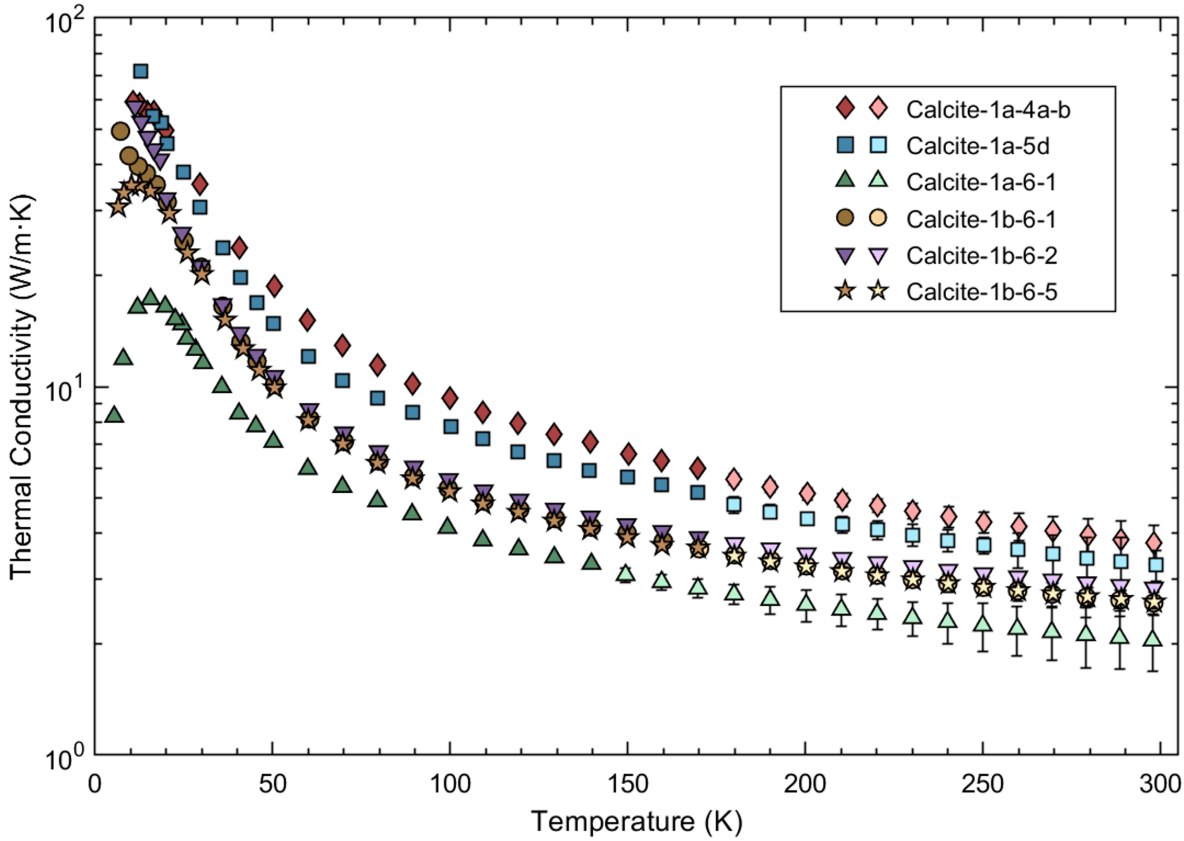

Figure 5.6: Thermal conductivity of the six calcite samples between 5 and 300 K. The $1/T$ trend lines are omitted for clarity. The transition from CFMS-measured data to corrected data is indicated by a change in colour (dark to light), which highlights the temperature range where radiative heat loss effects are observed.

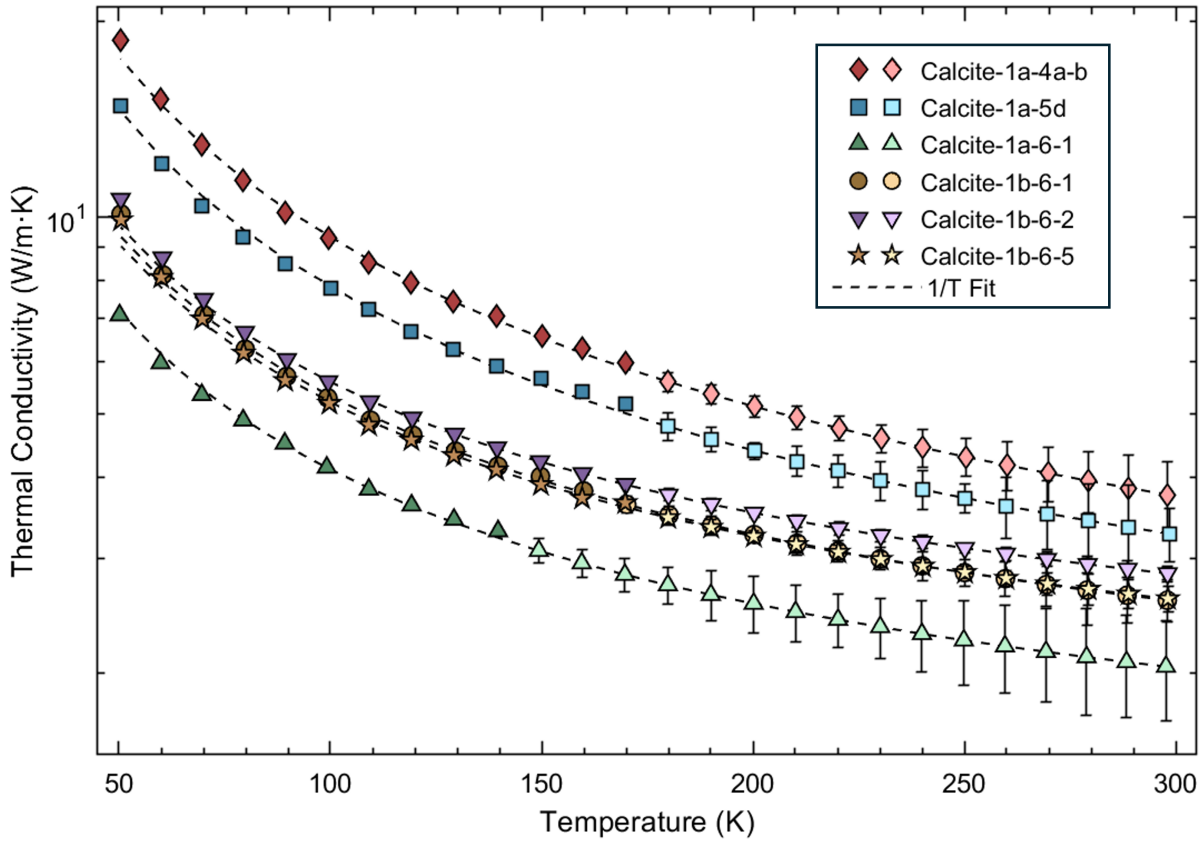

Figure 5.7: Thermal conductivity results of the six calcite samples between 50 and 300 K. The $1/T$ trend lines are included for reference. The transition from CFMS-measured data to corrected data is indicated by a change in colour (dark to light), which highlights the temperature range where radiative heat loss effects are observed.

The "b-samples" (1b-6-1, 1b-6-2, and 1b-6-5), which were cut parallel to each other, exhibit similar thermal conductivity behaviour (Figures 5.6 and 5.7). In contrast, the "a-samples", which were also cut parallel to each other but perpendicular to the "b samples", show more variation in their conductivity trends.

Below 50 K, only two samples show the characteristic thermal conductivity peak and turnover: 1a-6-1 and 1b-6-5. The peak occurs around 15 K for 1a-6-1 and 10 K for 1b-6-5. Similar to the behaviour observed in the Quartz-2 sample, most calcite samples unexpectedly deviate above the $1/T$ trend. Below 30 K, the thermal conductivities of samples 1a-4a-b, 1a-5d, and 1b-6-2 begin to converge. Although sample 1b-6-1 appears to approach a turnover, this behaviour could not be fully captured within the measurement range.

Radiative heat loss corrections are shown in Figure 5.8 ("a samples") and Figure 5.9 ("b samples"). Sample 1a-6-1 shows the most significant percent difference between the measured and corrected values (32%), while 1b-6-2 shows the smallest (8%). In all cases, the radiative component k_{rad} follows a T^3 trend (Figure 5.10). Lower R^2 values, such as that for 1b-6-5, reflect variability in the data rather than an actual deviation from the trend. The measured and corrected values at 300 K are provided in Table 5.3.

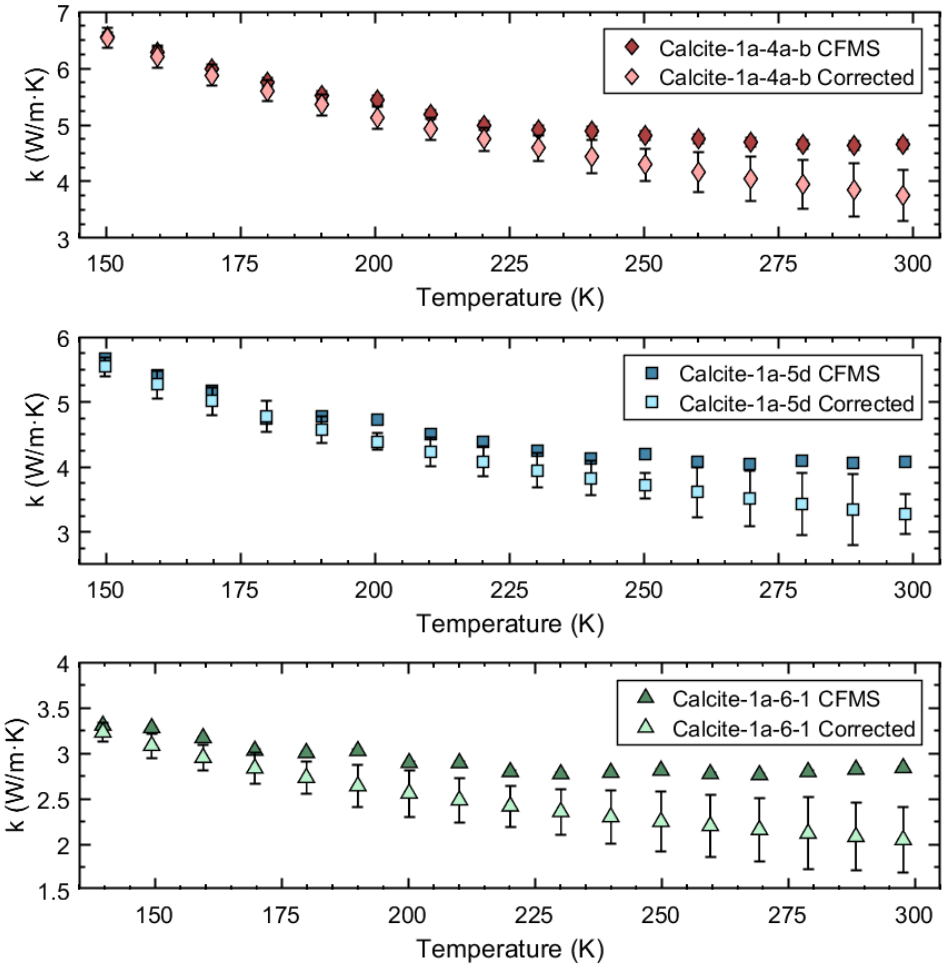

Figure 5.8: Comparison of CFMS-measured and corrected data for radiative heat loss for the calcite "a samples" (1a-4a-b, 1a-5d, 1a-6-1).

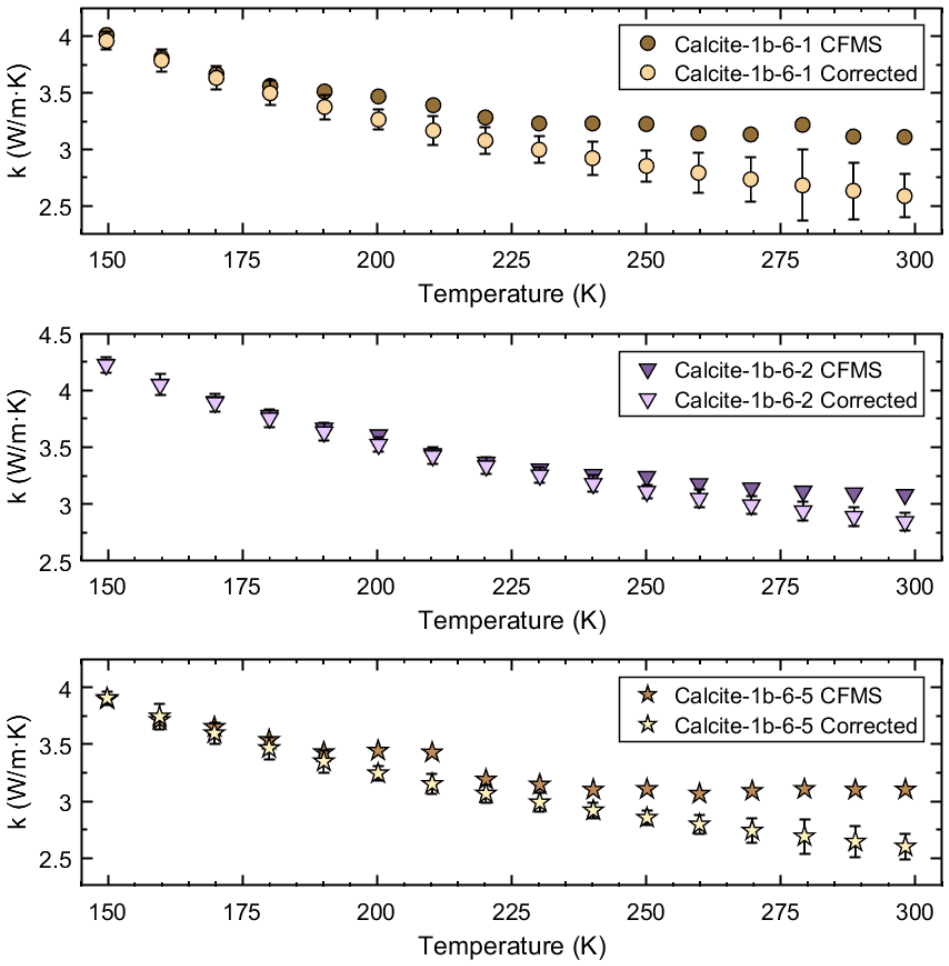

Figure 5.9: Comparison of CFMS-measured and corrected data for radiative heat loss for the calcite "b samples" (1b-6-1, 1b-6-2, 1b-6-5).

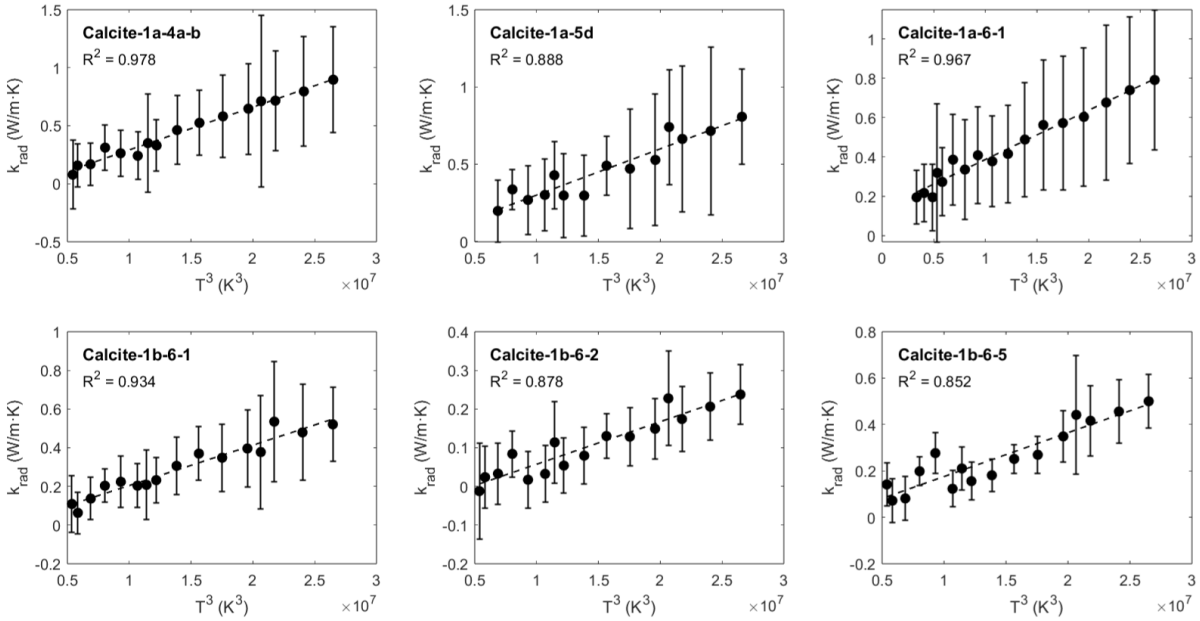

Figure 5.10: Radiation component (k_{rad}) as a function of T^3 for the six calcite samples.

Table 5.3: Calcite measured and corrected thermal conductivity (k) at 300 K.

Calcite Sample	**Measured *k*** ($Wm^{-1}K^{-1}$)	**Corrected *k*** ($Wm^{-1}K^{-1}$)
1a-4a-b	4.655 ± 0.003	3.8 ± 0.5
1a-5d	4.080 ± 0.002	3.3 ± 0.3
1a-6-1	2.84 ± 0.01	2.0 ± 0.4
1b-6-1	3.110 ± 0.003	2.6 ± 0.2
1b-6-2	3.083 ± 0.002	2.85 ± 0.08
1b-6-5	3.103 ± 0.002	2.6 ± 0.1

Albite

The thermal conductivity of the two albite samples (Albite-1 and Albite-2) between 5 and 300 K is shown in Figure 5.11. Albite-1, which was cut along the twin plane, follows the expected $1/T$ trend and deviates below it as the thermal conductivity approaches its peak (Figure 5.12). In contrast, Albite-2, which was cut across the twin plane, does not follow the $1/T$ trend; instead, a fourth-order $1/T$ polynomial was found to fit the data best. Notably,

the quality of these fits is slightly lower than observed in the calcite and quartz samples, with R^2 values of 0.975 for Albite-1 and 0.985 for Albite-2 (Table 5.2). Radiative effects appear around 100 K for both samples (Figure 5.13), which is lower than the temperatures at which radiation effects become apparent in calcite and quartz (T > 150). The radiation contribution (k_{rad}) shows a strong correlation with a T^3 trend, with R^2 values of 0.989 for Albite-1 and 0.995 for Albite-2 (Figure 5.14). The measured thermal conductivity at 300 K for Albite-1 is 2.17 ± 0.01 W m^{-1} K^{-1}, and the corrected value is 1.4 ± 0.5 W m^{-1} K^{-1}. For Albite-2, the measured and corrected values are for Albite-2 3.91 ± 0.03 W m^{-1} K^{-1} and 2.6 ± 1.3 W m^{-1} K^{-1}, respectively.

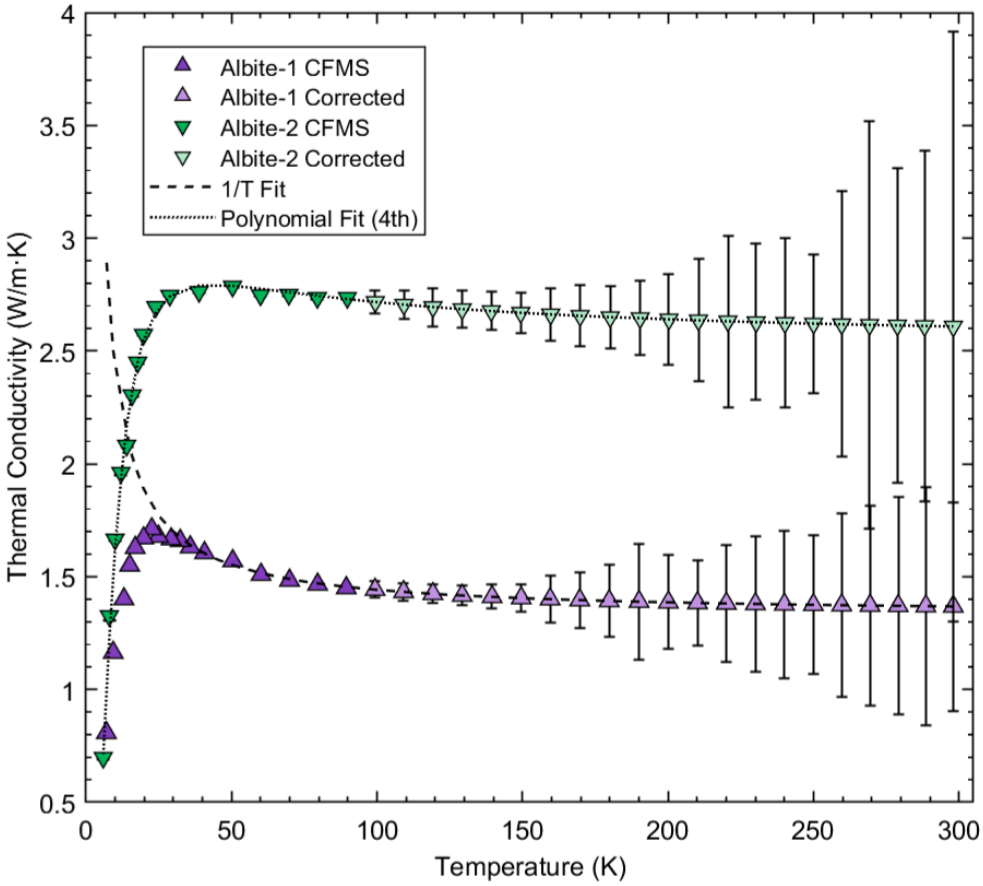

Figure 5.11: Thermal conductivity results of the two albite samples between 5 and 300 K: Albite-1, cut parallel to the (010) twin plane ($\perp$ b-axis), and Albite-2, cut perpendicular to the (010) twin plane ($\parallel$ b-axis). Trend lines are included for reference. The transition from CFMS-measured data to corrected data is indicated by a change in colour (dark to light), which highlights the temperature range where radiative heat loss effects are observed.

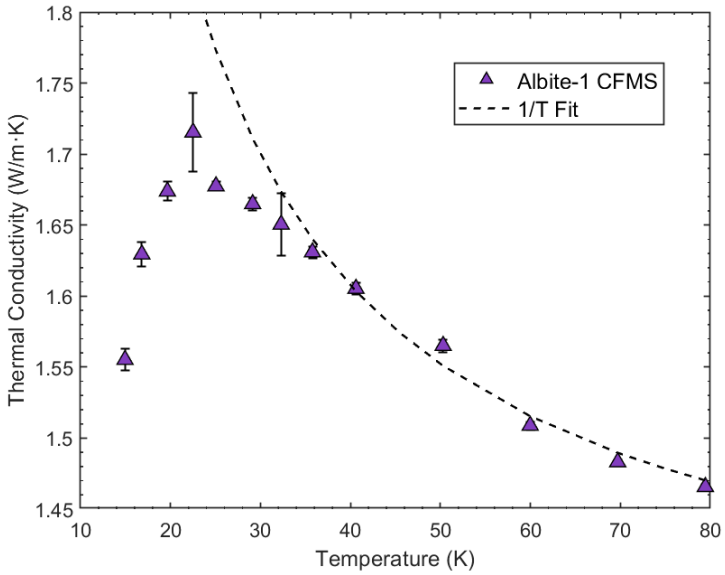

Figure 5.12: Thermal conductivity of Albite-1 between 10 and 80 K. The $1/T$ trend line is included for reference. The data shows a deviation below the trend starting at 40 K.

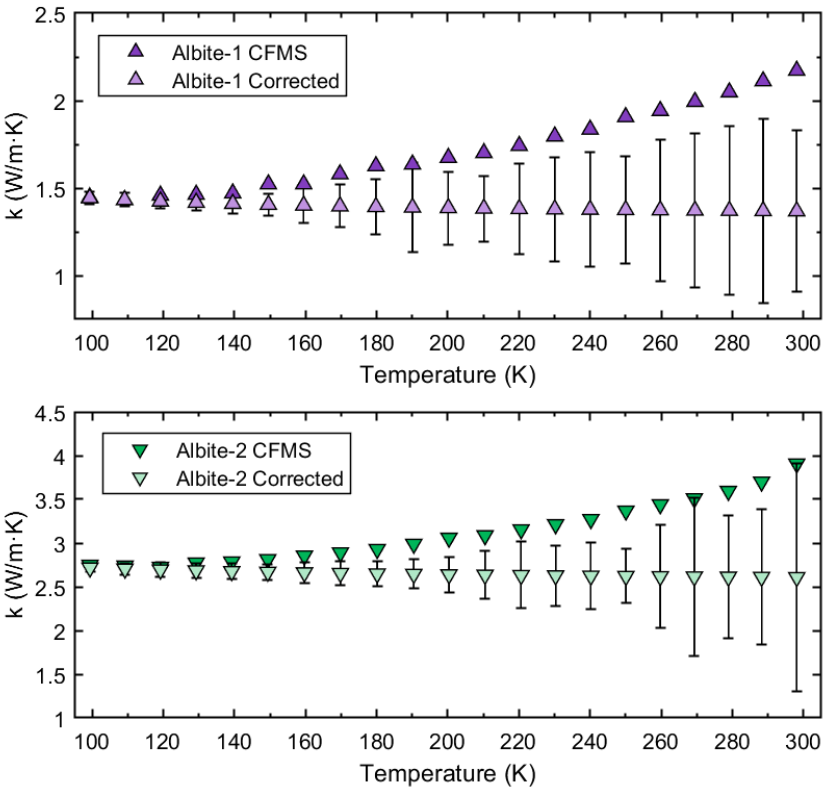

Figure 5.13: Comparison of CFMS-measured and corrected data for radiative heat loss for Albite-1 (top) and Albite-2 (bottom).

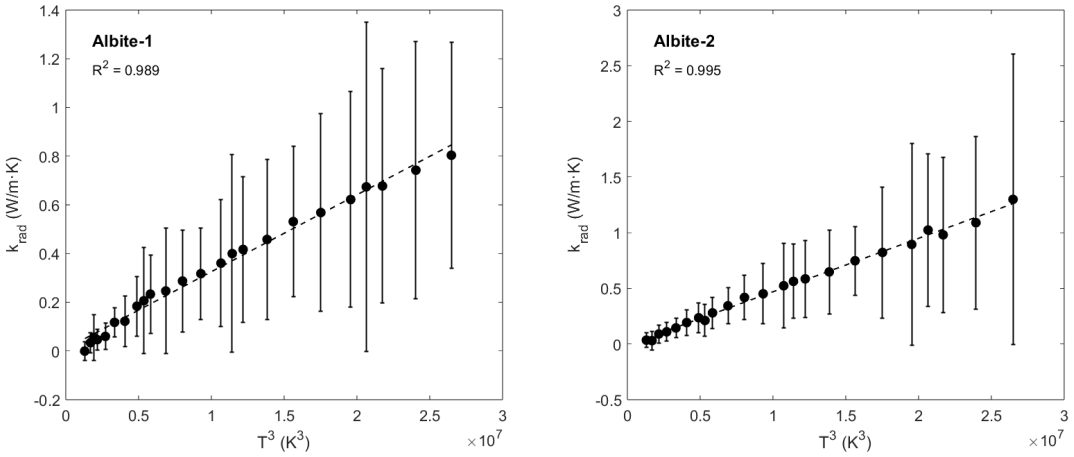

Figure 5.14: Radiation component (k_{rad}) vs. T^3 for Albite-1 (left) and Albite-2 (right).

Pyrite

The thermal conductivity of the three pyrite samples is shown in Figure 5.15. For comparison, data from Popov et al. (2013) for two pyrite samples (Popov-1 and Popov-2), collected between 50 and 300 K, are also included. Among the three samples, Pyrite-2 has the largest cross-sectional area (~ 9 mm^2) and exhibits the lowest overall thermal conductivity. At 300 K, Pyrite-1 (~ 4 mm^2) is 50.0 ± 0.3 W m^{-1} K^{-1}, Pyrite-2 is 38.9 ± 0.2 W m^{-1} K^{-1}, and Pyrite-3 (~ 2 mm^2) is 44.6 ± 0.2 W m^{-1} K^{-1}. Pyrite-1 is most similar to the data for Popov-2 from 50 to 200 K, after which it starts to align more with the Popov-1 sample. Below 70 K, Pyrite-1 and Pyrite-3 exhibit similar conductivity.

Although a $1/T$ fit was applied to the pyrite data, none of the samples followed this trend in a way that yielded physically reasonable extrapolations at 300 K. For instance, fitting the Pyrite-1 data between 60 and 170 K ($R^2 = 0.985$) resulted in an extrapolated thermal conductivity of approximately 16 W m^{-1} K^{-1} at 300 K—representing a 103% difference from the measured value of 50 W m^{-1} K^{-1}. Due to this discrepancy, the pyrite data could not be corrected for radiative effects using this method. This issue is explored further in the *Discussion* section.

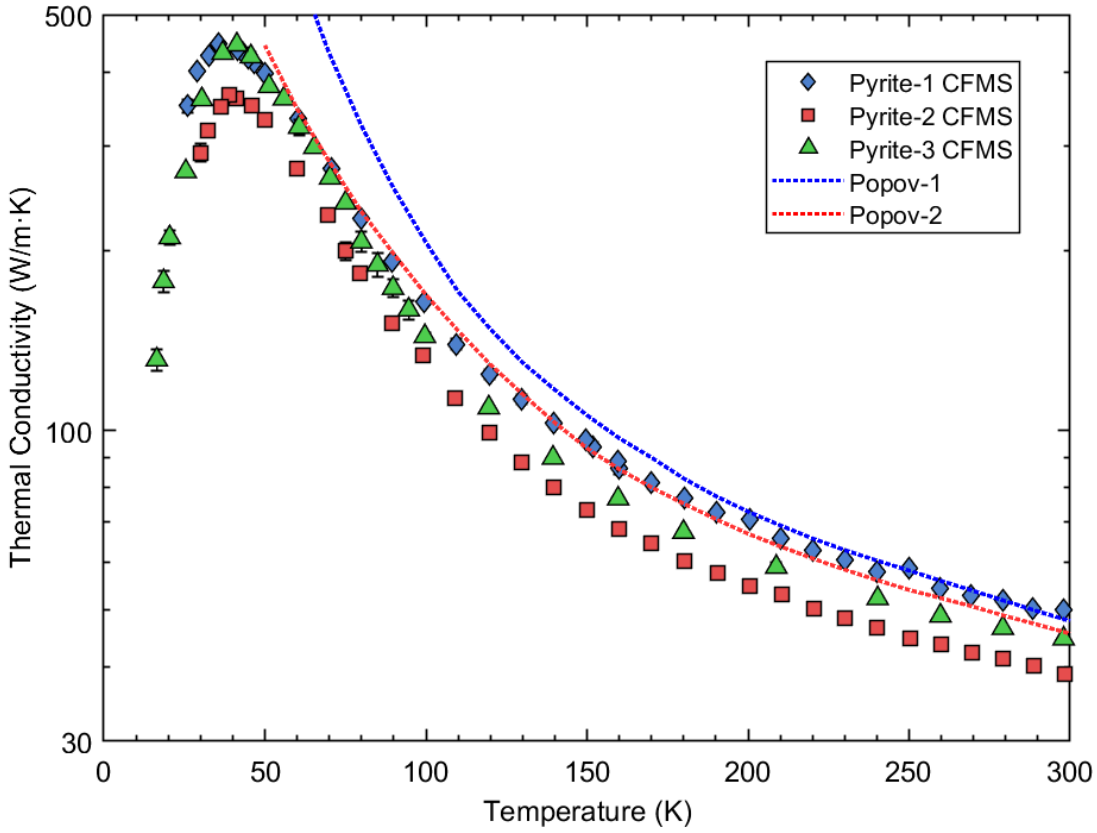

Figure 5.15: The thermal conductivity (5 to 300 K) of the three pyrite samples analyzed in this study, compared with data from the two samples reported by Popov et al. (2013). Most error bars are not shown as they are smaller than the symbol size.

5.2.2 Discussion

Quartz

The anisotropy of quartz is clearly observed in the thermal conductivity measurements of the two quartz samples (Figure 5.1). Quartz exhibits its highest thermal conductivity when heat flows parallel to the c-axis (Birch and Clark, 1940a; Birch, 1942; Clauser and Huenges, 1995), consistent with the results presented here. This reflects the atomic arrangement in the crystal structure, where atoms are packed less densely along the c-axis than along the a-axis, implying lower resistance to heat flow in the c-axis direction.

The peak thermal conductivity of quartz in the direction of the c-axis is expected to occur

at approximately 10 K (de Haas and Biermasz, 1935; Zeller and Pohl, 1971). However, measurements with the CFMS could only be completed down to 25 K, as data collected below this temperature were compromised by excessive temperature drift (>5 K), making them unsuitable for analysis. Considerable effort was made to extend measurements below 25 K, including manually adjusting the VTI flow rate to increase cooling power and spending several weeks optimizing the configuration settings (Section 3.2.3).

The thermal conductivity of the two quartz samples at 300 K compares well with those reported in the literature (Table 5.4). On average, the reported thermal conductivity of quartz is 11.7 ± 1.3 W m^{-1} K^{-1} for heat flow parallel to the c-axis (Kaye and Higgins, 1926; Birch and Clark, 1940a; Kanamori et al., 1968; Dreyer, 1974), and 6.37 ± 0.18 W m^{-1} K^{-1} perpendicular to the c-axis (Kaye and Higgins, 1926; Birch and Clark, 1940a; Ratcliffe, 1959). At 300 K, the corrected thermal conductivity of Quartz-1 is 12.48 ± 0.31 W m^{-1} K^{-1}, and Quartz-2 is 6.65 ± 0.80 W m^{-1} K^{-1}. The Quartz-1 average falls within the standard deviation of the reported mean for the parallel direction, whereas the Quartz-2 value does not for the perpendicular direction. However, Quartz-2 is in agreement with the maximum value reported for that orientation (6.62 W m^{-1} K^{-1}, Table 5.4).

Above 70 K, both datasets follow a $1/T$ trend. Thermal radiation is less apparent in the Quartz-1 data than in Quartz-2, with onset temperatures of 270 K and 150 K, respectively (Figure 5.2). The lower R^2 value for Quartz-1 (0.838) in evaluating the radiative component (k_{rad}) reflects the limited number of corrected data points and greater measurement variability, rather than a deviation from linearity (Figure 5.3). This variability is further influenced by fluctuations in the Quartz-1 thermal conductivity data between 200 and 300 K (Figure 5.2). In contrast, Quartz-2 displays a clear linear relationship with T^3, consistent with radiative heat loss. The difference in the radiation effects between the two samples may result from the anisotropic nature of quartz emissivity (Chapter 7); emissivity is reported to be higher perpendicular to the c-axis than parallel to it (Wenrich and Christensen, 1996). Alternatively, the variability above 200 K may be masking some of the radiation effects.

Table 5.4: Reported thermal conductivity (k) values for quartz at 300 K.

k (W m^{-1} K^{-1})	Source
12.48 ± 0.31 ($\parallel c$)	Quartz-1 (This study)
6.65 ± 0.80 ($\perp c$)	Quartz-2 (This study)
11.3 ($\parallel c$)	Dreyer (1974) (via Clauser and Huenges (1995))
6.50 ($\perp c$)	Dreyer (1974) (via Clauser and Huenges (1995))
12.5 ($\parallel c$)	Clark (1966) ($\sim$30°C)
6.62 ($\perp c$)	Clark (1966) ($\sim$30°C)
10.4 ($\parallel c$)	Birch and Clark (1940a) (Interpolation to 25°C)
6.24 ($\perp c$)	Birch and Clark (1940a) (Interpolation to 25°C)
10.7 ($\parallel c$)	Beck et al. (1978) (Interpolation to 25°C)
6.09 ($\perp c$)	Beck et al. (1978) (Interpolation to 25°C)
11.1 ($\parallel c$)	Horai and Simmons (1969)
6.31 ($\perp c$)	Horai and Simmons (1969)
13.9 ($\parallel c$)	Kanamori et al. (1968)
6.49 ($\perp c$)	Kanamori et al. (1968)
6.32 ($\perp c$)	Ratcliffe (1959)

At temperatures below 70 K, the two quartz samples begin to follow different trends. The thermal conductivity of Quartz-1 continues to follow the expected $1/T$ relationship, suggesting that impurity scattering is not significant between 30 and 300 K. Phonon-impurity interactions result in a constant phonon mean free path, which would cause the thermal conductivity to deviate below the $1/T$ trend at low temperatures (Figures 2.4). No such deviation is observed in the Quartz-1 data.

Conversely, the low-temperature behaviour of Quartz-2 deviates from expectations based on kinetic theory. Below 80 K, its thermal conductivity begins to rise above the $1/T$ trend line, eventually intersecting with the Quartz-1 data (Figure 5.1). While both quartz samples exhibit visible imperfections, such as small bubbles and wisps, these types of impurities would typically reduce thermal conductivity by scattering phonons, causing the data to fall below the $1/T$ trend rather than above it. Therefore, the upward deviation observed in Quartz-2 is not consistent with established physical models of thermal transport in crystalline

solids at low temperatures. Possible reasons for this behaviour are explored in the following paragraphs.

Measurements below 30 K are particularly challenging with the CFMS due to two main limitations: temperature drift and thermocouple sensitivity. Temperature drift refers to changes in the heat sink temperature during a measurement. While the heat sink is thermalized to the sample environment prior to a measurement, insufficient cooling power can lead to heat accumulation, causing the heat sink temperature to rise over time. This reduces data reliability, as measurements are then performed over a temperature range that deviates from the intended set point, which can alter a material's thermal response. To ensure accuracy at low temperatures, temperature drifts exceeding an empirical limit of 2 K are flagged during data analysis. All low-temperature Quartz-2 data presented here fall within this limit.

Another contributing factor is that the measured temperature difference (ΔT) across the sample may be too small at low temperatures due to the high thermal conductivity of quartz, which is approximately 18 times greater at 25 K than at 300 K for Quartz-2. As thermal conductivity increases, heat flows more efficiently through the sample, resulting in a smaller ΔT for a given applied power. Although increasing the power could compensate for this, doing so at low temperatures risks inducing temperature drift or disrupting thermal equilibrium. As a result, the measured ΔT may fall below the resolution limit of the thermocouple. If ΔT is underestimated—due to low signal-to-noise ratio, calibration issues, or alternative heat paths (e.g., through thermocouple wires)—the calculated thermal conductivity will appear artificially high.

To overcome power limitations at low temperatures, sample geometry can be optimized to increase the measured ΔT. Thermal conductance depends on the cross-sectional area and length between thermocouple tabs ($G = (kA)/L$); reducing the area or increasing L lowers the conductance, thereby increasing ΔT for a given power input ($\Delta T = P/G$). Although Quartz-2 has a smaller cross-sectional area and longer thermocouple spacing than Quartz-

1 (Table 5.1), only Quartz-2 exhibits anomalous behaviour. Both samples have similar conductance values at low temperatures, indicating that geometry alone cannot account for the discrepancy. However, the combination of sample dimensions and limited thermocouple sensitivity may explain why thermal conductivity data could not be acquired below 25 K for either quartz sample, as the ΔT may simply be too small to resolve.

Calcite

The thermal conductivity measurements reported here represent the first low-temperature data for calcite. The anisotropic nature of calcite's thermal conductivity is evident in the results. Table 5.3 presents the 300 K thermal conductivity measurements for all samples, compared with literature values for calcite oriented along known crystallographic directions. Samples 1a-4a-b and 1a-5d are most consistent with reported values of calcite cut perpendicular to the c-axis (Birch and Clark, 1940a; Clark, 1966). All other samples exhibit lower thermal conductivity than previously reported, which is not unexpected given that their orientations relative to the crystallographic axes are unknown. However, the thermal conductivity data from these samples contribute new data that further characterizes the directional variability of heat transport in calcite.

Above 50 K, all samples follow the expected $1/T$ trend consistent with phonon-phonon scattering (Figure 5.7). The thermal conductivity of the three "b samples" is consistent, although sample 1b-6-2 shows a slight increase. This similarity is expected as these samples were cut parallel to each other. The elevated conductivity in 1b-6-2 is likely due to a slight offset introduced during sample preparation (e.g., cutting or polishing).

In contrast, the "a samples", which were cut perpendicular to the "b samples", display three distinct trends above 50 K, despite also being cut parallel to each other. Specifically, sample 1a-4a-b exhibits the highest thermal conductivity among the six calcite samples, followed by 1a-5d, while 1a-6-1 has the lowest overall thermal conductivity. This variation is likely due to differences in sample preparation. The "a samples" were cut from three

separate pieces of the bulk calcite sample, whereas the "b samples" were cut from a single piece (Figure 4.19). These results highlight the sensitivity of calcite's thermal conductivity to even slight deviations in the direction of heat flow.

All samples show evidence of radiative heat loss (Figures 5.8 to 5.10), which was corrected by extrapolating a linear $1/T$ fit to the data (Table 5.2). Notably, radiation effects become apparent at a lower temperature in sample 1a-6-1 (150 K) than the other samples, which show effects beginning around 175 K. A discrepancy is also observed in sample 1b-6-2, which shows a smaller overall radiation effect compared to the other "b" samples. As with the quartz samples, these differences are likely due to variations in emissivity associated with the direction of heat flow (Lane, 1999).

Below 50 K, all samples except 1a-6-1 deviate above the expected $1/T$ trend (Figures 5.4 and 5.5). As discussed previously for Quartz-2, this behaviour is attributed to measurement limitations at low temperatures. Sample 1a-6-1 appears to follow the $1/T$ trend down to the peak at approximately 15 K. This is unusual, as deviation below the trend is typically expected as the sample approaches its maximum thermal conductivity due to phonon-impurity interactions. It is possible that such deviation exists, but is too subtle to resolve with the current data set. Sample 1b-6-5 also displays a peak near 10 K; however, the validity of this turnover is uncertain, as the upward drift from the $1/T$ line suggests that the true peak may occur at lower temperatures.

Albite

The thermal conductivity measurements of albite presented in this study are the first to be conducted with respect to crystallographic orientation, as well as the first to extend to low temperatures. Previously reported values for albite correspond to mineral aggregates at 300 K (Birch and Clark, 1940a; Sass, 1965; Horai and Simmons, 1969; Horai, 1971; Dreyer, 1974), which are consistent with the results obtained in this study (Table 5.6).

Two distinct thermal conductivity trends are observed in the albite samples. Albite-1,

Table 5.5: Reported thermal conductivity (k) values for calcite at 300 K.

k (W/m·K)	Source
3.8 ± 0.5	1a-4a-b (This study)
3.3 ± 0.3	1a-5d (This study)
2.0 ± 0.4	1a-6-1 (This study)
2.6 ± 0.2	1b-6-1 (This study)
2.85 ± 0.08	1b-6-2 (This study)
2.6 ± 0.1	1b-6-5 (This study)
5 ($\parallel c$)	Dreyer (1974) (via Clauser and Huenges (1995))
4.2 ($\perp c$)	Dreyer (1974) (via Clauser and Huenges (1995))
4.18 ($\parallel c$)	Clark (1966) ($\sim$30°C)
3.52 ($\perp c$)	Clark (1966) ($\sim$30°C)
3.70 ($\parallel c$)	Birch and Clark (1940a) (Interpolation to 25°C)
3.24 ($\perp c$)	Birch and Clark (1940a) (Interpolation to 25°C)
3.59 (aggregate)	Horai (1971)

cut parallel to the twin plane ($\perp$ b-axis), exhibits an overall lower thermal conductivity and follows a clear $1/T$ dependence up to $\sim$40 K, after which it begins to deviate, likely due to increased phonon scattering from boundaries and impurities. The fit to Albite-1 also yields a slightly lower R^2 value (0.977) compared to the calcite and quartz fits (both > 0.99), possibly reflecting greater variability in the data or the influence of additional scattering mechanisms not accounted for in the simple $1/T$ model. In contrast, Albite-2, cut across the twin plane ($\parallel$ b-axis), does not display the characteristic low-temperature conductivity peak, nor does it follow a $1/T$ trend. Instead, its behaviour closely resembles the thermal conductivity of meteorites reported by Opeil et al. (2010), Opeil et al. (2012), and Opeil et al. (2020), where phonon-boundary scattering dominates due to pore spaces and grain boundaries. In those studies, a quadratic fit was applied to k vs. T data, whereas Albite-2 is represented by a fourth-degree polynomial in k vs. $1/T$, similarly capturing the absence of a low-temperature peak. Considering that the albite samples in this study are single crystals, grain boundaries and porosity are not expected to play a significant role. The thermal conductivity trend in Albite-2 is likely attributed to enhanced phonon-boundary scattering along twin boundaries

within the crystal structure (Vandersande and Pohl, 1982; Liu et al., 2017; Liu et al., 2022; Peri et al., 2022).

Interestingly, despite twin boundaries being known to reduce thermal conductivity (Liu et al., 2017; Liu et al., 2022; Peri et al., 2022), Albite-1 exhibits a lower conductivity than Albite-2. This apparent contradiction may result from a slight misalignment during sample preparation. Specifically, Albite-1 may have been cut at an oblique angle relative to the twin plane, increasing the number of effective boundary interactions along the direction of heat flow. This could lead to enhanced phonon scattering and a lower overall thermal conductivity, potentially also contributing to the lower R^2 value of the $1/T$ fit.

Table 5.6: Reported thermal conductivity (k) values for albite at 300 K.

k (W/m·K)	Source
1.4 ± 0.5	Albite-1 (This Study)
2.6 ± 1.3	Albite-2 (This Study)
2.32	Horai and Simmons (1969) (Ab99An1*)
2.35	Horai and Simmons (1969) (Ab96An4*)
1.94	Horai and Simmons (1969) (Ab94An6*)
1.97	Horai (1971) (Ab92An8*)
2.14	Horai (1971) (Experimentally derived after Sass et al. (1971))
2.0 ± 0.1	Dreyer (1974) (via Clauser and Huenges (1995))
2.34	Sass (1965)
2.03	Birch and Clark (1940a) (Interpolation to 25°C)

* Albite (Ab) is part of a solid solution series with anorthite (An); composition is given by relative Ab–An content.

Pyrite

The thermal conductivity of the three pyrite samples at 300 K compares well with literature values (Table 5.7). However, radiative heat loss effects are not apparent in the thermal conductivity data at temperatures above 100 K. This conclusion is based on the inability to fit the data to a $1/T$ trend to obtain a physically meaningful extrapolation. The reasoning behind this is discussed in the following paragraphs.

Although pyrite is an iron sulphide and therefore classified as a semiconductor, its thermal conductivity is dominated by lattice vibrations. While both electrons and phonons typically contribute to heat transfer in semiconductors, electrical conductivity measurements by others indicate that the electronic contribution in pyrite is negligible compared to the lattice component (Popov et al., 2013; Zuñiga-Puelles et al., 2019). As a result, thermal transport in pyrite is primarily governed by phonon processes, such as Umklapp scattering, at high temperatures.

In terms of temperature dependence, Popov et al. (2013) observed that between 50 and 150 K, the thermal conductivity of one of their pyrite samples followed a trend close to $1/T^{-2}$, while at 300 K, it aligned with the typical $1/T$ trend driven by phonon-phonon scattering. Similarly, Zuñiga-Puelles et al. (2019) measured the thermal conductivity of a natural pyrite crystal between 2 and 600 K and reported a $1/T$ dependence from 300 to 600 K. These two studies clearly indicate that radiative heat transfer does not contribute significantly to pyrite's thermal conductivity at temperatures below 600 K.

Although parameters such as sample size and emissivity can influence thermal radiation, they do not fully explain the absence of observable radiative contributions in pyrite, especially considering that emissivity can vary with physical and experimental conditions (see Chapter 7). A more likely explanation lies in the complexity of pyrite's crystal structure. Pyrite has 12 atoms per unit cell, resulting in 33 optical modes of vibration (Verble and Wallis, 1969). Its structure includes both ionic Fe–S bonds and covalent S–S bonds. Vibrations primarily occur between sulphur atoms, with iron atoms remaining relatively stationary. However, these S–S vibrations may not induce sufficient dipole moment changes to activate infrared radiation modes, which could explain the minimal radiative contribution to thermal conductivity (Verble and Wallis, 1969).

The differences in thermal conductivity between the three pyrite samples (Figure 5.15) can be attributed to boundary and defect scattering. Popov et al. (2013) observed that their two samples diverged at low temperatures, attributing the difference to point defects,

with the Popov-2 sample considered less pure based on its thermal conductivity behaviour. Although the samples in this study were cut from the same pyrite cube, variations in their low-temperature thermal conductivity trends suggest differences in purity.

In purer materials, boundary scattering dominates at low temperatures, and the phonon mean free path becomes constant, limited by the sample dimensions. As a result, smaller samples typically exhibit lower thermal conductivity peaks (Figure 2.6). Based on this reasoning, and considering that all pyrite samples were cut from the same crystal, Pyrite-2 would be expected to have the highest thermal conductivity maximum because it has the largest diameter. Pyrite-3, by contrast, would be expected to show the lowest. However, Pyrite-2 exhibits lower thermal conductivity overall. This may be due to its larger volume incorporating more trace minerals, which can introduce grain boundaries that scatter phonons at low temperatures and reduce the overall thermal conductivity at higher temperatures, given that the trace minerals likely conduct heat less efficiently. Above 70 K, Pyrite-1 and Pyrite-3 follow different trends, with Pyrite-3 remaining lower, but below 70 K, their curves converge. This suggests that Pyrite-3 may have been cut from a region with fewer impurities or inclusions, allowing it to reach a thermal conductivity maximum similar to Pyrite-1. At 300 K, Pyrite-1 most closely matches the Popov-1 sample, but at lower temperatures it resembles Popov-2, consistent with increased phonon–impurity scattering.

The thermal conductivity peak in the pyrite samples occurs at 40 K, while Zuñiga-Puelles et al. (2019) observed the peak at 75 K. This lower peak temperature is consistent with increased phonon scattering due to impurities, which reduce the phonon mean free path and cause the material to reach its maximum thermal conductivity at a lower temperature. Therefore, this implies that the pyrite samples in this study are less pure than the one measured by Zuñiga-Puelles et al. (2019).

At low temperatures, thermal conductivity typically follows a T^3 dependence. However, the data for these pyrite samples do not show this behaviour below the peak, likely due to the absence of measurements below 10 K, where the T^3 trend is most clearly observed. Instead,

the data reflect the expected deviation from T^3 as the heat capacity begins to diverge from the Debye model at higher temperatures (Figure 2.5).

Overall, the thermal conductivity results for the pyrite samples behave as expected. The absence of observable radiation effects between 100 and 300 K suggests that radiation heat loss from the thermal assemblies and surrounding epoxy is negligible, at least in the case of pyrite.

Table 5.7: Reported thermal conductivity (k) values for pyrite at 300 K.

k (W/m·K)	Source
50.0 ± 0.3	Pyrite-1 (This Study)
38.9 ± 0.2	Pyrite-2 (This Study)
44.6 ± 0.2	Pyrite-2 (This Study)
45.5 ± 2.3	Popov et al. (2013) (Sample 1)
47.8 ± 2.4	Popov et al. (2013) (Sample 2)
37.9	Dreyer (1974) (via Clauser and Huenges (1995))
19.2	Horai and Simmons (1969)
23 ± 2	Diment and Pratt (1988) (35°C; 34 bar)

5.2.3 Conclusion

The thermal conductivity results of the single-crystal minerals provide insight into both the thermal behaviour of geological materials and operational limitations of the CFMS. The results presented in this study show that measurements above 50 K are reliable across all samples. However, below 50 K, challenges arise due to temperature drift and reduced thermocouple sensitivity. These issues primarily affect crystalline materials that exhibit a significant increase in thermal conductivity at low temperatures, such as quartz and calcite. In contrast, measurements down to 5 K are possible for minerals like albite, where the thermal conductivity remains low across the temperature range. Similarly, for materials such as pyrite, where the conductivity peak occurs above 30 K, reliable data can still be acquired below the peak, as the thermal conductivity begins to decrease with decreasing temperature. To overcome limitations at low temperatures, a heat pulse method should

be employed to minimize overheating and improve resolution in high-conductivity materials (Tritt and Weston, 2006).

5.3 Preliminary Obsidian Data

Data collected for obsidian offers insight into the behaviour of thermal conductivity in amorphous solids. The averaged thermal conductivity results for obsidian between 5 and 300 K are shown in Figure 5.16. These data have not been corrected for radiative heat transfer. All individual measurements of obsidian that passed the quality check process are included in Appendix D.

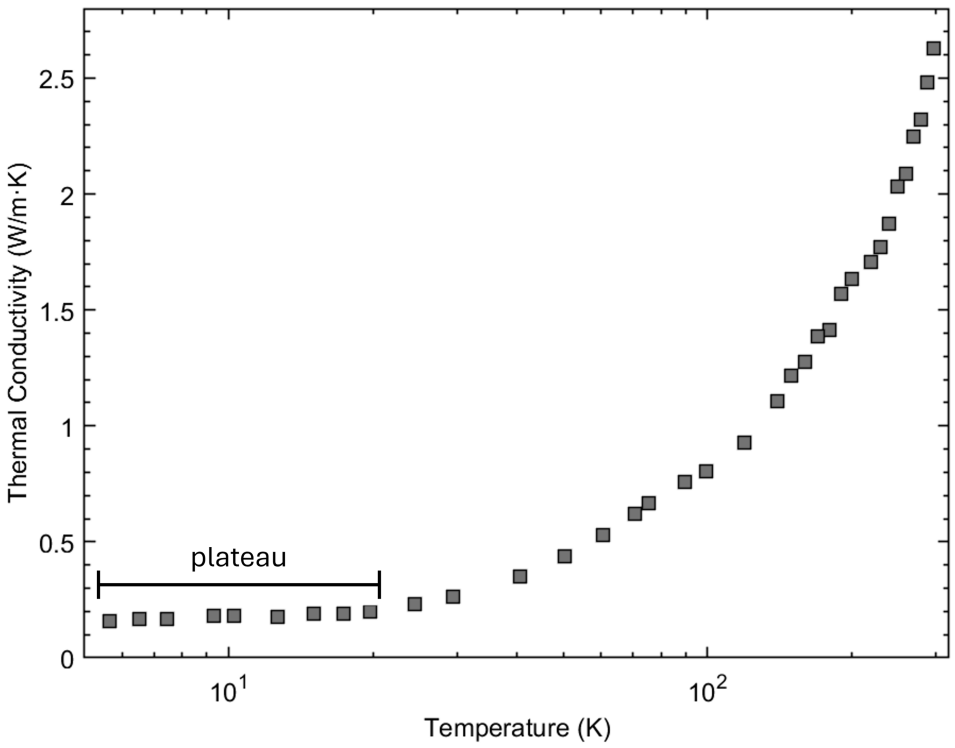

Figure 5.16: Thermal conductivity results for obsidian between 5 and 300 K, uncorrected for radiative heat loss. A plateau between 5 and 20 K is observed, characteristic of amorphous materials. Results represent averaged data. Error bars are smaller than the data markers.

A plateau in the thermal conductivity data is seen between 5 and 20 K, which is characteristic of amorphous materials. As discussed in Chapter 2, the plateau may represent the transition zone between propagons and diffusons. Above the plateau, where diffusons are

associated with higher frequencies (Allen et al., 1999), the thermal conductivity increases with temperature. Unlike crystalline samples, which show a $1/T$ dependence at higher temperatures, amorphous solids lack a well-defined temperature dependence above the plateau due to their disordered atomic structure. Instead, the thermal conductivity closely follows the minimum thermal conductivity (Section 2.2.4), typically exhibiting a slow increase or plateau with increasing temperature (Cahill and Pohl, 1988; Cahill and Pohl, 1989).

The CFMS-measured average thermal conductivity at 300 K for obsidian is 2.627 ± 0.004 W m^{-1} K^{-1}, and comparably, the average of the reported literature values is 1.42 ± 0.06 W m^{-1} K^{-1} (Birch and Clark, 1940a; Čermák and Rybach, 1982). The difference is highly suggestive that the CFMS-measured data is affected by radiative heat loss. However, without a specific temperature trend to fit and extrapolate data, correcting the thermal conductivity for obsidian becomes challenging.

The Stefan–Boltzmann law adapted for the CFMS (Equation 3.9), which accounts for radiation from both the sample and heater assemblies, could be used to estimate the radiative heat loss in obsidian. However, this approach is not ideal, as it requires values for emissivity and surface area of both the sample and assemblies, which are particularly difficult to determine for the heater assemblies (see Chapter 3.3.3).

Alternatively, the optical properties of obsidian could be used to isolate the radiative component:

$$k_{\text{rad}} = \frac{16 n^2 \sigma T^3}{3e} \tag{5.1}$$

where n is the refractive index, σ is the Stefan–Boltzmann constant, and e is the mean extinction coefficient (Chapter 3.3.3). However, applying this approach would require detailed optical analysis to determine the values of n and e for obsidian (e.g., Stein et al., 1981). Additionally, it does not account for radiative heat loss associated with the thermal assemblies.

Given that the trend fitting proved successful for the single-crystal minerals, fitting of the obsidian data above the plateau was attempted despite no reported trend for amorphous

materials. A best fit of the data (40 to 120 K) was found to be logarithmic, $k(T) = a \cdot log(T) + b$, with an R^2 value of 0.985 ($a = 0.55 \pm 0.02$, $b = -1.71 \pm 0.08$).

Figure 5.17 shows the corrected thermal conductivity data. The effect of radiative heat loss in obsidian is apparent between 140 and 300 K (Figure 5.18). At 300 K, the corrected value is 1.4 ± 0.7 W m^{-1} K^{-1}, which is consistent with the literature average (1.42 ± 0.06 W m^{-1} K^{-1}).

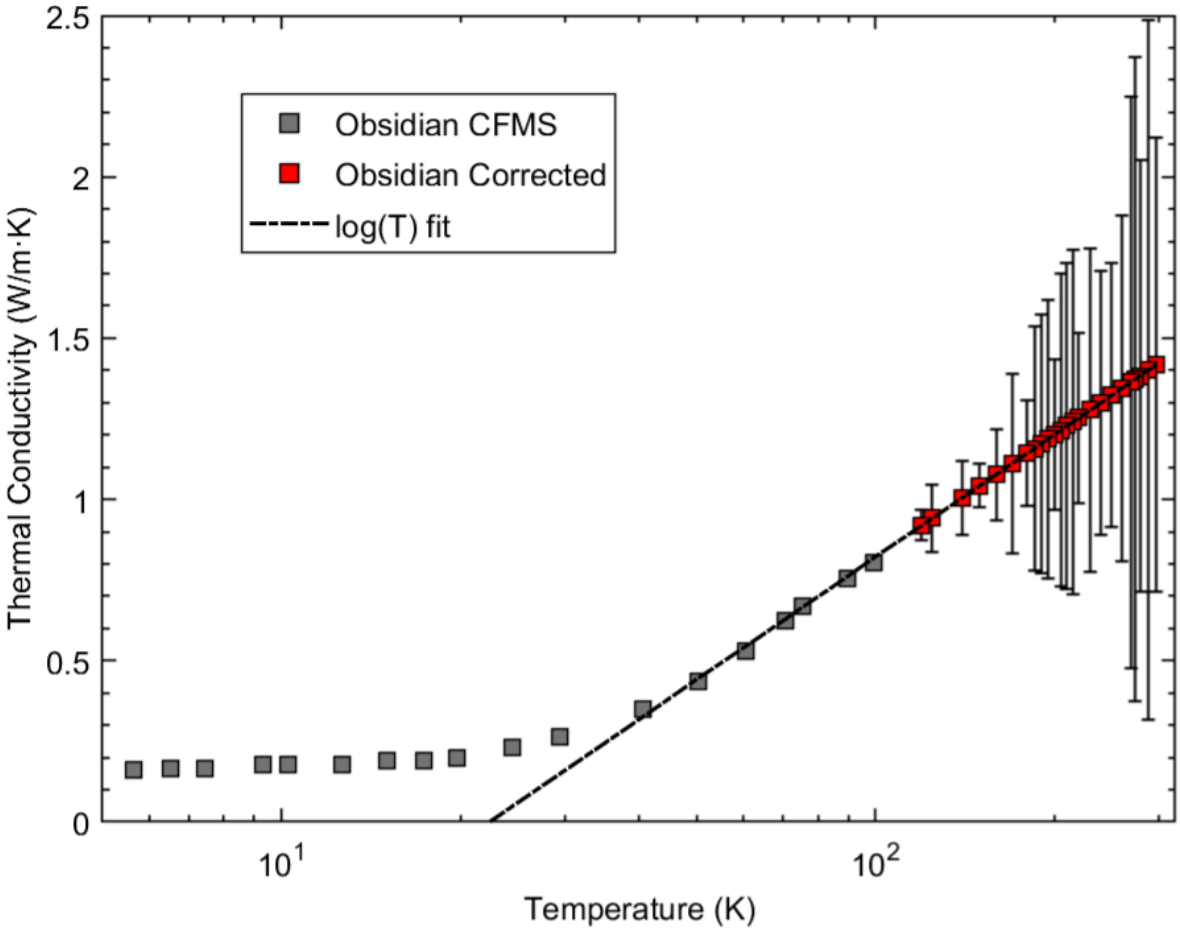

Figure 5.17: Corrected thermal conductivity of obsidian. Dark grey squares indicate data unaffected by thermal radiation (Obsidian CFMS), while red squares show data corrected for radiative heat loss (Obsidian Corrected). A dashed line represents the empirical fit of $a \cdot log(T) + b$, which closely matches the CFMS data above the plateau region (40 to 120 K).

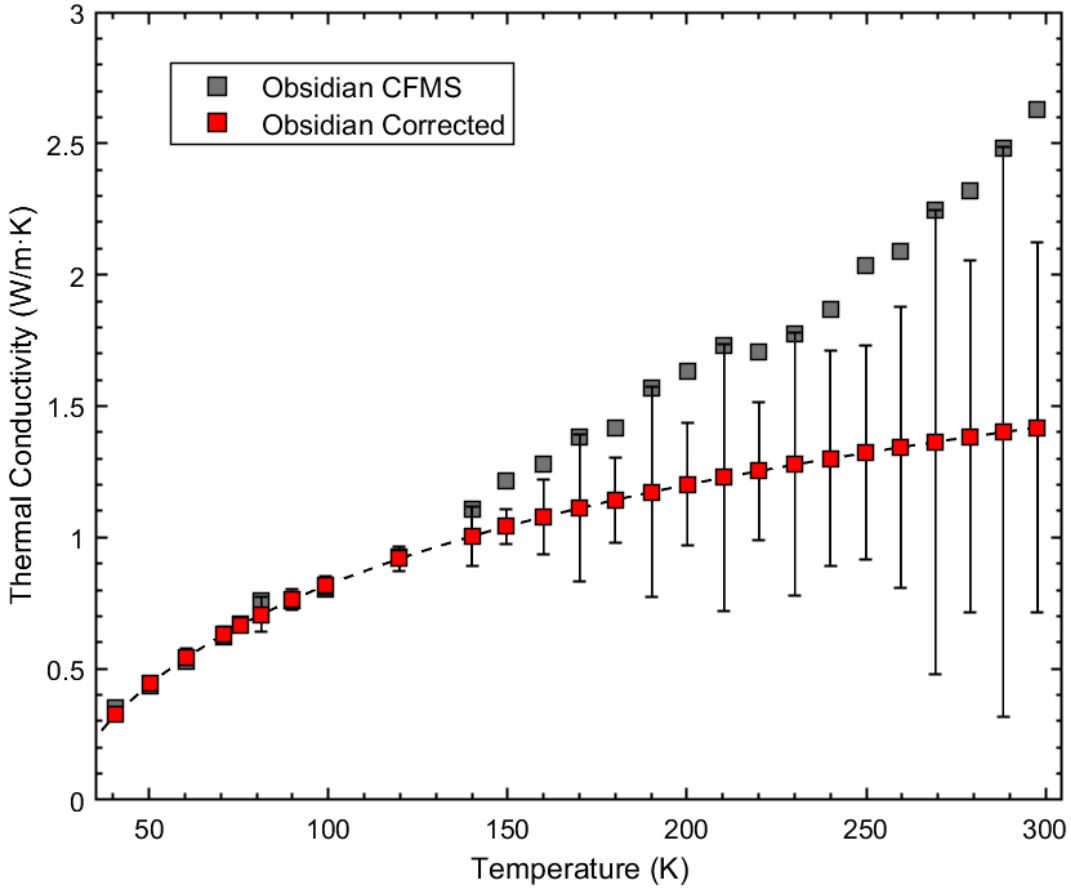

Figure 5.18: Comparison between the CFMS-measured (grey squares) and corrected (red squares) thermal conductivity for obsidian. The data corrected for thermal radiation effects was extrapolated from the log(T) fit.

The fact that the corrected data at 300 K matches the reported average may be a coincidence. As mentioned above, there is no well-defined temperature dependence for the thermal conductivity of amorphous material. However, a plot of k_{rad} vs. T^3 confirms that the difference between measured and corrected thermal conductivity supports radiative heat loss effects (Figure 5.19). Therefore, a $a \cdot log(T) + b$ dependence appears to exist for obsidian above the plateau, or at least for the sample used in this study. Further investigation of this trend is needed to confirm these results (see Future Work).

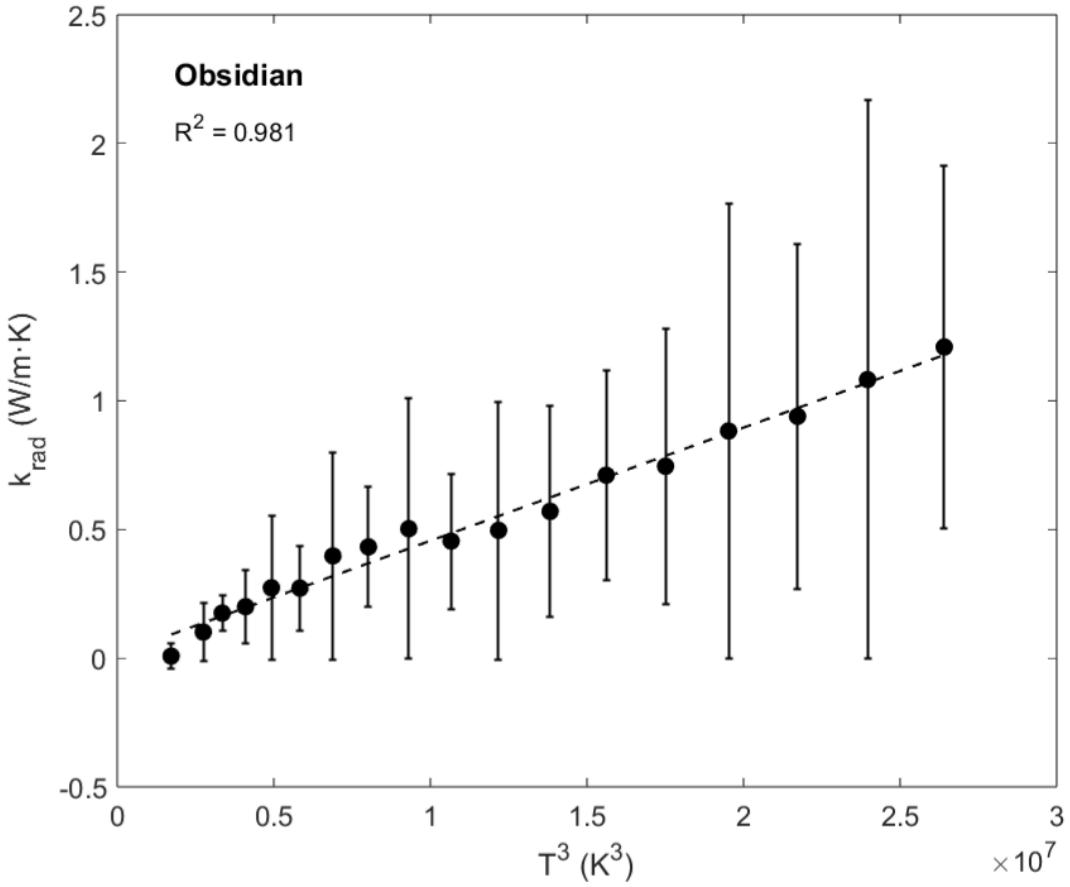

Figure 5.19: Plot of k_{rad} vs. T^3 for obsidian. The strong linear correlation ($R^2 = 0.981$) indicates that measurements above 120 K were affected by radiative heat loss.

5.4 Summary Table

Table 5.8 provides a summary of the results presented in this chapter for the single-crystal minerals and obsidian.

Table 5.8: Summary of sample properties and thermal conductivity results for single-crystal minerals and obsidian.

Sample	**Crystal System**	**Anisotropy**	**Dimensions (mm)** $w \times h \times l$	**A (mm^2)**	**L (mm)**	**Measured k** *@ 300 K*	**Corrected k** *@ 300 K*	**Literature Average**
Quartz-1 ($\parallel c$)	Trigonal	Anisotropic	2.65 × 2.64 × 20.3	6.971 ± 0.006	11.429 ± 0.007	13.10 ± 0.01	12.48 ± 0.31	11.7 ± 1.3 ($\parallel c$)[a]
Quartz-2 ($\perp c$)			2.59 × 2.60 × 20.0	6.737 ± 0.007	12.127 ± 0.013	8.23 ± 0.01	6.65 ± 0.80	6.37 ± 0.18 ($\perp c$)[b]
Calcite-1a-4a-b	Trigonal	Anisotropic	3.02 × 2.71 × 19.2	8.201 ± 0.005	11.427 ± 0.007	4.655 ± 0.003	3.8 ± 0.5	
Calcite-1a-5d			2.86 × 3.01 × 19.6	8.618 ± 0.010	11.846 ± 0.008	4.080 ± 0.002	3.3 ± 0.3	
Calcite-1a-6-1			2.76 × 2.72 × 18.7	7.518 ± 0.024	10.218 ± 0.007	2.84 ± 0.01	2.0 ± 0.4	4.3 ± 0.7 ($\parallel c$)[c]
Calcite-1b-6-1			2.89 × 2.11 × 21.4	6.085 ± 0.006	11.721 ± 0.018	3.110 ± 0.003	2.6 ± 0.2	3.7 ± 0.5 ($\perp c$)[c]
Calcite-1b-6-2			2.80 × 2.93 × 19.0	8.218 ± 0.002	11.288 ± 0.013	3.083 ± 0.002	2.85 ± 0.08	
Calcite-1b-6-5			2.61 × 2.91 × 21.3	7.593 ± 0.007	11.549 ± 0.007	3.103 ± 0.002	2.6 ± 0.1	
Albite-1 ($\perp b$)	Triclinic	Anisotropic	2.48 × 2.52 × 20.6	6.249 ± 0.009	12.061 ± 0.006	2.17 ± 0.01	1.4 ± 0.5	2.1 ± 0.2[d]
Albite-2 ($\parallel b$)			2.40 × 2.59 × 19.9	6.202 ± 0.009	12.182 ± 0.008	3.91 ± 0.03	2.6 ± 1.3	
Pyrite-1	Cubic	Isotropic	2.03 × 2.07 × 19.9	4.196 ± 0.003	11.043 ± 0.014	50 ± 0.3	N/A	
Pyrite-2			2.89 × 3.12 × 17.4	9.014 ± 0.009	10.024 ± 0.009	38.9 ± 0.2	N/A	35 ± 13[e]
Pyrite-3			1.67 × 1.22 × 20.0	2.027 ± 0.004	11.917 ± 0.006	44.6 ± 0.2	N/A	
Obsidian	Amorphous	Isotropic	2.51 × 2.63 × 20.1	6.598 ± 0.007	12.829 ± 0.009	2.627 ± 0.004	1.4 ± 0.7	1.42 ± 0.06[f]

Note: Thermal conductivity values are in W m^{-1} K^{-1}.

[a] Birch and Clark (1940a), Clark (1966), Kanamori et al. (1968), Horai and Simmons (1969), and Dreyer (1974) (via Clauser and Huenges (1995))

[b] Refs. [a] including Ratcliffe (1959)

[c] Birch and Clark (1940a), Clark (1966), and Dreyer (1974) (via Clauser and Huenges (1995))

[d] Birch and Clark (1940a), Sass (1965), Horai and Simmons (1969), Horai (1971), and Dreyer (1974) (via Clauser and Huenges (1995))

[e] Horai and Simmons (1969), Dreyer (1974) (via Clauser and Huenges (1995), Diment and Pratt (1988), and Popov et al. (2013)

[f] Average values interpolated to 25°C from Birch and Clark (1940a) and Sakvarelidze (1973) (via Čermák and Rybach (1982)).

6 Results: Meteorites

This chapter presents the thermal conductivity results for the four meteorites examined in this study: North Chile, Holbrook, Buzzard Coulee, and Allende. A summary of these samples is provided in Table 4.2 and is also reproduced below as Table 6.1 for quick reference.

As mentioned in Chapter 4, this work includes the first direct thermal conductivity measurements for North Chile, Buzzard Coulee, and Allende. Holbrook is the only sample with previously reported measurements (Opeil et al., 2012), which are included here for reference. Additional context is provided through density and porosity measurements, along with X-ray computed tomography (XCT) 3D visualizations of porosity, grain boundaries, and compositional and textural heterogeneity.

Table 6.1: Repost of Table 4.2: Summary of meteorites

Meteorite	**Type**	**Shocked?**	**Weathered?**	**Mineralogy**
North Chile	IIAB	No	No	Fe-Ni metal (kamacite), rhabdite inclusions
Holbrook	L/LL6	Yes	Yes	Olivine, pyroxene, plagioclase, Fe-Ni metal, troilite, chromite
Buzzard Coulee	H4	Yes	No	Olivine, pyroxene, Fe-Ni metal, troilite, devitrified glass
Allende	CV3	No	No	Olivine, pyroxene, carbonates, spinel, chromite, troilite, CAIs, AOAs

6.1 Results

6.1.1 Thermal Conductivity

Ordinary Chondrites

The measured thermal conductivity of the ordinary chondrites—Holbrook and two samples of Buzzard Coulee—between 5 and 300 K is shown in Figure 6.1. Their thermal behaviour is consistent with that of amorphous solids, which exhibit an increase in thermal conductivity with temperature due to their disordered atomic structure. As noted by Opeil et al. (2010, 2012, 2020) and Macke et al. (2024), this similarity is attributed to the structural disorder in stony meteorites caused by porosity, grain boundaries, and defects. As phonons transport thermal energy through the material, they scatter frequently off these features, limiting their mean free path (ℓ). According to the kinetic theory expression for thermal conductivity, $k = \frac{1}{3}Cv\ell$, where the phonon velocity v remains approximately constant, a limited ℓ implies that thermal conductivity is primarily controlled by the temperature-driven changes in heat capacity (Opeil et al., 2020). This is reflected in some samples, where the thermal conductivity plateaus or increases gradually at higher temperatures (Figures 6.2 to 6.4).

Some meteorites, however, show a thermal conductivity peak followed by a decrease as temperature increases—for example, Bath Furnace and La Cienega (Figure 6.2), and NWA 6950 (Figure 6.4). The enstatite chondrite Abee, studied by Opeil et al. (2010), shows an extreme case of this trend, where it behaves like a crystalline solid (i.e., follows T^3 at low temperatures and $1/T$ at higher temperatures). In Abee, this behaviour is likely driven by the presence of metal-rich clasts that enhance conductivity, combined with porosity and mineral heterogeneity that suppress it (Opeil et al., 2010). The extent of porosity and orientation of shock-induced microcracks may also facilitate phonon-phonon scattering at high temperatures, which can also effectively lower the thermal conductivity (Opeil et al., 2012).

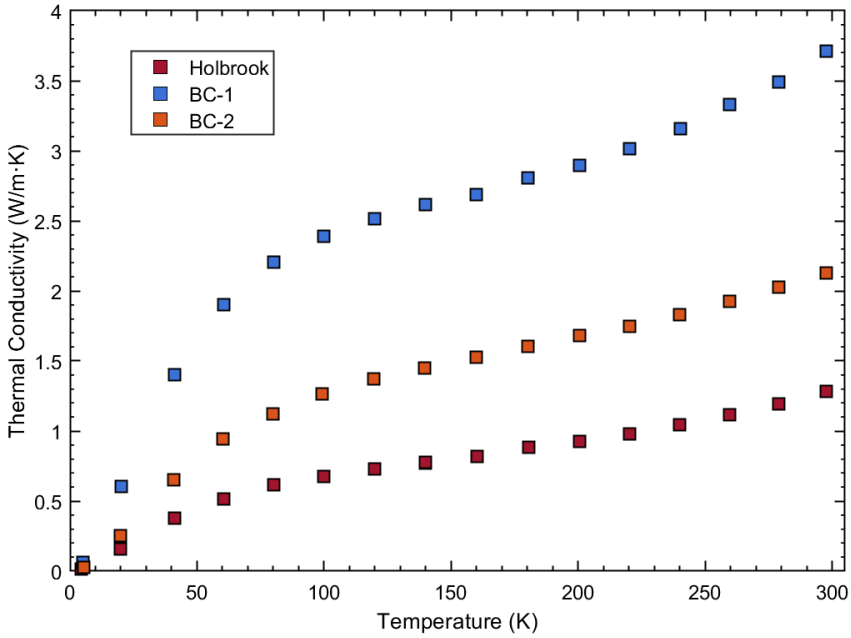

Figure 6.1: Measured thermal conductivity between 5 and 300 K for the three ordinary chondrite samples: Holbrook and two samples of Buzzard Coulee (BC-1 and BC-2). Error bars are smaller than the symbols.

The physical complexity of meteorites makes their thermal conductivity behaviour challenging to interpret, and the effects of thermal radiation may not always be apparent. Unlike crystalline solids, which typically exhibit a $1/T$ decrease in thermal conductivity at high temperatures due to phonon-phonon scattering, meteorites often lack a consistent temperature trend in this region, where radiative effects are most apparent. In Figure 6.1, the measured thermal conductivity of the three ordinary chondrites gradually increases with temperature—a trend that, as previously discussed, is not uncommon. However, when comparing the Holbrook data collected in this study with those reported by Opeil et al. (2012), the increase appears steeper than expected (Figure 6.5). Rather than levelling off, the curve continues to rise with temperature, suggesting that radiative heat loss may be influencing the measurements.

Considering that meteorite thermal conductivity does not follow the same behaviour as crystalline materials, the radiative correction method typically applied to crystalline solids

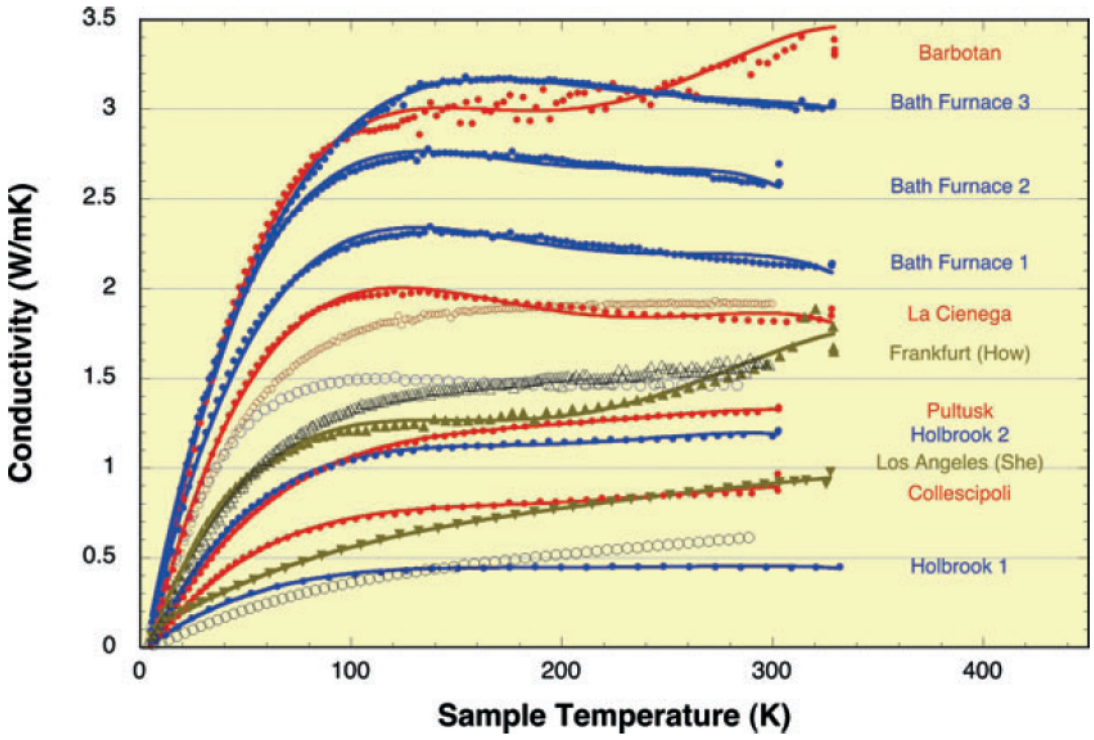

Figure 6.2: Thermal conductivity measurements of stony meteorites. Open symbols represent data from Opeil et al. (2010), while closed symbols are from Opeil et al. (2012). Red symbols correspond to H chondrites, blue to L chondrites, and light brown to differentiated stony meteorites (achondrites). Figure from Opeil et al. (2012).

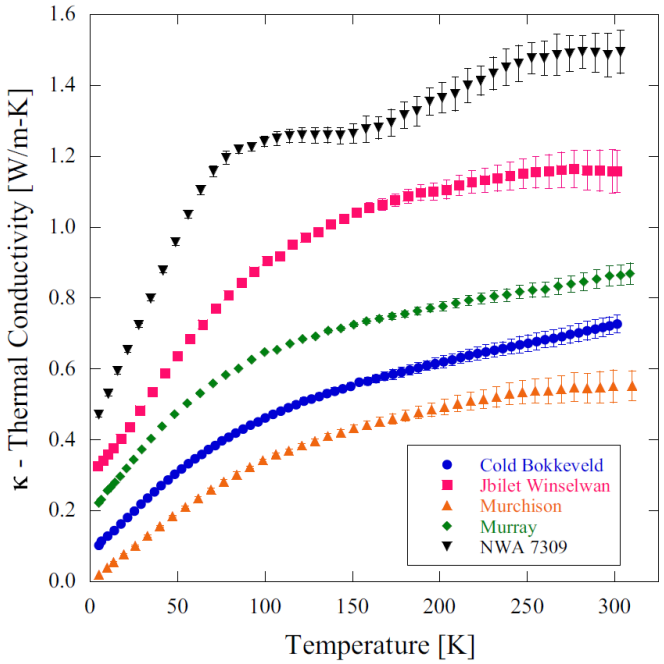

Figure 6.3: Thermal conductivity measurements of CM carbonaceous chondrites. The data are vertically offset by multiples of 0.1 W m^{-1} K^{-1}. Figure and data from Opeil et al. (2020).

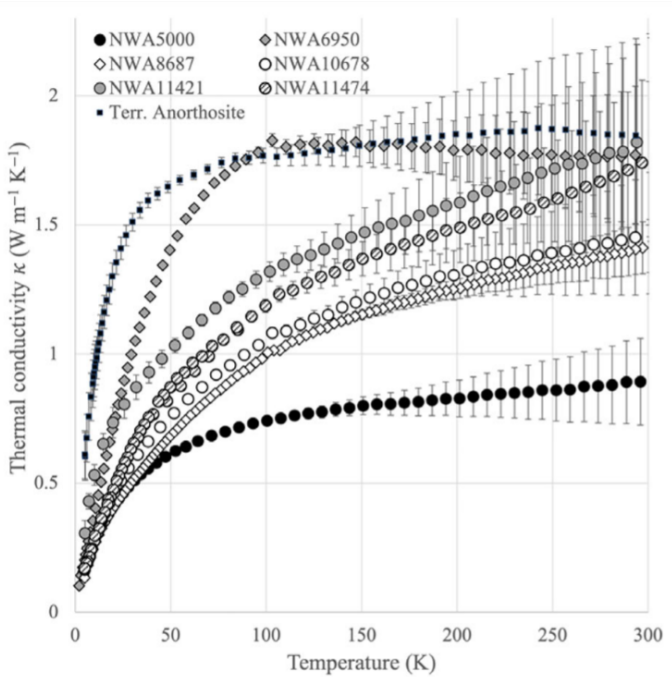

Figure 6.4: Thermal conductivity measurements of lunar meteorites. Figure and data from Macke et al. (2024).

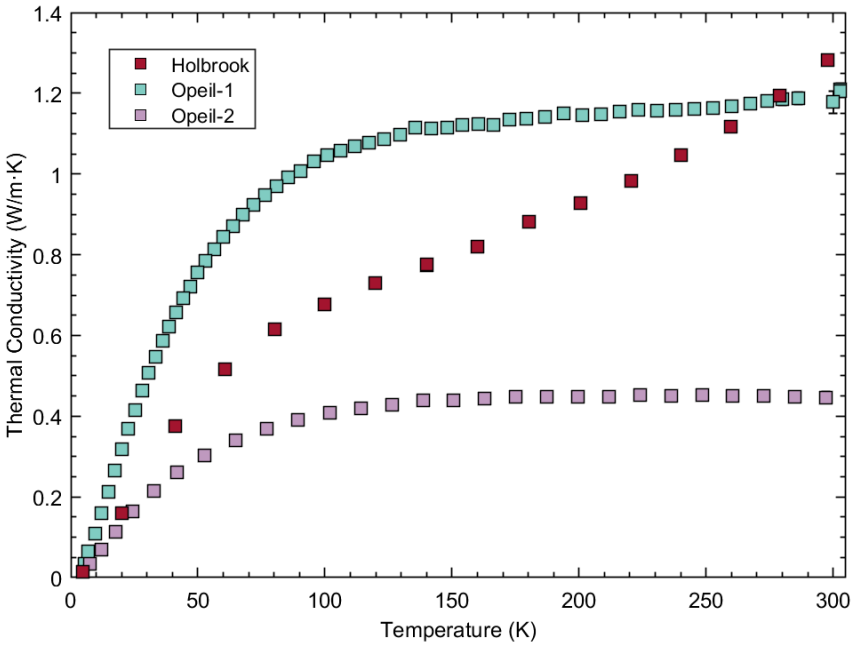

Figure 6.5: Thermal conductivity of Holbrook measured in this study using the CFMS compared with two Holbrook samples reported by Opeil et al. (2012). Most error bars are smaller than the symbols.

(i.e., a linear $1/T$ fit; see Chapter 5) is not suitable in this case. Instead, an alternative method is required to correct for radiative heat loss in meteorite samples. Using a modified fitting approach, an empirical model was developed to account for these effects in CFMS-measured data:

$$k = \frac{aT^2 + bT + c}{1 + dT} \tag{6.1}$$

At low temperatures, the thermal conductivity follows a T^2 relationship. Although crystalline materials typically exhibit $k \propto T^3$ at low temperatures, as predicted by the Debye model, meteorites show an amorphous-like trend instead. In amorphous solids, this T^2 dependence arises from scattering by two-level systems (TLS) (Anderson et al., 1972; Phillips, 1972) (Chapter 2). While the dominant low-temperature scattering mechanism in meteorites is phonon-boundary scattering rather than TLS, their thermal conductivity still resembles that of disordered solids.

The additional $bT + c$ terms in the numerator account for the gradual increase in thermal conductivity that may begin to occur between 50 and 100 K, where phonon scattering remains constrained by structural disorder. In such instances, the thermal conductivity is still primarily governed by the heat capacity.

At higher temperatures, thermal conductivity tends to plateau or gradually increase, resembling the behaviour observed in amorphous materials. This behaviour in meteorites is modelled by the denominator term $(1 + dT)$, which reflects the saturation in thermal conductivity caused by a constant phonon mean free path. Such behaviour is primarily due to persistent scattering from porosity and defects, which continue to restrict heat flow even at elevated temperatures. However, this model does not account for situations where thermal conductivity decreases with increasing temperature, as would be expected when phonon-phonon interactions become significant. Acknowledging this limitation, the model was applied under the assumption that conductivity plateaus or increases gradually with temperature, consistent with phonon-limited transport governed primarily by the temperature dependence of heat capacity. The model performs well under these assumptions, as

demonstrated by the results below.

Using Equation 6.1, fits were applied to the ordinary chondrite data over temperature ranges between 5 and 200 K, depending on the sample. Data above 200 K were excluded from the fitting process to avoid incorporating thermal conductivity values affected by radiative heat loss, which becomes increasingly significant at higher temperatures. The fitted curves were then extrapolated to 300 K to estimate the true thermal conductivity without contributions from radiative heat loss. The validity of the model was further assessed by applying it to the two Holbrook samples measured by Opeil et al. (2012). The resulting fit parameters are summarized in Table 6.2 and illustrated in Figures 6.6 and 6.7.

Table 6.2: Best-fit coefficients for ordinary chondrites using the model $k = \frac{aT^2+bT+c}{1+dT}$.

Sample	$\boldsymbol{a \times 10^{-5}}$	$\boldsymbol{b}$	$\boldsymbol{c}$	$\boldsymbol{d}$	**Range (K)**	$\boldsymbol{R^2}$
Buzzard Coulee-1	−5.820	0.208	−3.648	0.059	40–160	0.999
Buzzard Coulee-2	−2.160	0.034	−0.357	0.012	20–160	0.999
Holbrook	−1.260	0.020	−0.183	0.014	20–140	0.999
Opeil-1 (Holbrook)	−3.450	0.045	−0.409	0.026	15–255	0.999
Opeil-2 (Holbrook)	−1.150	0.013	−0.070	0.018	5–300	0.999

These results support the model's ability to correct for radiative heat loss in thermal conductivity measurements. It captures the overall thermal behaviour across most of the measured temperature range where radiation is negligible, as reflected by consistently high R^2 values ($R^2 = 0.999$). However, it does not fully reproduce the trend at low temperatures (e.g., below 40 K), which may reflect limitations in the fit itself, constraints on thermocouple sensitivity, or a combination of both. Given the available data, this model currently provides the best approximation of the observed trends.

The Opeil-2 Holbrook sample is a notable exception to the limitations, as the model fits the full 5 to 300 K range well (Figure 6.7). For Opeil-1, the fit is reliable between approximately 20 and 100 K but begins to under- or over-predict outside that range, despite maintaining an R^2 of 0.999. In particular, the model does not capture the slight upward

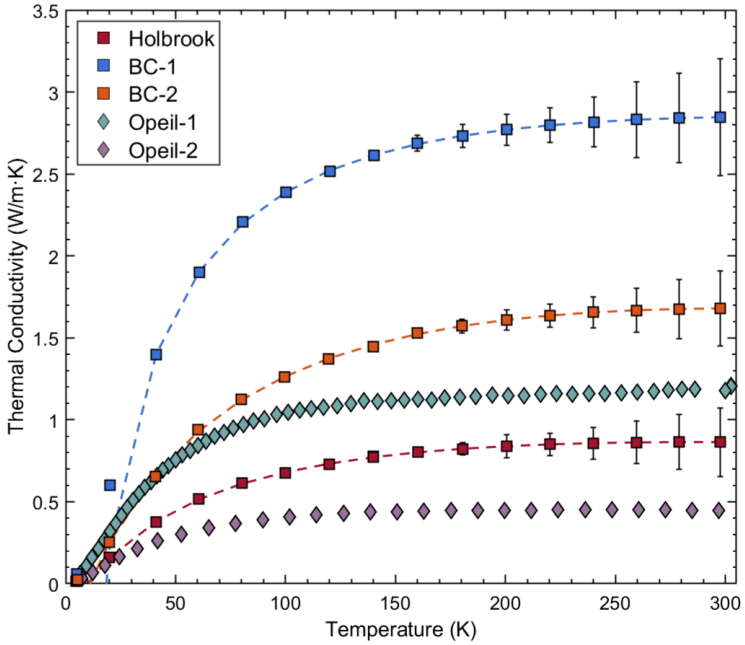

Figure 6.6: Corrected thermal conductivity data for Holbrook and the two Buzzard Coulee (BC-1 and BC-2) samples from this study. Dashed lines represent best-fit curves using the empirical model (Equation 6.1) applied to Holbrook and Buzzard Coulee datasets. The two Holbrook samples from Opeil et al. (2012) (Opeil-1 and Opeil-2) are included for comparison.

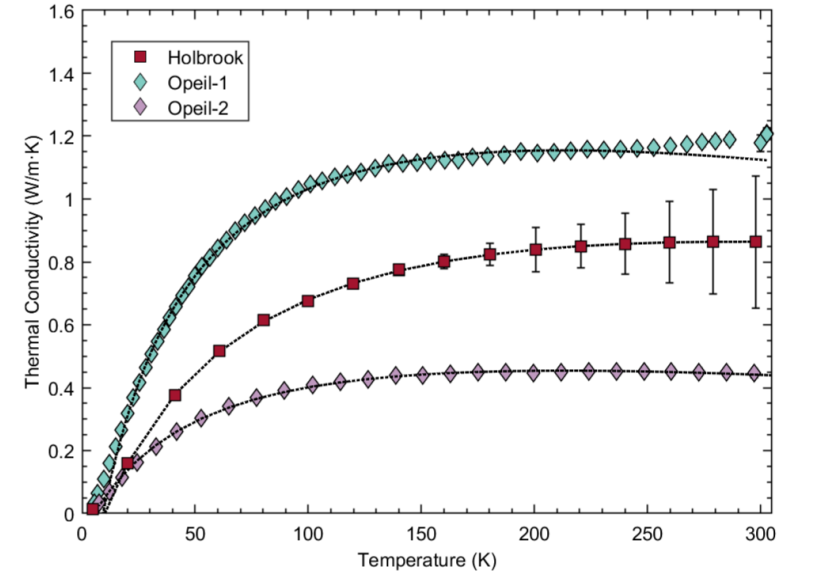

Figure 6.7: Comparison between the corrected thermal conductivity data for Holbrook from this study and the two Holbrook samples reported by Opeil et al. (2012). The black dotted lines represent best-fit curves using the empirical model (Equation 6.1).

curvature at higher temperatures in Opeil-1. Similarly, it also does not account for scenarios where phonon-phonon interactions are significant at higher temperatures, indicated by a decreasing thermal conductivity with increasing temperature. Therefore, the model may have over- or under-corrected the ordinary chondrite data in this study. This discrepancy demonstrates that the model does not fully capture the thermal behaviour in some cases, and further refinement is necessary to better represent such variations.

The effectiveness of the model for the ordinary chondrites in this study is further supported by the strong linear relationship observed between the radiative component (k_{rad})—defined as the difference between measured and corrected values (Figure 6.8)—and T^3 for all three samples (Figures 6.9 and 6.10). This correlation supports the interpretation that the unexpected increase in thermal conductivity at higher temperatures is driven by radiative heat loss.

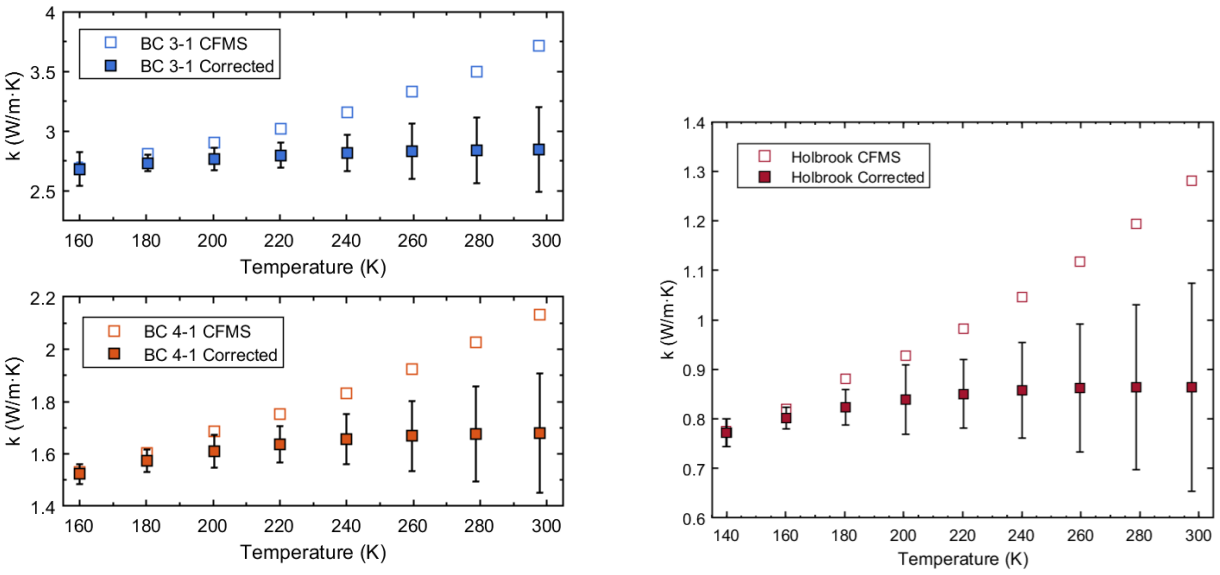

(a) Buzzard Coulee (b) Holbrook

Figure 6.8: Comparison of CFMS-measured and corrected data for radiative heat loss in (a) Buzzard Coulee and (b) Holbrook.

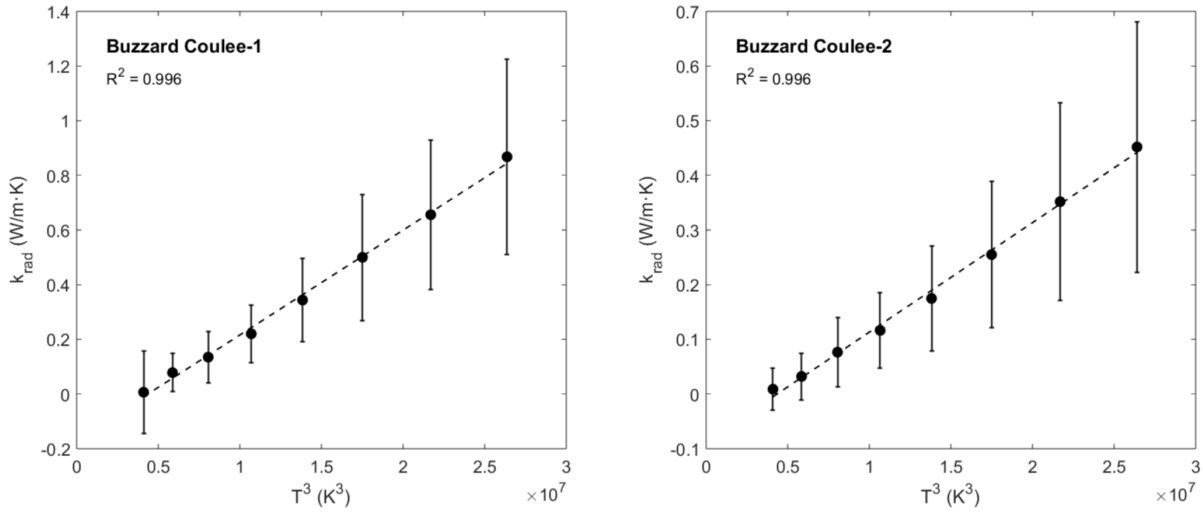

Figure 6.9: Radiation component (k_{rad}) as a function of T^3 for Buzzard Coulee-1 (left) and Buzzard Coulee-2 (right).

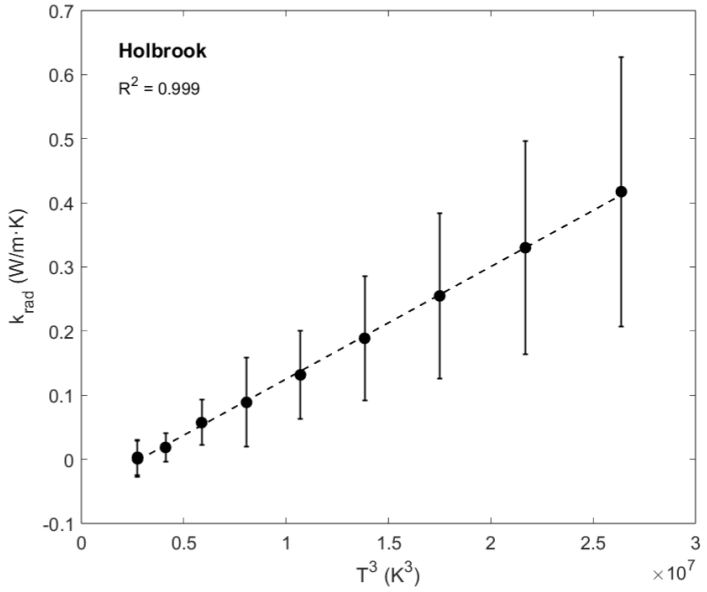

Figure 6.10: Radiation component (k_{rad}) as a function of T^3 for Holbrook.

Allende

Allende measurements were only collected down to 140 K (Figure 6.11), as repairs required for the CFMS halted low-temperature measurements beyond the timeline of this Ph.D. Once the system is operational again, measurements will resume. However, because the available data coincides with the temperature range where radiative effects typically become significant, a reliable radiation correction cannot be applied until data are obtained below 140 K. Based on the corrected trends observed in the Holbrook and Buzzard Coulee samples, the true thermal conductivity of Allende at 300 K is estimated to lie between 0.8 and 0.9 W m^{-1} K^{-1}. For comparison, a thermal conductivity value of 1.4 W m^{-1} K^{-1} has been reported for Allende, calculated from its thermal diffusivity, bulk density, and heat capacity (Szurgot, 2011b).

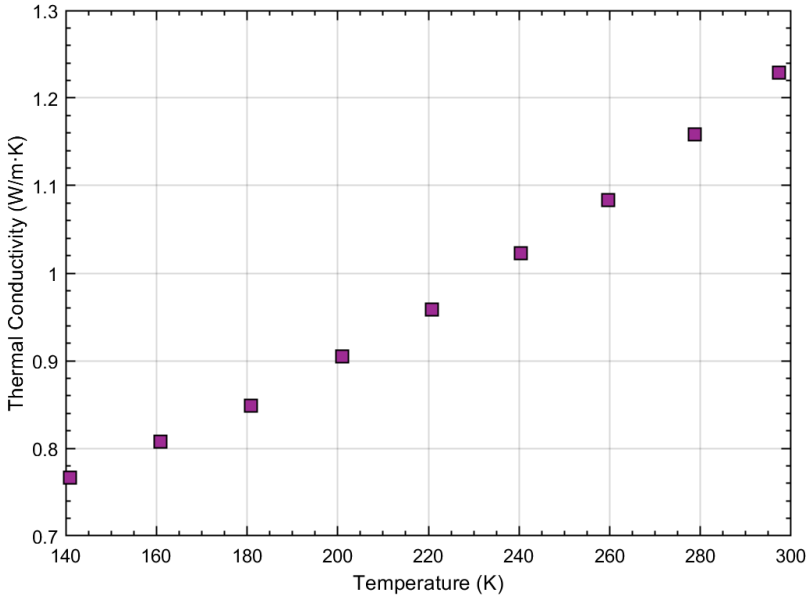

Figure 6.11: Measured thermal conductivity between 140 and 300 K for Allende. Error bars are smaller than the symbols.

North Chile

The thermal conductivity of North Chile was measured between 5 and 300 K. These data are compared to the thermal conductivity of the iron meteorites from Noyes et al. (2022)—Agoudal, Canyon Diablo, Muonionalusta, and Sikhote-Alin—in Figure 6.12. The agreement of North Chile with the iron meteorites suggests that heat loss due to radiation may not be significant in the measurements. The data was fit to the empirical model to test this theory, which resulted in an over-correction of the data.

The thermal conductivity trend for iron meteorites shows no evidence of phonon-phonon scattering, as conductivity continues to increase with temperature. Noyes et al. (2022) attributes the scattering from grain boundaries, impurities, and defects, similar to the mechanisms governing thermal conductivity in chondrites. However, unlike chondrites, which are porous and exhibit numerous grain boundaries to their diverse mineralogy, grain boundary scattering in iron meteorites is primarily associated between kamacite and taenite crystals (Noyes et al., 2022).

Among the samples analyzed by Noyes et al. (2022), Canyon Diablo, Muonionalusta, and Sikhote-Aline are octahedrites composed of both kamacite and taenite, whereas Agoudal is dominated by kamacite. In Agoudal, the kamacite displays a coarse, interlocking texture formed through recrystallization, with rhabite crystals located within kamacite crystals and along grain boundaries (Chennaoui et al., 2013). Similarly, North Chile is a hexahedrite composed primarily of kamacite, but it does not exhibit any textural features. However, rhabdite crystals are distributed three-dimensionally throughout North Chile (Gilmour and Herd, 2020), which likely dominate phonon-boundary scattering. Additionally, visible cracks on the surface of the North Chile sample (Figure 4.37) may also contribute to phonon scattering.

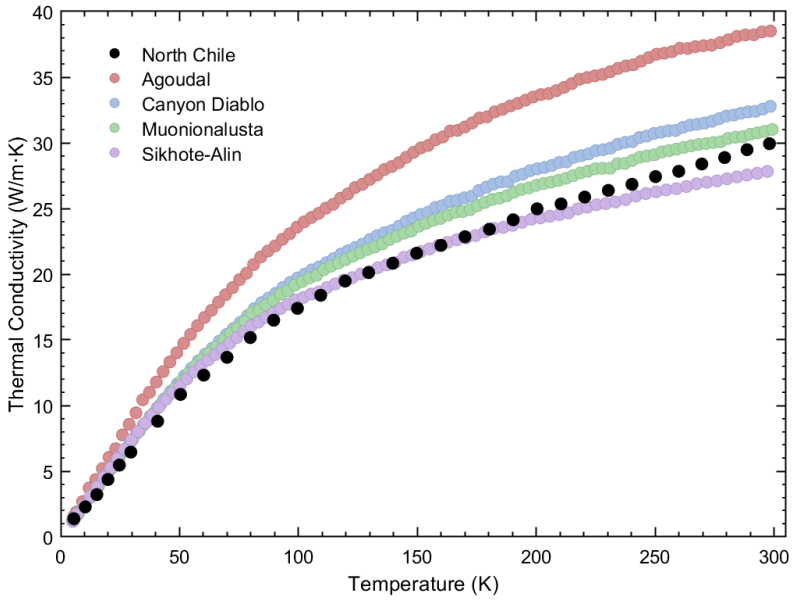

Figure 6.12: Thermal conductivity of the North Chile meteorite compared with four iron meteorites from Noyes et al. (2022) (Agoudal, Canyon Diablo, Muonionalusta, and Sikhote-Alin). Error bars are smaller than the symbols.

6.1.2 Density and Porosity

The bulk density, grain density, and porosity for the meteorites in this study are provided in Table 6.3. Reported literature averages are also included, denoted in italics. Overall, the results compare well with those previously reported, and fall within the expected density and porosity ranges for their respective meteorite types (Macke, 2010). These measurements help explain the variability observed in thermal conductivity, particularly the influence of porosity and internal structure on heat flow.

The effects of porosity are evident among the two Buzzard Coulee samples, which show that even small differences in porosity can lead to significant changes in thermal conductivity. Although their porosity differs by only $\sim 0.6\%$, their thermal conductivity at 300 K varies by nearly a factor of two (Figure 6.6). Internal heterogeneity among the four stony meteorites was further investigated with XCT imaging, which provided 3D visualizations of porosity and other structural features (Figures 6.14 to 6.13). Images of the North Chile iron

Table 6.3: Meteorite physical properties: dimensions, mass, bulk & grain densities, porosity. Italicized numbers are literature-reported averages.

Sample	**Type**	**Dimensions** (mm) $w \times h \times l$	**Mass** (g)	**Bulk ρ** (g cm^{-3})	**Grain ρ** (g cm^{-3})	**Porosity** (%)
Allende	CV3	2.78 × 2.87 × 20.1	0.4526	2.829 ± 0.002 *2.863 ± 0.004*	3.59 ± 0.04 *3.66 ± 0.04*	21.2 ± 0.9 *20.5 ± 0.2*
Holbrook	L/LL6	2.65 × 3.07 × 20.0	0.4948	3.05 ± 0.01 *3.188 ± 0.004*	3.48 ± 0.02 *3.519 ± 0.003*	12.4 ± 0.6 *10.7 ± 0.2*
Buzzard Coulee-1	H4	3.25 × 2.25 × 20.1	0.5013	3.418 ± 0.002 *3.46 ± 0.02*	3.737 ± 0.003 *3.69 ± 0.03*	8.5 ± 0.1 *6.2 ± 0.1*
Buzzard Coulee-2	H4	2.74 × 2.69 × 20.1	0.5162	3.494 ± 0.003 *3.46 ± 0.02*	3.79 ± 0.04 *3.69 ± 0.03*	7.9 ± 0.8 *6.2 ± 0.1*
North Chile	IIAB	2.42 × 2.09 × 21.5	0.8327	7.69 ± 0.01 *7.55 ± 0.06*	7.74 ± 0.08 *7.79 ± 0.02*	0.7 ± 1.0 *2.84 ± 0.83*

Reported averages for Allende, Holbrook, and North Chile are from Macke (2010). For North Chile, the reported values represent averages for IIAB meteorites. Reported averages for Buzzard Coulee are from Fry et al. (2013).

meteorite were not acquired, as its low porosity and overall kamacite homogeneity offered few structural features of interest, despite the presence of micron-scale rhabdite inclusions. The XCT scans captured only the central portion of each sample (approximately 10 mm), corresponding to the region where the temperature gradient is measured during thermal conductivity analysis. While Buzzard Coulee-1 and Buzzard Coulee-2 have similar cross-sectional areas, the former is more rectangular and contains a higher concentration of visible pore spaces. This highlights how small-scale differences in pore distribution—on the order of millimetres—can strongly influence heat transport, especially when combined with the mineralogical and textural differences visible in the 2D basal sections (Figures 6.14 and 6.15).

Across all four stony meteorites, XCT imaging reveals both macroscopic and microscopic heterogeneities, including grain boundaries, microcracks, and compositional and textural variations. These features disrupt the thermal path and contribute to variability in thermal conductivity, even among samples from the same parent meteorite. The Buzzard Coulee and Holbrook samples show this effect (Figure 6.6), with noticeable differences in thermal

conductivity despite following similar temperature trends. This behaviour is consistent with thermal conductivity data from three Bath Furnace meteorite samples measured by Opeil et al. (2012), where the conductivity curves follow similar temperature trends but are offset in magnitude due to differences in internal structure. However, visual inspection alone may not fully capture these subtleties. For example, Allende appears to have the least observable porosity (Figure 6.16) despite having the highest porosity (Table 6.3), likely due to the presence of pores smaller than the resolution of the XCT scans. This highlights the limitation of visual analysis and the need to consider both qualitative and quantitative structural data.

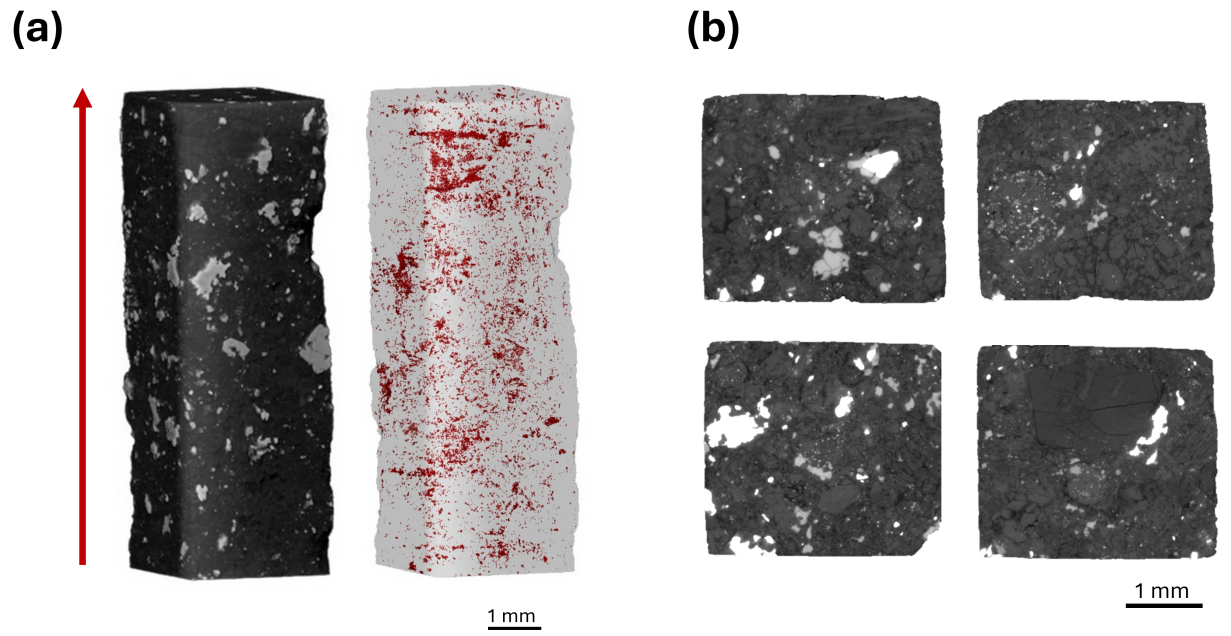

Figure 6.13: XCT data for Holbrook. (a) 3D images of the central portion of the sample, showing external surface texture and mineralogical contrast (left) alongside the internal distribution of porosity highlighted in red (right). The red arrow indicates the direction of heat flow during thermal conductivity measurements. (b) Four representative 2D basal sections showing mineralogical and textural variability throughout the sample.

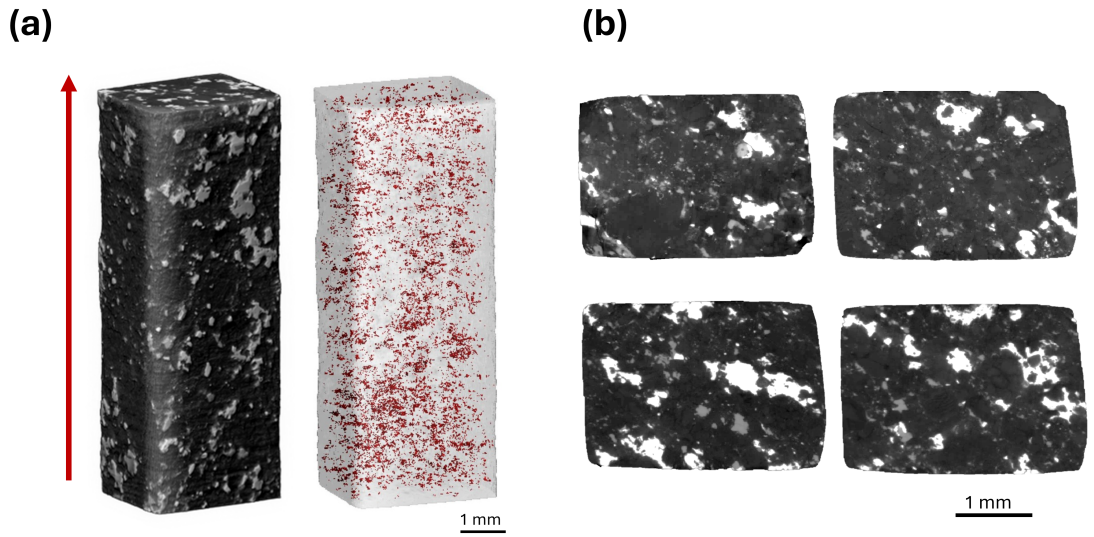

Figure 6.14: XCT data for Buzzard Coulee-1. (a) 3D images of the central portion of the sample, showing external surface texture and mineralogical contrast (left) alongside the internal distribution of porosity highlighted in red (right). The red arrow indicates the direction of heat flow during thermal conductivity measurements. (b) Four representative 2D basal sections showing mineralogical and textural variability throughout the sample.

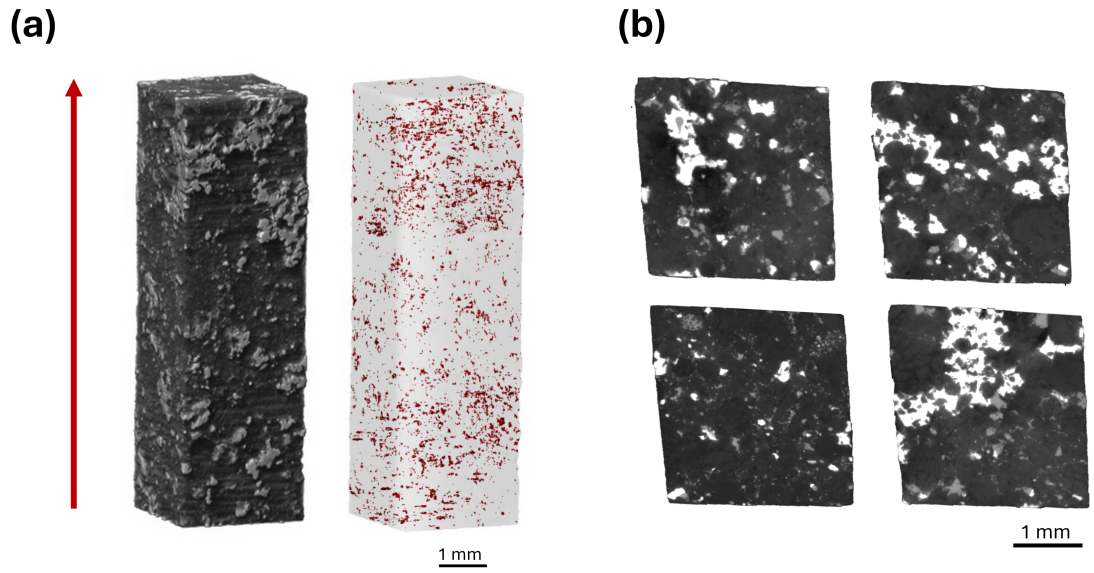

Figure 6.15: XCT data for Buzzard Coulee-2. (a) 3D images of the central portion of the sample, showing external surface texture and mineralogical contrast (left) alongside the internal distribution of porosity highlighted in red (right). The red arrow indicates the direction of heat flow during thermal conductivity measurements. (b) Four representative 2D basal sections showing mineralogical and textural variability throughout the sample.

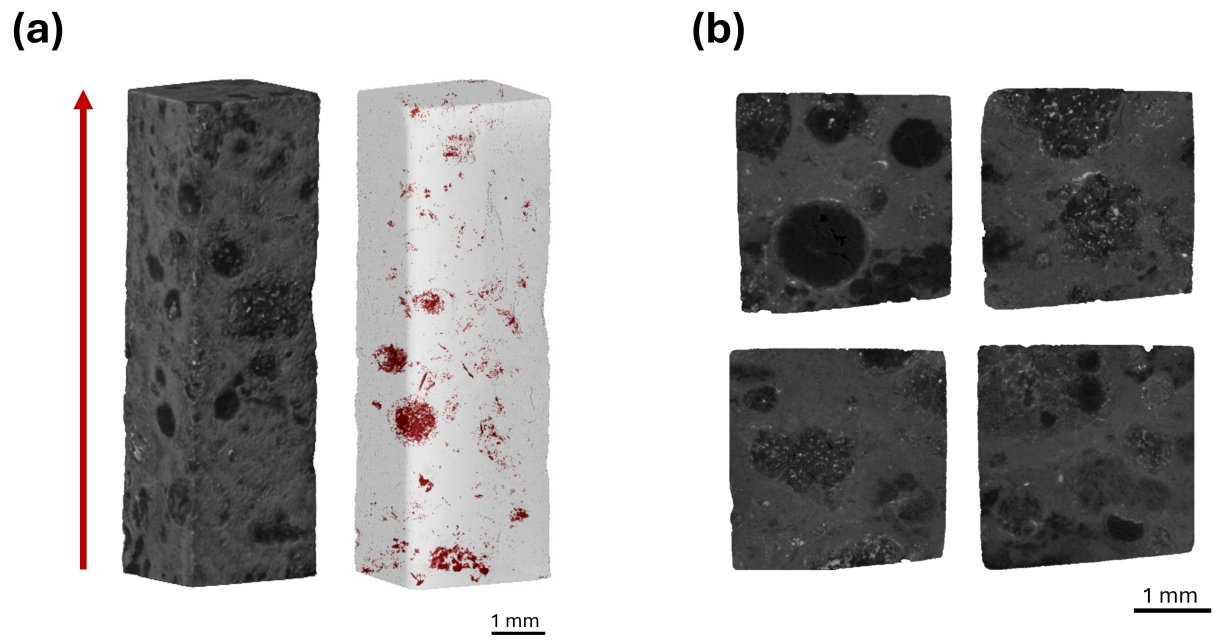

Figure 6.16: XCT data for Allende. (a) 3D images of the central portion of the sample, showing external surface texture and mineralogical contrast (left) alongside the internal distribution of porosity highlighted in red (right). The red arrow indicates the direction of heat flow during thermal conductivity measurements. (b) Four representative 2D basal sections showing mineralogical and textural variability throughout the sample.

A strong correlation between thermal conductivity and the inverse of porosity has been reported by Opeil et al. (2012) ($R^2 = 0.95$). To evaluate how the results from this study compare, thermal conductivity values at 200 K for the three ordinary chondrites measured here were plotted with the data from Opeil et al. (2010, 2012) (Figure 6.17). Although the linear fit derived in this study ($y = 0.13x - 0.04$) differs from the one reported by Opeil et al. (2012) ($y = 3.56 + 6.78x$), the underlying data are identical, as demonstrated by the inclusion of their original plot in the right panel of Figure 6.17. This discrepancy likely arises from differences in how the regression was applied, such as whether or not data were weighted by uncertainty. Regardless, with the addition of the three chondrites from this study, the correlation between thermal conductivity and inverse porosity remains strong, with an R^2 value of 0.85.

However, this relationship does not account for anisotropy within samples, which can

lead to a spread in thermal conductivity values for a given meteorite. For example, the two Buzzard Coulee samples measured here have similar porosity ($1/\text{porosity} \approx 12\%$); however, the difference in thermal conductivity is noticeable in Figure 6.17, likely due to differences in pore distribution and mineral boundaries and textures. This effect is also observed in the three samples of Bath Furnace and two samples of Holbrook measured by Opeil et al. (2012), where the anisotropic behaviour is not captured by a simple linear trend.

A similar linear relationship has been observed between thermal conductivity and bulk density (Szurgot, 2011a; Szurgot, 2011b). In this study, the thermal conductivity at 140 K was plotted against bulk density, calculated from each sample's mass and measured dimensions (Figure 6.18). This temperature was selected because radiative heat loss is negligible at 140 K, as demonstrated by the correction data for Holbrook and Buzzard Coulee (Figure 6.8), making it a reliable point for comparison. Although radiative corrections could not be applied to Allende due to limited data, its 140 K measurement can still be confidently included based on this consistency. Including North Chile in the plot reinforces the strength of this relationship, with the iron's high density and conductivity anchoring the upper end of the trend. However, similar to the relationship with the inverse of porosity, this trend may also not fully capture the anisotropy, as evident from the Buzzard Coulee data.

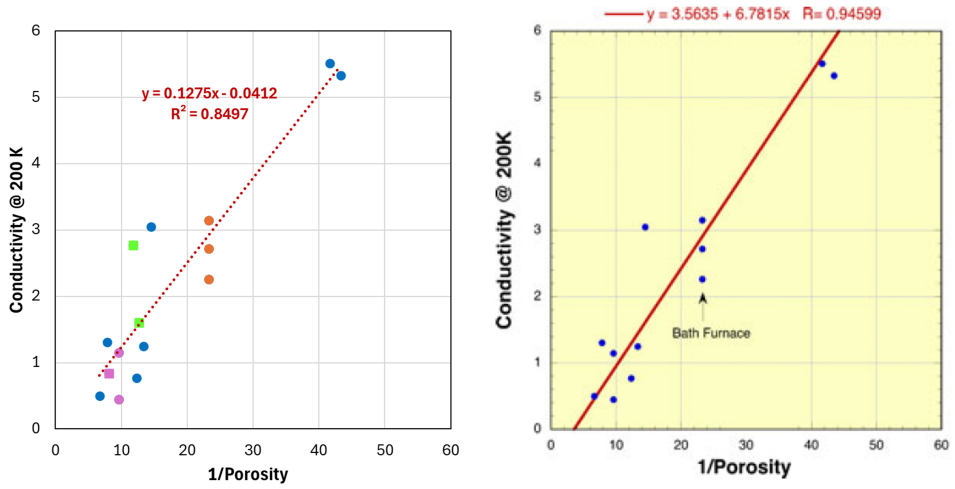

Figure 6.17: Thermal conductivity at 200 K as a function of the inverse of porosity. The left plot shows measurements for stony meteorites from Opeil et al. (2010) and Opeil et al. (2012) (circles) along with the three ordinary chondrites from this study (squares): Holbrook = pink, Buzzard Coulee = green; Bath Furnace = orange, blue = other meteorites. The plot on the right is taken directly from Opeil et al. (2010) to demonstrate that although the linear fits differ between this study and theirs, the underlying data are the same.

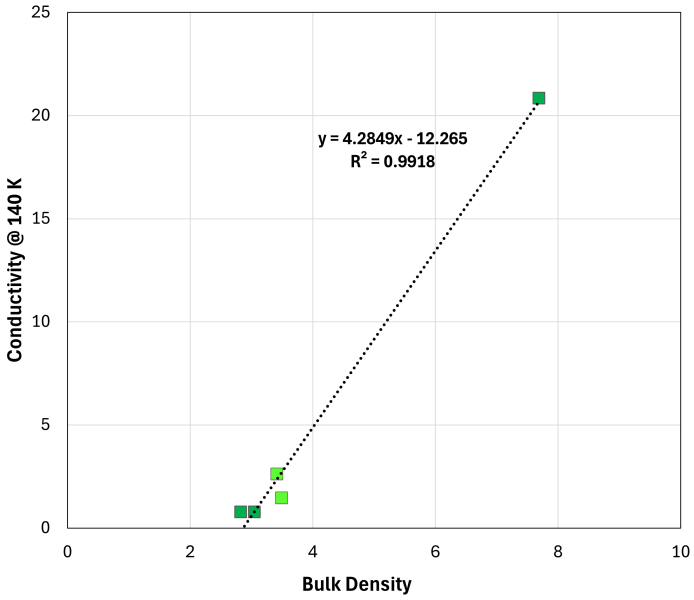

Figure 6.18: Thermal conductivity at 140 K as a function of bulk density for the five meteorite samples in this study. The Buzzard Coulee samples are the lime green data points.

6.2 Discussion and Conclusions

Measuring the thermal conductivity of meteorites is inherently challenging due to the complex and anisotropic nature of their internal structures. Pore spaces, microcracks, and grain boundaries are known to interfere with thermal transport within meteorites (Opeil et al., 2012). In stony meteorites, porosity appears to be the most significant suppressor of heat flow, introducing variability even among samples of the same meteorite type. By contrast, in low-porosity materials like the iron meteorite North Chile, phonon scattering at grain boundaries plays a more dominant role in limiting heat transport.

The ordinary chondrite thermal conductivity measurements in this study compare well with those reported by Opeil et al. (2010, 2012) (Figure 6.19). Although variability between samples of the same meteorite type is observed in both datasets, the overall agreement across two different cryogenic instruments supports the reliability of the CFMS for measuring meteorite thermal conductivity. Notably, the thermal conductivity of the Holbrook sample measured in this study falls between the two Holbrook samples from Opeil et al. (2012), highlighting the influence of small-scale structural variability within a single meteorite (Figure 6.7). Buzzard Coulee is reported to exhibit low variability among its physical properties (Fry et al., 2013); however, this is not reflected in its thermal conductivity, providing further evidence that microstructural heterogeneities significantly impact thermal behaviour.

In iron meteorites, thermal transport is governed by both phonons and electrons. However, grain boundaries serve as a major scattering mechanism for both carriers, limiting their mean free path. As a result, their thermal conductivity trends in iron meteorites closely resemble their heat capacity curves (Noyes et al., 2022). This behaviour is seen in North Chile, whose conductivity matches previously reported values for other iron meteorites (Figure 6.12), suggesting that radiative heat loss may be negligible below 300 K. To quantify the relative contributions of electrons and phonons and assess radiative effects at higher temperatures, electrical resistivity measurements of iron meteorites are required. The elec-

tronic component of thermal conductivity can be calculated using the Wiedemann–Franz law (Equation 2.28) and subtracted from the total conductivity to isolate the lattice contribution, which can be influenced by radiative heat loss at higher temperatures.

Although metal grains are present in ordinary chondrites, the electronic contribution is generally minimal as heat transport in these samples is dominated by porosity and microcracks rather than mineralogy. Furthermore, the movement of free electrons throughout the sample is limited by the surrounding silicate grains (Opeil et al., 2020).

The anisotropic nature of thermal conductivity in meteorites appears to impose limitations on linear relationships with inverse porosity and bulk density. These observations are based on measurements conducted at the millimetre scale, raising the question of whether thermal conductivity values derived from small samples introduce scale-dependent biases. Notably, the measurements in this study were obtained using a one-directional steady-state heat flow, whereas thermal transport in natural geological settings occurs in multiple directions (Wenk and Bulakh, 2016). This multidirectional transport may effectively average out anisotropic effects in larger bodies. However, the physical constraints of cryogenic thermal property instruments limit the ability to assess at what scale anisotropy becomes less significant, if at all. While anisotropic effects may diminish over the larger thermal diffusion scales of planetary bodies like asteroids, porosity and grain boundaries remain intrinsic barriers to heat transfer regardless of scale.

These findings highlight the need for continued research to further improve our understanding of thermal conductivity in meteorites. Ideally, measurements should be conducted on multiple samples of the same meteorite across a range of sizes to investigate the extent and scale-dependence of heat suppression in these insulating materials. Just as Macke (2010) developed a comprehensive database of density and porosity measurements, expanding such datasets to include thermal conductivity, thermal diffusivity, thermal inertia, and heat capacity would significantly improve our ability to model heat flow in asteroid parent bodies and other airless planetary bodies.

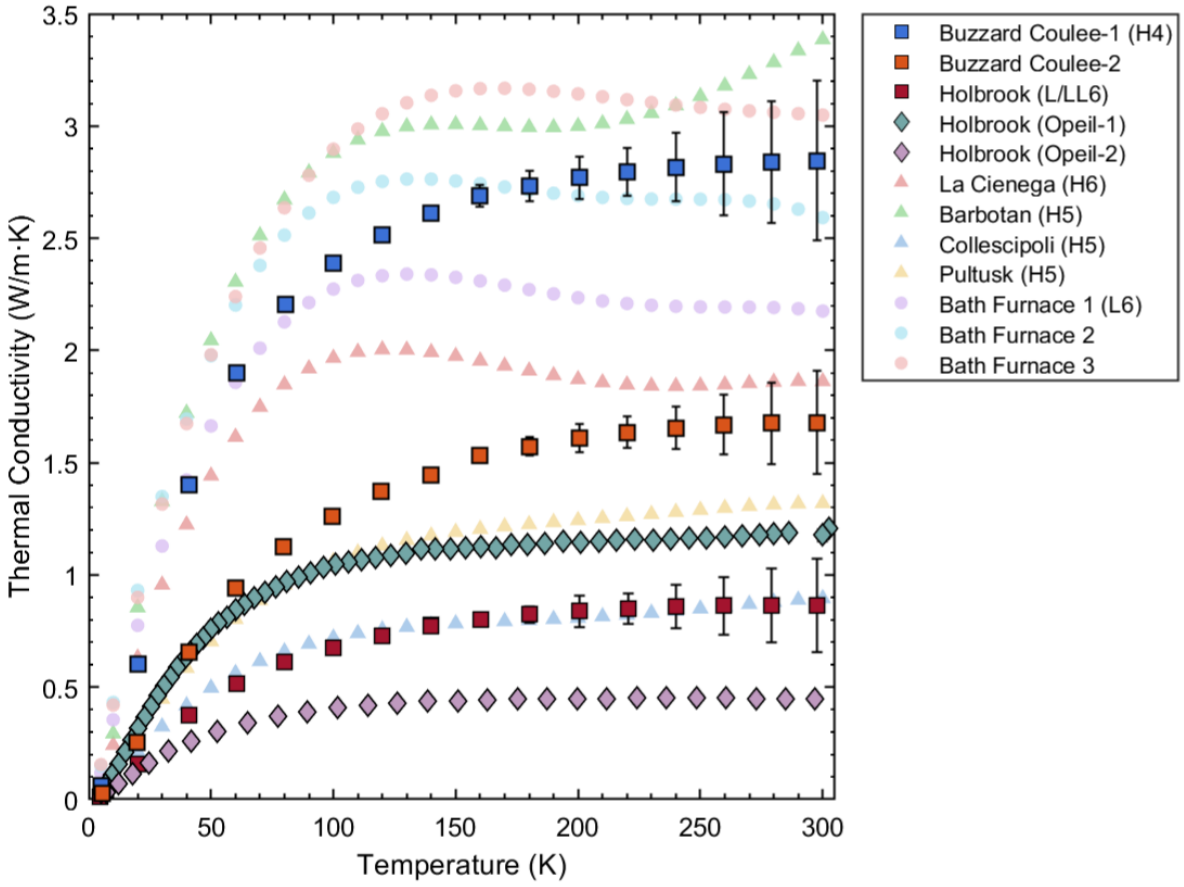

Figure 6.19: Comparison of the corrected thermal conductivity data for the three ordinary chondrites in this study (Holbrook and two Buzzard Coulee samples) with the ordinary chondrites measured by Opeil et al. (2012). The Opeil Holbrook samples are emphasized with diamond symbols.

7 Emissivity of Geological Samples

Understanding how emissivity behaves in geological materials is relevant to this study, as radiative heat transfer occurs during thermal conductivity measurements (Chapter 3). This chapter provides an overview of emissivity in geological samples to support future investigations. Although direct emissivity measurements were not a primary objective of this PhD project, the topic was researched extensively to determine the most effective way to correct thermal conductivity data for radiative heat loss. The fitting-based correction method described in Chapters 5 and 6 has proven effective; however, the availability of emissivity data enables a comparison with the Stefan–Boltzmann law, expressed in Equation 3.11:

$$P_r = 4\sigma A \varepsilon T^3 \Delta T$$

7.1 Introduction to Emissivity

Like thermal conductivity, the emissivity of geological materials is influenced by many factors—including temperature, pressure, illumination conditions, surface roughness, incidence angle, heat distribution, anisotropy, mineral distribution (in rocks), and, for particulate samples, grain size and packing—all of which have been investigated in various studies (Lyon, 1964; Lyon, 1965; Conel, 1969; Logan and Hunt, 1970; Logan et al., 1973; Salisbury and Walter, 1989; Salisbury et al., 1991b; Salisbury and Wald, 1992; Rivard et al., 1995; Feely and Christensen, 1999; Ramsey and Christensen, 1998; Mathew et al., 2009; Hanna et al., 2012; Thomas et al., 2012a; Loehle et al., 2017; Lane and Bishop, 2019; Shirley and Glotch, 2019). In the case of meteorites, oxidation of metal due to weathering may also have a slight effect on emissivity (Ostrowski and Bryson, 2019).

Emissivity is most commonly measured in particulate samples (Conel, 1969; Logan and Hunt, 1970; Logan et al., 1973; Salisbury et al., 1988; Salisbury and Walter, 1989; Salisbury and D'Aria, 1992; Rivard et al., 1995; Christensen et al., 2000; Cooper et al., 2002; Maturilli

et al., 2008; Mathew et al., 2009; Baldridge et al., 2009; Hanna et al., 2012; Thomas et al., 2012a; Shirley and Glotch, 2019). This emphasis on particulate samples reflects the need to compare laboratory measurements with thermal infrared (IR) remote-sensing data collected for airless, regolith-covered bodies. However, particulate emissivity analysis is not feasible for this type of study, as the samples must remain intact for thermal conductivity measurements. Instead, emissivity should be determined either by measuring the emitted radiance of solid samples (Salisbury et al., 1988; Wyatt et al., 2001; Cooper et al., 2002; Danov et al., 2007; Mathew et al., 2009), or by using an infrared camera or temperature gun (Ostrowski and Bryson, 2020; Mineo and Pappalardo, 2021).

Under ambient conditions, emissivity typically decreases with increasing particle size, meaning that larger grains or solid samples generally have lower emissivity than fine-grained particulates (Conel, 1965; Conel, 1969; Lyon, 1964; Salisbury and Wald, 1992; Shirley and Glotch, 2019). This behaviour arises from differences in surface and volume scattering of IR radiation. Fine-grained powdered samples, which have small grain sizes and high porosity, are dominated by volume scattering and absorption. As a result, the intensity of spectral features decreases with decreasing particle size, effectively increasing the emission over the thermal IR wavelength range (Figure 7.1). In contrast, solid surfaces are dominated by surface scattering, which leads to more pronounced spectral features and a corresponding decrease in overall emissivity.

Interestingly, while emissivity increases with decreasing particle size under ambient conditions, Shirley and Glotch (2019) observed the opposite trend when particulate mineral samples were measured under simulated lunar temperature and pressure conditions: emissivity decreased as particle size decreased. While their study focused on particulate samples, it provides valuable insight into how whole rock samples, such as those used in this PhD study, emit thermal radiation in cryogenic vacuum environments like the CFMS. The extent to which the emissivity of solid materials changes under these conditions remains unknown and presents an opportunity for future research. However, based on the findings of Shirley

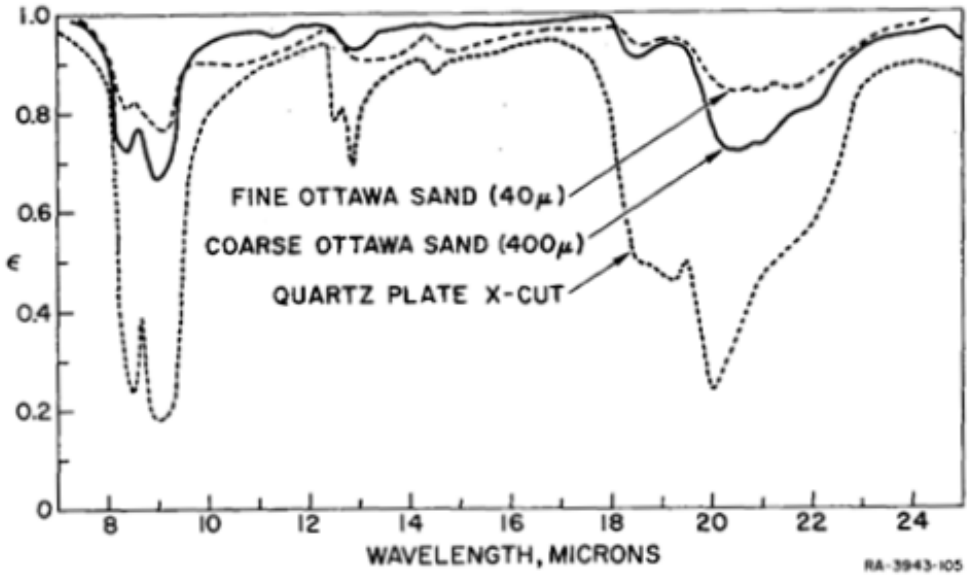

Figure 7.1: This figure shows how emissivity spectra of quartz can vary based on sample size. Figure from Lyon (1964): *"Spectra for fine Ottawa sand (40 μm) are dashed and for coarse Ottawa sand (400 μm) are as solid curves. An X-cut quartz plate is shown as the lower (dashed) curve in the figure."*

and Glotch (2019), whole rock emissivity may be greater than that of particulate samples when measured under low-temperature vacuum conditions. This possibility is discussed in the next section.

Under vacuum or low-pressure conditions, emissivity spectra are typically lower in intensity than those measured at ambient pressure (Logan and Hunt, 1970; Logan et al., 1973; Henderson et al., 1996; Hanna et al., 2012; Thomas et al., 2012a; Shirley and Glotch, 2019). Lower pressures and temperatures reduce the amount of thermal radiation emitted onto the sample, causing the surface to cool more quickly than the interior, creating a steep temperature gradient (Logan and Hunt, 1970; Logan et al., 1973; Henderson and Jakosky, 1994; Henderson and Jakosky, 1997). These gradients lower the average emissivity, as the emitted radiation becomes dominated by the cooler surface rather than the warmer interior.

To estimate radiative heat loss using Equation 3.11, the average emissivity can be used. This value can be determined by integrating emissivity over the thermal IR wavelength range of 8 to 14 μm, as described in Appendix E. This concept is also further addressed in the

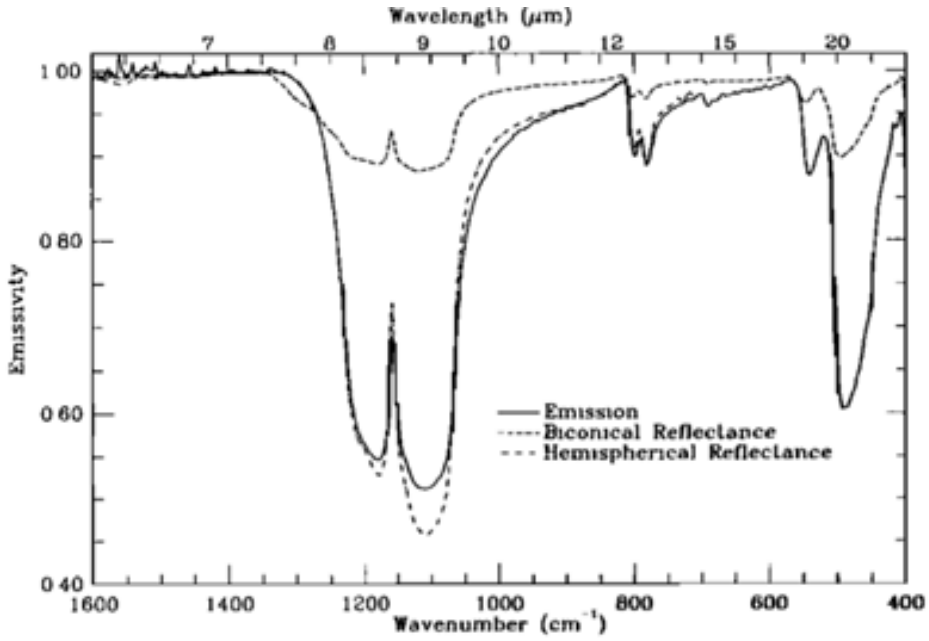

Figure 7.2: Comparison of emissivity derived from biconical and hemispherical reflectance spectra using Kirchhoff's law ($\varepsilon = 1 - R$) with a directly measured emissivity spectrum. Differences between the converted and measured data highlight the limitations of Kirchhoff's law. Figure Christensen et al. (2000).

following section.

According to Kirchhoff's law ($\varepsilon = 1 - R$), reflectance spectra (R) can be converted to emissivity, provided that hemispherical reflectance is used. This is because biconical and bidirectional reflectance measurements do not account for backscattered radiation, whereas hemispherical measurements incorporate scattering in all directions (Nicodemus, 1965; Salisbury and D'Aria, 1992; Salisbury et al., 1994; Christensen et al., 2000; Hapke, 2012). Figure 7.2 illustrates this difference: emissivity derived from biconical reflectance has less spectral contrast than that derived from hemispherical reflectance. Kirchhoff's law is valid at any temperature, provided that isothermal conditions are maintained; the presence of a thermal gradient violates this assumption and does not yield true emissivity (Salisbury and Walter, 1989; Henderson et al., 1996).

7.2 Single-Crystal Emissivity

Average emissivity values representative of the four single-crystal minerals analyzed in this study (quartz, calcite, albite, and pyrite), along with obsidian, were calculated using the integration method described in Appendix E. These values are presented in Table 7.1, and the corresponding emissivity spectra used in their calculation are shown in Figures 7.3 to 7.7. It is important to note that these values were not directly measured from the same samples used for thermal conductivity analysis. Instead, they serve as illustrative examples of how average emissivity can be estimated using existing spectral data and the integration method. Because emissivity is a sample-dependent property, these values should be considered as general references only. Direct emissivity measurements are recommended for any sample prior to thermal conductivity measurements. In cases where emissivity measurements are conducted under ambient conditions, the resulting values may still offer a reasonable approximation for solid samples, as discussed below.

Like thermal conductivity, emissivity is also an anisotropic property. Anisotropic minerals exhibit variations in their emissivity spectra depending on the orientation of their surface relative to the optic axis (Lane, 1999; Lane and Bishop, 2019; Salisbury et al., 1991b; Wenrich and Christensen, 1996). This effect is illustrated in Figure 7.3, which shows emissivity spectra for two quartz samples measured parallel and perpendicular to the c-axis, from Wenrich and Christensen (1996). Although calcite and albite are anisotropic, only one average emissivity value is included for each in Table 7.1. While Lane (1999) reported orientation-dependent emissivity spectra for calcite, those measurements were based on Icelandic spar, which is optically distinct from the calcite used in this study. Therefore, an average emissivity value was calculated from five calcite spectra in the ASU Spectral Library v1.1 (Christensen et al., 2000). For albite, orientation-specific emissivity data were not available, so the average emissivity was estimated using a spectrum from an unshocked chip reported by Johnson et al. (2003). A pyrite spectrum was provided directly by Dr. Melissa Lane (Fibernetics LLC),

and the emissivity of obsidian was calculated from a hemispherical reflectance spectrum in the ECOSTRESS Spectral Library (Baldridge et al., 2009; Meerdink et al., 2019), using Kirchhoff's law.

Table 7.1: Calculated average emissivity values for single crystal samples.

Sample	**Average Emissivity**	**Source**
Quartz	c-axis: 0.71 a-axis: 0.78	Wenrich and Christensen (1996)
Calcite	0.94	ASU Spectral Library (Christensen et al., 2000), average of calcite #507, #508, #509, #511, and #519
Pyrite	0.90	Provided by M. Lane (personal communication)
Albite	0.90	Johnson et al. (2003), unshocked plagioclase chip
Obsidian	0.85	ECOSTRESS Spectral Library (Baldridge et al., 2009; Meerdink et al., 2019)

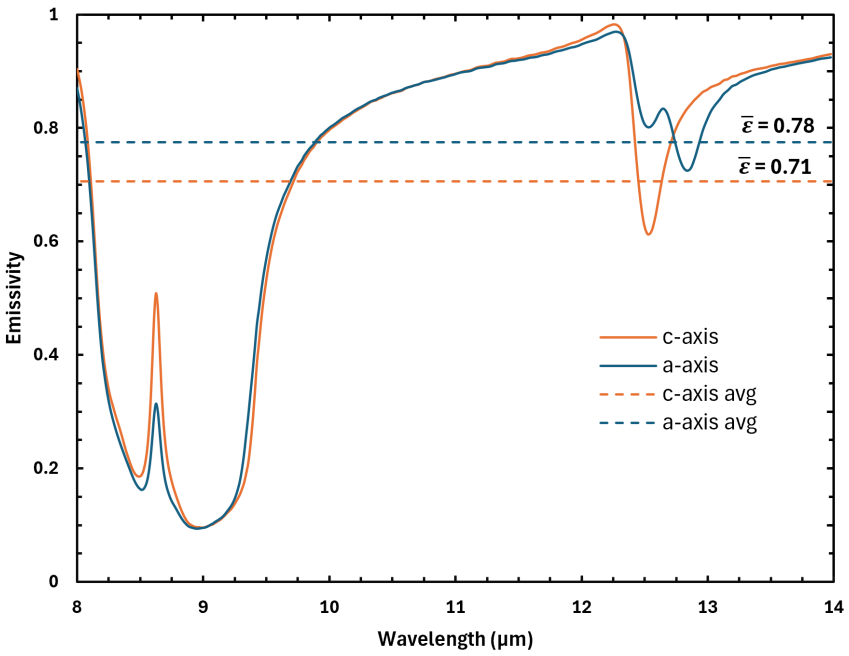

Figure 7.3: Emissivity spectra of two quartz samples measured along the c- and a-axes. Dashed lines indicate the calculated average emissivity for each orientation. Data from Wenrich and Christensen (1996).

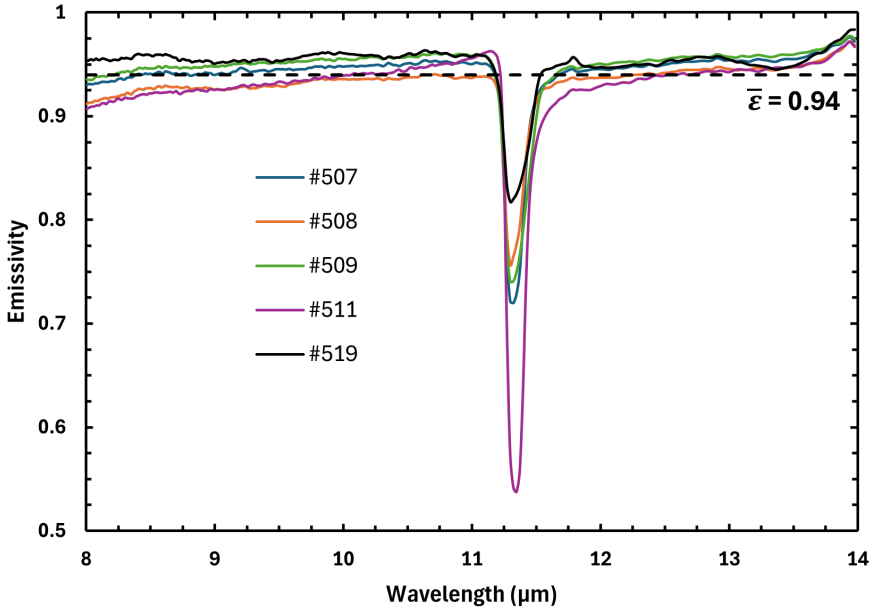

Figure 7.4: Emissivity spectra of five calcite samples (#507, #508, #509, #511, and #519) from the ASU Spectral Library (Christensen et al., 2000). Sample orientations are unknown. The dashed line indicates the calculated average emissivity across all five samples.

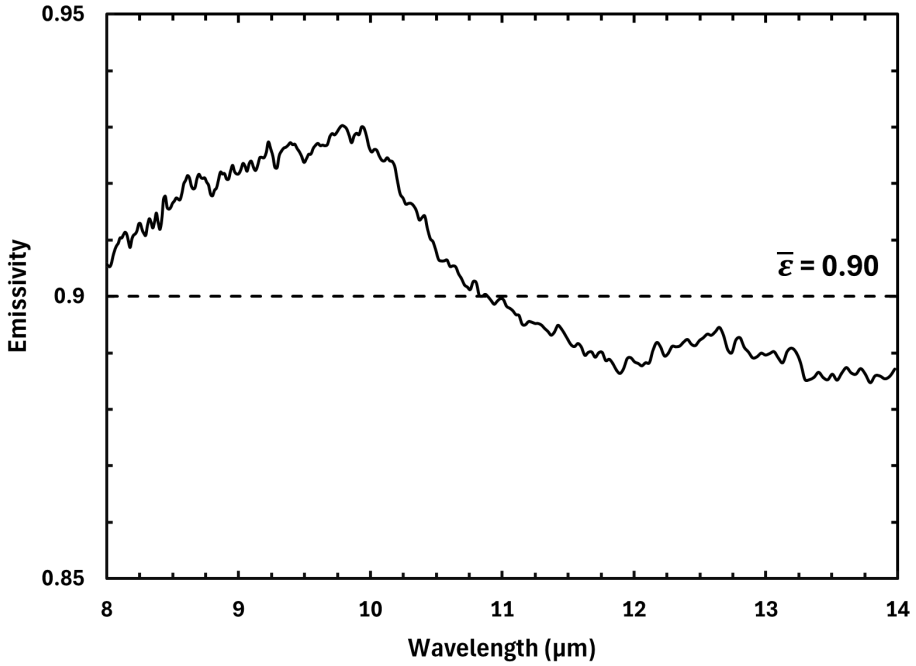

Figure 7.5: Emissivity spectrum of a solid pyrite sample provided by M. Lane (personal communication). The dashed line represents the calculated average emissivity.

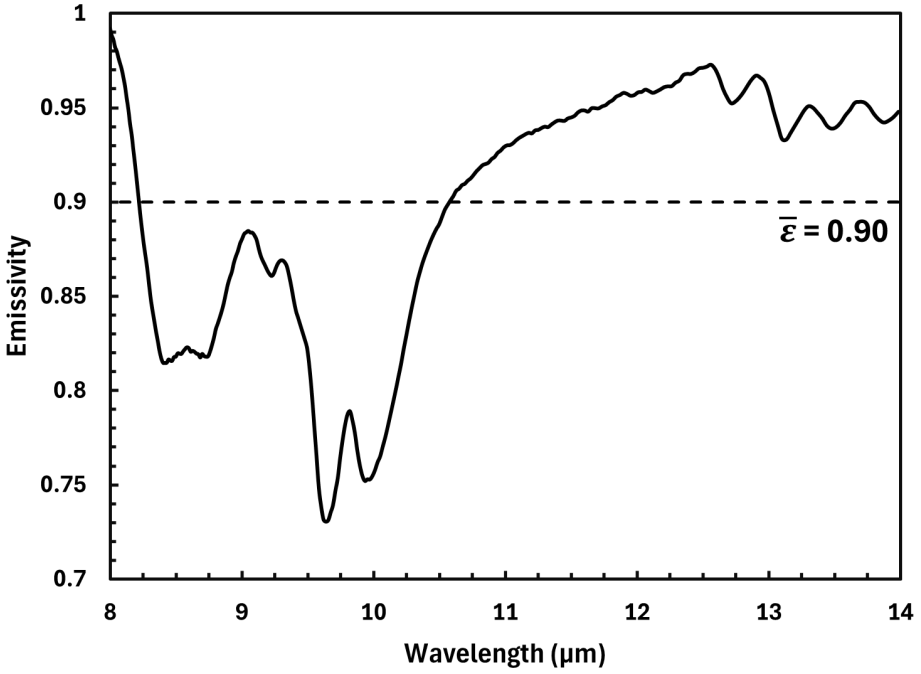

Figure 7.6: Emissivity spectrum of an unshocked albite chip from Johnson et al. (2003). The sample orientation is unknown. The dashed line represents the calculated average emissivity.

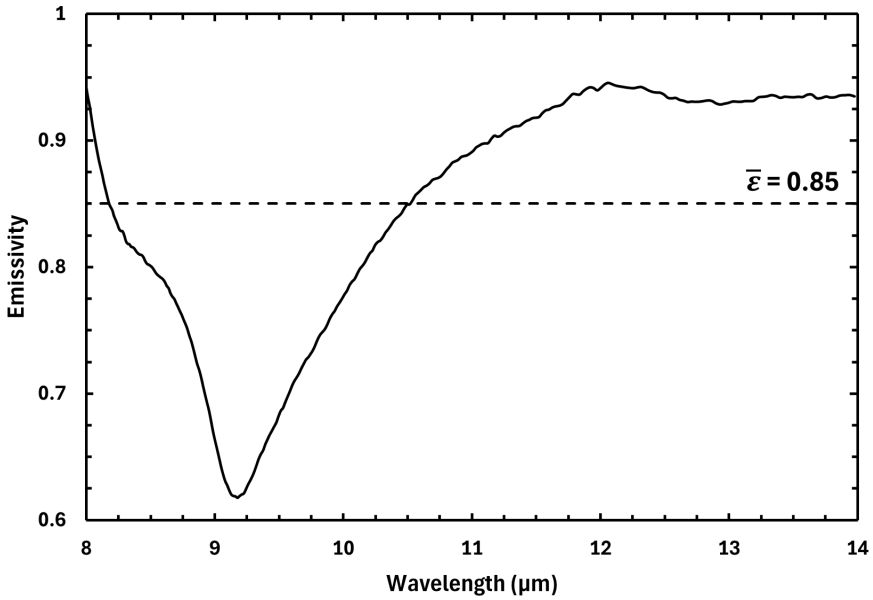

Figure 7.7: Emissivity spectrum of a solid obsidian sample, converted from hemispherical reflectance, obtained from the ECOSTRESS Spectral Library (Baldridge et al., 2009; Meerdink et al., 2019), using Kirchhoffs law. The dashed line represents the calculated average emissivity.

The values listed in Table 7.1 were calculated from data collected under ambient pressure and temperature conditions. Although the behaviour of emissivity in solid samples under vacuum is not well understood, it can be reasonably assumed that emissivity remains relatively constant between ambient and cryogenic vacuum conditions. This assumption is supported by mineral spectral data from Shirley and Glotch (2019). For this study, average emissivity values were calculated from their spectra measured under both ambient and simulated lunar conditions (temperature and pressure). When plotted, these values show increasing similarity between the two measurement conditions as grain size increases (Figure 7.8). Shirley and Glotch (2019) attributed this trend to the presence of thermal gradients, which become more pronounced under the vacuum and temperature conditions of the simulated lunar environment. Larger grains span more of the gradient depth, so the emitted infrared signal reflects a broader range of internal temperatures, reducing spectral contrast and making the emissivity more comparable to that measured under ambient conditions.

Because all samples in this study were fully thermalized to the CFMS chamber tem-

perature prior to thermal conductivity measurements, the effects of internal temperature gradients are minimized. As a result, emissivity spectra collected under ambient conditions may be suitable for correcting radiative heat loss in thermal conductivity measurements using the Stefan–Boltzmann law. However, further investigation is needed to evaluate the accuracy of this assumption for cryogenic vacuum-based thermophysical studies of solid materials.

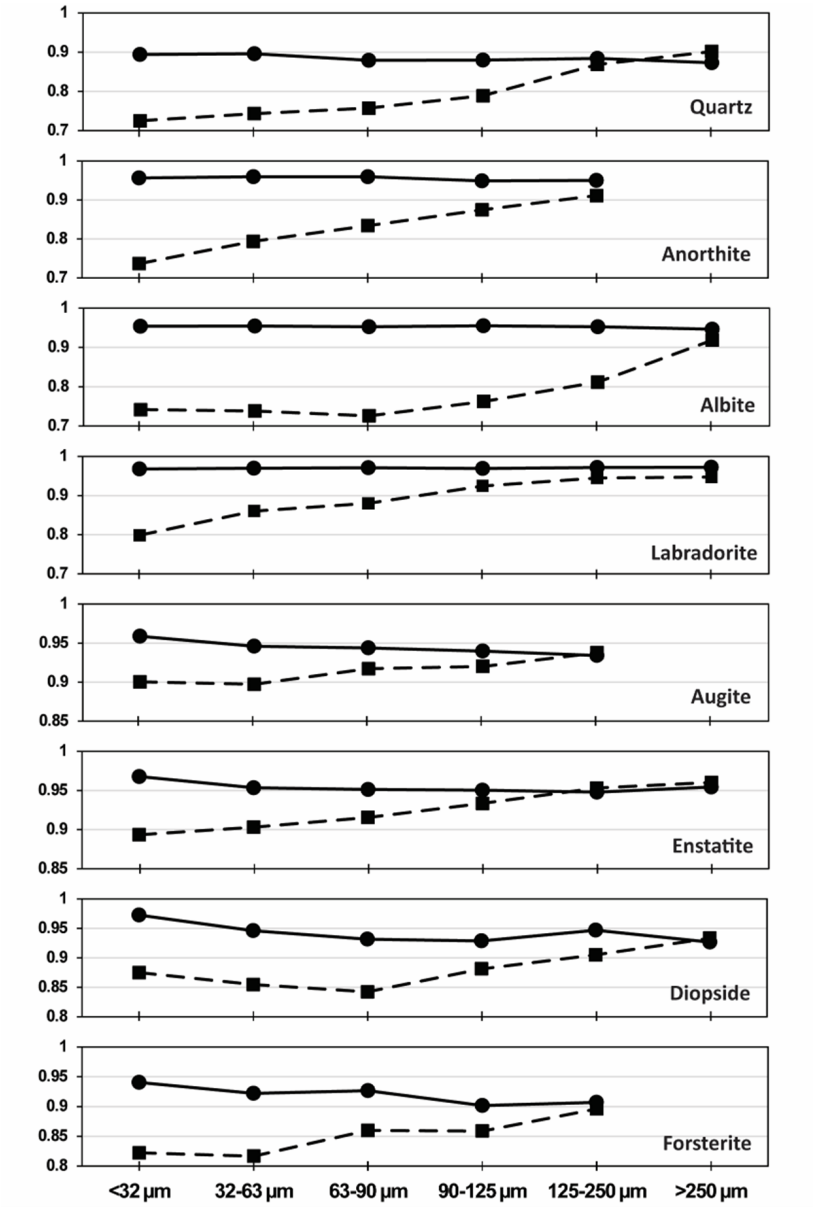

Figure 7.8: Comparison of the average emissivity (y-axis) of silicate grain size fractions (x-axis) under ambient (solid line) and simulated lunar (dashed line) conditions. Average emissivity values were calculated from spectral data collected by Shirley and Glotch (2019).

7.3 Meteorite Emissivity

For stony meteorites such as ordinary and carbonaceous chondrites, some average emissivity values are reported in the physical property summary by Ostrowski and Bryson (2019). In this summary, Allende (CV3) is reported to have an average emissivity of 0.993. H4 chondrites, representative of Buzzard Coulee, have an average emissivity of 0.990, while the average emissivity for L6 and LL6 chondrites, representative of Holbrook, is 0.986. The overall average emissivity for all chondrite meteorites reported in the summary by Ostrowski and Bryson (2019) is 0.99. Ostrowski and Bryson (2019) noted that the oxidation of iron in Antarctic L6 chondrites results in a slight reduction in emissivity; however, this effect is considered to be within the measurement uncertainty of the group average. Therefore, the presence of oxidized iron in Holbrook (Chapter 4.4) is not expected to affect its radiative properties significantly.

The average emissivity values reported by Ostrowski and Bryson (2019) were derived from reflectance spectra of particulate samples collected over 8 to 14 μm under ambient conditions, using data from Salisbury et al. (1991a) and Baldridge et al. (2009). While the specific calculation method is not mentioned, it is assumed to be similar to the integration method described in Appendix E. As a complement to the particulate analysis, Ostrowski and Bryson (2020) measured emissivity directly from 1.5 cm cubes of ordinary chondrites using a thermal thermometer and found values ranging approximately from 0.98 to 0.99. These results suggest that the emissivity of particulate and solid ordinary chondrites is generally comparable under ambient conditions, likely governed more by bulk composition than by sample form or texture (Ostrowski and Bryson, 2020).

In contrast, the emissivity of iron meteorites, such as North Chile, is not as well established and requires further investigation. Ostrowski and Bryson (2019) reported a total emissivity of 0.67 for the Odessa iron meteorite. However, Odessa is an oxidized type IAB octahedrite containing silicate clasts and inclusions (Bunch et al., 1970; Buchwald, 1975b;

Choi et al., 1995; Pirim et al., 2014), whereas North Chile is a IIAB hexahedrite composed primarily of kamacite, with rhabdite (schreibersite) inclusions (Chapter 4.4). Since silicate minerals tend to have high emissivity (Table 7.1), and oxidation is known to increase emissivity (Jo et al., 2017), Odessa is likely to have a higher emissivity than North Chile.

The emissivity of North Chile can be estimated based on a thermal IR reflectance spectrum for a chip of the Sikhote-Alin IIAB iron meteorite (ID: TB-MDD-364) that is available on the PDS Geosciences Node spectral library (Milliken, 2020); however, this data was acquired using biconical reflectance geometry, which prevents direct emissivity conversion using Kirchhoff's law. As discussed earlier, biconical-derived emissivity underestimates spectral contrast relative to hemispherical measurements, due to limited directional scattering (Figure 7.2). While biconical reflectance-based emissivity does not satisfy Kirchhoff's law, it can serve as a conservative upper limit. Based on the Sikhote-Alin data, this suggests that North Chile's emissivity does not exceed 0.52.

Given that North Chile's composition is dominated by iron, the emissivity of polished iron was used as a reference. Polished iron has emissivity values that can range between 0.14 and 0.38 (Beysens, 2022). Since the surface of North Chile exhibits cracks and polish marks (Figure 4.37), which increase surface roughness and therefore also increase emissivity (Jo et al., 2017), the upper bound of 0.38 is the most representative estimate. This value satisfies the requirement that North Chile's emissivity be lower than that of Odessa (0.67) and the biconical-derived upper limit from Sikhote-Alin (0.52). Of course, this estimate should be validated through direct measurement.

7.4 Thermal Assembly Considerations

As mentioned in Chapter 3 (Section 3.3.3), the thermal assemblies and silver epoxy are also sources of radiative heat loss. The radiating surfaces of the heater and thermocouple hot tab consist of a copper-alloy tab and STYCAST 2850FT black epoxy, while the silver epoxy used to bond the thermal assemblies to the sample is a conductive adhesive from RS

PRO. However, quantifying radiation from these components (Equation 3.9) is challenging because the size, geometry, and epoxy distribution vary from sample to sample (Figure 3.6). These surfaces are irregular, and the proportion of exposed copper versus STYCAST differs between assemblies, affecting the overall emissivity. As a result, the effective emissivity and total radiating surface area are difficult to determine with precision. Accurate surface area estimates would likely require X-ray computed tomography (XCT) analysis. In addition to surface area investigations, the emissivity of each individual component (STYCAST epoxy, copper tab, and silver epoxy) should be measured separately to better constrain the effective emissivity based on their relative surface areas. Preliminary emissivity estimates for these components are provided below.

The silver epoxy used in this project is a 1:1 mixture of silver epoxy resin and hardener. Although not the exact composition, an emissivity of 0.15 has been reported for a 1:1 mixture of Ag powder and epoxy resin (Zhang et al., 2023).

The emissivity of STYCAST 2850FT is not well known. One study used an emissivity of 0.8 during the development of microwave calibration units (Schröder et al., 2017), although this may be low compared to other black epoxies. MAP® EPOX BLACK ESD, a black electrically conductive epoxy used in space applications, has reported emissivities of 0.83 for 7 µm thick coatings and 0.90 for 14 µm thick coatings (Reymond et al., 2021). In comparison, NASA reports that black coatings commonly used for thermal management exhibit emissivity values ranging from 0.84 to 0.94 (Henninger, 1984). Averaging these values, including the 0.9 value for MAP® EPOX BLACK ESD and the 0.8 value from Schröder et al. (2017), yields 0.89 ± 0.01, which coincidentally matches the reported emissivity for black epoxy paint (Beysens, 2022). Therefore, an emissivity of 0.89 is considered a reasonable estimate for STYCAST.

The copper tabs used for the thermocouple and heater assemblies have a semi-reflective surface with visible polishing or etching marks (Figure 7.9). The surface texture suggests increased roughness, which typically results in higher emissivity than polished copper. The

emissivity of polished copper generally is between 0.02 and 0.05 (Beysens, 2022), whereas roughly polished and etched copper have reported emissivities of 0.07 and 0.09, respectively (OMEGA Engineering, n.d.). Given the surface condition and possible oxidation, the emissivity of the copper tabs may exceed 0.1, though this remains a rough estimate.

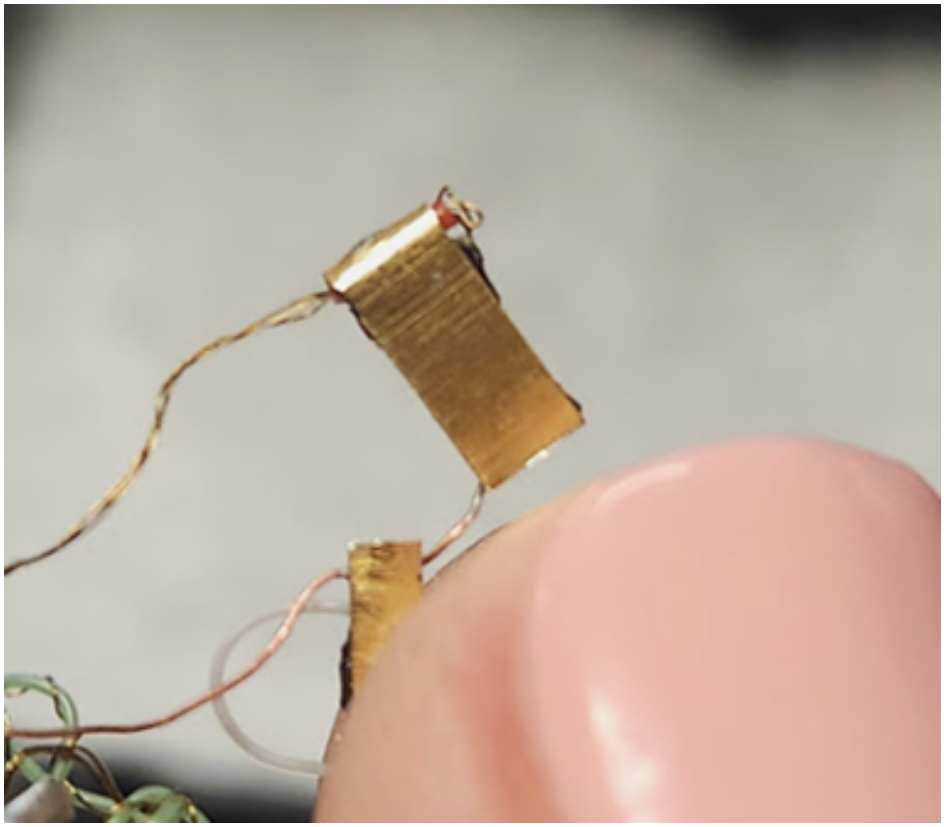

Figure 7.9: Copper heater tab showing a semi-reflective surface with fine surface marks, possibly from etching or polishing.

8 Conclusions and Future Work

8.1 Conclusion

This dissertation describes the successful adaptation of the Cryogen-Free Measurement System (CFMS) for measuring the thermal conductivity of geological materials, with a particular focus on planetary samples such as meteorites. Using this approach, thermal conductivity was successfully measured below 300 K under vacuum conditions ($< 10^{-4}$ mbar), extending the instrument's application beyond its original industrial purpose. Achieving this objective required addressing several practical and methodological challenges. Sample preparation was a critical aspect of the study, particularly for friable meteorite samples. Because mechanical cutting often caused sample damage, hand-polishing techniques were implemented to preserve structural integrity while achieving the required geometries for thermal conductivity measurements. Procedural adaptations for geological samples included determining appropriate thermalization times to ensure thermal equilibrium at each temperature, and developing a rigorous data quality protocol to assess each measurement based on stability duration, PID behaviour, and temperature drift.

A significant challenge in steady-state thermal conductivity measurements is heat loss through radiation. Although the CFMS thermal probe includes a radiation shield, it does not eliminate radiative contributions, particularly above 100 K. This loss results in an overestimation of thermal conductivity that obscures the true thermal response of the material. To address this effect, a correction method was implemented based on the approach described by MacPherson and Schloessin (1982) and Pope et al. (2001), using temperature-dependent models fitted to low-temperature data where radiative losses are minimal. These models were tailored to each material type: a linear 1/T dependence for crystalline minerals, a log(T) dependence for amorphous obsidian, and an empirically derived model for meteorites. Extrapolating these fits to 300 K provided reliable estimates of the true thermal conductivity

at higher temperatures. The validity of this correction method was confirmed by comparison with published thermal conductivity values for comparable geological materials.

Thermal conductivity measurements from this study offer new insight into heat transport in terrestrial geological materials at cryogenic temperatures. The behaviour of the single-crystal minerals quartz, calcite, pyrite, and albite generally aligns with theoretical models of phonon transport in insulating solids, where thermal conductivity is governed by phonon–phonon, impurity, and boundary scattering. These results highlight the anisotropic nature of thermal conductivity in crystalline materials. In anisotropic minerals, heat flow varies with crystallographic orientation, whereas in isotropic minerals such as pyrite, differences in conductivity are primarily governed by impurities and grain boundaries. Pyrite exhibits a distinct thermal conductivity peak at low temperatures, reflecting a transition from boundary and impurity scattering to phonon–phonon scattering as temperature increases. In albite, which commonly exhibits polysynthetic twinning, a thermal conductivity peak is observed when heat flows parallel to the twin planes, but is suppressed when heat flows across them due to increased phonon scattering at twin boundaries. Quartz and calcite have steep increases in thermal conductivity below 50 K, with values exceeding their room-temperature conductivity by more than an order of magnitude. At these low temperatures, the high thermal conductivity reduces the temperature gradient across the sample, making stable measurements difficult due to thermocouple sensitivity and temperature drift. As a result, thermal conductivity in these minerals could not be measured below 30 K.

Obsidian, a volcanic glass, offers a valuable contrast to the crystalline minerals. Due to its disordered atomic structure, heat conduction in obsidian does not follow the same phonon transport pathways as in crystalline solids. Instead, thermal energy is transported by delocalized vibrational modes known as propagons and diffusons, which dominate at different temperature regimes. A plateau in the thermal conductivity of obsidian is observed between approximately 5 and 20 K, consistent with a transition from propagating, wave-like transport (propagons) to more diffusive behaviour (diffusons) (Allen et al., 1999). Above this range,

thermal conductivity increases gradually with temperature, following a logarithmic trend. Because amorphous materials lack long-range periodicity, they do not exhibit a well-defined high-temperature dependence predicted by phonon-based models. Therefore, the observed trend in obsidian is purely empirical. However, when this logarithmic fit was used to model radiative corrections, the resulting corrected thermal conductivity at 300 K closely matched the average value reported in the literature, supporting the reliability of this approach.

Like obsidian, meteorites present a unique challenge for thermal conductivity analysis due to their structural complexity. Although composed of crystalline minerals, their bulk thermal behaviour more closely resembles that of disordered materials. This is primarily due to structural features such as porosity, microcracks, and grain boundaries, which limit the phonon mean free path and suppress thermal conductivity across all temperatures. Measurements in this study confirm that porosity is the primary influence on thermal conductivity in stony meteorites, whereas grain boundary scattering has a more significant effect in low-porosity samples such as the iron meteorite North Chile. Despite these complexities, the results align well with previous studies on ordinary chondrites and iron meteorites (Opeil et al., 2010; Opeil et al., 2012; Noyes et al., 2022), demonstrating that comparable thermal conductivity values can be obtained even in structurally anisotropic samples. This agreement with literature values supports the use of the CFMS method for the analysis of planetary materials.

In addition to validating the CFMS method, the thermal conductivity data collected from meteorites provide insight into how heat was conducted within their parent bodies. Internal structural features, such as porosity and grain boundaries, can produce anisotropic thermal behaviour, even among samples from the same meteorite type. Whether these directional effects persist at larger scales or are averaged out by multidirectional heat flow and lithologic mixing remains unclear. If anisotropy is retained, it has important implications for how meteorite parent bodies evolved in response to internal heating and cooling. Addressing this question will require an integrated approach combining laboratory measurements, thermal

modelling, and in-situ data from future planetary missions.

This study presents direct thermal conductivity measurements intended to support future modelling of parent body evolution. These data more accurately represent the thermal behaviour of parent body material than commonly used estimates based on mineral constituents or analogue materials, as they capture the effects of internal structural heterogeneity. Incorporating these data into heat flow models will enable researchers to better constrain internal thermal histories and refine predictions of parent body evolution. Ultimately, this study contributes not only to our understanding of meteoritic materials but also to broader efforts to model the thermal evolution of small planetary bodies.

8.2 Future Work

There are several opportunities to advance the methods developed in this study and expand the measured dataset. A key priority is to improve the reliability of thermal conductivity measurements below 30 K. This includes refining procedures to better control thermal gradients and reduce temperature drift, particularly in highly conductive geological samples. One approach involves systematically varying sample geometry, such as cross-sectional area and thermocouple spacing, for materials like quartz to determine the optimal dimensions for stable low-temperature measurements. Additionally, alternative techniques such as the heat-pulse method could be explored to improve measurement accuracy.

Future work should include additional measurements of obsidian to evaluate the reliability of the logarithmic temperature trend used in the radiative correction model. Expanding the analysis to other glasses and disordered solids would offer valuable insight into heat transport in amorphous materials, which remains poorly understood. A more comprehensive dataset would help clarify whether the observed logarithmic behaviour in obsidian is representative of a broader class of disordered materials.

Since heat transfer in metallic samples like pyrite and North Chile involves both phonons and electrons, further work should aim to separate these contributions. The CFMS is capa-

ble of measuring electrical resistivity, which can be used with the Wiedemann–Franz law to estimate the electronic component of thermal conductivity. This approach would be particularly valuable for confirming prior findings, such as those for pyrite by Popov et al. (2013) and Zuñiga-Puelles et al. (2019), which suggest a negligible electronic contribution. Isolating the lattice and electronic components would also offer further insight into the apparent lack of radiative heat loss in pyrite and North Chile. This analysis is especially relevant for iron meteorites, which often exhibit amorphous-like thermal behaviour, suggesting that electrons are the dominant energy carrier. By separating these contributions, it becomes possible to better identify the limiting factors that control heat transport in metal-rich meteorites.

Following the work of Opeil et al. (2010, 2012, 2020), Noyes et al. (2022), and Macke et al. (2024), future efforts should focus on expanding the thermal conductivity dataset for meteorites. Now that the CFMS method has been validated for these materials, a broader suite of measurements can be collected for meteorites with varying porosity, mineralogy, and shock histories. This expanded dataset would help refine the empirical model used for radiative corrections in stony meteorites and support more meaningful comparisons of thermal behaviour across different meteorite types. In addition to thermal conductivity, the CFMS can also be used to measure heat capacity. When combined with existing density data, these measurements allow for accurate estimation of thermal diffusivity and contribute to a more comprehensive understanding of internal heat transport in planetary materials.

Finally, it would be worthwhile to directly measure the emissivity of the CFMS thermal assemblies, including the silver epoxy used to bond these components to the samples. Knowing these values would help determine how much the assemblies contribute to radiative heat loss during thermal conductivity measurements. There is also a broader lack of emissivity data for solid geological materials, particularly under vacuum and at cryogenic temperatures. Obtaining such data and understanding how emissivity changes under experimental conditions would support the use of the radiative correction model defined in Equation 3.9 and help validate or refine the empirical fitting approach used in this study.

References

Allen, P. B., and F. and Wooten (1999). Diffusons, Locons and Propagons: Character of Atomic Vibrations in Amorphous Si. *Philosophical Magazine B* 79.11–12, pp. 1715–1731. DOI: 10.1080/13642819908223054.

Altunayar-Unsalan, C., O. Unsalan, M. A. Szurgot, and R. A. Wach (2021). Specific Heat and Thermal History of the Sariçiçek Howardite. *Meteoritics & Planetary Science* 56.11, pp. 2103–2117. DOI: 10.1111/maps.13754.

Altunayar-Unsalan, C., O. Unsalan, R. A. Wach, and M. A. Szurgot (2025). Physical and Thermal Properties of Bursa L6 Chondrite: A Combination of Density, Porosity, Specific Heat, Water Content, Thermal Conductivity, and Thermal Diffusivity Results. *Astrophysics and Space Science* 370.5, p. 53. DOI: 10.1007/s10509-025-04443-6.

Anderson, P. w., and c. M. and Varma (1972). Anomalous Low-Temperature Thermal Properties of Glasses and Spin Glasses. *The Philosophical Magazine: A Journal of Theoretical Experimental and Applied Physics* 25.1, pp. 1–9. DOI: 10.1080/14786437208229210.

Arai, T., T. Nakamura, S. Tanaka, H. Demura, Y. Ogawa, N. Sakatani, Y. Horikawa, H. Senshu, T. Fukuhara, and T. Okada (2017). Thermal Imaging Performance of TIR Onboard the Hayabusa2 Spacecraft. *Space Science Reviews* 208.1, pp. 239–254. DOI: 10.1007/s11214-017-0353-9.

Aronson, J. R., L. H. Bellotti, S. W. Eckroad, A. G. Emslie, R. K. McConnell, and P. C. von Thüna (1970). Infrared Spectra and Radiative Thermal Conductivity of Minerals at High Temperatures. *Journal of Geophysical Research (1896-1977)* 75.17, pp. 3443–3456. DOI: 10.1029/JB075i017p03443.

Baggioli, M. and A. Zaccone (2020). Unified Theory of Vibrational Spectra in Hard Amorphous Materials. *Physical Review Research* 2.1, p. 013267. DOI: 10.1103/PhysRevResearch.2.013267.

Baldridge, A. M., S. J. Hook, C. I. Grove, and G. Rivera (2009). The ASTER Spectral Library Version 2.0. *Remote Sensing of Environment* 113.4, pp. 711–715. DOI: 10.1016/j.rse.2008.11.007.

Bates, H. C., R. Aspin, C. Y. Fu, C. S. Harrison, E. Feaver, E. Branagan-Harris, A. J. King, J. F. J. Bryson, S. Sridhar, and C. I. O. Nichols (2024). Extent of Alteration, Paleomagnetic History, and Infrared Spectral Properties of the Tarda Ungrouped Carbonaceous Chondrite. *Meteoritics & Planetary Science* 59.9, pp. 2411–2431. DOI: 10.1111/maps.14224.

Beck, A., D. Darbha, and H. Schloessin (1978). Lattice Conductivities of Single-Crystal and Polycrystalline Materials at Mantle Pressures and Temperatures. *Physics of the Earth and Planetary Interiors* 17.1, pp. 35–53. DOI: 10.1016/0031-9201(78)90008-0.

Beech, M., I. M. Coulson, W. Nie, and P. McCausland (2009). The Thermal and Physical Characteristics of the Gao-Guenie (H5) Meteorite. *Planetary and Space Science* 57.7, pp. 764–770. DOI: 10.1016/j.pss.2009.01.002.

Beltukov, Y. M., C. Fusco, D. A. Parshin, and A. Tanguy (2016). Boson Peak and Ioffe-Regel Criterion in Amorphous Siliconlike Materials: The Effect of Bond Directionality. *Physical Review E* 93.2, p. 023006. DOI: 10.1103/PhysRevE.93.023006.

Beltukov, Y. M., V. I. Kozub, and D. A. Parshin (2013). Ioffe-Regel Criterion and Diffusion of Vibrations in Random Lattices. *Physical Review B* 87.13, p. 134203. DOI: 10.1103/PhysRevB.87.134203.

Beysens, D. (2022). *Dew Water*. CRC Press. 370 pp. ISBN: 978-1-000-79391-8.

Birch, A. F. and H. Clark (1940a). The Thermal Conductivity of Rocks and Its Dependence upon Temperature and Composition, Part 1. *American Journal of Science* 238.8, pp. 529–558.

Birch, A. F. and H. Clark (1940b). The Thermal Conductivity of Rocks and Its Dependence upon Temperature and Composition, Part 2. *American Journal of Science* 238.9, pp. 613–635.

Birch, F. (1942). "Thermal conductivity and diffusivity". In: *Handbook of Physical Constants*. Ed. by F. Birch, J. F. Schairer, and H. C. Spicer. Vol. 36. Special Paper. New York: Geological Society of America, pp. 243–266.

Bischoff, A., E. R. D. Scott, K. Metzler, and C. A. Goodrich (2006). "Nature and Origins of Meteoritic Breccias". In: *Meteorites and the Early Solar System II*. Ed. by D. S. Lauretta and H. Y. McSween. University of Arizona Press, pp. 679–712.

Blackwell, D. D. and J. L. Steele (1989). "Thermal conductivity of sedimentary rocks: measurement and significance". In: *Thermal history of sedimentary basins: methods and case histories*. Springer, pp. 13–36.

Bland, P. A., F. J. Berry, and C. T. Pillinger (1998). Rapid Weathering in Holbrook: An Iron-57 Mössbauer Spectroscopy Study. *Meteoritics & Planetary Science* 33.1, pp. 127–129. DOI: 10.1111/j.1945-5100.1998.tb01614.x.

Bland, P. A., M. E. Zolensky, G. K. Benedix, M. A. Sephton, R. P. Binzel, R. M. Walker, and A. G. W. Cameron (2006). "Weathering of Chondritic Meteorites". In: *Meteorites and the Early Solar System II*. Ed. by D. S. Lauretta and H. Y. McSween. University of Arizona Press, pp. 853–868. DOI: 10.2307/j.ctv1v7zdmm.45.

Blinova, A. I., T. J. Zega, C. D. K. Herd, and R. M. Stroud (2014). Testing variations within the Tagish Lake meteorite–I: Mineralogy and petrology of pristine samples. *Meteoritics & Planetary Science* 49, pp. 473–502.

Bonal, L., E. Quirico, M. Bourot-Denise, and G. Montagnac (2006). Determination of the Petrologic Type of CV3 Chondrites by Raman Spectroscopy of Included Organic Matter. *Geochimica et Cosmochimica Acta* 70.7, pp. 1849–1863. DOI: 10.1016/j.gca.2005.12.004.

Bottke, W. F., D. Vokrouhlický, D. P. Rubincam, and D. Nesvorný (2006). THE YARKOVSKY AND YORP EFFECTS: Implications for Asteroid Dynamics. *Annual Review of Earth and Planetary Sciences* 34.1, pp. 157–191. DOI: 10.1146/annurev.earth.34.031405.125154.

Brearley, A. J. and R. H. Jones (1998). "Chondritic meteorites". In: *Reviews in Mineralogy, Volume 36: Planetary Materials*. Ed. by J. J. Papike. Washington: Mineralogical Society of America, pp. 3-1–3-398.

Britt, D. T. and G. J. S. J. Consolmagno (2003). Stony Meteorite Porosities and Densities: A Review of the Data through 2001. *Meteoritics & Planetary Science* 38.8, pp. 1161–1180. DOI: 10.1111/j.1945-5100.2003.tb00305.x.

Browning, L. B., H. Y. J. McSween, and M. E. Zolensky (1996). Correlated alteration effects in CM carbonaceous chondrites. *Geochimica et Cosmochimica Acta* 60, pp. 2621–2633.

Buchwald, V. F. (1975a). *Handbook of Iron Meteorites Volume 1*. Vol. 1. 3 vols.

Buchwald, V. F. (1975b). "Iron Meteorites: North Portugal – Okahandja". In: *Handbook of Iron Meteorites: Their History, Distribution, Composition and Structure*. University of California Press, pp. 937–942.

Buchwald, V. F. (1975c). "Iron Meteorites: Norfork - North Chile (Union)". In: *Handbook of Iron Meteorites Volume 3*. University of California Press.

Bunch, T., K. Keil, and E. Olsen (1970). Mineralogy and Petrology of Silicate Inclusions in Iron Meteorites. *Contributions to Mineralogy and Petrology* 25.4, pp. 297–340. DOI: 10.1007/BF00399290.

Butler, C. P. and R. J. Jenkins (1963). Thermal Properties of Meteoritic Iron from -150° to 300° Celsius. *Science* 139.3554, pp. 486–487. DOI: 10.1126/science.139.3554.486.

Cahill, D. G. and R. O. Pohl (1988). Lattice Vibrations and Heat Transport in Crystals and Glasses. *Annual Review of Physical Chemistry* 39 (Volume 39,), pp. 93–121. DOI: 10.1146/annurev.pc.39.100188.000521.

Cahill, D. G. and R. O. Pohl (1987). Thermal Conductivity of Amorphous Solids above the Plateau. *Physical Review B* 35.8, pp. 4067–4073. DOI: 10.1103/PhysRevB.35.4067.

Cahill, D. G. and R. O. Pohl (1989). Heat Flow and Lattice Vibrations in Glasses. *Solid State Communications* 70.10, pp. 927–930. DOI: 10.1016/0038-1098(89)90630-3.

Campbell, A. J. and M. Humayun. 1999. Microanalysis of Platinum Group Elements in Iron Meteorites Using Laser Ablation ICP-MS. Lunar and Planetary Science Conference. Abstract #1974. CD-ROM.

Casimir, H. B. G. (1938). Note on the Conduction of Heat in Crystals. *Physica* 5.6, pp. 495–500. DOI: 10.1016/S0031-8914(38)80162-2.

Čermák, V. and L. Rybach (1982). "Thermal properties: Thermal conductivity and specific heat of minerals and rocks". In: *Landolt-Börnstein: Numerical Data and Function Relationships in Science and Technology*. Ed. by G. Angenesister. Vol. 1a. Berlin: Springer, pp. 305–343.

Chennaoui, A. H., L. A. J. Garvie, C. D. K. Herd, G. Chen, and M. Abouhlaris. 2013. Agoudal: The Most Recent Iron Meteorite from Morocco (Abstract #5025). Lunar and Planetary Science Conference. id.5025.

Childs, G. E., L. J. Ericks, and R. L. Powell (1973). *Thermal Conductivity of Solids at Room Temperature and Below: A Review and Compilation of the Literature*. NIST Pubs NBS MONO 131. Gaithersburg, MD: National Institute of Standards and Technology, p. 608.

Choi, B.-G., X. Ouyang, and J. T. Wasson (1995). Classification and Origin of IAB and IIICD Iron Meteorites. *Geochimica et Cosmochimica Acta* 59.3, pp. 593–612. DOI: 10.1016/0016-7037(94)00384-X.

Christensen, P. R., J. L. Bandfield, V. E. Hamilton, D. A. Howard, M. D. Lane, J. L. Piatek, S. W. Ruff, and W. L. Stefanov (2000). A Thermal Emission Spectral Library of Rock-Forming Minerals. *Journal of Geophysical Research: Planets* 105.E4, pp. 9735–9739. DOI: 10.1029/1998JE000624.

Clark, S. P. (1966). "Section 21: Thermal Conductivity". In: *Handbook of Physical Constants*. Ed. by S. P. C. Jr. Vol. 97. Memoir. Geological Society of America, pp. 459–482.

Clauser, C. and E. Huenges (1995). "Thermal Conductivity of Rocks". In: *Rock Physics & Phase Relations: A Handbook of Physical Constants*. Ed. by T. J. Ahrens. Vol. 3. AGU Reference Shelf. American Geophysical Union, pp. 105–126.

Cohen, B. A. and R. F. Coker (2000). Modeling of liquid water on CM meteorite parent bodies and implications for amino acid racemization. *Icarus* 145, pp. 369–381.

Colorado School of Mines (2014). *Solid State Physics in a Nutshell: Topic 6-3: Thermal Conductivity*. Video. Produced by the Colorado School of Mines Physics Department.

Conel, J. E. (1965). *Infrared thermal emission from silicates*. Technical Memorandum 475–483. Jet Propulsion Laboratory.

Conel, J. E. (1969). Infrared emissivities of silicates: Experimental results and a cloudy atmosphere model of spectral emission from condensed particulate mediums. *Journal of Geophysical Research* 74.6, pp. 1614–1634. DOI: 10.1029/JB074i006p01614.

Consolmagno, G. J. and D. T. Britt (1998). The Density and Porosity of Meteorites from the Vatican Collection. *Meteoritics & Planetary Science* 33.6, pp. 1231–1241. DOI: 10.1111/j.1945-5100.1998.tb01308.x.

Consolmagno, G. J., D. T. Britt, and R. J. Macke (2008). The Significance of Meteorite Density and Porosity. *Geochemistry* 68.1, pp. 1–29. DOI: 10.1016/j.chemer.2008.01.003.

Consolmagno, G. J., M. W. Schaefer, B. E. Schaefer, D. T. Britt, R. J. Macke, M. C. Nolan, and E. S. Howell (2013). The Measurement of Meteorite Heat Capacity at Low Temperatures Using Liquid Nitrogen Vaporization. *Planetary and Space Science* 87, pp. 146–156. DOI: 10.1016/j.pss.2013.07.009.

Cooper, B. L., J. W. Salisbury, R. M. Killen, and A. E. Potter (2002). Midinfrared Spectral Features of Rocks and Their Powders. *Journal of Geophysical Research: Planets* 107.E4, pp. 1-1-1–17. DOI: 10.1029/2000JE001462.

Courtens, E., M. Foret, B. Rufflé, and R. Vacher (2007). Elasticity and anelasticity of oxide glasses. *Physics and Chemistry of Glasses* 48, pp. 9–18.

Cryogenic Limited (2018). *Mini Cryogen-Free Magnet System User Manual*. London, UK.

Cryogenic Limited (2019). *Thermal Transport Option: Owner's Manual*. London, UK.

Danov, M., V. Tsanev, and D. Stoyanov (2007). Measuring the Spectral Emissivity of Rocks and the Minerals That Form Them. *Spie Newsroom*. DOI: 10.1117/2.1200702.0788.

Davies, H. (2013). *Earth Tok*. Ed. by R. Davies. Third. Alan Caudell and Associates. ISBN: 978-0-9876020-0-8.

De Waele, A. T. A. M. (2011). Basic Operation of Cryocoolers and Related Thermal Machines. *Journal of Low Temperature Physics* 164.5–6, pp. 179–236. DOI: 10.1007/s10909-011-0373-x.

De Haas, W. J. and Th. Biermasz (1935). The Thermal Conductivity of Quartz at Low Temperatures. *Physica* 2.1, pp. 673–682. DOI: 10.1016/S0031-8914(35)90143-4.

Delbó, M., A. dell'Oro, A. W. Harris, S. Mottola, and M. Mueller (2007). Thermal Inertia of Near-Earth Asteroids and Implications for the Magnitude of the Yarkovsky Effect. *Icarus* 190.1, pp. 236–249. DOI: 10.1016/j.icarus.2007.03.007.

Delbó, M. and A. W. Harris (2002). Physical Properties of near-Earth Asteroids from Thermal Infrared Observations and Thermal Modeling. *Meteoritics & Planetary Science* 37.12, pp. 1929–1936. DOI: 10.1111/j.1945-5100.2002.tb01174.x.

DellaGiustina, D. N., J. P. Emery, D. R. Golish, B. Rozitis, C. A. Bennett, K. N. Burke, R.-L. Ballouz, K. J. Becker, P. R. Christensen, C. Y. Drouet d'Aubigny, V. E. Hamilton, D. C. Reuter, B. Rizk, A. A. Simon, E. Asphaug, J. L. Bandfield, O. S. Barnouin, M. A. Barucci, E. B. Bierhaus, R. P. Binzel, W. F. Bottke, N. E. Bowles, H. Campins, B. C. Clark, B. E. Clark, H. C. Connolly, M. G. Daly, J. de Leon, M. Delbo', J. D. P. Deshapriya, C. M. Elder, S. Fornasier, C. W. Hergenrother, E. S. Howell, E. R. Jawin, H. H. Kaplan, T. R. Kareta, L. Le Corre, J.-Y. Li, J. Licandro, L. F. Lim, P. Michel, J. Molaro, M. C. Nolan, M. Pajola, M. Popescu, J. L. R. Garcia, A. Ryan, S. R. Schwartz, N. Shultz, M. A. Siegler, P. H. Smith, E. Tatsumi, C. A. Thomas, K. J. Walsh, C. W. V. Wolner, X.-D. Zou, and D. S. Lauretta (2019). Properties of Rubble-Pile Asteroid (101955) Bennu from OSIRIS-REx Imaging and Thermal Analysis. *Nature Astronomy* 3.4, pp. 341–351. DOI: 10.1038/s41550-019-0731-1.

Di Sipio, E., S. Chiesa, E. Destro, A. Galgaro, A. Giaretta, G. Gola, and A. Manzella (2013). Rock thermal conductivity as key parameter for geothermal numerical models. *Energy Procedia* 40, pp. 87–94.

Diment, W. H. and H. R. Pratt (1988). *Thermal Conductivity of Some Rock-Forming Minerals: A Tabulation*. Open-File Report 88–690. United States Geological Survey.

Dreyer, W. (1974). *Properties of Anisotropic Solid-State Materials: Thermal and Electric Properties. Materialverhalten anisotroper Festkörper: Thermische und elektrische Eigenschaften*. German. In German, 295 pp. Wien: Springer.

Duda, J. C., T. S. English, D. A. Jordan, P. M. Norris, and W. A. Soffa (2011). Controlling Thermal Conductivity of Alloys via Atomic Ordering. *Journal of Heat Transfer* 134.1, p. 014501. DOI: 10.1115/1.4004843.

Dunn, T. L., G. Cressey, H. Y. J. McSween, and T. J. McCoy (2010). Analysis of ordinary chondrites using powder X-ray diffraction: 1. Modal mineral abundances. *Meteoritics & Planetary Science* 45, pp. 123–134.

Al-Edani, M. C. and K. S. Dubey (1978). Boundary Scattering and Phonon Conductivity: Application to GaAs. *physica status solidi (b)* 87.1, K47–K52. DOI: 10.1002/pssb.2220870161.

Ekin, J. (2006). *Experimental Techniques for Low-Temperature Measurements: Cryostat Design, Material Properties and Superconductor Critical-Current Testing*. Oxford University Press. ISBN: 978-0-19-857054-7. DOI: 10.1093/acprof:oso/9780198570547.001.0001.

Emery, J., Y. Fernández, M. Kelley, K. Warden (Nèe Crane), C. Hergenrother, D. Lauretta, M. Drake, H. Campins, and J. Ziffer (2014). Thermal Infrared Observations and Thermophysical Characterization of OSIRIS-REx Target Asteroid (101955) Bennu. *Icarus* 234, pp. 17–35. DOI: 10.1016/j.icarus.2014.02.005.

Encyclopædia Britannica (1998). *Albite Twinning in Plagioclase*. Image 1998 Encyclopædia Britannica, Inc. Accessed: 2025-05-12.

Enss, C. and S. Hunklinger (2005). *Low-Temperature Physics*. Germany: Springer. 573 pp. ISBN: 978-3-540-23164-6.

Eucken, A. (1911). The heat conductivity of certain crystals at low temperatures. *Phys. Zs* 12, p. 1005.

Farmer, S. (2014). *Lecture 11: Crystallography, Part 4: Crystal Forms and Twinning*. Accessed: 2025-05-12. SlideServe.

Feely, K. C. and P. R. Christensen (1999). Quantitative Compositional Analysis Using Thermal Emission Spectroscopy: Application to Igneous and Metamorphic Rocks. *Journal of Geophysical Research: Planets* 104.E10, pp. 24195–24210. DOI: 10.1029/1999JE001034.

Fendrich, K. V. and D. S. Ebel (2021). Comparison of the Murchison CM2 and Allende CV3 Chondrites. *Meteoritics & Planetary Science* 56.1, pp. 77–95. DOI: 10.1111/maps.13623.

Fitzgerel, R. K. and F. H. Verhoek (1960). The Law of Dulong and Petit. *Journal of Chemical Education* 37.10, p. 545. DOI: 10.1021/ed037p545.

Fry, C., D. Melanson, C. Samson, P. J. A. McCausland, R. K. Herd, R. E. Ernst, J. Umoh, and D. W. Holdsworth (2013). Physical Characterization of a Suite of Buzzard Coulee H4 Chondrite Fragments. *Meteoritics & Planetary Science* 48.6, pp. 1060–1073. DOI: 10.1111/maps.12130.

Fujii, N. and M. Osako (1973). Thermal Diffusivity of Lunar Rocks under Atmospheric and Vacuum Conditions. *Earth and Planetary Science Letters* 18.1, pp. 65–71. DOI: 10.1016/0012-821X(73)90035-6.

Fukao, Y. (1969). On the Radiative Heat Transfer and Thermal Conductivity in the Upper Mantle. *Bulletin of the Earthquake Research Institute* 47, pp. 549–569.

Gail, H.-P. and M. Trieloff (2018). Thermal Evolution and Sintering of Chondritic Planetesimals - IV. Temperature Dependence of Heat Conductivity of Asteroids and Meteorites. *Astronomy & Astrophysics* 615, A147. DOI: 10.1051/0004-6361/201732456.

Gail, H.-P. and M. Trieloff (2019). Thermal history modelling of the L chondrite parent body. *Astronomy & Astrophysics* 628, A77.

Gałązka, K., S. Populoh, W. Xie, J. Hulliger, and A. Weidenkaff (2016). Radiative Heat Losses in Thermal Conductivity Measurements: A Correction for Linear Temperature Gradients. *Measurement* 90, pp. 187–191. DOI: 10.1016/j.measurement.2016.04.059.

Gallagher, K., M. Ramsdale, L. Lonergan, and D. Morrow (1997). The role of thermal conductivity measurements in modelling thermal histories in sedimentary basins. *Marine and Petroleum Geology* 14.2, pp. 201–214.

Ganguly, J., M. Tirone, and K. Domanik (2016). Cooling Rates of LL, L and H Chondrites and Constraints on the Duration of Peak Thermal Conditions: Diffusion Kinetic Modeling and Implications for Fragmentation of Asteroids and Impact Resetting of Petrologic Types. *Geochimica et Cosmochimica Acta* 192, pp. 135–148. DOI: 10.1016/j.gca.2016.07.030.

Gibson, E. K. and D. D. Bogard (1978). Chemical Alterations of the Holbrook Chondrite Resulting from Terrestrial Weathering. *Meteoritics* 13.3, pp. 277–289. DOI: 10.1111/j.1945-5100.1978.tb00467.x.

Gilmour, C. (2017). "Economic Significance of Platinum Group Elements and Water in Asteroids: Insights from Chondritic Meteorites". Available from the Education and Research Archive (ERA). M.Sc. thesis. University of Alberta. DOI: 10.7939/R3RV0DF1K.

Gilmour, C. M. and C. D. K. Herd (2020). In Situ Analysis of Platinum Group Elements in Equilibrated Ordinary Chondrite Kamacite and Taenite. *Meteoritics & Planetary Science* 55.3, pp. 679–702. DOI: 10.1111/maps.13436.

Gilmour, C. M., C. D. K. Herd, and P. Beck (2019). Water abundance in the Tagish Lake meteorite from TGA and IR spectroscopy: Evaluation of aqueous alteration. *Meteoritics & Planetary Science* 54.9, pp. 1951–1972. DOI: 10.1111/maps.13362.

Giri, A., J. L. Braun, and P. E. Hopkins (2018). Reduced Dependence of Thermal Conductivity on Temperature and Pressure of Multi-Atom Component Crystalline Solid Solutions. *Journal of Applied Physics* 123.1, p. 015106. DOI: 10.1063/1.5010337.

Goncharov, A. F., P. Beck, V. V. Struzhkin, B. D. Haugen, and S. D. Jacobsen (2009). Thermal Conductivity of Lower-Mantle Minerals. *Physics of the Earth and Planetary Interiors*. Advances in High Pressure Mineral Physics: From Deep Mantle to the Core 174.1, pp. 24–32. DOI: 10.1016/j.pepi.2008.07.033.

Guilbert-Lepoutre, A., J. Lasue, C. Federico, A. Coradini, R. Orosei, and E. D. Rosenberg (2011). New 3D thermal evolution model for icy bodies: application to trans-Neptunian objects. *Astronomy & Astrophysics* 529, A71.

Halbert, D. and J. Parnell (2022). Thermal Conductivity of Basalt between 225 and 290 K. *Meteoritics & Planetary Science* 57.8, pp. 1617–1626. DOI: 10.1111/maps.13829.

Hanna, K. L. D., I. R. Thomas, N. E. Bowles, B. T. Greenhagen, C. M. Pieters, J. F. Mustard, C. R. M. Jackson, and M. B. Wyatt (2012). Laboratory emissivity measurements of the plagioclase solid solution series under varying environmental conditions. *Journal of Geophysical Research: Planets* 117. DOI: 10.1029/2012JE004184.

Hanowski, N. P. and A. J. Brearley (2001). Aqueous alteration of chondrules in the CM carbonaceous chondrite, Allan Hills 81002: Implications for parent body alteration. *Geochimica et Cosmochimica Acta* 65, pp. 495–518.

Hapke, B. (2012). "Thermal Emission and Emittance Spectroscopy". In: *Theory of Reflectance and Emittance Spectroscopy*. 2nd ed. Cambridge: Cambridge University Press, pp. 412–439. ISBN: 978-0-521-88349-8. DOI: 10.1017/CBO9781139025683.

Henderson, B. G. and B. M. Jakosky (1994). Near-Surface Thermal Gradients and Their Effects on Mid-Infrared Emission Spectra of Planetary Surfaces. *Journal of Geophysical Research: Planets* 99.E9, pp. 19063–19073. DOI: 10.1029/94JE01861.

Henderson, B. G. and B. M. Jakosky (1997). Near-Surface Thermal Gradients and Mid-IR Emission Spectra: A New Model Including Scattering and Application to Real Data. *Journal of Geophysical Research: Planets* 102.E3, pp. 6567–6580. DOI: 10.1029/96JE03781.

Henderson, B. G., P. G. Lucey, and B. M. Jakosky (1996). New Laboratory Measurements of Mid-IR Emission Spectra of Simulated Planetary Surfaces. *Journal of Geophysical Research: Planets* 101.E6, pp. 14969–14975. DOI: 10.1029/96JE01089.

Henke, S., H.-P. Gail, and M. Trieloff (2016). Thermal evolution and sintering of chondritic planetesimals. III. Modelling the heat conductivity of porous chondrite material. *Astronomy & Astrophysics* 589, A41. DOI: 10.1051/0004-6361/201527687.

Henke, S., H.-P. Gail, M. Trieloff, W. H. Schwarz, and T. Kleine (2012). Thermal history modelling of the H chondrite parent body. *Astronomy & Astrophysics* 545, A135.

Henninger, J. H. (1984). *Solar Absorptance and Thermal Emittance of Some Common Spacecraft Thermal-Control Coatings.*

Herd, C. D. K., A. Blinova, D. N. Simkus, Y. Huang, R. Tarozo, C. M. O. Alexander, F. Gyngard, L. R. Nittler, G. D. Cody, M. L. Fogel, Y. Kebukawa, A. L. D. Kilcoyne, R. W. Hilts, G. F. Slater, D. P. Glavin, J. P. Dworkin, M. P. Callahan, J. E. Elsila, B. T. De Gregorio, and R. M. Stroud (2011). Origin and evolution of prebiotic organic matter as inferred from the Tagish Lake meteorite. *Science* 332, pp. 1304–1307.

Higgins, M. D., C. D. Herd, and E. L. Walton. 2011. Micro-XRF Study of the Buzzard Coulee Meteorite. 42nd Lunar and Planetary Science Conference.

Hildebrand, A. R., E. P. Milley, P. G. Brown, P. J. A. McCausland, W. Edwards, M. Beech, A. Ling, G. Sarty, M. D. Paulson, L. A. Maillet, S. F. Jones, and M. R. Stauffer. 2009. Characteristics of a Bright Fireball and Meteorite Fall at Buzzard Coulee, Saskatchewan, Canada, November 20, 2008. 40th Lunar and Planetary Science Conference. Abstract #2505. CD-ROM.

Hofmeister, A. M., J. M. Branlund, and M. Pertermann (2007). "Properties of Rocks and Minerals - Thermal Conductivity of the Earth". In: *Mineral Physics*. Vol. 2. Elsevier, pp. 543–577. DOI: 10.1016/B978-044452748-6.00048-1.

Hooshmand Zaferani, S., R. Ghomashchi, and D. Vashaee (2019). Strategies for Engineering Phonon Transport in Heusler Thermoelectric Compounds. *Renewable and Sustainable Energy Reviews* 112, pp. 158–169. DOI: 10.1016/j.rser.2019.05.051.

Horai, K.-i. (1971). Thermal Conductivity of Rock-Forming Minerals. *Journal of Geophysical Research* 76.5, pp. 1278–1308. DOI: 10.1029/JB076i005p01278.

Horai, K.-I. and N. Fujii (1972). Thermophysical Properties of Lunar Material Returned by Apollo Missions. *The Moon* 4.3–4, pp. 447–475. DOI: 10.1007/BF00562011.

Horai, K.-i. and G. Simmons (1969). Thermal Conductivity of Rock-Forming Minerals. *Earth and Planetary Science Letters* 6.5, pp. 359–368. DOI: 10.1016/0012-821X(69)90186-1.

Horai, K. .-. and J. L. Winkler Jr. (1975). Thermal Diffusivity of Lunar Rock Sample 12002,85. *Lunar and Planetary Science Conference Proceedings* 3, pp. 3207–3215.

Howard, K. T., C. M. O. Alexander, D. L. Schrader, and K. A. Dyl (2014). Classification of hydrous meteorites (CR, CM and C2 ungrouped) by phyllosilicate fraction: PSD-XRD modal mineralogy and planetesimal environments. *Geochimica et Cosmochimica Acta* 149, pp. 206–222.

Huang, Z., W. Zeng, Q. Gu, Y. Wu, W. Zhong, and K. Zhao (2021). Investigations of variations in physical and mechanical properties of granite, sandstone, and marble after temperature and acid solution treatments. *Construction and Building Materials* 307, p. 124943.

Hust, J. G. and A. B. Lankford (1984). *Thermal Conductivity of Aluminum, Copper, Iron, and Tungsten for Temperatures from 1 K to the Melting Point*. NIST Pubs NBS IR 84-3007. Gaithersburg, MD: National Institute of Standards and Technology.

Hust, J. G., R. L. Powell, and D. H. Weitzel (1970). Thermal Conductivity Standard Reference Materials From 4 to 300 K. I. Armco Iron: Including Apparatus Description and Error Analysis. *Journal of Research of the National Bureau of Standards. Section A, Physics and Chemistry* 74A.5, pp. 673–690. DOI: 10.6028/jres.074A.056. PMID: 32523219.

Hutson, M., A. Ruzicka, E. Milley, and A. Hildebrand. 2009. A First Look at the Petrography of the Buzzard Coulee (H4) Chondrite, a Recently Observed Fall from Saskatchewan. 40th Lunar and Planetary Science Conference. Abstract #1893.

Jo, H., J. L. King, K. Blomstrand, and K. Sridharan (2017). Spectral Emissivity of Oxidized and Roughened Metal Surfaces. *International Journal of Heat and Mass Transfer* 115, pp. 1065–1071. DOI: 10.1016/j.ijheatmasstransfer.2017.08.103.

Johnson, J. R., F. Hörz, and M. I. Staid (2003). Thermal Infrared Spectroscopy and Modeling of Experimentally Shocked Plagioclase Feldspars. *American Mineralogist* 88.10, pp. 1575–1582. DOI: 10.2138/am-2003-1020.

Kanamori, H., N. Fujii, and H. Mizutani (1968). Thermal Diffusivity Measurement of Rock-Forming Minerals from 300° to 1100°K. *Journal of Geophysical Research* 73.2, pp. 595–605. DOI: 10.1029/JB073i002p00595.

Kaviany, M. (2008). *Heat Transfer Physics*. Cambridge: Cambridge University Press.

Kaye, G. W. C. and W. F. Higgins (1926). The thermal conductivity of vitreous silica, with a note on crystalline quartz. *Proceedings of the Royal Society of London. Series A, Containing Papers of a Mathematical and Physical Character* 113, pp. 335–351.

Keil, K. (2000). Thermal Alteration of Asteroids: Evidence from Meteorites. *Planetary and Space Science* 48.10, pp. 887–903. DOI: 10.1016/S0032-0633(00)00054-4.

Kerridge, J. F. (1985). Carbon, Hydrogen and Nitrogen in Carbonaceous Chondrites: Abundances and Isotopic Compositions in Bulk Samples. *Geochimica et Cosmochimica Acta* 49.8, pp. 1707–1714. DOI: 10.1016/0016-7037(85)90141-3.

Kim, W. (2015). Strategies for Engineering Phonon Transport in Thermoelectrics. *Journal of Materials Chemistry C* 3.40, pp. 10336–10348. DOI: 10.1039/C5TC01670C.

Kittel, C. (1949). Interpretation of the Thermal Conductivity of Glasses. *Physical Review* 75.6, pp. 972–974. DOI: 10.1103/PhysRev.75.972.

Kittel, C. (2005). *Introduction to Solid State Physics*. Eighth Edition. John Wiley & Sons. 722 pp. ISBN: 978-1-119-45416-8. Google Books: S3gAugEACAAJ.

Kojima, T. and K. Tomeoka (1996). Indicators of Aqueous Alteration and Thermal Metamorphism on the CV Parent Body: Microtextures of a Dark Inclusion from Allende. *Geochimica et Cosmochimica Acta* 60.14, pp. 2651–2666. DOI: 10.1016/0016-7037(96)00116-0.

Kornacki, A. S. and J. A. Wood (1984). The Mineral Chemistry and Origin of Inclusion Matrix and Meteorite Matrix in the Allende CV3 Chondrite. *Geochimica et Cosmochimica Acta* 48.8, pp. 1663–1676. DOI: 10.1016/0016-7037(84)90335-1.

Krot, A. N., K. Keil, E. R. D. Scott, C. A. Goodrich, and M. K. Weisberg (2014). "1.1 - Classification of meteorites and their genetic relationships". In: *Treatise on Geochemistry*. Ed. by H. Holland and K. Turekian. 2nd ed. Oxford: Elsevier, pp. 1–63.

Labus, M. and K. Labus (2018). Thermal Conductivity and Diffusivity of Fine-Grained Sedimentary Rocks. *Journal of Thermal Analysis and Calorimetry* 132.3, pp. 1669–1676. DOI: 10.1007/s10973-018-7090-5.

Lake Shore Cryotronics (n.d.). *Pulse Tube Cryocoolers vs. Gifford-McMahon Cryocoolers*. Accessed: 2025-04-15.

Lalla, E. A., A. Sanz Arranz, G. Lopez Reyes, M. Konstantinidis, M. Veneranda, R. O. Aquilano, F. Rull, M. Aznar, J. Medina, and J. Martínez Frías (2020a). Mineralogical study using spectroscopic techniques (Raman-FTIR-XRD-XRF) of volcanic samples from the Chamorga outcrop (Tenerife, Spain). *Journal of the Geological Society of Spain* 33.1, pp. 71–93.

Lalla, E. A., K. Cote, D. Hickson, S. Garnitschnig, M. Konstantinidis, P. Such, C. Czakler, C. Schroder, A. Frigeri, M. Ercoli, A. Losiak, S. Gruber, and G. Groemer (2020b). Laboratory Analysis of Returned Samples from the AMADEE-18 Mars Analog Mission. *Astrobiology* 20.11, pp. 1303–1320. DOI: 10.1089/ast.2019.2038. PMID: 33179966.

Lane, M. D. and J. L. Bishop (2019). "Mid-infrared (Thermal) Emission and Reflectance Spectroscopy: Laboratory Spectra of Geologic Materials". In: *Remote Compositional Analysis: Techniques for Understanding Spectroscopy, Mineralogy, and Geochemistry of Planetary Surfaces*. Ed. by J. F. B. III, J. L. Bishop, and J. E. Moersch. Cambridge

Planetary Science. Cambridge: Cambridge University Press, pp. 42–67. DOI: 10.1017/9781316888872.005.

Lane, M. D. (1999). Midinfrared Optical Constants of Calcite and Their Relationship to Particle Size Effects in Thermal Emission Spectra of Granular Calcite. *Journal of Geophysical Research: Planets* 104.E6, pp. 14099–14108. DOI: 10.1029/1999JE900025.

Lang, S., M. Gerschitzka, D. Bauer, and H. Drück (2016). Thermal Conductivity of Vacuum Insulation Materials for Thermal Energy Stores in Solar Thermal Systems. *Energy Procedia* 91, pp. 172–181. DOI: 10.1016/j.egypro.2016.06.196.

Le Comptoir Géologique (2025). *Cubic System – Glossary*. Page active since at least 2008.

Liu, Q., H. Luo, L. Wang, and S. Shen (2017). Tuning the Thermal Conductivity of Silicon Carbide by Twin Boundary: A Molecular Dynamics Study. *Journal of Physics D: Applied Physics* 50.6, p. 065108. DOI: 10.1088/1361-6463/aa553d.

Liu, Y., J. Zhang, G. Ren, and A. Chernatynskiy (2022). Utilizing Twin Interfaces to Reduce Lattice Thermal Conductivity of Superlattice. *International Journal of Heat and Mass Transfer* 189, p. 122700. DOI: 10.1016/j.ijheatmasstransfer.2022.122700.

Loehle, S., P. Jenniskens, H. Böhrk, T. Bauer, H. Elsäβer, D. W. Sears, M. E. Zolensky, and M. H. Shaddad (2017). Thermophysical Properties of Almahata Sitta Meteorites (Asteroid 2008 TC3) for High-Fidelity Entry Modeling. *Meteoritics & Planetary Science* 52.2, pp. 197–205. DOI: 10.1111/maps.12788.

Logan, L. M. and G. R. Hunt (1970). Emission spectra of particulate silicates under simulated lunar conditions. *Journal of Geophysical Research* 75.32, pp. 6539–6548. DOI: 10.1029/JB075i032p06539.

Logan, L. M., G. R. Hunt, J. W. Salisbury, and S. R. Balsamo (1973). Compositional implications of Christiansen frequency maximums for infrared remote sensing applications. *Journal of Geophysical Research* 78.23, pp. 4983–5003. DOI: 10.1029/JB078i023p04983.

Lovering, J. F., W. Nichiporuk, A. Chodos, and H. Brown (1957). The Distribution of Gallium, Germanium, Cobalt, Chromium, and Copper in Iron and Stony-Iron Meteorites

in Relation to Nickel Content and Structure. *Geochimica et Cosmochimica Acta* 11.4, pp. 263–278. DOI: 10.1016/0016-7037(57)90099-6.

Ltd, D. E. P. (2024). *Properties of PTFE and Some Other Insulating Materials*.

Lubchenko, V. and P. G. Wolynes (2003). The Origin of the Boson Peak and Thermal Conductivity Plateau in Low-Temperature Glasses. *Proceedings of the National Academy of Sciences* 100.4, pp. 1515–1518. DOI: 10.1073/pnas.252786999.

Lv, W. and A. Henry (2016). Non-Negligible Contributions to Thermal Conductivity From Localized Modes in Amorphous Silicon Dioxide. *Scientific Reports* 6.1, p. 35720. DOI: 10.1038/srep35720.

Lyon, R. J. P. (1964). *Evaluation of infrared spectrophotometry for compositional analysis of lunar and planetary soils. Part II: Rough and powdered surfaces*. Tech. rep. NASA-CR-100. NASA.

Lyon, R. J. P. (1965). Analysis of Rocks by Spectral Infrared Emission (8 to 25 Microns). *Economic Geology* 60.4, pp. 715–736. DOI: 10.2113/gsecongeo.60.4.715.

Macke, R. J. (2010). "Survey of Meteorite Physical Properties: Density, Porosity and Magnetic Susceptibility". Ph.D. Thesis. Orlando, Florida: University of Florida, Department of Physics.

Macke, R. J., W. S. Kiefer, A. J. Irving, and D. T. Britt. 2016. Density and Porosity Measurements of Lunar and Martian Materials. 47th Annual Lunar and Planetary Science Conference.

Macke, R. J., C. P. Opeil, D. T. Britt, G. J. Consolmagno, and A. Irving (2024). Low-Temperature Thermal and Physical Properties of Lunar Meteorites. *Meteoritics & Planetary Science* 59.7, pp. 1610–1631. DOI: 10.1111/maps.14171.

Macke, R. J., D. T. Britt, and G. J. Consolmagno (2011a). Density, Porosity, and Magnetic Susceptibility of Achondritic Meteorites. *Meteoritics & Planetary Science* 46.2, pp. 311–326. DOI: 10.1111/j.1945-5100.2010.01155.x.

Macke, R. J., G. J. Consolmagno, and D. T. Britt (2011b). Density, Porosity, and Magnetic Susceptibility of Carbonaceous Chondrites. *Meteoritics & Planetary Science* 46.12, pp. 1842–1862. DOI: 10.1111/j.1945-5100.2011.01298.x.

Macke, R. J., G. J. Consolmagno, D. T. Britt, and M. L. Hutson (2010). Enstatite Chondrite Density, Magnetic Susceptibility, and Porosity. *Meteoritics & Planetary Science* 45.9, pp. 1513–1526. DOI: 10.1111/j.1945-5100.2010.01129.x.

Macke, R. J., C. Opeil, and G. J. Consolmagno (2019). Heat Capacities of Ordinary Chondrite Falls below 300 K. *Meteoritics & Planetary Science* 54.11, pp. 2729–2743. DOI: 10.1111/maps.13385.

MacLennan, E. M. and J. P. Emery (2022). Thermophysical Investigation of Asteroid Surfaces. II. Factors Influencing Grain Size. *The Planetary Science Journal* 3.2, p. 47. DOI: 10.3847/PSJ/ac4967.

MacPherson, W. R. and H. H. Schloessin (1982). Lattice and Radiative Thermal Conductivity Variations through High p, T Polymorphic Structure Transitions and Melting Points. *Physics of the Earth and Planetary Interiors*. Special Issue Properties of Materials at High Pressures and High Temperatures 29.1, pp. 58–68. DOI: 10.1016/0031-9201(82)90138-8.

Malinovsky, V. K. and A. P. Sokolov (1986). The Nature of Boson Peak in Raman Scattering in Glasses. *Solid State Communications* 57.9, pp. 757–761. DOI: 10.1016/0038-1098(86)90854-9.

Manga, M. and R. Jeanloz (1997). Thermal Conductivity of Corundum and Periclase and Implications for the Lower Mantle. *Journal of Geophysical Research: Solid Earth* 102.B2, pp. 2999–3008. DOI: 10.1029/96JB02696.

Mason, B. (1975). Allende meteorite. Cosmochemistry's Rosetta Stone. *Accounts of Chemical Research* 8.7, pp. 217–224.

Mason, B. and H. B. Wiik (1961). The Holbrook, Arizona, Chondrite. *Geochimica et Cosmochimica Acta* 21.3, pp. 276–283. DOI: 10.1016/S0016-7037(61)80062-8.

Mathew, G., A. Nair, T. K. G. Rao, and K. Pande (2009). Laboratory technique for quantitative thermal emissivity measurements of geological samples. *Journal of Earth System Science* 118, pp. 391–404. DOI: 10.1007/s12040-009-0035-4.

Matsui, T. and M. Osako (1979). Thermal property measurement of Yamato meteorites. *Memoirs of the National Institute of Polar Research, Special Issue* 15, pp. 243–252.

Maturilli, A., J. Helbert, and L. Moroz (2008). The Berlin Emissivity Database (BED). *Planetary and Space Science* 56.3, pp. 420–425. DOI: 10.1016/j.pss.2007.11.015.

McSween, H. Y., A. Ghosh, R. E. Grimm, L. Wilson, and E. D. Young (2002). Thermal evolution models of asteroids. *Asteroids III* 559, pp. 559–572.

Meerdink, S. K., S. J. Hook, D. A. Roberts, and E. A. Abbott (2019). The ECOSTRESS Spectral Library Version 1.0. *Remote Sensing of Environment* 230, p. 111196. DOI: 10.1016/j.rse.2019.05.015.

Midttomme, K. and E. Roaldset (1998). The Effect of Grain Size on Thermal Conductivity of Quartz Sands and Silts. *Petroleum Geoscience* 4.2, pp. 165–172. DOI: 10.1144/petgeo.4.2.165.

Milliken, R. (2020). *RELAB Spectral Library Bundle*. Archive. urn:nasa:pds:relab::3.0. NASA Planetary Data System. DOI: 10.17189/1519032.

Mineo, S. and G. Pappalardo (2021). Rock Emissivity Measurement for Infrared Thermography Engineering Geological Applications. *Applied Sciences* 11.9, p. 3773. DOI: 10.3390/app11093773.

Mittlefehldt, D. W., T. J. McCoy, C. A. Goodrich, and A. Kracher (1998). "Non-chondritic meteorites from asteroidal bodies". In: *Reviews in Mineralogy, Volume 36: Planetary Materials*. Ed. by J. J. Papike. Washington: Mineralogical Society of America, pp. 4-1–4-195.

Mizutani, H. and M. Osako (1974). Elastic-Wave Velocities and Thermal Diffusivities of Apollo 17 Rocks and Their Geophysical Implications. *Lunar and Planetary Science Conference Proceedings* 3, pp. 2891–2901.

Monaco, G. and S. Mossa (2009). Anomalous Properties of the Acoustic Excitations in Glasses on the Mesoscopic Length Scale. *Proceedings of the National Academy of Sciences* 106.40, pp. 16907–16912. DOI: 10.1073/pnas.0903922106.

Moon, J. and A. J. Minnich (2016). Sub-Amorphous Thermal Conductivity in Amorphous Heterogeneous Nanocomposites. *RSC Advances* 6.107, pp. 105154–105160. DOI: 10.1039/C6RA24053D.

Moriel, A., E. Lerner, and E. Bouchbinder (2024). Boson Peak in the Vibrational Spectra of Glasses. *Physical Review Research* 6.2, p. 023053. DOI: 10.1103/PhysRevResearch.6.023053.

Murashov, V. and M. A. White (2006). "Thermal Conductivity of Insulators and Glasses". In: *Thermal Conductivity: Theory, Properties, and Applications*. Ed. by T. M. Tritt. Boston, UNITED STATES: Springer, pp. 93–121. ISBN: 978-0-387-26017-4.

Nicodemus, F. E. (1965). Directional Reflectance and Emissivity of an Opaque Surface. *Applied Optics* 4.7, pp. 767–775. DOI: 10.1364/AO.4.000767.

NIST (2010). *National Institute of Standards and Technology: Cryogenic Material Properties: OFHC Copper*. Accessed: 2025-03-11. National Institude of Standards and Technology: Material Properties.

NIST (n.d.). *National Institute of Standards and Technology: Cryogenic Material Properties: Polyurethane*. Accessed: 2025-03-03. NIST: Material Properties.

Nolas, G. and H. Goldsmid (2006). "Thermal Conductivity of Semiconductors". In: *Thermal Conductivity: Theory, Properties, and Applications*. Ed. by T. M. Tritt. Boston, UNITED STATES: Springer, pp. 105–121. ISBN: 978-0-387-26017-4.

Nolze, G., G. Wagner, R. S. Neumann, R. Skala, and V. Geist (2006). Orientation Relationships of Carlsbergite in Schreibersite and Kamacite in the North Chile Iron Meteorite. *Mineralogical Magazine* 70.4, pp. 373–382. DOI: 10.1180/0026461067040342.

Noyes, C. S., Guy. J. Consolmagno, R. J. Macke, D. T. Britt, and C. P. Opeil (2022). Low-Temperature Thermal Properties of Iron Meteorites. *Meteoritics & Planetary Science* 57.9, pp. 1706–1721. DOI: 10.1111/maps.13895.

Nunes, C., A. Mahendrasingam, and R. Suryanarayanan (2005). Quantification of Crystallinity in Substantially Amorphous Materials by Synchrotron X-ray Powder Diffractometry. *Pharmaceutical Research* 22.11, pp. 1942–1953. DOI: 10.1007/s11095-005-7626-9.

Okada, T., T. Fukuhara, S. Tanaka, M. Taguchi, T. Imamura, T. Arai, H. Senshu, Y. Ogawa, H. Demura, K. Kitazato, R. Nakamura, T. Kouyama, T. Sekiguchi, S. Hasegawa, T. Matsunaga, T. Wada, J. Takita, N. Sakatani, Y. Horikawa, K. Endo, J. Helbert, T. G. Müller, and A. Hagermann (2017). Thermal Infrared Imaging Experiments of C-Type Asteroid 162173 Ryugu on Hayabusa2. *Space Science Reviews* 208.1, pp. 255–286. DOI: 10.1007/s11214-016-0286-8.

OMEGA Engineering (n.d.). *Emissivity of Common Materials*. Accessed: 2025-05-31.

Opeil, C. P., D. T. Britt, R. J. Macke, and G. J. Consolmagno (2020). The Surprising Thermal Properties of CM Carbonaceous Chondrites. *Meteoritics & Planetary Science* 55.8, maps.13556. DOI: 10.1111/maps.13556.

Opeil, C. P., G. J. Consolmagno, D. J. Safarik, and D. T. Britt (2012). Stony Meteorite Thermal Properties and Their Relationship with Meteorite Chemical and Physical States. *Meteoritics & Planetary Science* 47.3, pp. 319–329. DOI: 10.1111/j.1945-5100.2012.01331.x.

Opeil, C., G. Consolmagno, and D. Britt (2010). The Thermal Conductivity of Meteorites: New Measurements and Analysis. *Icarus* 208.1, pp. 449–454. DOI: 10.1016/j.icarus.2010.01.021.

Ostrowski, D. and K. Bryson (2019). The physical properties of meteorites. *Planetary and Space Science* 165, pp. 148–178. DOI: 10.1016/j.pss.2018.11.003.

Ostrowski, D. and K. Bryson (2020). Laboratory examination of the physical properties of ordinary chondrites. *Meteoritics & Planetary Science* 55, pp. 2007–2020. DOI: 10.1111/maps.13562.

Özatay, Ö. (2021). *Week 8-3: Thermal Conduction by Phonons*. Video lecture.

Peri, L., D. Prete, V. Demontis, V. Zannier, F. Rossi, L. Sorba, F. Beltram, and F. Rossella (2022). Giant Reduction of Thermal Conductivity and Enhancement of Thermoelectric Performance in Twinning Superlattice InAsSb Nanowires. *Nano Energy* 103, p. 107700. DOI: 10.1016/j.nanoen.2022.107700.

Phillips, W. A. (1972). Tunneling States in Amorphous Solids. *Journal of Low Temperature Physics* 7.3, pp. 351–360. DOI: 10.1007/BF00660072.

Pillinger, C. T., R. C. Greenwood, J. M. Gibson, J. M. Pillinger, and E. K. Gibson. 2013. The Holbrook Meteorite: 99 Years Out in the Weather. 44th Lunar and Planetary Science Conference.

Piqueux, S., T. H. Vu, J. Bapst, L. A. J. Garvie, M. Choukroun, and C. S. Edwards (2021). Specific Heat Capacity Measurements of Selected Meteorites for Planetary Surface Temperature Modeling. *Journal of Geophysical Research: Planets* 126.11, e2021JE007003. DOI: 10.1029/2021JE007003.

Pirim, C., M. A. Pasek, D. A. Sokolov, A. N. Sidorov, R. D. Gann, and T. M. Orlando (2014). Investigation of Schreibersite and Intrinsic Oxidation Products from Sikhote-Alin, Seymchan, and Odessa Meteorites and Fe3P and Fe2NiP Synthetic Surrogates. *Geochimica et Cosmochimica Acta* 140, pp. 259–274. DOI: 10.1016/j.gca.2014.05.027.

Pope, A. L., B. Zawilski, and T. M. Tritt (2001). Description of Removable Sample Mount Apparatus for Rapid Thermal Conductivity Measurements. *Cryogenics* 41.10, pp. 725–731. DOI: 10.1016/S0011-2275(01)00140-0.

Popov, P. A., P. P. Fedorov, and S. V. Kuznetsov (2013). Thermal Conductivity of FeS2 Pyrite Crystals in the Temperature Range 50–300 K. *Crystallography Reports* 58.2, pp. 319–321. DOI: 10.1134/S1063774513020223.

Popova, M., A. Ristić, V. Mavrodinova, D. Maučec, L. Mindizova, and N. Novak Tušar (2014). Design of Cobalt Functionalized Silica with Interparticle Mesoporosity as a Promising Catalyst for VOCs Decomposition. *Catalysis Letters* 144.6, pp. 1096–1100. DOI: 10.1007/s10562-014-1246-0.

Powell, R. L. and F. R. Fickett (1979). *Cryogenic Properties of Copper*. International Copper Research Association.

Powell, R. W., C. Y. Ho, and P. E. Liley (1996). *Thermal Conductivity of Selected Materials*. NSRDS-NBS 8. National Institute of Standards and Technology, p. 169.

Powell, R. L., W. M. Rogers, and D. O. Coffin (1957). An Apparatus for Measurement of Thermal Conductivity of Solids at Low Temperatures. *J. Res. Nat. Bur. Stand.(US)* 59, pp. 349–355.

Prialnik, D. and R. Merk (2008). Growth and evolution of small porous icy bodies with an adaptive-grid thermal evolution code. I. Application to Kuiper Belt objects and Enceladus. *Icarus* 197, pp. 211–220.

Qian, X., J. Zhou, and G. Chen (2021). Phonon-engineered extreme thermal conductivity materials. *Nature Materials* 20.9, pp. 1188–1202. DOI: 10.1038/s41563-021-00918-3.

Ramsey, M. S. and P. R. Christensen (1998). Mineral Abundance Determination: Quantitative Deconvolution of Thermal Emission Spectra. *Journal of Geophysical Research: Solid Earth* 103.B1, pp. 577–596. DOI: 10.1029/97JB02784.

Ratcliffe, E. H. (1959). Thermal Conductivities of Fused and Crystalline Quartz. *British Journal of Applied Physics* 10.1, p. 22. DOI: 10.1088/0508-3443/10/1/306.

Reymond, S., S. Perraud, and G. Sierra (2021). *MAP® EPOX BLACK ESD: Low Outgassing Electrically Conductive Epoxy Primer and Coating*. https://www.map-coatings.com/web/content/116837. Technical datasheet, MAP Space Coatings.

Richards, P. (2015). *Miller-Bravais Indices: Really Necessary?* https://www.mineral-forum.com/messageboard/viewtopic.php?t=4346.

Rivard, B., P. J. Thomas, and J. Giroux (1995). Precise Emissivity of Rock Samples. *Remote Sensing of Environment* 54.2, pp. 152–160. DOI: 10.1016/0034-4257(95)00130-S.

Robertson, E. C. (1988). *Thermal Properties of Rocks*. Open-File Report 88-441. Reston, Virginia: United States Department of the Interior, Geological Survey, p. 106.

Robertson, E. C. and D. L. Peck (1974). Thermal Conductivity of Vesicular Basalt from Hawaii. *Journal of Geophysical Research (1896-1977)* 79.32, pp. 4875–4888. DOI: 10.1029/JB079i032p04875.

Rowe, M. C. and B. J. Brewer (2018). AMORPH: A Statistical Program for Characterizing Amorphous Materials by X-ray Diffraction. *Computers & Geosciences* 120, pp. 21–31. DOI: 10.1016/j.cageo.2018.07.004.

Rozitis, B., A. J. Ryan, J. P. Emery, P. R. Christensen, V. E. Hamilton, A. A. Simon, D. C. Reuter, M. Al Asad, R.-L. Ballouz, J. L. Bandfield, O. S. Barnouin, C. A. Bennett, M. Bernacki, K. N. Burke, S. Cambioni, B. E. Clark, M. G. Daly, M. Delbo, D. N. DellaGiustina, C. M. Elder, R. D. Hanna, C. W. Haberle, E. S. Howell, D. R. Golish, E. R. Jawin, H. H. Kaplan, L. F. Lim, J. L. Molaro, D. P. Munoz, M. C. Nolan, B. Rizk, M. A. Siegler, H. C. M. Susorney, K. J. Walsh, and D. S. Lauretta (2020). Asteroid (101955) Bennu's Weak Boulders and Thermally Anomalous Equator. *Science Advances* 6.41, eabc3699. DOI: 10.1126/sciadv.abc3699.

Rozitis, B., A. J. Ryan, J. P. Emery, M. C. Nolan, S. F. Green, P. R. Christensen, V. E. Hamilton, M. G. Daly, O. S. Barnouin, and D. S. Lauretta (2022). High-Resolution Thermophysical Analysis of the OSIRIS-REx Sample Site and Three Other Regions of Interest on Bennu. *Journal of Geophysical Research: Planets* 127.6, e2021JE007153. DOI: 10.1029/2021JE007153.

Rubin, A. E., J. M. Trigo-Rodriguez, H. Huber, and J. T. Wasson (2007). Progressive aqueous alteration of CM carbonaceous chondrites. *Geochimica et Cosmochimica Acta* 71, pp. 2361–2382.

Rubin, A. E. (1990). Kamacite and Olivine in Ordinary Chondrites: Intergroup and Intragroup Relationships. *Geochimica et Cosmochimica Acta* 54.5, pp. 1217–1232. DOI: 10.1016/0016-7037(90)90148-E.

Rubin, A. E., K. Ziegler, and E. D. Young (2008). Size Scales over Which Ordinary Chondrites and Their Parent Asteroids Are Homogeneous in Oxidation State and Oxygen-Isotopic Composition. *Geochimica et Cosmochimica Acta* 72.3, pp. 948–958. DOI: 10.1016/j.gca.2007.11.023.

Rudajevová, A., M. Švantner, D. Vasylyev, O. Musil, and V. Lang (2006). Influence of Radiation Losses on Thermal Conductivity Determination at Low Temperatures. *International Journal of Thermophysics* 27.4, pp. 1241–1249. DOI: 10.1007/s10765-006-0074-x.

Sahijpal, S. (2021). Thermal Evolution of Non-Spherical Asteroids in the Early Solar System. *Icarus* 362, p. 114439. DOI: 10.1016/j.icarus.2021.114439.

Sahijpal, S. (2022). Possible Thermal Evolutionary Pathways of Irregular Shaped Small Asteroids and Planetesimals. *Journal of Earth System Science* 131.2, p. 72. DOI: 10.1007/s12040-022-01813-4.

Sakvarelidze, E. A. (1973). *Verkhnaya Mantiya*. No. 12, p. 125. Moscow: Izd. Nauka.

Salisbury, J. W. and D. M. D'Aria (1992). Emissivity of terrestrial materials in the 8–14 µm atmospheric window. *Remote Sensing of Environment* 42, pp. 83–106. DOI: 10.1016/0034-4257(92)90092-X.

Salisbury, J. W., D. M. D'Aria, and E. Jarosewich (1991a). Midinfrared (2.5–13.5 µm) reflectance spectra of powdered stony meteorites. *Icarus* 92, pp. 280–297. DOI: 10.1016/0019-1035(91)90052-U.

Salisbury, J. W. and A. Wald (1992). The role of volume scattering in reducing spectral contrast of reststrahlen bands in spectra of powdered minerals. *Icarus* 96, pp. 121–128. DOI: 10.1016/0019-1035(92)90009-V.

Salisbury, J. W., A. Wald, and D. M. D'Aria (1994). Thermal-infrared remote sensing and Kirchhoff's law: 1. Laboratory measurements. *Journal of Geophysical Research: Solid Earth* 99, pp. 11897–11911. DOI: 10.1029/93JB03600.

Salisbury, J. W. and L. S. Walter (1989). Thermal infrared (2.5–13.5 µm) spectroscopic remote sensing of igneous rock types on particulate planetary surfaces. *Journal of Geophysical Research: Solid Earth* 94, pp. 9192–9202. DOI: 10.1029/JB094iB07p09192.

Salisbury, J. W., L. S. Walter, and D. D'Aria (1988). *Mid-infrared (2.5 to 13.5 mm) spectra of igneous rocks*. Tech. rep. USGS Report. United States Geological Survey (USGS).

Salisbury, J. W., L. S. Walter, N. Vergo, and D. M. D'Aria (1991b). *The Infrared Spectra (2.1–25 Micron) of Minerals*. Johns Hopkins University Press.

Sass, J. H. (1965). The Thermal Conductivity of Fifteen Feldspar Specimens. *Journal of Geophysical Research* 70.16, pp. 4064–4065. DOI: 10.1029/JZ070i016p04064.

Sass, J. H., A. H. Lachenbruch, and R. J. Munroe (1971). Thermal Conductivity of Rocks from Measurements on Fragments and Its Application to Heat-Flow Determinations. *Journal of Geophysical Research* 76.14, pp. 3391–3401. DOI: 10.1029/JB076i014p03391.

Schirmacher, W., G. Ruocco, and T. Scopigno (2007). Acoustic Attenuation in Glasses and Its Relation with the Boson Peak. *Physical Review Letters* 98.2, p. 025501. DOI: 10.1103/PhysRevLett.98.025501.

Schober, H. R. (2004). Vibrations and Relaxations in a Soft Sphere Glass: Boson Peak and Structure Factors. *Journal of Physics: Condensed Matter* 16.27, S2659. DOI: 10.1088/0953-8984/16/27/005.

Schrader, D. L., E. A. Cloutis, D. M. Applin, J. Davidson, Z. A. Torrano, D. Foustoukos, C. M. O. Alexander, K. J. Domanik, M. Matsuoka, T. Nakamura, T. J. Zega, G. A. Brennecka, and J. Render (2024). Tarda and Tagish Lake: Samples from the Same Outer Solar System Asteroid and Implications for D- and P-type Asteroids. *Geochimica et Cosmochimica Acta* 380, pp. 48–70. DOI: 10.1016/j.gca.2024.07.007.

Schröder, A., A. Murk, R. Wylde, K. Jacob, K. Pike, M. Winser, M. B. Pujades, and V. Kangas (2017). Electromagnetic Design of Calibration Targets for MetOp-SG Microwave Instruments. *IEEE Transactions on Terahertz Science and Technology* 7.6, pp. 677–685. DOI: 10.1109/TTHZ.2017.2757442.

Schubert, G., J. D. Anderson, B. J. Travis, and J. Palguta (2007). Enceladus: Present internal structure and differentiation by early and long-term radiogenic heating. *Icarus* 188, pp. 345–355.

Schwinger, S., R. Dohmen, and H.-P. Schertl (2016). A Combined Diffusion and Thermal Modeling Approach to Determine Peak Temperatures of Thermal Metamorphism Experienced by Meteorites. *Geochimica et Cosmochimica Acta* 191, pp. 255–276. DOI: 10.1016/j.gca.2016.06.015.

Sears, D. W. and R. T. Dodd (1988). "Overview and classification of meteorites". In: *Meteorites and the Early Solar System*. Ed. by J. F. Kerridge and M. S. Matthews. Tucson: University of Arizona Press, pp. 3–31.

Sharma, P. K. and R. Bahadur (1975). Thermal Conductivity for Phonon Scattering by Substitutional Defects in Crystals. *Physical Review B* 12.4, pp. 1522–1530. DOI: 10.1103/PhysRevB.12.1522.

Sheats, D. C., Z. S. Roth, and J. W. Snyder (2006). Autotune of PID Temperature Control Based on Closed-loop Step Response Tests. *AIP Conference Proceedings* 823.1, pp. 259–266. DOI: 10.1063/1.2202424.

Shin, S., Q. Wang, J. Luo, and R. Chen (2020). Advanced Materials for High-Temperature Thermal Transport. *Advanced Functional Materials* 30.8, p. 1904815. DOI: 10.1002/adfm.201904815.

Shintani, H. and H. Tanaka (2008). Universal Link between the Boson Peak and Transverse Phonons in Glass. *Nature Materials* 7.11, pp. 870–877. DOI: 10.1038/nmat2293. PMID: 18849975.

Shirley, K. and T. Glotch (2019). Particle Size Effects on Mid-Infrared Spectra of Lunar Analog Minerals in a Simulated Lunar Environment. *Journal of Geophysical Research: Planets* 124. DOI: 10.1029/2018JE005533.

Sibbitt, W., J. Dodson, and J. Tester (1978). *Thermal conductivity of rocks associated with energy extraction from hot dry rock geothermal systems*. Springer.

Simon, N. J., E. S. Drexler, and R. P. Reed (1992). *Properties of Copper and Copper Alloys at Cryogenic Temperatures*. NIST MONO-177. National Inst. of Standards and Technology (MSEL), Boulder, CO (United States). Materials Reliability Div. DOI: 10.2172/5340308.

Slack, G. A. (1979). "The Thermal Conductivity of Nonmetallic Crystals". In: *Solid State Physics*. Ed. by H. Ehrenreich, F. Seitz, and D. Turnbull. Vol. 34. Academic Press, pp. 1–71. DOI: 10.1016/S0081-1947(08)60359-8.

Smith, D. S., A. Alzina, J. Bourret, B. Nait-Ali, F. Pennec, N. Tessier-Doyen, K. Otsu, H. Matsubara, P. Elser, and U. T. Gonzenbach (2013). Thermal Conductivity of Porous Materials. *Journal of Materials Research* 28.17, pp. 2260–2272. DOI: 10.1557/jmr.2013.179.

Snelling, A. A. (2014). Radioisotope dating of meteorites II: The ordinary and enstatite chondrites. *Answers Research Journal* 7, pp. 239–296.

Soini, A.-J., I. T. Kukkonen, T. Kohout, and A. Luttinen (2020). Thermal and Porosity Properties of Meteorites: A Compilation of Published Data and New Measurements. *Meteoritics & Planetary Science* 55.2, pp. 402–425. DOI: 10.1111/maps.13441.

Spitzer, D. P. (1970). Lattice Thermal Conductivity of Semiconductors: A Chemical Bond Approach. *Journal of Physics and Chemistry of Solids* 31.1, pp. 19–40. DOI: 10.1016/0022-3697(70)90284-2.

Stein, J., T. J. Shankland, and U. Nitsan (1981). Radiative Thermal Conductivity in Obsidian and Estimates of Heat Transfer in Magma Bodies. *Journal of Geophysical Research: Solid Earth* 86.B5, pp. 3684–3688. DOI: 10.1029/JB086iB05p03684.

Stylianou, I. I., S. Tassou, P. Christodoulides, I. Panayides, and G. Florides (2016). Measurement and analysis of thermal properties of rocks for the compilation of geothermal maps of Cyprus. *Renewable Energy* 88, pp. 418–429.

Szurgot, M. 2011. On the Specific Heat Capacity and Thermal Capacity of Meteorites. 42nd Lunar and Planetary Science Conference. Abstract #1150, CD-ROM.

Szurgot, M. 2011. Thermal Conductivity of Meteorites. 74th Annual Meteoritical Society Meeting. Abstract No. 5074.

Szurgot, M., K. Rożniakowski, T. W. Wojtatowicz, and K. Polański (2008). Investigation of Microstructure and Thermophysical Properties of Morasko Iron Meteorites. *Crystal Research and Technology* 43.9, pp. 921–930. DOI: 10.1002/crat.200711173.

Szurgot, M., R. A. Wach, and M. Matusiak. 2014. Thermophysical Properties of NWA 4560 Chondrite. 77th Annual Meteoritical Society Meeting. Abstract No. 5007.

Szurgot, M. A. (2021). The Thermal Conductivity of the Jezersko Meteorite. *Nafta-Gaz* 77.1, pp. 10–19.

Szurgot, M., R. A. Wach, and T. A. Przylibski (2012). Thermophysical properties of the Sołtmany meteorite. *Meteorites* 2, pp. 53–65.

Tang, B., C. Zhu, N. Qiu, Y. Cui, S. Guo, X. Luo, B. Zhang, K. Li, W. Li, and X. Fu (2021). Analyzing and estimating thermal conductivity of sedimentary rocks from mineral composition and pore property. *Geofluids* 2021.1, p. 6665027.

Taylor, J. R. (1997). *An Introduction to Error Analysis: The Study of Uncertainties in Physical Measurements*. 2nd ed. Sausalito, CA: University Science Books.

Tec-Science (2020). *Thermal Conductivity in Solids and Ideal Gases*. Accessed: 2025-05-05.

The Engineering ToolBox (2003). *Thermocouples*. Accessed: 2025-04-15. The Engineering ToolBox.

The Quartz Page (2016). *Crystals – Introduction*.

Thomas, I. R., B. T. Greenhagen, N. E. Bowles, K. L. D. Hanna, J. Temple, and S. B. Calcutt (2012a). A new experimental setup for making thermal emission measurements

in a simulated lunar environment. *Review of Scientific Instruments* 83.12, p. 124502. DOI: 10.1063/1.4769084.

Thomas, S.-M., C. R. Bina, S. D. Jacobsen, and A. F. Goncharov (2012b). Radiative Heat Transfer in a Hydrous Mantle Transition Zone. *Earth and Planetary Science Letters* 357–358, pp. 130–136. DOI: 10.1016/j.epsl.2012.09.035.

Tomás, G., D. Martins, A. Cooper, and G. Bonfait (2015). Low-Temperature Thermal Conductivity of Highly Porous Copper. *IOP Conference Series: Materials Science and Engineering* 101, p. 012004. DOI: 10.1088/1757-899X/101/1/012004.

Toriumi, M. (1989). Grain Size Distribution of the Matrix in the Allende Chondrite. *Earth and Planetary Science Letters* 92.2, pp. 265–273. DOI: 10.1016/0012-821X(89)90051-4.

Tritt, T. M. and D. Weston (2006). "Measurement Techniques and Considerations for Determining Thermal Conductivity of Bulk Materials". In: *Thermal Conductivity: Theory, Properties, and Applications*. Ed. by T. M. Tritt. Boston, USA: Springer, pp. 187–203. ISBN: 978-0-387-26017-4.

Uher, C. (2006). "Thermal Conductivity of Metals". In: *Thermal Conductivity: Theory, Properties, and Applications*. Ed. by T. M. Tritt. Boston, USA: Springer, pp. 21–104. ISBN: 978-0-387-26017-4.

Van Sciver, S. W. (2012). "Low-Temperature Materials Properties". In: *Helium Cryogenics*. Ed. by S. W. Van Sciver. New York, NY: Springer, pp. 17–58. ISBN: 978-1-4419-9979-5. DOI: 10.1007/978-1-4419-9979-5_2.

Vandersande, J. W. and R. O. Pohl (1982). Negligible Effect of Grain Boundaries on the Thermal Conductivity of Rocks. *Geophysical Research Letters* 9.8, pp. 820–822. DOI: 10.1029/GL009i008p00820.

Vasseur, G., F. Brigaud, and L. Demongodin (1995). Thermal conductivity estimation in sedimentary basins. *Tectonophysics* 244.1-3, pp. 167–174.

Verble, J. L. and R. F. Wallis (1969). Infrared Studies of Lattice Vibrations in Iron Pyrite. *Physical Review* 182.3, pp. 783–789. DOI: 10.1103/PhysRev.182.783.

Vokrouhlický, D., W. F. Bottke, S. R. Chesley, D. J. Scheeres, and T. S. Statler (2015). "The Yarkovsky and YORP effects". In: *Asteroids IV*. Ed. by P. Michel, F. E. DeMeo, and W. F. Bottke. Tucson: University of Arizona Press, pp. 509–531. DOI: 10.2458/azu_uapress_9780816532131-ch027.

Vosteen, H.-D. and R. Schellschmidt (2003). Influence of Temperature on Thermal Conductivity, Thermal Capacity and Thermal Diffusivity for Different Types of Rock. *Physics and Chemistry of the Earth, Parts A/B/C* 28.9-11, pp. 499–509. DOI: 10.1016/S1474-7065(03)00069-X.

Wach, R. A., A. Adamus, and M. Szurgot. 2013. Specific Heat Capacity of Sołtmany and NWA 4560 Meteorites. 76th Annual Meteoritical Society Meeting. Abstract No. 5017.

Wach, R. A., M. Szurgot, and M. Matusiak. 2014. Thermal Properties of Kilabo Chondrite. 77th Annual Meteoritical Society Meeting. Abstract No. 5010.

Wahl, W. (1952). The Brecciated Stony Meteorites and Meteorites Containing Foreign Fragments. *Geochimica et Cosmochimica Acta* 2.2, pp. 91–117. DOI: 10.1016/0016-7037(52)90002-1.

Walsh, J. B. and E. R. Decker (1966). Effect of Pressure and Saturating Fluid on the Thermal Conductivity of Compact Rock. *Journal of Geophysical Research* 71.12, pp. 3053–3061. DOI: 10.1029/JZ071i012p03053.

Walton, E. and C. Herd. 2009. Mineralogy and Petrology of the Buzzard Coulee H4 Chondrite. AGU Spring Meeting Abstracts.

Walton, E. and C. Herd. 2009. Mineralogy, petrology and cosmogenic radionuclide chemistry of the Buzzard Coulee H4 chondrite. 40th Lunar and Planetary Science Conference. Abstract #2072.

Wasson, J. T. (1967). The Chemical Classification of Iron Meteorites: I. A Study of Iron Meteorites with Low Concentrations of Gallium and Germanium. *Geochimica et Cosmochimica Acta* 31.2, pp. 161–180. DOI: 10.1016/S0016-7037(67)80043-7.

Wasson, J. T., B.-G. Choi, E. A. Jerde, and F. Ulff-Møller (1998). Chemical Classification of Iron Meteorites: XII. New Members of the Magmatic Groups. *Geochimica et Cosmochimica Acta* 62.4, pp. 715–724. DOI: 10.1016/S0016-7037(97)00379-7.

Wasson, J. T., J. Willis, C. M. Wai, and A. Kracher (1980). Origin of Iron Meteorite Groups IAB and IIICD. *Zeitschrift für Naturforschung A* 35.8, pp. 781–795. DOI: 10.1515/zna-1980-0801.

Wasson, J., X. Ouyang, J. Wang, and E. Jerde (1989). Chemical Classification of Iron-Meteorites: XI. Multi-Element Studies of 38 New Irons and the High Abundance of Ungrouped Irons from Antarctica. *GEOCHIMICA ET COSMOCHIMICA ACTA* 53.3, pp. 735–744. DOI: 10.1016/0016-7037(89)90016-1.

Wenk, H.-R. and A. Bulakh (2016). *Minerals: Their Constitution and Origin*. 2nd ed. Cambridge University Press, pp. 149–155.

Wenrich, M. L. and P. R. Christensen (1996). Optical Constants of Minerals Derived from Emission Spectroscopy: Application to Quartz. *Journal of Geophysical Research: Solid Earth* 101.B7, pp. 15921–15931. DOI: 10.1029/96JB01153.

White, M. A. (2018). *Physical Properties of Materials, Third Edition*. 3rd ed. Boca Raton: CRC Press. 518 pp. ISBN: 978-0-429-46826-1. DOI: 10.1201/9780429468261.

Wischnewski, A., and J. L. and Zarestky (1998). Neutron Scattering Analysis of Low-Frequency Modes in Silica. *Philosophical Magazine B* 77.2, pp. 579–589. DOI: 10.1080/13642819808204986.

Woodside, W. and J. H. Messmer (1961). Thermal Conductivity of Porous Media. II. Consolidated Rocks. *Journal of Applied Physics* 32.9, pp. 1699–1706. DOI: 10.1063/1.1728420.

Wyatt, M. B., V. E. Hamilton, H. Y. McSween Jr., P. R. Christensen, and L. A. Taylor (2001). Analysis of Terrestrial and Martian Volcanic Compositions Using Thermal Emission Spectroscopy: 1. Determination of Mineralogy, Chemistry, and Classification Strategies. *Journal of Geophysical Research: Planets* 106.E7, pp. 14711–14732. DOI: 10.1029/2000JE001356.

Xia, Y., Y. Song, H. Liu, Z. Lu, J. Zheng, F. Liu, and M. Song (2022). The Effect of Different Copper Discs on the Discharge of Superconducting Coils. *Crystals* 12.8 (8), p. 1118. DOI: 10.3390/cryst12081118.

Xiong, Z., B. Zhang, J. Ge, S. Zhai, and X. Guo (2021). Thermal Diffusivity and Thermal Conductivity of Alkali Feldspar at 0.8–3 GPa and 300–873 K. *Contributions to Mineralogy and Petrology* 176.6, p. 42. DOI: 10.1007/s00410-021-01797-2.

Yang, J. (2006). "Theory of Thermal Conductivity". In: *Thermal Conductivity: Theory, Properties, and Applications*. Ed. by T. M. Tritt. Boston, UNITED STATES: Springer, pp. 1–20. ISBN: 978-0-387-26017-4.

Yaşar, E. and Y. Erdoğan (2008). Strength and thermal conductivity in lightweight building materials. *Bulletin of Engineering Geology and the Environment* 67, pp. 513–519.

Yomogida, K. and T. Matsui (1983). Physical properties of ordinary chondrites. *Journal of Geophysical Research* 88, pp. 9513–9533.

Yu, C. C. and H. M. Carruzzo (2022). "Two-Level Systems and the Tunneling Model: A Critical View". In: *Low-Temperature Thermal And Vibrational Properties Of Disordered Solids: A Half-century Of Universal "Anomalies" Of Glasses*. Ed. by M. A. Ramos. World Scientific, pp. 113–140. ISBN: 978-1-80061-259-4. Google Books: sTOJEAAAQBAJ.

Zakharov, D. (n.d.). *Plagioclase: Albite-Anorthite Series*. The Petrographer.

Zeller, R. C. and R. O. Pohl (1971). Thermal Conductivity and Specific Heat of Noncrystalline Solids. *Physical Review B* 4.6, pp. 2029–2041. DOI: 10.1103/PhysRevB.4.2029.

Zhang, W., Y. Lv, D. Lv, L. Pan, and Z. Sun (2023). Low Infrared Emissivity Epoxy Resin/Ag Composite Coating with Outstanding Mechanical Properties and Saltwater Resistance. *Materials Express* 13.11, pp. 1959–1966. DOI: 10.1166/mex.2023.2534.

Zhou, J., X. Li, C. Chen, W. Zhou, T. R. Fielitz, P. V. Braun, and D. G. Cahill (2024). Thermal Conductivity of Polyurethane Thin Films. *Macromolecules* 57.14, pp. 6838–6847. DOI: 10.1021/acs.macromol.4c00401.

Zhou, W.-X., Y. Cheng, K.-Q. Chen, G. Xie, T. Wang, and G. Zhang (2020). Thermal Conductivity of Amorphous Materials. *Advanced Functional Materials* 30.8, p. 1903829. DOI: 10.1002/adfm.201903829.

Zuñiga-Puelles, E., R. Cardoso-Gil, M. Bobnar, I. Veremchuk, C. Himcinschi, C. Hennig, J. Kortus, G. Heide, and R. Gumeniuk (2019). Structural Stability and Thermoelectric Performance of High Quality Synthetic and Natural Pyrites (FeS2). *Dalton Transactions* 48.28, pp. 10703–10713. DOI: 10.1039/C9DT01902B.

Appendices

A CFMS Data Quality Check MATLAB Code

A.1 Main MATLAB Script

```
%% CODE FOR PROCESSING GEOLOGIC SAMPLES
% Matlab script to automatically process CFMS data files.
% Reads the three temporary files to calculate thermal conductivity of
    sample.
% Make sure convergence period is the same as used by the CFMS if you want
     to compare the values
% Authors: Cosette Gilmour, Jim Freemantle (York University), and Don
    Gilmour (Independent Collaborator)

%% Enter sample name, width, height, and length between tabs (mid to mid)
%%% Replace [] with values

sampleName = 'SAMPLE NAME'; % Enter sample name

W = [];         % Width
W_err = [];     % Standard error of width
H = [];         % Height
H_err = [];     % Standard error of height
Ltabs = [];     % Distance between thermal tabs (mid-to-mid)
Ltabs_err = []; % Standard error of Ltabs

% Cross sectional-area
A = W*H;
A_err = abs(A)*sqrt((W_err/W)^2+(H_err/H)^2); %Error in cross-sectional
    area

%% Configuration file information: Max Temp and Convergence Time

configconfirm = input('Do you have the config file for this sample? [Y/N]
    ','s');

if strcmpi(configconfirm, 'Y')
    %Get configuration file
    [tfiles,tdir] = uigetfile('*.ini','Select configuration file','
        MultiSelect','off', 'C:\MATLAB');
    if isequal(tfiles, 0)
        error('No file selected. Exiting script.');
    end

    filename = fullfile(tdir,tfiles);
    config_data = readconfig(filename);

    % Organize and transpose data
    data_T = config_data(:,1:3:end).';          %Tranpose temperature date
```

```
    data_time = config_data(:,2:3:end).';      %Tranpose stability time
        data
    data_timeout = config_data(:,3:3:end).';   %Tranpose timeout time

    % Combine all colums for sorting
    config_data = [data_T, data_time, data_timeout];

    % Sort rows by the first column in descending order
    config_data = sortrows(config_data,'descend');


elseif strcmpi(configconfirm, 'N')
    %Manually enter config information
    prompt = 'Enter space separated "temperature,dT time,timeout" triads (
        K,sec,sec)';
    x = inputdlg(prompt, 'Config Settings', [1 50]);

    % Validate input
    if isempty(x)
        error('No input provided. Exiting script.');
    end

    % Convert input string to a numerical array
    config_data = textscan(x{:}, '%f,%f,%f'); % Read space-separated
        numeric values into three columns
    config_data = [config_data{:}]; % Convert cell array to a numerical
        matrix

    % Ensure that the input is in correct triads
    if mod(size(config_data, 2), 3) ~= 0
        error('Invalid input format. Please provide data in temperature,
            dT time, and timeout triads.');
    end

else
    error('Invalid input. Please enter Y or N.');
end

%% Gather temporary files (e.g., dT = 0.1, 0.2, 0.3)

% Select folder that contains temporary folders
folder =  uigetdir('C:\Users\...\'); % UPDATE FOLDER WHERE TEMPORARY FILES
    ARE SAVED
tempdata = tempfiles(folder);
N = numel(tempdata);

% Pre-allocate and read each file to gather data
time = cell(N,1);       %Measurement time
dT = cell(N,1);         %deltaT
W = cell(N,1);          %Power
T_heatsink = cell(N,1); %Heatsink temperature

for i = 1:N
    fullFileName = fullfile(tempdata(i).folder, tempdata(i).name);
    fileID = fopen(fullFileName, 'rt');
    fileText = fileread(fullFileName);
    lines = splitlines(fileText);
```

```
90
91      firstLine = 0;  % Hold the index of the first line
92      for h = 1:length(lines)
93          lineStr = strtrim(lines{h});  % Remove extra spaces
94          if ~isempty(lineStr)          % Only check non-empty lines
95              firstChar = lineStr(1);   % Get the first character
96              % Check if first character is a number
97              if (firstChar >= '0' && firstChar <= '9')
98                  firstLine = h;
99                  break;  % Stop as soon as we find the first numeric line
100             end
101         end
102     end
103
104     allLines = strjoin(lines(firstLine:end), newline);
105     data = textscan(allLines, '%f%f%f%f%f', 'MultipleDelimsAsOne', true);
106     fclose(fileID);
107
108     time{i} = data{1}; dT{i} = data{2}; W{i} = data{4}; T_heatsink{i} =
            data{5};
109 end
110
111 % Create structure array for the data collected from the temporary files
112 FileName = {tempdata.name}'; Date = {tempdata.date}';
113 DataArray = struct('File', FileName, 'Date', Date, 'Time', time, 'dT', dT,
        'W', W, 'Heatsink_Temp', T_heatsink);
114
115 % Separate data into the three arrays (e.g., dT = 0.1, 0.2, 0.3)
116 if N == 3
117     % Special case for N = 3
118     date_array = reshape(Date, [], 3); % Create a single row with 3
            elements
119     filename_array = reshape(FileName, [], 3);
120 else
121     % Reshape for grouping into sets of 3 and transpose
122     date_array = reshape(Date, 3, [])';
123     filename_array = reshape(FileName, 3, [])';
124 end
125
126 %Temporary File Data
127 arrayIdx = reshape(1:N, 3, [])';
128 n = N/3;
129 time_array = cell(n, 1); dT_array = cell(n, 1);
130 W_array = cell(n, 1); T_heatsink_array = cell(n, 1);
131
132 for k = 1:n
133     idx = arrayIdx(k, :);
134     time_array{k} = time(idx); dT_array{k} = dT(idx);
135     W_array{k} = W(idx); T_heatsink_array{k} = T_heatsink(idx);
136 end
137
138 % Get first temperature for each sequence run (dT1)
139 T_heatsink_dT1 = cellfun(@(x) x(1), T_heatsink(1:3:end));
140
141 % Assign configuration time
142 config_time = zeros(n,1);
143
```

```
for r = 1:n
    for u = 1:numel(config_data(:,1))
         if T_heatsink_dT1(r) <= config_data(u,1)
             config_time(r) = config_data(u,2);
         end
    end
end

% Assign timeout time
timeout = zeros(n,1);

for r = 1:n
    for u = 1:numel(config_data(:,3))
         if T_heatsink_dT1(r) <= config_data(u,1)
             timeout(r) = config_data(u,3);
         end
    end
end

% Combine heatsink temperature, config. time, and and timeout into a
    single cell array
config = [num2cell(T_heatsink_dT1), num2cell(config_time), num2cell(
    timeout)];


%% Gather heatsink temperature, dT, and W collected over configuration
    time

% Calculate average time between measurements for each array (e.g., dT =
    0.1, 0.2, 0.3)
avg_time = reshape(cellfun(@(x) x(end) / (numel(x)-1), time), 3, []).';

% Preallocate arrays to store values and errors
time_data = cell(n,3);
T_heatsink_data = cell(n,3);
dT_data = cell(n,3);
W_data = cell(n,3);
T_heatsink_err = cell(n,3);
dT_err = cell(n,3);
W_err = cell(n,3);
avg_Temp = cell(n,1);

for z = 1:n
    config_duration = config_time(z); % Get configuration time for the
        measurement array
    for p = 1:3
        avg_t = avg_time(z, p); % Get the average time for each array (e.g
            ., dT = 0.1, 0.2, 0.3)

        % Determine the number of data points over the configuration time
        idx_start = max(1, numel(T_heatsink_array{z, 1}{p}) - ceil((
            config_duration / avg_t) - 1));

        % Extract and store the relevant data
        time_data{z, p} = time_array{z, 1}{p}(idx_start:end);
        T_heatsink_data{z, p} = T_heatsink_array{z, 1}{p}(idx_start:end);
        dT_data{z, p} = dT_array{z, 1}{p}(idx_start:end);
```

```
194         W_data{z, p} = W_array{z, 1}{p}(idx_start:end);
195
196         % Calculate and store the standard error
197         T_heatsink_err{z, p} = std(T_heatsink_data{z, p}) / sqrt(numel(
                T_heatsink_data{z, p}));
198         dT_err{z, p} = std(dT_data{z, p}) / sqrt(numel(dT_data{z, p}));
199         W_err{z, p} = std(W_data{z, p}) / sqrt(numel(W_data{z, p}));
200     end
201      avg_Temp{z} = round(mean(vertcat(T_heatsink_data{z,:})));
202 end
203
204
205 %% Plot temporary data for visual QA
206
207 % Extract the last number in the folder path as the date
208 getpathNum = regexp(folder, '\d+', 'match'); % Gather all numbers in file
    path as strings
209 date = str2double(getpathNum{end}); % Use the last number in the list as
    the date
210
211 % Create master file directory for saving figures
212 dateStr = num2str(date); % Convert date to string for folder naming
213 figuresFolder = [dateStr, 'Figures']; % Name the "Figures" folder
214 fig_dir = fullfile(folder, figuresFolder); % Create full path for the "
    Figures" folder
215
216 % Ensure the "Figures" folder exists (create if not already present)
217 if ~exist(fig_dir, 'dir')
218     mkdir(fig_dir);
219 end
220
221 %% Linear regression to get conductance
222
223 % Linear regression; Pre-allocated for Temperature, Slope, SE, and R^2
224 linreg = zeros(n,4);
225
226 %Plot
227  for i = 1:n
228
229     x = vertcat(dT_data{i,:}); % dT values from file
230     y = vertcat(W_data{i,:}); % W values from file
231
232     % Perform linear regression for measured power
233     mdl = fitlm(x, y, 'linear');
234     slope = mdl.Coefficients.Estimate(2);
235     intercept1 = mdl.Coefficients.Estimate(1);
236     rsq = mdl.Rsquared.Ordinary;
237     linreg(i,:) = [avg_Temp{i}, slope, mdl.Coefficients.SE(2), rsq];  %
        Store regression results
238  end
239
240 % Convert results to table format
241 linreg = array2table(linreg, 'VariableNames', {'Temperature', 'Slope', 'SE
    ', 'Rsquared'});
242
243 %% All figures
244
```

```
set(0,'DefaultFigureWindowStyle','normal');
Fig = figure('Visible', 'off', 'Position', [150, 150, 1200, 500]);

TempEff = cell(n,1);
TempEnd = cell(n,1);

% Loop to create the figures
for i = 1:n
    tile = tiledlayout(1, 4, 'TileSpacing', 'Loose', 'Padding', 'Compact')
        ;

    % Overall time and heatsink temperature of full array (e.g., DT = 0.1,
        0.2, 0.3)
    Time1 = time_array{i,1}{1,1};
    Time2 = time_array{i,1}{2,1} + Time1(end);
    Time3 = time_array{i,1}{3,1} + Time2(end);
    Time = [Time1; Time2; Time3];
    Temp = vertcat(T_heatsink_array{i,1}{:});

    % Effective time range
    temporaryTime = time_array{i,1}{1,1}; % temporary variable
    num = numel(Time1) - numel(time_data{i,1}) + 1;
    effTime1 = temporaryTime(num:end, :);
    effTime2 = time_array{i,1}{2,1} + effTime1(end);
    effTime3 = time_array{i,1}{3,1} + effTime2(end);
    effTime = [effTime1; effTime2; effTime3];

    % Starting time to effective time range
    startTime = temporaryTime(1:(num-1));

    % Effective heatsink temperature range
    temporaryTemp = T_heatsink_array{i,1}{1,1}; % temporary variable
    num = numel(temporaryTemp) - numel(T_heatsink_data{i,1}) + 1;
    effTemp1 = temporaryTemp(num:end, :);
    effTemp = [effTemp1;  T_heatsink_array{i,1}{2,1}; T_heatsink_array{i
        ,1}{3,1}];

    % Starting temperature/time to Effective temperature/time
    startTemp = temporaryTemp(1:(num-1));

    % Plot dT vs. time
    nexttile;
    hold on;
    for j = 1:3
        plot(time_array{i, 1}{j, 1}, dT_array{i, 1}{j, 1});
        if time_array{i, 1}{j, 1}(end) > timeout(i) - 2
            text(0, dT_array{i, 1}{j, 1}(end), "TIME OUT", 'FontWeight', '
                bold', 'FontSize', 10, 'Color', 'r');
        end
    end
    title('dT vs. Time');  % Title for the current tile
    xlabel('Time (sec)');
    ylabel('dT (K)');
    legend('dT1', 'dT2', 'dT3', 'Location', 'southeast', 'FontSize', 9);
    box on;

    % Plot W vs. Time
```

```
    nexttile;
    hold on;
    for j = 1:3
        plot(time_array{i, 1}{j, 1}, W_array{i, 1}{j, 1});
    end
    title('Power vs. Time');
    xlabel('Time (sec)');
    ylabel('Power (W)');
    legend('dT1', 'dT2', 'dT3', 'Location', 'southeast', 'FontSize', 9);
    box on;

    % Plot Heatsink Temperature
    nexttile;
    hold on;

    % Annotate Heatsink Temperature
    Temp1 = startTemp(1);
    TempEff{i,1} = effTemp(1);
    TempEnd{i,1} = Temp(end);
    Tdrift = abs(TempEnd{i,1} - TempEff{i,1});

    % Determine plot color based on conditions
    if all(Temp1 >= 50) && all(Tdrift > 1)
        lineColor = [0.8500 0.3250 0.0980];
        effLineColor = 'm'; % Magenta
    elseif all(Temp1 < 50) && all(Tdrift > 2)
        lineColor = [0.8500 0.3250 0.0980];
        effLineColor = 'm'; % Magenta
    else
        lineColor = [0.8500 0.3250 0.0980];
        effLineColor = [0 0.4470 0.7410];
    end

    % Create plots
    plot1_str = sprintf('T_{1} - T_{e}: %.2f - %.2f K', Temp1, TempEff{i
        ,1});
    plot(startTime, startTemp, 'DisplayName', plot1_str, 'Color',
        lineColor, 'LineWidth', 1);
    hold on;

    plot2_str = sprintf('T_{e} - T_{f}: %.2f - %.2f K', TempEff{i,1},
        TempEnd{i,1});
    plot(effTime, effTemp, 'Color', effLineColor, 'DisplayName', plot2_str
        , 'LineWidth', 1);
    hold on;

    title('Heatsink Temp vs. Time');
    xlabel('Time (sec)');
    ylabel('Temperature (K)');
    box on;

    % Create and format legend
    lgd = legend('show', 'Location', 'southeast', 'FontSize', 8);
    lgdTitle_str = sprintf('Temp Range: %.2f - %.2f K', Temp1, TempEnd{i
        ,1});
    title(lgd, lgdTitle_str);

```

```
    % dT vs. W (conductance)
    nexttile;
    hold on;
    x = vertcat(dT_data{i,:}); % dT values from file
    y = vertcat(W_data{i,:}); % W values from file

    % Set R2 threshold
    rSquaredThreshold = 0.9;

    % Plot for measured power (blue)
    plotLinearFit(x, y, 'blue', 'o', 75, rSquaredThreshold, 0.05); %
        Measured power text

    % Title and labels
    title('dT vs. Power');
    xlabel('dT (K)');
    ylabel('Power (W)');

    % Add legend
    legend('Measured', 'Measured LR', 'Location', 'southeast');
    box on;

    % Figure title
    figTitle = title(tile, sprintf('%s %d K (%s)', sampleName, avg_Temp{i
        }, dateStr), 'FontWeight', 'bold', 'FontSize', 16);

    % pause(0.75);

    % Save figure
    tempValue = T_heatsink_array{i,1}{1,1}(1); % Extract numerical value
    tempStr = strrep(sprintf('%.2f', tempValue), '.', 'p'); % Convert to
        string and replace '.' with '-'
    figName = sprintf('%s_%s_%s', sampleName, tempStr, dateStr); % name of
         figure
    saveas(Fig, fullfile(fig_dir, figName), 'jpeg'); %saves Figure
    %Note: will get a warning if folder already exist

clf(tile);
end

close(Fig);

%% Update datasheet

% Select the CFMS data file for the corresponding measurement run
[tfile2,tdir2] = uigetfile(fullfile(folder,'*.dat*'));
filename = strcat(tdir2,tfile2);
data = readtable(filename, 'PreserveVariableNames', true);
dataname = strrep(tfile2, '.dat','_');
dataname = strcat(dataname, 'QA_', dateStr);

%Remove unncessary columns
data = removevars(data, 1); %Remove "Time"
data = removevars(data, 1); %Remove "B_digital_(T)"
data = removevars(data, 1); %Remove "B_analog_(T)"
data = removevars(data, 3); %Remove "Delta_T_(K)"
data = removevars(data, 3); %Remove "S_V/K"
```

```
data = removevars(data, 5); %Remove "Heater_power_(W)"
data = removevars(data, 7); %Remove "Magnet"
data = removevars(data, 7); %Remove "Switch"

% Calculate temperature difference between the VTI and sensorB
    temperatures
data.diff_senB_VTI = abs(data.(1)-data.(2)); %calculate difference between
     sensorB and VTI temperatures
data = movevars(data, size(data, 2), "Before", 2);

%Calculated conductivity and error
calc_conductivity = cell(n,1);
calc_conductivity_err = cell(n,1);
for k = 1:n
    calc_conductivity{k} = (linreg{k,2}*Ltabs)/A;
    calc_conductivity_err{k} = calc_conductivity{k}*sqrt((linreg{k,3}/
       linreg{k,2})^2+(Ltabs_err/Ltabs)^2+(A_err/A)^2);
end

%Update table
for i = 1:n
    Temp = vertcat(T_heatsink_data{i,:});
    data.Temp_avg(i) = mean(Temp); %Mean temperature of the three runs (
       averaged over the convergence time)
    data.err_Temp_avg(i) = std(Temp)/sqrt(numel(Temp)); %Standard error of
        mean temperature of the three runs (averaged over the convergence
       time)
    data.Calc_TC(i) = calc_conductivity{i}; %Calculated conductivity (mdl1
       )
    data.Err_CalcTC(i) = calc_conductivity_err{i}; %Calculated
       conductivity error (mdl1)
    data.Calc_Conductance(i) = linreg{i,2};  %Calculated conducantance (
       mdl1)
    data.Err_Conductance(i) = linreg{i,3}; %Error in conductance (slope of
        line) (mdl1)
    data.R2(i) = linreg{i,4}; %R-squared (mdl1)
    data.configTime(i) = config_time(i); %Stability time of DT (seconds)
    data.T_Sample_K_1(i) = T_heatsink_dT1(i); %starting temperature of
       measurement
    data.T_Sample_K_eff(i) = TempEff{i,1}; %starting temperature of
       effective temperature
    data.T_sample_K_end(i) = TempEnd{i,1}; %end temperature of measurement

    data.T_hs1(i) = mean(T_heatsink_data{i,1}); %average heatsink
       temperature over convergence time - first file
    data.T_hs2(i) = mean(T_heatsink_data{i,2}); %average heatsink
       temperature over convergence time - second file
    data.T_hs3(i) = mean(T_heatsink_data{i,3}); %average heatsink
       temperature over convergence time - third file
    data.err_T_hs1(i) = T_heatsink_err{i,1}; %SE of temperature over
       convergence time - first file
    data.err_T_hs2(i) = T_heatsink_err{i,2}; %SE of temperature over
       convergence time - second file
    data.err_T_hs3(i) = T_heatsink_err{i,3}; %SE of temperature over
       convergence time - third file

```

```
441     data.dT1(i) = mean(dT_data{i,1}); %average dT over convergence time -
            first file
442     data.dT2(i) = mean(dT_data{i,2}); %average dT over convergence time -
            second file
443     data.dT3(i) = mean(dT_data{i,3}); %average dT over convergence time -
            third file
444     data.err_dT1(i) = dT_err{i,1}; %SE of dT over convergence time - first
             file
445     data.err_dT2(i) = dT_err{i,2}; %SE of dT over convergence time -
            second file
446     data.err_dT3(i) = dT_err{i,3}; %SE of dT over convergence time - third
             file
447
448     data.P1(i) = mean(W_data{i,1}); %average power over convergence time -
             first file
449     data.P2(i) = mean(W_data{i,2}); %average power over convergence time -
             second file
450     data.P3(i) = mean(W_data{i,3}); %average power over convergence time -
             third file
451     data.err_P1(i) = W_err{i,1}; %SE of power over convergene time- first
            file
452     data.err_P2(i) = W_err{i,2}; %SE of power over convergene time- second
             file
453     data.err_P3(i) = W_err{i,3}; %SE of power over convergene time- first
            file
454
455     % Extract date and time for each temporary file
456     dt1 = datetime(date_array{i,1}, 'InputFormat', 'dd-MMM-yyyy HH:mm:ss')
            ;
457     dt2 = datetime(date_array{i,2}, 'InputFormat', 'dd-MMM-yyyy HH:mm:ss')
            ;
458     dt3 = datetime(date_array{i,3}, 'InputFormat', 'dd-MMM-yyyy HH:mm:ss')
            ;
459
460     data.File_prefix{i} = string(extractBefore(filename_array{1,1}, 'T'));
             % Prefix of temporary file names
461     data.Date1{i} = string(dt1,'yyyy-MM-dd');
462     data.Time1{i} = string(dt1,'hh:mm a');
463     data.Date2{i} = string(dt2,'yyyy-MM-dd');
464     data.Time2{i} = string(dt2,'hh:mm a');
465     data.Date3{i} = string(dt3,'yyyy-MM-dd');
466     data.Time3{i} = string(dt3,'hh:mm a');
467 end
468
469 data.Drift_T = abs(data.(20)-data.(19)); %Effective temperature drift (
        T_end - T_effective)
470
471 %Updated conductivity based on real measurements from calliper
472 %Note that original measurements were based off Ltabs = 11 mm and CA =
        0.03 mm2 provided by Cryogenics.
473 data.ReCalc_TC = (data.(4)*Ltabs)/A;
474
475 % Percent differences between measured and calculated data
476 data.per_diff_senB_Tavg = abs((data.(10)-data.(3))./((data.(10)+data.(3))
        /2))*100; %percent difference between CFMS sensorB temp and mean Temp
477 data.per_diff_TC = abs((data.(47)-data.(12))./((data.(47)+data.(12))/2))
        *100; %percent error between CFMS conductivity and MATLAB conductivity
```

```
data.per_diff_Conductance = abs((data.(4)-data.(14))./((data.(4)+data.(14))/2))*100; %percent error between CFMS conductance and MATLAB conductance

data = movevars(data, 6, "After", 50);
data = movevars(data, 6, "After", 50);
data = movevars(data, 6, "After", 50);
data = movevars(data, 6, "After", 50);
data = movevars(data, "per_diff_senB_Tavg", "After", "sensor_B_(K)");
data = movevars(data, "Temp_avg", "After", "per_diff_senB_Tavg");
data = movevars(data, "err_Temp_avg", "After", "Temp_avg");
data = movevars(data, "Calc_TC", "After", "err_Temp_avg");
data = movevars(data, "Err_CalcTC", "After", "Calc_TC");
data = movevars(data, "ReCalc_TC", "After", "Err_CalcTC");
data = movevars(data, "per_diff_TC", "After", "ReCalc_TC");
data = movevars(data, "Th_conductivity_(W/m_K)", "After", 50);
data = movevars(data, "per_diff_Conductance", "After", "Th_conductance_(W/K)");
data = movevars(data, "Drift_T", "Before", "T_hs1");

data

% Save table
save_data = [folder '\' dataname];
writetable(data, save_data, 'Delimiter', '\t');
```

A.2 MATLAB Function Files

Function: readconfig

```
% Make sure Python is installed on computer
% Make sure there are no spaces in file directory.
function data = readconfig(configfile)
C ={'py C:\MATLAB\readconfig.py',configfile}; % Update path if needed
dosCmd =strjoin(C);
[status,cmdout]=dos(dosCmd);
data=str2num(cmdout);
end
```

Function: tempdata

```
function tempdata = tempfiles(folder)
files = fullfile(folder, '*DT*.dat');
%files = fullfile(folder, '*.dat');
tempdata = dir(files);
tempdata = tempdata(~[tempdata.isdir]);
[~,idx] = sort([tempdata.datenum]); % Sort files by date/time
tempdata = tempdata(idx);
end
```

Function: plotLinearFit

```
function plotLinearFit(x, y, color, markerType, sizeData,
    rSquaredThreshold, textVerticalOffset)
    % Fit linear model
    mdl = fitlm(x, y, 'linear');

    % Extract coefficients
    slope = mdl.Coefficients.Estimate(2);
    intercept = mdl.Coefficients.Estimate(1);
    rsq = mdl.Rsquared.Ordinary;

    % Determine equation text color based on R2 value
    if rsq < rSquaredThreshold
        textColor = '#FFA500'; % Set to orange if R2 < threshold
    else
        textColor = color; % Use default color if R2 >= threshold
    end

    % Create the equation string
    if intercept > 0
        equationFormat = sprintf('y = %.4Ex + %.4E\nR^2 = %.3f', slope,
            intercept, rsq);
    elseif intercept < 0
        equationFormat = sprintf('y = %.4Ex - %.4E\nR^2 = %.3f', slope,
            abs(intercept), rsq);
    else
        equationFormat = sprintf('y = %.4Ex\nR^2 = %.3f', slope, rsq);
    end

    % Plot data points
    scatter(x, y, markerType, 'filled', 'MarkerEdgeColor', 'k', 'LineWidth
        ', 0.1, 'MarkerFaceColor', color, 'SizeData', sizeData);

    % Plot the regression line
    plot(x, predict(mdl, x), strcat(color, '--'), 'LineWidth', 0.4);

    % Get the current axis limits
    xLimits = xlim;
    yLimits = ylim;

    % Define text position based on plot limits and textVerticalOffset
    textPositionX = xLimits(1) + 0.01; % Slight offset from left edge
    textPositionY = yLimits(2) - textVerticalOffset * yLimits(2); %
        Adjusted Y position with offset

    % Display the equation with the determined text color
    text(textPositionX, textPositionY, equationFormat, ...
        'HorizontalAlignment', 'left', 'FontSize', 8.5, 'Color', textColor
            );
end
```

A.3 Python Script for Configuration File Parsing

This Python script reads the configuration files and extracts the data so it can be used in the main MATLAB code. *Written by J. Freemantle.*

```
# This code saved in the same place the configuration settings are saved.

import struct, sys
datalist = []
# mylist = ["P", "I", "D", "Temp", "dt Tol", "Stability Time", "Power tol
    ", "Timeout"]
# datalist.append(mylist)
mylist = []
# logfile = "c:\\Users\\jim\\iCloudDrive\\Documents\\cfms.cfg"
# logfile = input("Enter configuration file name: ")
logfile = str(sys.argv[1])
fp = open(logfile, "r")
lines = fp.readlines()
tempdata = lines[11]

x = tempdata[1:8]

# in lists 0 is first element
for i in range(1, int(x) + 1):
    for index in range(1, 9):
        j = index * 8 + (i - 1) * 64
        element = tempdata[j:j + 8]
        mylist.append(struct.unpack('!f', bytes.fromhex(element))[0])
    datalist.append(mylist)
    mylist = []

fp.close()

for x in datalist:
    # for y in x:
    #     out = "{},".format(y)
    #     print(out, end="")
    print(x[3], x[5], x[7], ' ', end='')
```

B Taylor Series Expansion of the Stefan–Boltzmann Law

The Stefan–Boltzmann law for radiating bodies is given by:

$$P_r = \sigma A \varepsilon \left[(T + \Delta T)^4 - T^4 \right]$$

To simplify this expression, a Taylor series expansion is applied to $(T + \Delta T)^4$, where:

$$f(x) = x^4$$

$$\Delta x = \Delta T$$

$$f(x + \Delta x) = (T + \Delta T)^4$$

Taylor expansion:

$$f(x + \Delta x) = f(x) + f'(x)\Delta x + \frac{f''(x)}{2!}(\Delta x)^2 + \frac{f^{(3)}(x)}{3!}(\Delta x)^3 + \frac{f^{(4)}(x)}{4!}(\Delta x)^4$$

$$(T + \Delta T)^4 = T^4 + 4T^3\Delta T + 6T^2\Delta T^2 + 4T\Delta T^3 + \Delta T^4$$

Substituting this back into the original equation:

$$P_r = \sigma A \varepsilon \left(T^4 + 4T^3\Delta T + 6T^2\Delta T^2 + 4T\Delta T^3 + \Delta T^4 - T^4 \right)$$

$$P_r = \sigma A \varepsilon \left(4T^3\Delta T + 6T^2\Delta T^2 + 4T\Delta T^3 + \Delta T^4 \right)$$

However, in thermal conductivity measurements, $\Delta T \ll T$, so the last three terms in the brackets are negligible.

$$\therefore P_r \approx 4\sigma A \varepsilon T^3 \Delta T$$

C Quantitative XRD Results for Minerals

Table C.1: Quantitative XRD results using a database standard (ICDD PDF-2).

PDF-2 Number	Phase name	Fraction[1]	RIR[2]	Weight %
060710	Pyrite	1.6	2.90	95.5 ± 6.7
	Global Amorphous	0.030	0.55	4.5 ± 1.8
461045	Quartz	1	3.41	98.9 ± 2.2
	Global Amorphous	0.006	0.55	1.1 ± 1.0
721214	Calcite	1	3.20	98.1 ± 3.1
	Global Amorphous	0.011	0.55	1.9 ± 1.3
090466	Albite	1	2.10	96.2 ± 4.2
	Global Amorphous	1	0.021	3.8 ± 1.7

[1] Arbitrary units used for internal reference ratio calculations.
[2] Reference Intensity Ratio; relative scale used to compare intensities of phases in XRD analysis.

D Individual Thermal Conductivity Data (Uncorrected)

The data presented in this appendix include all thermal conductivity measurements of the single-crystal minerals and obsidian. The data presented here passed the quality check process (Section 3.3.2). These values have not been corrected for radiative heat transfer.

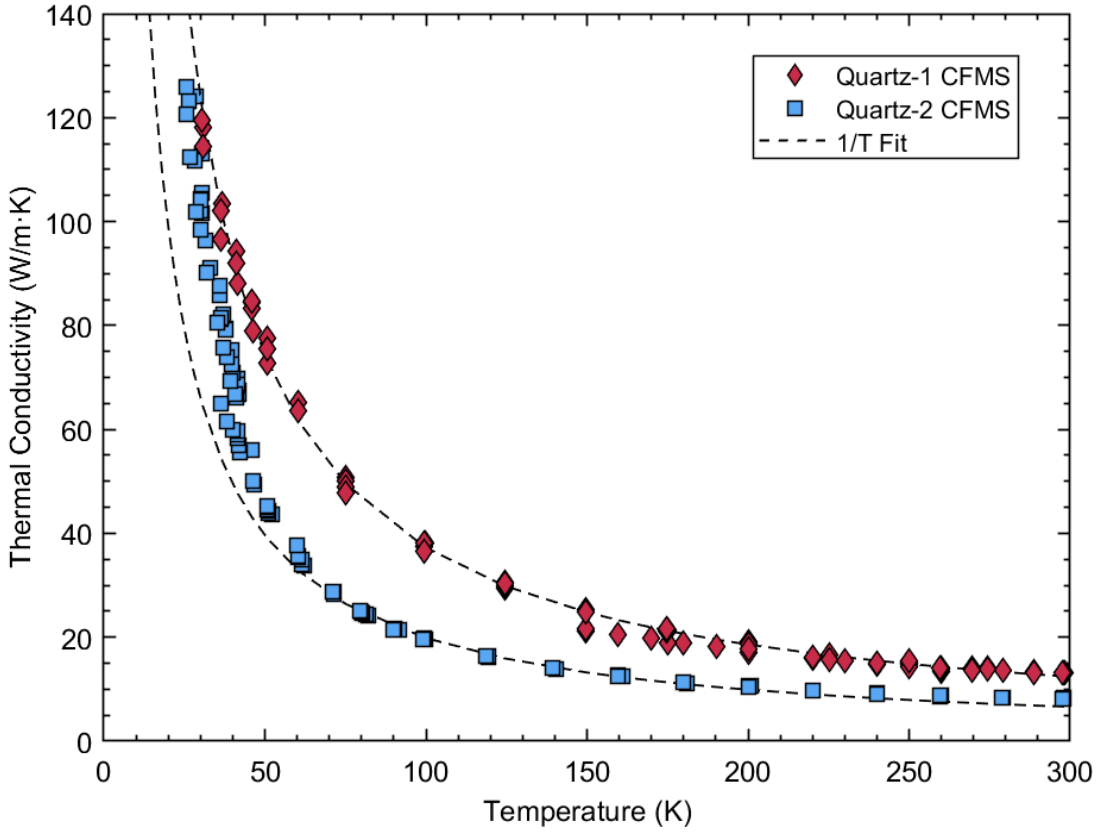

Figure D.1: Individual thermal conductivity measurements for Quartz-1 and Quartz-2. Error bars are smaller than the symbols and are not visible in the plots.

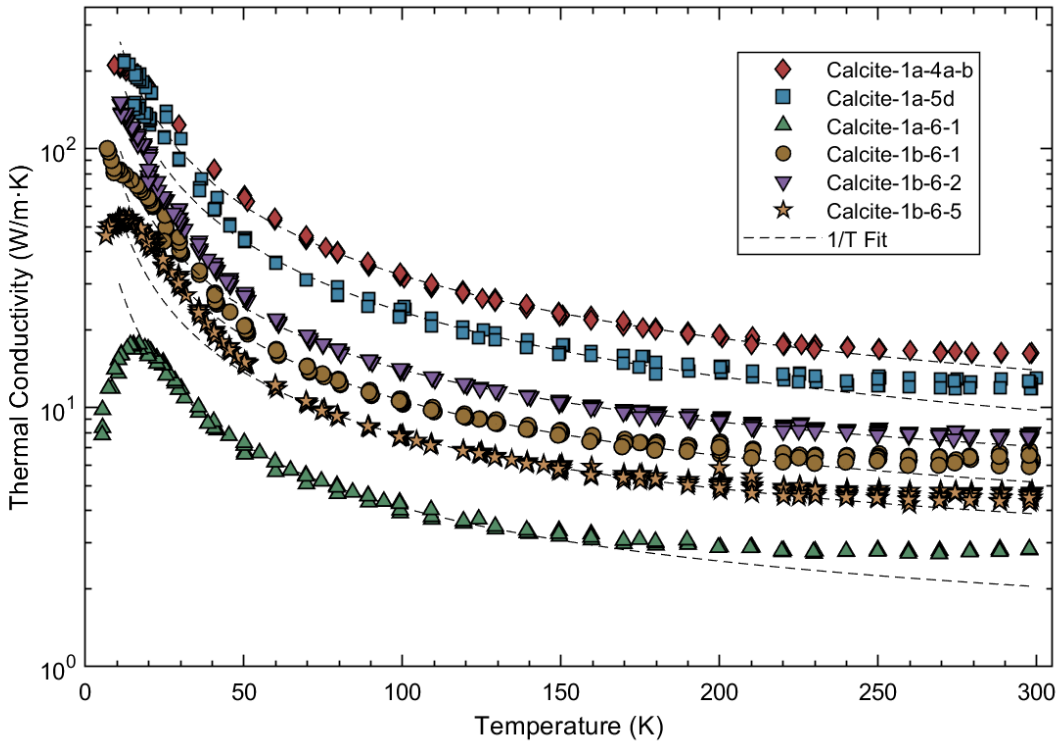

Figure D.2: Individual thermal conductivity measurements for the six calcite samples. Data values have been scaled by a factor of 0.5 for clarity. Error bars are smaller than the symbols and are not visible in the plots.

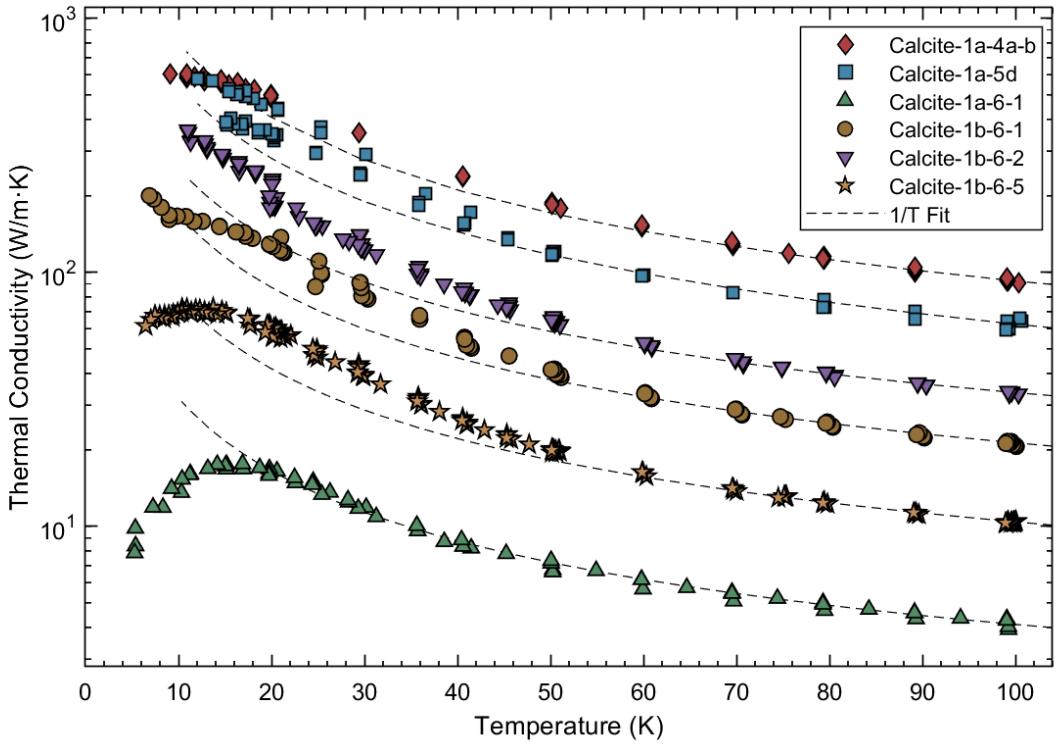

Figure D.3: Individual thermal conductivity measurements for the six calcite samples below 100 K. Data values have been scaled by a factor of 0.5 for clarity. Error bars are smaller than the symbols and are not visible in the plots.

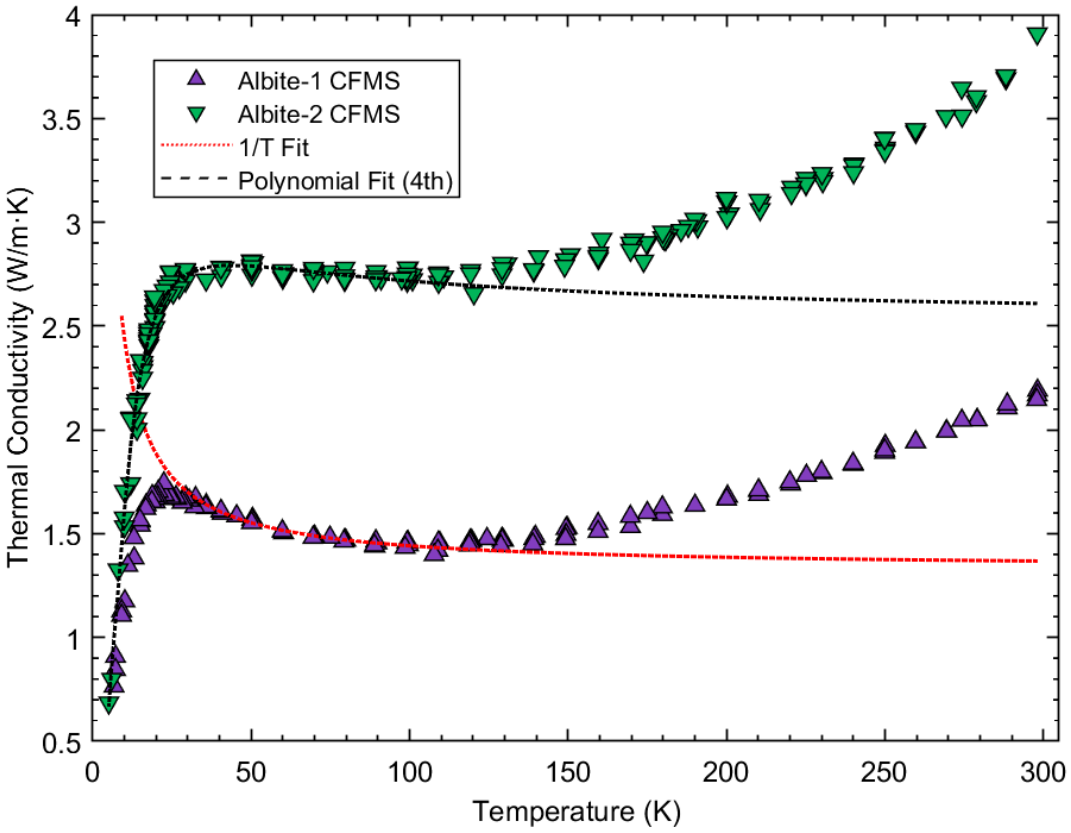

Figure D.4: Individual thermal conductivity measurements for Albite-1 and Albite-2. Error bars are smaller than the symbols and are not visible in the plots.

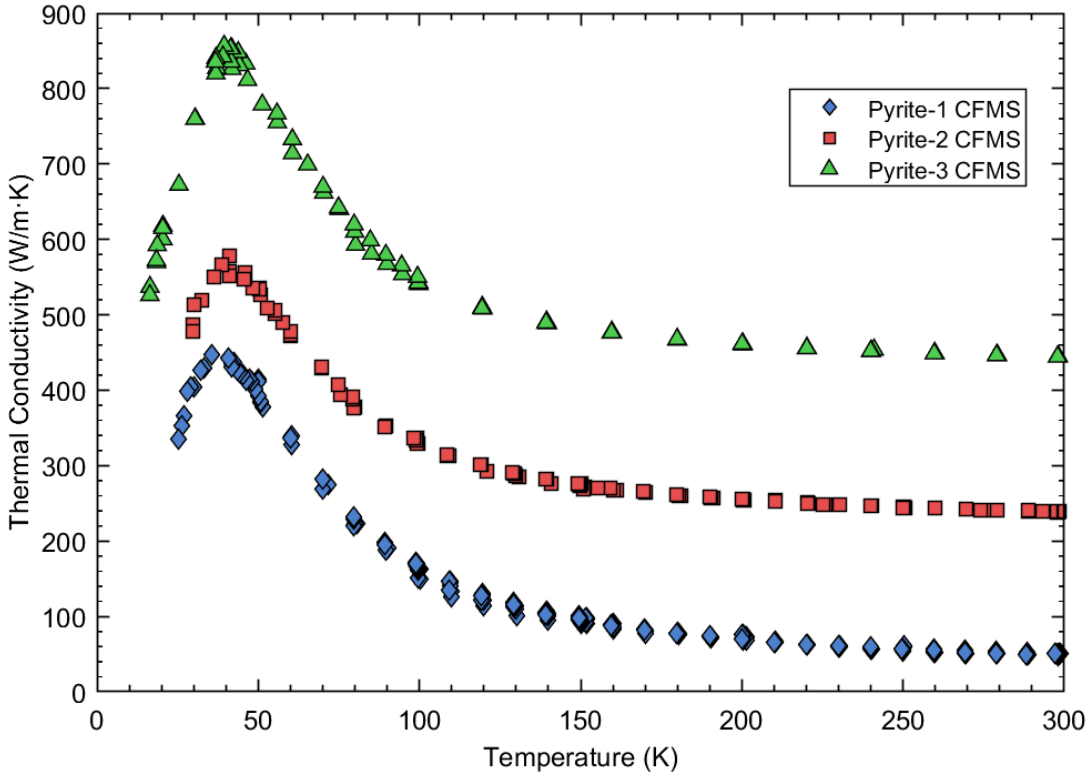

Figure D.5: Individual thermal conductivity measurements for the three pyrite samples. For clarity, Pyrite-1, Pyrite-2, and Pyrite-3 have been offset by 0, 200, and 400 W m^{-1} K^{-1}, respectively. Error bars are smaller than the symbols and are not visible in the plots.

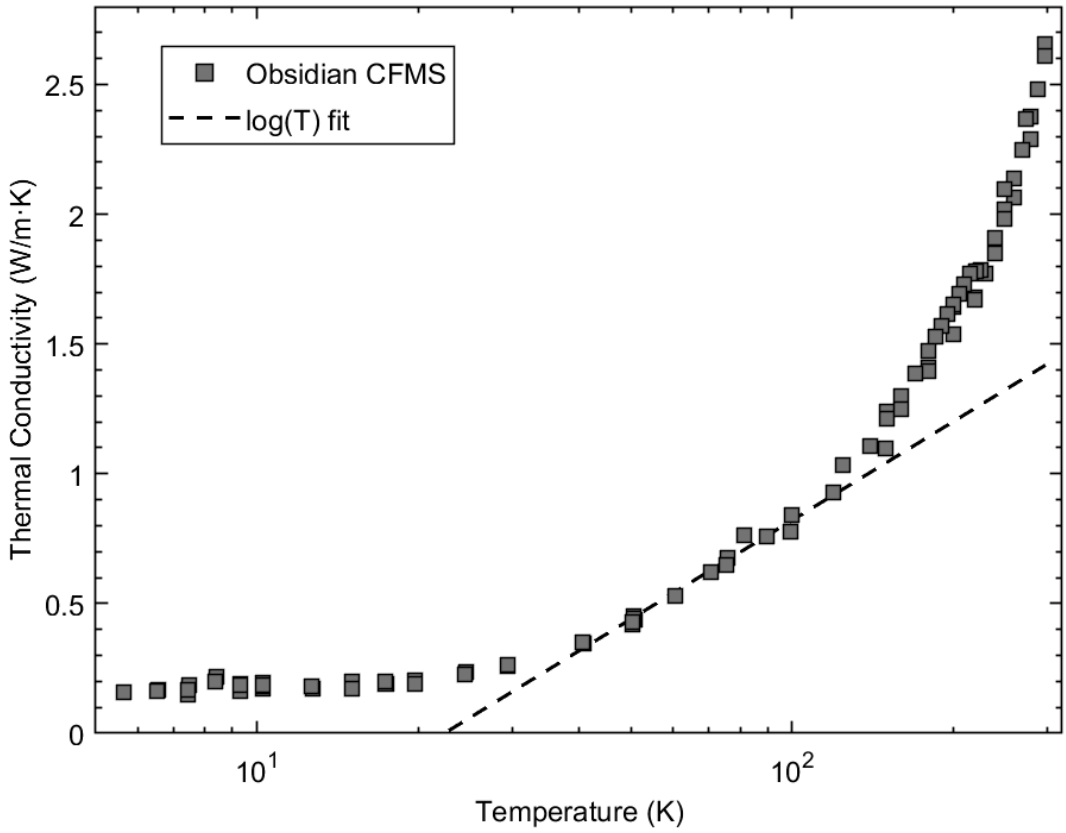

Figure D.6: Individual thermal conductivity measurements for the obsidian sample. Error bars are smaller than the symbols and are not visible in the plot. An empirical fit of $a \cdot log(T) + b$, applied to data above 40 K, is included for reference.

E Average Emissivity Calculation

The average (or total) emissivity of a sample is obtained by integrating the emission spectrum over the thermal infrared wavelength (λ) region (8–14 µm), divided by the total radiative power per unit area emitted by a black body integrated over the same wavelength range (Hapke, 2012):

$$\bar{\varepsilon} = \frac{\int_{8\ \mu\mathrm{m}}^{14\ \mu\mathrm{m}} \varepsilon(\lambda) U(\lambda, T)\, d\lambda}{\int_{8\ \mu\mathrm{m}}^{14\ \mu\mathrm{m}} U(\lambda, T)\, d\lambda} \tag{E.1}$$

where:

- $\varepsilon(\lambda)$ is the measured spectral emissivity at a specified temperature T and wavelength λ, defined as:

$$\varepsilon(\lambda) = \frac{U_o(\lambda, T)}{U(\lambda, T)} \tag{D.2}$$

- $U_o(\lambda, T)$ is the spectral radiance emitted by the object.

- $U(\lambda, T)$ is the spectral radiance of a black body, given by Planck's law:

$$U(\lambda, T) = \frac{2\pi h c^2}{\lambda^5} \cdot \frac{1}{\exp\left(\frac{hc}{\lambda k T}\right) - 1} \tag{D.3}$$

where h is Planck's constant (6.626×10^{-34} J·s), c is the speed of light (3×10^8 m/s), and k is Boltzmann's constant (1.381×10^{-23} J/K).

MATLAB Code for Average Emissivity

The following MATLAB code was used to compute the average emissivity from emission spectral data:

```
%% This MATLAB code calculates the average emissivity from emission spectra.
% If the spectral data is in reflectance, convert to emissivity using: e = 1 - R (Kirchhoff's Law)

% Input by user
lambda = []; % wavelength (micrometer)
e = [];      % emissivity
T = 300;     % temperature in Kelvin

% Refine data
lambda = lambda * 1e-6; % convert to meters
[lambda, idx] = sort(lambda);
e = e(idx);

% Constants
h = 6.626e-34; % Planck's constant (J.s)
c = 3e8;       % speed of light (m/s)
k = 1.38e-23;  % Boltzmann's constant (J/K)

% Spectral radiance of a black body
U = ((2 * pi * h * c^2) ./ lambda.^5) .* ...
    (1 ./ (exp(h * c ./ (lambda * k * T)) - 1));

% Integration
A = trapz(lambda, e .* U);
B = trapz(lambda, U);
e_avg = A / B;

disp(['Average Emissivity: ', num2str(e_avg)]);
```